A First Estimate of $\sigma(e^+p \rightarrow e^+W^\pm X)$ and Studies of High p_T Leptons with the ZEUS Detector at HERA

David Waters

—

Wolfson College
University of Oxford

Thesis submitted in partial fulfilment
of the requirements for the degree of
Doctor of Philosophy
University of Oxford, Hilary Term 1998

A First Estimate of $\sigma(e^+p \rightarrow e^+W^\pm X)$ and Studies of High p_T Leptons with the ZEUS Detector at HERA

David Waters
Wolfson College, University Of Oxford

Thesis submitted in partial fulfilment of the
requirements for the degree of Doctor of Philosophy
University of Oxford, Hilary Term 1998

Abstract

ZEUS events containing high p_T electrons and muons have been studied, with particular emphasis on the search for W and Z production and decay to leptons. An analysis of events containing high p_T electrons in addition to missing momentum has allowed a first estimate of the cross section for the process $e^+p \rightarrow e^+W^\pm X$ in e^+p collisions at $\sqrt{s} = 300$ GeV. The measured cross section is in good agreement with the Standard Model expectation of ~ 1 pb. Since the W production cross section is sensitive to couplings at the $WW\gamma$ vertex, the upper limit on the W production cross section set by the ZEUS data has been converted into constraints on the anomalous couplings $\Delta\kappa$ and λ at this vertex. The results of the search for W production in the muon channel are consistent with those in the electron channel and in particular the ZEUS data allows a constraint to be set on the cross section for high p_T muon production in the presence of large hadronic transverse momenta. The results of a search for $Z^0 \rightarrow l^+l^-$ are also presented and the high invariant mass multi-lepton data compared to Standard Model expectations. Finally, an analysis of radiative charged current scattering, $e^+p \rightarrow \bar{\nu}\gamma X$, provides another probe of the couplings at the $WW\gamma$ vertex which, it is shown, may be important in the future in excluding certain coupling combinations consistent with a measured value for the single W production cross section.

Acknowledgements

The size and nature of modern high energy physics experiments makes it impossible to acknowledge by name everyone who has helped and guided me over the years. My greatest debt is of course to my supervisor, Roman Walczak, for initiating me into world of ZEUS, suggesting the project that eventually developed into this thesis and generally taking a close interest in my work over the last three years. Other members of the Oxford ZEUS group, in particular Robin Devenish and Roger Cashmore, have been invaluable sources of wisdom and encouragement throughout.

The fact that the whole W and Z analysis effort exists at all within ZEUS is largely due to the efforts of Takanobu Ishii, Grzegorz Grzelak and Valerie Noyes. I would also have got nowhere had it not been for the day to day assistance of a number of people at DESY - in particular Bruce Straub, Uli Katz and other members of the exotics group helped me tremendously in the early days. More recently, the dedicated efforts of Masahiro Kuze, Takashi Matsushita and other collaborators from Tokyo have proved invaluable. I am grateful to the British Council for offering the funds to travel to Japan to develop this close cooperation. I dread to think of the number of people I have plagued with awkward questions over the years - here I must mention Ulrich Baur for his readiness and ability to clear up my frequent misunderstandings. In addition it has been a pleasure to share offices with and learn a lot from a number of people both in Oxford and DESY - James, Arnie, Jason, Jo, Helen, Dave Bailey and others.

It's my many friends in Oxford who have kept me sane over the years - I must mention in particular Chandy, Shond, Conor and John. Wolfson College has been a great place to spend my post-graduate years. In Germany, Eram and Andy turned what could have been a grim year at DESY into a very happy one. Jane, Paul and Vicky, Roger and Katy, the members of my language class at 'Der, Die, Das' and so many others contributed to my having a memorable time in Hamburg.

Finally, I would like to thank my family for providing a welcome retreat from the stress of research and Oxford and not asking *too* often when I was going to finish writing my thesis.

To Mum, Dad and Rob.

Contents

1 Introduction and Outline **1**

2 The ZEUS Detector at HERA **3**

2.1 HERA 3

2.1.1 Design and Operating Parameters 3

2.1.2 Luminosities 4

2.1.3 Upgrades 5

2.2 The ZEUS Detector 6

2.2.1 Uranium Scintillator Calorimeter 8

2.2.2 Central Tracking Detector 11

2.2.3 Barrel and Rear Muon System 13

2.2.4 Forward Muon System 14

2.2.5 Luminosity Monitor 14

2.2.6 Three Level Trigger 15

2.2.7 Offline Event Reconstruction 16

3 The Standard Model and Beyond **17**

3.1 Electron Proton Scattering 17

3.2 Photoproduction and DIS 19

3.2.1 Direct and Resolved Photoproduction 19

3.2.2 Increasing Q^2 20

3.2.3 Neutral and Charged Current DIS 21

3.3 Two Photon Processes 22

3.4 Gauge Boson Production 23

3.5 Gauge Boson Self-Couplings and the $WW\gamma$ Vertex 25

3.5.1 The Effective Lagrangian Approach 25

3.5.2 Existing Experimental Constraints 26

3.6 Beyond the Standard Model 29

4 W and Z Production at HERA **32**

4.1 W Production 32

4.1.1 Cross Section Calculation 32

4.1.2 Cross Section Uncertainties 35

4.1.3 Event Characteristics 37

4.1.4 Anomalous Couplings 39

4.2 Z Production 45

4.2.1 Cross Section Calculation 45

4.2.2 Event Characteristics 45

4.3 Limitations of EPVEC 47

5 Monte Carlo Simulation **50**

5.1 Deep Inelastic Scattering 50

5.1.1 Born-level Cross Sections 51

5.1.2 QED and Weak Corrections 51

5.1.3 QCD Corrections 53

5.1.4 Parton Distributions 54

5.1.5 Generator Level Cuts 54

5.2 Radiative Charged Current Scattering 54

5.3 Photoproduction 56

5.3.1 Generator Level Cuts 58

5.4 Bethe-Heitler Process 59

5.5 Vector Meson Production 60

5.6 QED Compton Events 61

5.7 Detector Simulation 61

6 Lepton Identification **63**

6.1 Introduction 63

6.2 Electron Identification 63

6.2.1 The SINISTRA Electron Finder 63

6.2.2 Electron Position Determination 65

6.2.3 Track Matching Requirements 67

6.2.4 Electron Isolation Requirements 67

6.2.5 Photon Identification 69
6.3 Muon Identification 69
6.3.1 Calorimeter Requirements 70
6.3.2 Tracking Requirements 72
6.3.3 Barrel and Rear Muon Chambers 74
6.4 Tau Identification 78

7 The Data Samples 79

7.1 Events with Missing p_T 79
7.1.1 Trigger Requirements 79
7.1.2 Missing p_T + Electron Sample 81
7.1.3 Missing p_T + Muon Sample 82
7.2 Events with High Transverse Energy 85
7.2.1 Trigger Requirements 85
7.2.2 High E_T Event Sample 86
7.3 Muon Triggered Events 87
7.3.1 Trigger Requirements 87
7.3.2 Barrel Muon Sample 88

8 High p_T Electrons 91

8.1 Electrons in Events with Missing p_T 91
8.1.1 Selecting $W \to e\nu$ Events 95
8.1.2 The Final Event Sample 101
8.1.3 Neutral Current Control Sample 102
8.1.4 Systematic Uncertainties in the Selection Efficiency 105
8.1.5 Error on the Background Estimate 108
8.1.6 Error on the Integrated Luminosity 109
8.1.7 Cross Section Upper Limit 109
8.2 Radiative Charged Current Scattering 110
8.2.1 Radiative Event Selection 112
8.2.2 Systematic Error on the Photon Finding Efficiency 115
8.2.3 Error on the Background Estimate 116
8.2.4 Cross Section Upper Limit 116
8.2.5 Relaxing the Cuts 117

8.3 Multi-Electron Events at High E_T 119
8.3.1 Selecting $Z^0 \rightarrow e^+e^-$ Events 121
8.3.2 High Mass Multi-Electron Events 121
8.3.3 Systematic Error on the $Z^0 \rightarrow e^+e^-$ Selection Efficiency 124
8.3.4 Error on the Background Estimate 125
8.3.5 Cross Section Upper Limit 125

9 High p_T Muons 127

9.1 Muon Finder Efficiencies 127
9.2 Transverse Momentum Measurements 134
9.2.1 Definitions 134
9.2.2 p_T Resolution 134
9.3 Muons in Events with Missing p_T 136
9.3.1 Systematic Uncertainties in the Selection Efficiency 140
9.3.2 Error on the Background Estimate 142
9.3.3 Cross Section Upper Limit 142
9.4 Barrel and Rear Muon Events 143
9.4.1 Systematic Uncertainties in the Selection Efficiency 146
9.4.2 Error on the Background Estimate 149
9.4.3 Cross Section Upper Limit 149
9.5 Multi-Muon Events 150
9.5.1 Selecting $Z^0 \rightarrow \mu^+\mu^-$ Events 150
9.5.2 Systematic Uncertainties in the Selection Efficiency 152
9.5.3 Error on the Background Estimate 155
9.5.4 Cross Section Upper Limit 155
9.5.5 $Z^0 \rightarrow \mu^+\mu^-$ Signal to Background Ratio 155

10 The 1997 Data 157

10.1 Neutral Current Backgrounds Revisited 157
10.2 $W \rightarrow e\nu$ Search 158
10.2.1 Properties of the Events 158
10.2.2 Extracting a Cross Section 163
10.3 Radiative Charged Current Scattering 165
10.4 $Z^0 \rightarrow e^+e^-$ Search 166

10.5 $W \to \mu\nu$ Search 168

10.5.1 Events with Missing p_T 168

10.5.2 Barrel and Rear Muon Events 170

10.6 $Z^0 \to \mu^+\mu^-$ Search 172

11 Interpretations and Conclusions 175

11.1 W Production and Decay $W \to e\nu$ 175

11.2 W Production and Decay $W \to \mu\nu$ 180

11.2.1 Events with Large Hadronic Transverse Momenta 180

11.3 Radiative Charged Current Scattering 182

11.4 Z Production and Leptonic Decay 183

11.5 Hadronic Decay Channels 185

11.6 Discussion 185

11.6.1 Future Limits from Single W Production 186

11.6.2 Future Limits from Radiative Charged Current Scattering 187

11.7 Conclusions 190

A Statistical Methods 192

A.1 Upper Limits 192

A.1.1 Upper Limits in the Presence of a Known Background 192

A.1.2 Incorporating Experimental Uncertainties 193

A.2 Maximum Likelihood Cross Section Determination 194

Chapter 1

Introduction and Outline

The production of W and Z bosons in ep collisions is a Standard Model process with a small but uncertain cross section. The original search for events with high p_T electrons in addition to missing p_T was intended to place limits on the cross section for W production and was reported in [1]. Such limits on the W production cross section enable limits to be placed on certain anomalous couplings at the $WW\gamma$ triple gauge boson vertex. In addition the leptonic decays of W and Z bosons constitute one of the most serious Standard Model backgrounds to many new physics searches, for which high p_T leptons and missing energy are common signatures. In this context the recent observation of a number of events with a high p_T lepton in addition to missing energy reported by the H1 experiment is interesting and deserves comparison with the ZEUS data [2].

The main body of this work is therefore devoted to the analysis of events with high p_T electrons and muons with missing p_T. Multi-lepton final states are also examined, mainly in the context of a search for Z production. Finally radiative charged current scattering, an alternative probe of the $WW\gamma$ vertex, forms the subject of a separate analysis.

With the full 1994-97 ZEUS data a first estimate of the W production cross section in e^+p collisions is possible. In future years, as the luminosities delivered by HERA continue to increase rapidly, so the cross sections for W production and other interesting processes in ep collisions will be measured with increasing accuracy, eventually allowing important tests of the Standard Model to be made and sensitive searches for new physics signals to be performed. This work should therefore be viewed only as a first attempt to explore some of the analyses and methods that will become increasingly interesting and important at HERA in future years.

The ZEUS experiment at HERA is introduced in chapter 2. Chapter 3 covers the basic kinematics of ep collisions and the important Standard Model sources of events with high p_T leptons. Also discussed are some of the scenarios for physics beyond the Standard Model that give rise to the generic signature of high p_T leptons and missing energy. W and Z production and its Monte Carlo implementation are examined in more detail in chapter 4, while chapter 5 briefly outlines the simulation of other physics processes at HERA. Chapter 6 is a description of the lepton identification techniques used and the resulting event samples are presented in chapter 7. Chapter 8 deals with the analysis of events containing high p_T electrons and radiative charged current scattering and chapter 9 with the analysis of events containing high p_T muons. A preliminary extension of some of the important analyses to include the 1997 ZEUS data is outlined in chapter 10. Finally, chapter 11 combines the results of previous chapters to draw some conclusions and briefly discuss the future prospects for these measurements at HERA.

Chapter 2

The ZEUS Detector at HERA

This chapter outlines the basic features of HERA and describes the main elements of the ZEUS detector, one of the two general purpose experiments located at HERA. Since the ZEUS detector is comprised of many complex sub-detectors, only the important components for the analysis presented here are described in any detail.

2.1 HERA

2.1.1 Design and Operating Parameters

The **H**adron **E**lectron **R**ing **A**ccelerator is located at the Deutsches Elektronen-Synchrotron (DESY) in Hamburg [3]. It is the first accelerator capable of colliding electron and proton beams, enabling an increase in the available *ep* centre of mass energy by more than an order of magnitude compared to the previous generation of fixed target deep inelastic scattering experiments.

The layout of HERA and the pre-accelerator complex are shown in fig. 2.1. The HERA electron [1] and proton storage rings are 6.3 km in circumference, with experiments located at four equidistant straight sections as indicated. The pre-accelerator complex consists of separate e^+ (or e^-) and H$^-$ LINAC's that accelerate the electrons and hydrogen ions to 450 MeV and 50 MeV respectively. The electrons are further accelerated to an energy of 7 GeV in the DESY II synchrotron and the protons from the stripped hydrogen ions are accelerated to an energy of 7.5 GeV in the parallel DESY III synchrotron. The final stage of pre-acceleration takes place in the larger PETRA [2] ring, modified to store both electrons and protons. Separate radio-frequency (r-f) cavities accelerate the electrons and protons to their final HERA injection energies of of 12 GeV and 40 GeV respectively. During

---

[1] In the following electron is used as a generic term to denote either electron or positron.

[2] '**P**ositron **E**lectron **T**andem **R**ing **A**ccelerator.'

Figure 2.1: *The layout of the HERA main accelerator and pre-accelerator complex.*

the pre-acceleration sequence the bunch structure is also arranged and the bunch charges accumulated to their final HERA values.

HERA itself consists of separate electron and proton storage rings mounted alongside each other. The electron beam energy is limited by the synchrotron radiation losses in the curved sections of the ring and to this end 16 powerful superconducting radio-frequency cavities augment the main r-f cavity system. The electron beam bending magnets create a modest 0.165 T magnetic field. By contrast the proton beam energy is limited by the magnetic fields required to contain the beam and the main technical challenge in the construction of HERA was the installation of 4.65 T superconducting magnets in the curved sections of the proton beam line. Other important HERA design and operating parameters are listed in table 2.1.

2.1.2 Luminosities

As indicated in table 2.1, the instantaneous luminosities achieved to date are approaching the design values, and specific luminosities have in fact exceeded design expectations. However this has coincided with lower than anticipated electron and proton beam currents, which has restricted the total integrated luminosities delivered by HERA. Remarkable progress has nevertheless been made in recent years, as indicated by fig. 2.2. The main reasons for this are the switch from electron to positron running in 1994 and a general improvement in HERA operational efficiency over the years.

HERA Parameter	Design Value		1995	
	electrons	protons	electrons	protons
Energy (GeV)	30	820	27.52	820
Centre of Mass Energy (GeV)	314		300	
Circumference (m)	6336			
Energy Loss per. Turn (MeV)	125	6×10^{-6}	125	6×10^{-6}
Superconducting r-f Cavities	16	-	16	-
r-f Voltage (MV)	200	2.4	200	2.4
r-f Frequency (MHz)	500	208/52	500	208/52
Bending Magnet Field (T)	0.165	4.68	0.165	4.68
Superconducting Magnets	-	640	-	640
Number of Bunches (+ unpaired)	210	210	174 (+15)	174 (+6)
Beam Current (mA)	58	163	~ 30	~ 55
Instantaneous Luminosity ($\text{cm}^{-2}\text{s}^{-1}$)	1.6×10^{31}		$\sim 7 \times 10^{30}$	
Beam σ_x at Interaction Point (mm)	0.30	0.27	0.27	0.18
Beam σ_y at Interaction Point (mm)	0.06	0.09	0.06	0.06
Bunch Length (cm)	0.8	11	0.8	11

Table 2.1: *Some important HERA operating parameters. The design values and those realised during 1995 running are compared.*

The main analyses presented in this work use e^+p data taken during the years 1994-1996. Selecting only good runs [3] corresponds to an integrated luminosity recorded by ZEUS of 20.1 pb^{-1}. The preliminary figure for the 1997 integrated luminosity, making the same good run requirements, is 26.6 pb^{-1}.

2.1.3 Upgrades

During the 1997/1998 break in HERA operations new vacuum pumps were installed in the electron ring which will enable efficient running in e^-p as well as e^+p mode. The electron

---

[3] A good run is a data taking period for which the main ZEUS detector components were fully and correctly operational. A certain number of calorimeter 'holes' or dead cells are nonetheless tolerated and non-critical components, for example the forward muon system, need not be operational. Such components will have separate lists of good runs.

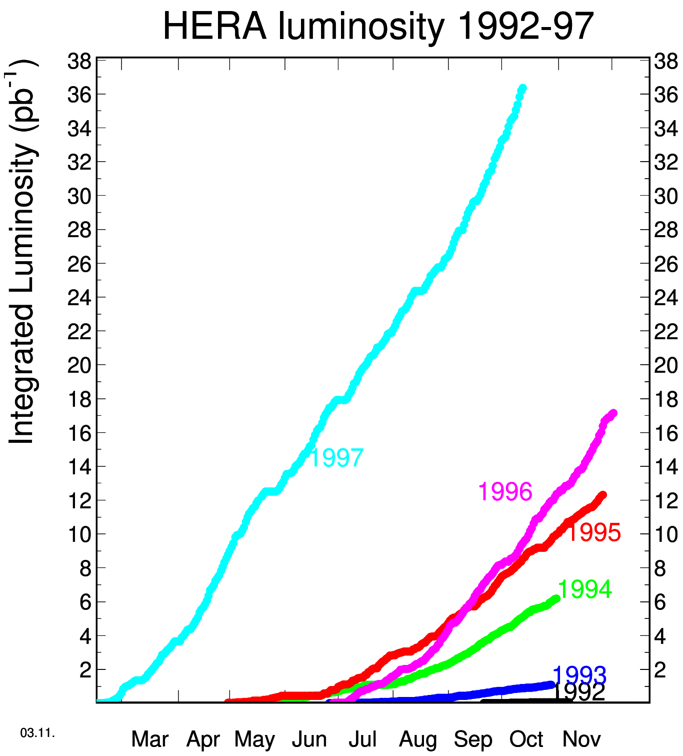

Figure 2.2: *Integrated luminosities delivered by HERA in the years 1992-1997.*

data will complement the positron data, particularly in the areas of new physics searches and electroweak measurements at high Q^2. It is proposed that during the 1999/2000 shutdown a major accelerator upgrade will take place [4]. The goal will be to provide integrated luminosities of the order of 150 pb^{-1} per year by moving quadrupole focusing magnets closer to the ZEUS interaction point (IP). The installation of electron spin rotators in subsequent years and the resulting high longitudinal lepton beam polarisations will make possible many high Q^2 and electroweak precision measurements [5, 6].

2.2 The ZEUS Detector

The ZEUS collaboration consists of over 450 physicists from 11 countries and at least as many support and technical staff from collaborating institutions. The ZEUS detector itself was completed in 1991, approximately five years after formal approval, and began data taking in 1993. It is an almost hermetic detector designed to provide excellent measurements of both the scattered electron and the hadronic final state in electron-proton collisions.

Two cut away views of the detector are shown in figures 2.3 and 2.4. The ZEUS coor-

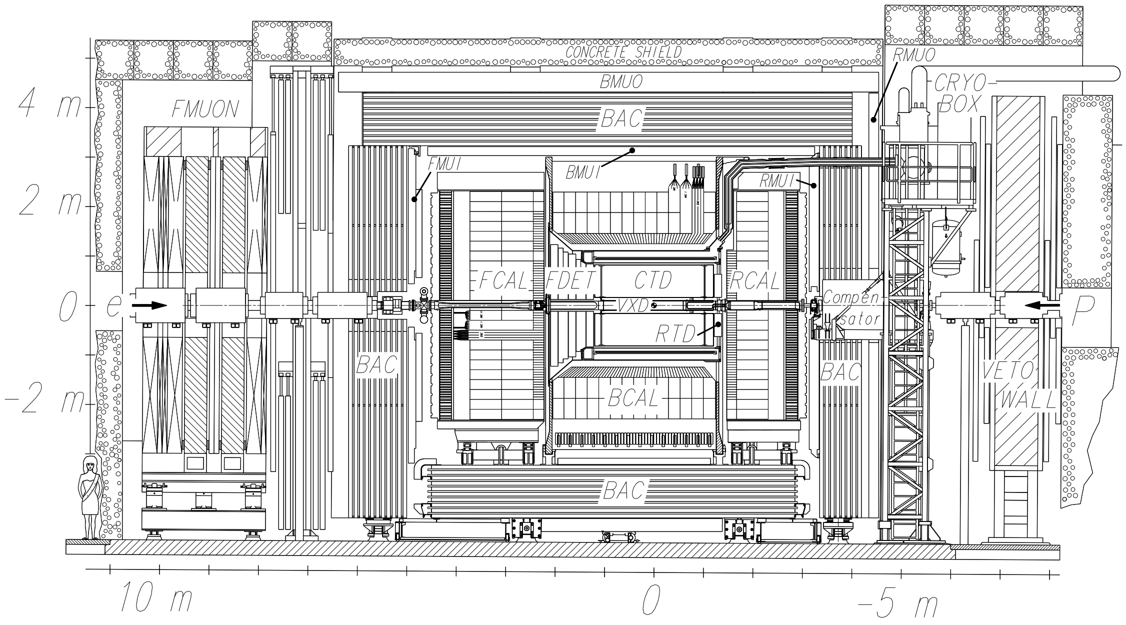

Figure 2.3: *Cross section of the ZEUS detector in the* $\{y, z\}$ *plane at* $x = 0$. *The electron beam enters from the left and the proton beam from the right.*

dinate system is right handed with the z-axis in the direction of the incoming proton beam and the x-axis pointing horizontally towards the centre of HERA. The polar angle, θ, is measured with respect to the incoming proton direction and the azimuthal angle, ϕ, with respect to the x-axis. The main components of the detector that will be described are the uranium scintillating calorimeter (UCAL), the central tracking detector (CTD), the barrel and rear muon detectors (B/RMU) and, briefly, the forward muon spectrometer (FMUON). The upstream luminosity monitor (LUMI), not indicated in the figures, is also described in more detail below. Other components include the forward and rear tracking detectors (FDET and RTD), multi-wire drift chambers that improve the tracking performance and particle identification at small scattering angles. However, for most of the data taking period considered here the FDET was not fully operational. Similarly the vertex detector (VXD), another wire drift chamber, was removed from the end of data taking in 1994.

A superconducting solenoid located between the CTD and the inner face of the calorimeter creates a 1.43 T magnetic field for the measurement of charged particle momenta in the central tracking detectors. The plates of the iron return yoke, interleaved with layers of proportional tubes, form the backing calorimeter (BAC), designed to measure the energies of showers that ‘punch through’ the UCAL and provide additional muon identification.

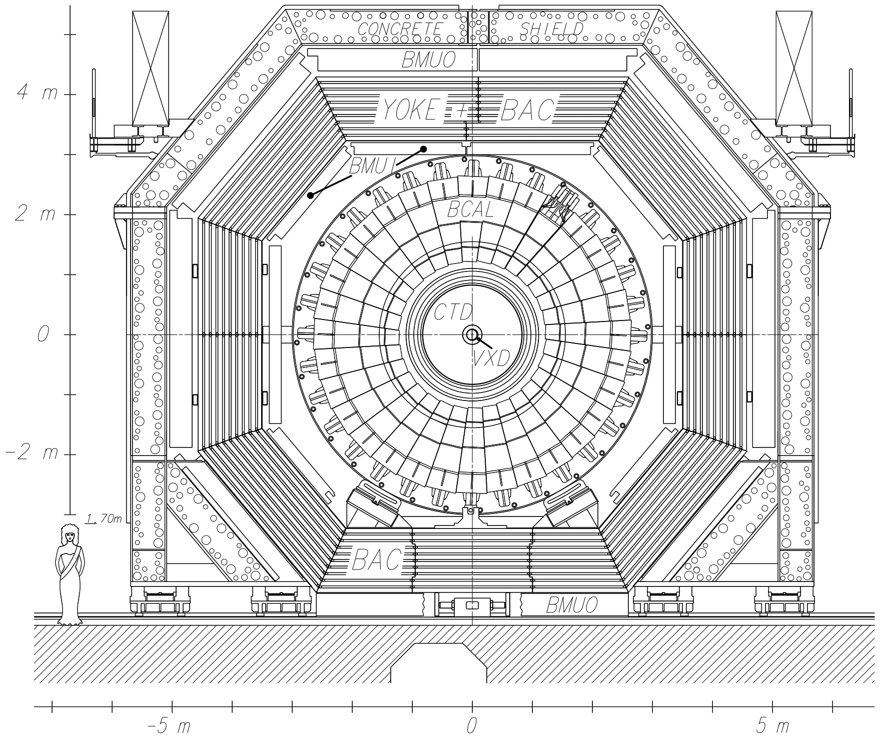

Figure 2.4: *Cross section of the ZEUS detector in the* $\{x, y\}$ *plane at* $z = 0$.

The magnetic field of the return yoke also allows an independent measurement of muon momenta by the barrel muon system. Finally, the iron-scintillator VETOWALL, situated 7.5 m upstream of the IP, absorbs a certain fraction of beam-related background particles and allows events to be vetoed by the passage of penetrating particles. All these detectors any many others are described in full detail in [7, 8].

2.2.1 Uranium Scintillator Calorimeter

The ZEUS uranium scintillator calorimeter is a finely segmented detector covering 99.7% of the solid angle. It provides excellent containment and energy resolution and, above energies of a few hundred MeV, is compensating. The equal response to electrons and hadrons, achieved by tuning the ratio of scintillator to absorber thickness, significantly reduces the systematic uncertainties in the measurement of jet and hadronic final state energies. The polar angle coverages of the three main calorimeters are :

Forward Calorimeter (FCAL)	$2.2° < \theta < 39.9°$,
Barrel Calorimeter (BCAL)	$36.7° < \theta < 129.1°$,

Figure 2.5: *A cut-away view of a ZEUS FCAL module, showing alternating layers of depleted uranium and scintillator strips, wavelength shifters and photomultipliers.*

Rear Calorimeter (RCAL)	$128.1^\circ < \theta < 176.5^\circ$.

Fig. 2.5 shows a module of the forward calorimeter. Each module is divided into towers with 20×20 cm square faces. Each tower is segmented longitudinally into an electromagnetic (EMC) section with a depth of 25 radiation lengths (χ_0) or 1 interaction length (λ) and two hadronic (HAC) sections with depths of 3.1 λ each. The blue light created by the passage of charged particles through the scintillator material enters the wavelength shifter material which absorbs the light in a specially chosen dye and re-emits it isotropically. A fraction of this secondary light is internally reflected along the length of the wavelength shifter and enters the photomultiplier tubes (PMT's) mounted at the the rear of each CAL module. Two wavelength shifters are attached to each hadronic section and eight to each EMC section, resulting in 20 × 5 cm EMC 'cells'. The barrel calorimeter and rear calorimeter modules have very similar designs, but with shallower hadronic sections of $2 \times 2.1\lambda$ and $1 \times 3.1\lambda$ respectively, since the greatest hadronic energy flows are in the proton beam

direction. Furthermore, the RCAL EMC section is subdivided into 10×20 cm cells and the BCAL EMC into approximately 5×24 cm cells due to the different barrel geometry.

The fact that each calorimeter cell is read out by two independent photomultiplier tubes is crucial for detailed event reconstruction. Measuring the difference between the two PMT responses (the so called cell imbalance) provides information on the lateral position of the shower and enables the identification of calorimeter 'sparks', large fake energy deposits due to random photomultiplier discharges. The rate of calorimeter holes or dead cells is also very low since to a good approximation doubling the output from a single working PMT corrects for a second dead PMT.

The uranium calorimeter was originally calibrated with electron, pion and muon test beams up to an energy of around 100 GeV at the CERN SPS [9]. A number of techniques exist, for example using the natural radioactivity of the depleted uranium, lasers and charge injectors to test all the links in the readout scheme and correct calibration constants and PMT voltages as required. Such corrections are expected, for example from the deterioration of the scintillator attenuation length due to exposure to natural and beam related radiation.

The measured calorimeter energy resolutions, in agreement with simulations, are :

$$\frac{\sigma(E)}{E} = \frac{35\%}{\sqrt{E}} \oplus 2\%$$

for hadrons, and

$$\frac{\sigma(E)}{E} = \frac{18\%}{\sqrt{E}} \oplus 1\%$$

for electrons, with E measured in GeV. In addition to energy measurements the calorimeter cells provide an accurate time determination. For example, the resolution with which the time is measured for 15 GeV deposits in the EMC sections is less than 0.7 ns. Good timing is critical for rejecting beam related and cosmic muon backgrounds at the trigger level and offline.

The energy resolutions quoted above were measured in test beam conditions with no inactive material placed in front of the calorimeter cells. The presence in reality of the superconducting coil and various mechanical and support structures between the interaction point and the calorimeter, plotted in units of radiation lengths in figure fig. 2.6, affects the energy measurement in a number of ways. One effect is the energy loss of single particles traversing the inactive material before entering the active volume of the calorimeter and to this end the dead material map shown here enters into the calculation of the corrected hadronic p_T and electron energy discussed in chapter 10. Electrons can also shower in the regions of high dead material before reaching the calorimeter and events are observed, for example, where an early showering electron in the B/RCAL boundary region [4] gives rise to a fake low energy muon signal in the calorimeter. In general the polar angle structures visible in fig. 2.6 are reflected in the lepton finding efficiencies presented in chapter 6, although there are other effects at the calorimeter boundaries, such as the efficiency with which energy clusters in different calorimeter sections are combined, that can also affect lepton identification in these regions.

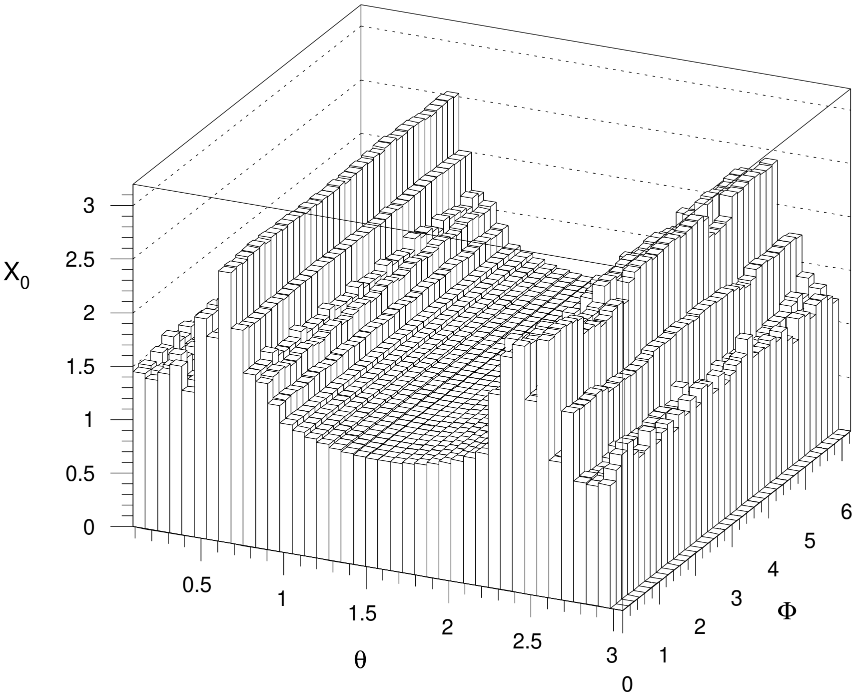

Figure 2.6: *The inactive material between the nominal interaction point and face of the calorimeter as a function of polar and azimuthal angles, measured in radiation lengths.*

2.2.2 Central Tracking Detector

The ZEUS central tracking detector is a large multi-wire drift chamber that sits at the heart of the ZEUS detector. It is designed to operate in high magnetic fields in order to provide a good momentum measurement for the highest p_T tracks, dE/dx information for particle identification and to locate the primary interaction vertex. The latter function is particularly important for the rejection of beam related backgrounds at the trigger level.

---

[4] The boundaries between the different calorimeter sections are sometimes referred to as 'cracks'.

More details of the design and construction of the CTD can be found in [10, 11].

A single CTD octant is shown in fig. 2.7. Rows of eight sense wires alternate with rows of high voltage field shaping wires. Ground wires located between each pair of sense wires ensure an approximately uniform electric field perpendicular to the wire rows. A Lorentz angle of 45%, obtained by selecting a suitable gas mixture (currently $Ar/CO_2/C_2H_6$: 90/8/2) and electric field strength, gives ionisation drift trajectories approximately along lines of constant radius, resulting in the best sagitta determination and hence track momentum resolution.

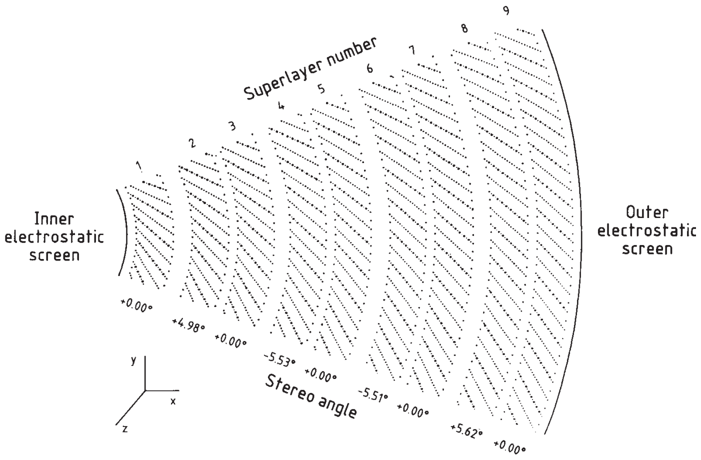

Figure 2.7: *An end-on view of a single CTD octant. Sense wires are indicated by larger dots than the more numerous field shaping wires.*

There are a total of nine superlayers extending from a radius of 18.2 to 79.4 cm. Stereo superlayers, with a tilt of 5° to the beam axis, allow the reconstruction of polar angles for full length tracks with a similar precision to the reconstruction of azimuthal angles. In addition, all eight sense wires in superlayer 1 and four out of eight in superlayers 3 and 5 are instrumented with a fast z-by-timing system, which allows a determination of the z-coordinate of the wire hit with a resolution of $\sim$ 4 cm by comparing the difference in pulse arrival times at the two ends of the detector. This is primarily of use in the ZEUS first level trigger (see below). All sense wires are read out via Flash Analogue to Digital Converters (FADC's) which digitise the wire pulses at a rate of 104 MHz. Once an event t_0 has been determined the drift times can thus be reconstructed and pulse sizes measured for the dE/dx determination.

The nominal transverse momentum resolution for tracks at 90° is

$$\frac{\sigma_{p_T}}{p_T} = 0.0021\, p_T \ (\mathrm{GeV/c}) \oplus 0.0029 \ ,$$

where the first error corresponds to the intrinsic resolution of the chamber and the second is due to multiple scattering. Tracks are well measured [5] in the polar angle region $15^\circ < \theta < 164^\circ$, although superlayer 1 only tracks can be reconstructed at even shallower angles.

2.2.3 Barrel and Rear Muon System

The barrel muon system, covering the polar angle range $34^\circ < \theta < 133^\circ$ and the rear muon system, extending the coverage as far as $\sim 170^\circ$, are designed to identify the passage of minimum ionising particles and provide an independent momentum measurement where possible from the CTD. A second momentum measurement is particularly important in separating prompt muons from those originating from the secondary decays of particles in the detector. The azimuthal coverage of the muon chambers is limited only in the downward direction by the presence of inner detector support structures (see chapter 6).

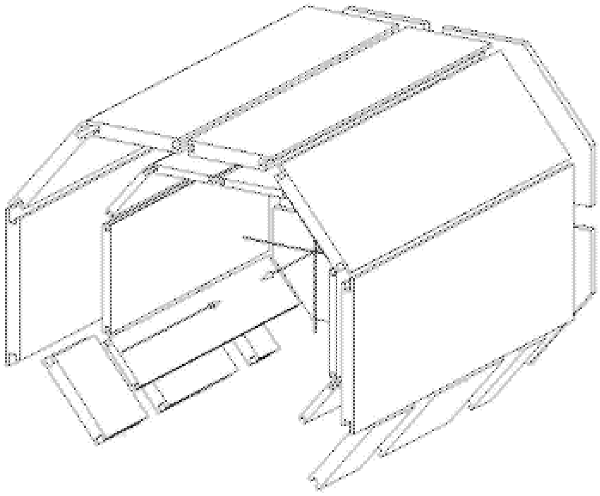

Figure 2.8: *View of the barrel and rear muon chambers. The double planes of limited streamer tubes that make up the inner and outer muon chambers are visible.*

The barrel and rear muon systems are divided into parallel inner (B/RMUI) and outer (B/RMUO) muon chambers, as indicated in figures 2.3 and 2.8. Each muon chamber is itself composed of four planes of limited streamer tubes, arranged in two double layers 20 cm

---

[5] Demanding hits in at least two superlayers.

apart in the BMUI and 40 cm in the BMUO. There are 250 tubes in a typical plane, each 9 mm square and up to 10 m in length. The tubes run parallel to the beam line in the BMU planes and parallel to the x-axis in the RMU system. The drift time determination gives the hit coordinate across each tube to within $\sim$ 1 mm and 13 mm wide analogue strips mounted perpendicular to the LST's give the hit position along each tube with a similar precision.

The arrangement of LST planes ensures that muon track segments can be reconstructed separately in the inner and outer chambers and the momentum determination is made by comparing the two directions across the specially magnetised iron yoke [6]. The overall momentum resolution for well measured tracks is $\sigma(p)/p \simeq 20\%$ for 10 GeV muons.

2.2.4 Forward Muon System

The forward muon spectrometer (FMUON) consists of planes of drift chambers (for accurate track reconstruction) and limited streamer tubes (for fast triggering) placed forward of the main calorimeter. A toroidal system of magnets generates a field of around 1.7 T for an accurate momentum measurement of the highest p_T muons. The forward muon trigger has to cope with large background rates and track occupancy, especially at small polar angles near the beam pipe and in the direction of the proton remnant. In a certain polar angle range there is also no independent momentum determination by the forward muon system, and knowledge of the muon momentum relies on extrapolations and fits between FMU hits and CTD tracks. For these reasons it is difficult to calculate the efficiency with which muons from W and Z decay are reconstructed in the forward muon system and at present forward muon triggered events are not included in the high p_T lepton samples considered here. There are plans to further optimise the forward muon trigger and reconstruction in future to maximise the efficiency with which such events can be tagged down to the smallest possible polar angles.

2.2.5 Luminosity Monitor

The luminosity monitor is designed to measure the instantaneous luminosity by recording the rate of Bremsstrahlung events of the type

$$ep \to e\gamma p \ , \tag{2.1}$$

---

[6] The return flux from the solenoid does not provide a strong enough magnetic field. Normal conducting coils create a nominal toroidal magnetic field of 1.6 T.

for which the cross section of around 329 mb [7] is known with a theoretical error less than 1.0% [12]. The large cross section gives high enough rates to ensure a continuous and accurate luminosity determination during data taking. The electrons from Bremsstrahlung events, having energies lower than the incident beam energy, are deflected out of the beam line by bending magnets and enter a lead-scintillator calorimeter 34 m upstream of the interaction point. Photons leave the beam pipe through a small window 104 m upstream and enter a separate detector where their energies are measured in a second lead-scintillator calorimeter.

Although originally anticipated as a coincidence counter between the electron and photon calorimeters, a more accurate determination of the luminosity is found to be possible using only the rate of tagged photons. This avoids large systematic uncertainties in the knowledge of the electron calorimeter acceptance [12].

In addition to measuring the luminosity, the upstream taggers can be used to tag both photoproduction and radiative events. For photoproduction events with Q^2 in the range $\sim 4 \times 10^{-4}$ to $\sim 10^{-2}$ GeV^2 the scattered electron can be detected with reasonable efficiency in the electron tagger and radiative events can be identified by the presence of a photon in the photon tagger, in coincidence with some activity in the central detector.

2.2.6 Three Level Trigger

A number of factors have dictated the need for a complex and fast trigger system for the ZEUS detector. Firstly, the HERA bunch crossing time is only 96 ns, giving a rate of ~ 10 MHz with which the whole trigger system must be cycled. Secondly, the bunch crossing time is also short compared to the maximum CTD drift time of ~ 500 ns which, along with the processing time taken to reach a trigger decision ($\sim$ few μs), necessitates the use of extensive pipelining. Finally, the expected beam related background rate of $10 - 100$ kHz dwarfs the physics rate of a few Hz. The trigger must thus be extremely discriminating as well as fast. The strategy adopted was to have a three level trigger system combining speed at the lower levels and increasingly sophisticated background rejection at higher levels. A complete description may be found in [13].

The ZEUS first level trigger (FLT) is a hardware trigger distributed across the different components. The output from each component is fed into separate 96 ns pipelines while processors, sometimes taking information from several bunch crossings, take a maximum of 2.5 μs to perform internal component calculations and pass the resulting information

---

[7] This is for $0.1 < E_\gamma < 27.52$ GeV.

to the global first level trigger (GFLT). In the case of the CTD this information is based on a crude estimate of the number of vertex to non-vertex tracks and for the calorimeter consists of fast regional energy sums. The GFLT combines the information from the various component FLT's and issues an accept signal exactly 46 bunch crossings or 4.4 μs after the initial bunch crossing. The only deadtime incurred is therefore in the transfer of data to the second level trigger upon a GFLT accept signal. Overall the first level trigger reduces the 10 MHz bunch crossing rate to an accept rate below 1 kHz.

The ZEUS second level trigger (SLT) is a transputer based trigger distributed across individual components in a similar way to the FLT. There is sufficient time at the SLT to partially reconstruct CTD tracks and use the full calorimeter granularity in the calculation of global energy sums such as missing p_T and transverse energy. The global second level trigger (GSLT), combining the information from the component SLT's, reduces the accept rate to around 100 Hz.

Upon a GSLT accept signal all components send their buffered data to the Event Builder, which combines them together to form whole events. The third level trigger (TLT), a software based trigger employing a large CPU farm, then runs a reduced version of the offline reconstruction code on the events. Since the TLT is the first trigger level at which the data from different components is combined it is possible to calculate vertex corrected calorimeter quantities and find matches between different tracking detectors. The final output rate from the TLT is a few Hz.

For the analysis described in this thesis specific first, second and third level trigger requirements are made. These are described in detail in chapter 7.

2.2.7 Offline Event Reconstruction

Events accepted by the third level trigger are delivered by optical fibre link to the DESY central computing centre and stored on magnetic tape. Before being made available for analysis the events are reconstructed using the full reconstruction software with no trigger related speed restrictions. The final stage of this offline reconstruction uses information from many components to classify the events according to their topology and set corresponding data selection bits, which can be used in the first stage of a specific event selection.

Chapter 3

The Standard Model and Beyond

The first sections of this chapter deal briefly with the kinematics of electron proton scattering and the distinction between deep inelastic and photoproduction processes in *ep* collisions. Two specific processes of interest here, namely lepton pair production and the production of electroweak gauge bosons at HERA are discussed separately and the related topic of triple gauge boson couplings is introduced. Finally, some scenarios for physics beyond the Standard Model are discussed, with particular emphasis on those sharing similar signatures to those for W and Z production.

3.1 Electron Proton Scattering

Figures 3.1(a) and (b) depict single boson exchange neutral current (NC) and charged current (CC) scattering processes in electron proton collisions. The incoming electron and proton have four momenta $k = (E_e, \mathbf{k})$ and $p = (E_p, \mathbf{p})$ respectively, while the scattered lepton has four momentum $k' = (E'_e, \mathbf{k}')$. The centre of mass energy at HERA is sufficiently large that individual fermion masses may be neglected. Then the quantity Q^2 is related to the four momentum transfer q via the expression

$$Q^2 = -q^2 = -(k - k')^2 \ , \tag{3.1}$$

while further Lorentz-invariant kinematic variables are traditionally defined as

$$x = \frac{-q^2}{2p \cdot q} \qquad (0 \leq x \leq 1) \ , \tag{3.2}$$

and

$$y = \frac{p \cdot q}{k \cdot p} \qquad (0 \leq y \leq 1) \ . \tag{3.3}$$

The variable x carries the interpretation in the quark parton model as the fraction of the proton's momentum carried by the struck quark and y is the fraction of the electron's energy

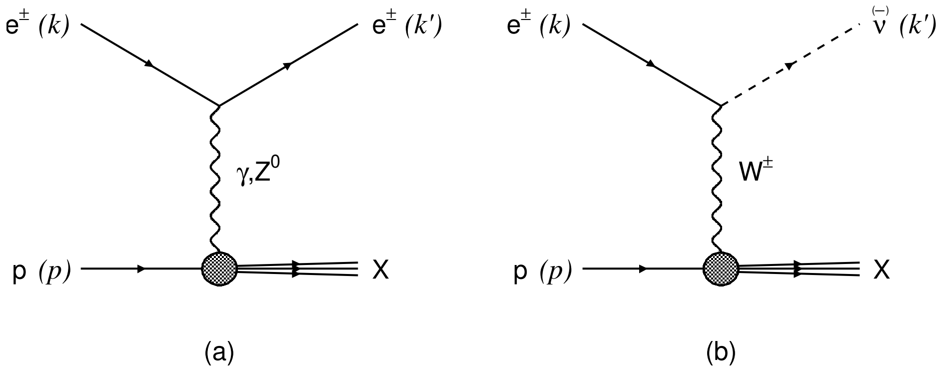

Figure 3.1: *Single boson exchange (a) neutral current and (b) charged current electron proton scattering*

transferred to the hadronic system in the rest frame of the proton. Q^2, x and y are not independent but are related by the equation

$$Q^2 = s \cdot x \cdot y \ , \tag{3.4}$$

where $s = (k+p)^2$ is the square of the centre of mass energy. Thus, the values for any two of the above variables completely specify the kinematics of an event. Importantly, the above definitions assume nothing in particular about the underlying physics of the scattering process and would apply equally, for example, in the case of multi-boson exchange or s-channel processes.

For neutral current events in which the energy E'_e and angle θ'_e of the scattered electron are well measured in the ZEUS detector, a natural method of reconstructing the event kinematics is the so called electron method. Using equations 3.1 and 3.3 we have

$$Q^2 = 2\,E_e\,E'_e\,(1+\cos\theta'_e) \ , \tag{3.5}$$

$$y = 1 - \frac{E'_e}{2E_e}\,(1-\cos\theta'_e) \ , \tag{3.6}$$

where polar angles are measured with respect to the incident proton direction.

For charged current events in which the scattered lepton is a neutrino only a measurement of the hadronic system X allows a reconstruction of the kinematics of the event. The method of Jacquet-Blondel [14] relies on summations over all final state hadrons to calculate the net transverse momentum

$$p_T = \sqrt{(\sum_i p_{x,i})^2 + (\sum_i p_{y,i})^2} \ , \tag{3.7}$$

and the quantity δ, given by [1]

$$\delta = \sum_i (E_i - p_{z,i}) \ . \tag{3.8}$$

The Jacquet-Blondel estimators of y and Q^2 are then

$$y_{JB} = \frac{\delta}{2E_e} \ , \tag{3.9}$$

$$Q_{JB}{}^2 = \frac{p_T{}^2}{1 - y_{JB}} \ . \tag{3.10}$$

In practise the sums over all final state hadrons are replaced by sums over all calorimeter cells above some noise threshold, each energy deposit being treated as a massless pseudo-particle with momentum vector calculated using the geometric centre of the cell and the measured event vertex. The usefulness of the Jacquet-Blondel estimators of Q^2 and y lies in their insensitivity to forward beam pipe losses, with the proton remnant generally contributing little to p_T or δ.

Clearly for NC events the reconstruction of kinematic variables is over constrained by simultaneous measurements of the scattered electron and hadronic final state. Alternative reconstruction schemes, for example the so called double angle method [15], employ both electron and hadron information and are better estimators of Q^2 and y in certain kinematic regions.

3.2 Photoproduction and DIS

3.2.1 Direct and Resolved Photoproduction

Photoproduction strictly refers to processes involving real or on-shell photons. Since the photon exchanged in neutral current electron proton scattering can never be exactly on shell the term photoproduction refers, in the context of HERA physics, to processes involving *quasi-real* photons with $Q^2 \approx 0$ GeV^2. A loose experimental definition of a photoproduction process is one in which the scattered beam electron is lost in the rear beam pipe [2], which typically restricts Q^2 to be less than a few GeV^2. The generic signature for photoproduction processes is therefore the absence of a scattered electron in the main detector combined with a low value for the longitudinal momentum balance $(E - p_Z)$, defined in equation 3.8 above.

---

[1] For fully contained events with no missing energy δ, sometimes referred to as $(E - p_Z)$, should equal $2 \times E_e = 55$ GeV.

[2] Electrons outside the main ZEUS detector may nevertheless be tagged in down stream detectors, taking the Q^2 coverage as low as $O(10^{-4})$ GeV^2 (see section 2.2.5).

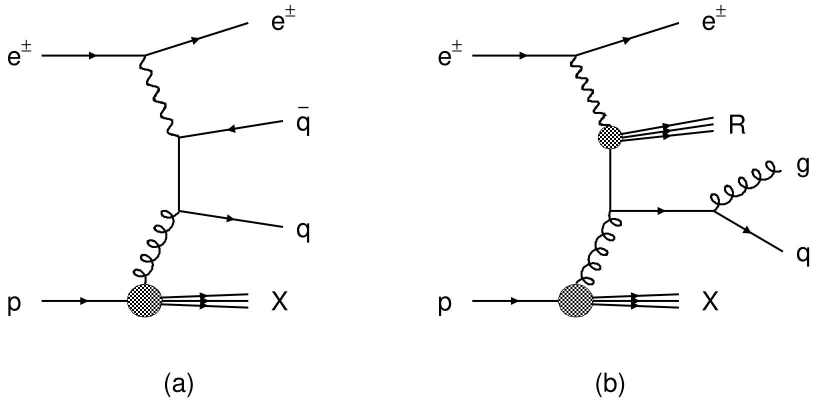

Figure 3.2: *Examples of leading order diagrams for (a) direct and (b) resolved type photoproduction processes. The photon remnant is labelled R.*

The bulk of the total photoproduction cross section is soft, but early results from the ZEUS and H1 experiments have shown that agreement with perturbative QCD calculations exists for that part of phase space in which comparatively large jet transverse momenta, E_T^{jet}, provide a hard scale [16, 17]. Such events consist predominantly of two back-to-back jets, and can be separated at leading order into direct and resolved type processes, as indicated in fig. 3.2 . In direct type photoproduction the full energy of the photon participates in the hard scatter whereas in the resolved process only a fraction of the photon's momentum, associated with a partonic constituent of the photon, enters the hard sub-process. Such events are characterised by extra hadronic activity in a similar direction to that of the incoming electron that is associated with the photon remnant, and have a cross section sensitive to the parton densities inside the photon [18].

3.2.2 Increasing Q^2

If $q = (\nu, \mathbf{q})$ is the four momentum of the virtual photon in the rest frame of the proton then the photon's wavelength is given by [3]

$$\lambda \approx \frac{1}{|\mathbf{q}|} \approx \frac{1}{\sqrt{\nu^2 + Q^2}} \approx \frac{2m_p x}{Q^2} , \tag{3.11}$$

where m_p is the proton mass and $Q^2 \gg (2m_p x)^2$ is assumed. Therefore the inverse wavelength or resolving power of the exchanged photon increases with Q^2 for a given value of x. For Q^2 above a few GeV^2 the partonic constituents of the proton can be resolved and

---

[3] Unless otherwise stated natural units are assumed, where $\hbar = c = 1$.

neutral and charged current deep inelastic scattering (DIS) can be viewed simply as the scattering of electrons from point-like constituents of the proton (see also section 5.1).

The transition region between photoproduction and deep inelastic scattering is closely related to the question of how far down in Q^2 perturbative QCD, through the evolution of the parton densities in the proton, can describe the cross section for *ep* scattering. This is an area of great interest for the HERA experiments, with new data at very low Q^2 allowing this interesting region to be probed for the first time [19].

3.2.3 Neutral and Charged Current DIS

In the deep inelastic scattering regime, cross sections are calculated in the quark parton model. That is to say, *ep* cross sections are calculated simply by folding *eq* cross sections with the quark densities inside the proton. Neglecting radiative corrections and longitudinal structure functions, the differential neutral current cross section in the one-boson exchange approximation is then given by [20] :

$$\frac{d^2\sigma_{NC}(e^\pm p)}{dx\,dQ^2} = \frac{2\pi\alpha^2}{xQ^4}[\{1+(1-y)^2\}\,F_2(x,Q^2)\;\mp\;\{1-(1-y)^2\}\,xF_3(x,Q^2)]\ , \qquad (3.12)$$

where α is the electromagnetic fine structure constant. The structure functions F_2 and F_3 can themselves be written as

$$F_2(x,Q^2) = \sum_f A_f(Q^2)[xq_f(x,Q^2) + x\bar{q}_f(x,Q^2)]\ , \qquad (3.13)$$

$$xF_3(x,Q^2) = \sum_f B_f(Q^2)[xq_f(x,Q^2) - x\bar{q}_f(x,Q^2)]\ , \qquad (3.14)$$

where $q_f(\bar{q}_f)$ describe the density of quarks(anti-quarks) of flavour f inside the proton. The coefficients A_f and B_f contain the electroweak couplings of the γ and the Z to the electron and quarks as well as the effect of the Z propagator mass :

$$A_f(Q^2) = e_f^2 - 2e_f v_e v_f P_Z + (v_e^2 + a_e^2)(v_f^2 + a_f^2)P_Z^2\ , \qquad (3.15)$$

$$B_f(Q^2) = -2e_f a_e a_f P_Z + 4v_e v_f a_e a_f P_Z^2\ . \qquad (3.16)$$

Here e_f, v_f and a_f are the electric charge and the vector and axial vector couplings of the quark flavour f to the Z boson; v_e and a_e are the corresponding couplings of the electron to the weak neutral current. $P_Z = Q^2/(Q^2+m_Z^2)$ denotes the ratio of γ and Z propagators, entering linearly in the $\gamma - Z$ interference terms and quadratically in the pure Z exchange terms.

The differential charged current cross sections for e^+p and e^-p scattering may be written as :

$$\frac{d^2\sigma_{CC}(e^+p)}{dx\,dQ^2} = \frac{G_F^2}{2\pi}\left(\frac{m_W^2}{m_W^2+Q^2}\right)^2 \sum_{i=1}^{2}[\bar{u}_i(x,Q^2)+(1-y)^2 d_i(x,Q^2)] \ , \tag{3.17}$$

$$\frac{d^2\sigma_{CC}(e^-p)}{dx\,dQ^2} = \frac{G_F^2}{2\pi}\left(\frac{m_W^2}{m_W^2+Q^2}\right)^2 \sum_{i=1}^{2}[u_i(x,Q^2)+(1-y)^2 \bar{d}_i(x,Q^2)] \ , \tag{3.18}$$

where $G_F = \pi\alpha/\sqrt{2}\sin^2\theta_W m_W^2$ is the Fermi coupling constant and the summations are over the up and down-type quarks and anti-quarks from the first two quark generations. Parameters m_W and θ_W denote the W boson mass and the weak mixing angle respectively. The propagator dependence is explicit in the cross section formulae for e^+p and e^-p charged current scattering as is the $(V-A)$ structure of the weak interaction, reflected in the $(1-y)^2$ factor suppressing the quark and anti-quark contributions respectively.

In the naïve quark parton model the parton distributions entering the above equations would be functions of the scaling variable x only. The inclusion of scale dependent parton distributions $q_f(x,Q^2)$, evolved in Q^2 using the DGLAP equations [21, 22, 23], takes into account the leading logarithmic QCD corrections to the Born level cross section. Electroweak and higher order radiative corrections are comparatively small and are discussed further in chapter 5.

Fig. 3.3 shows the neutral and charged current cross sections measured by ZEUS at values of Q^2 some two orders of magnitude larger than previously measured at fixed target experiments [24, 25]. For the first time values of $Q^2 \geq m_W^2$ and m_Z^2, for which the neutral and charged current cross sections become comparable, have been reached. The steep fall of the cross sections at the highest Q^2 points is due to the combined effect of the propagator dependence and the steep fall of the parton densities at very high x. With the much higher luminosities expected to be delivered by HERA in the future, measurements of the neutral and charged current cross sections at high Q^2 will enable precision tests of the electroweak Standard Model to be performed [5].

3.3 Two Photon Processes

The most important Standard Model sources of high invariant mass lepton pairs are two photon processes. The Bethe-Heitler process, illustrated in fig. 3.4, dominates the cross section. Compton type processes, in which a photon radiated from the lepton or quark fluctuates into a lepton anti-lepton pair, also contribute to lepton pair production, but at a level of less than 1% of the combined cross section in almost all regions of phase space [26].

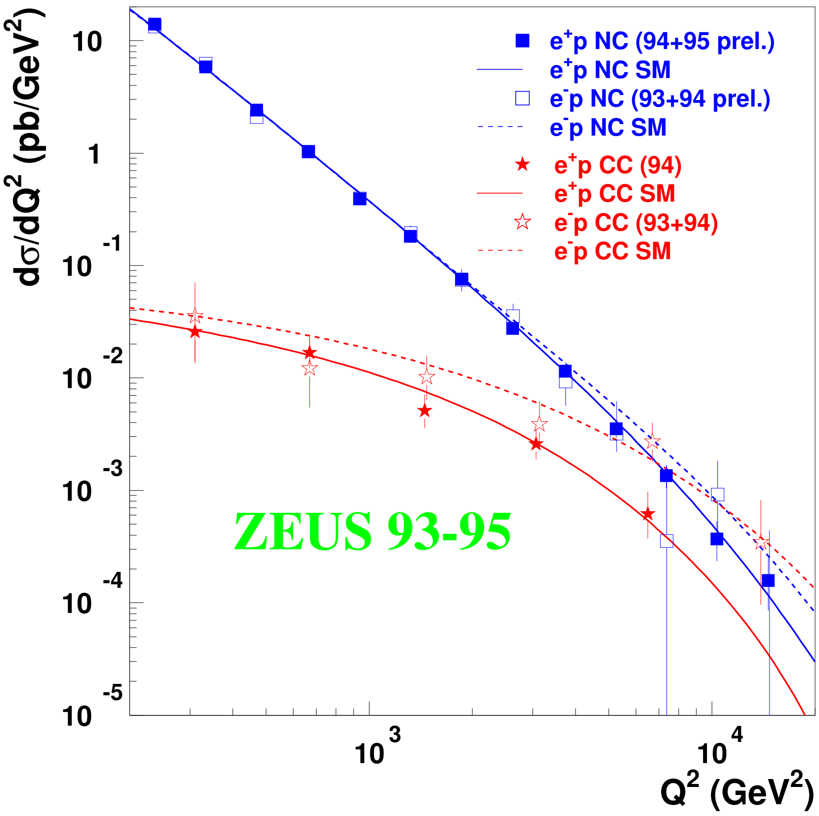

Figure 3.3: *Differential neutral and charged current cross sections at high* Q^2 *measured by the ZEUS experiment.*

The diagrams in fig. 3.4 contain two t-channel photons, and the cross section consequently behaves roughly like $|t_1^{-1}t_2^{-1}|$, where $t_1 = q_1^2$ and $t_2 = q_2^2$ are the virtualities of the two photons. The four momentum transfer to the proton q_2 can be small even for large lepton pair invariant masses, such that elastic pair production (where the term 'elastic' here means that the beam proton emerges intact from the scattering process) is always an important contribution to the total cross section. Moreover inelastic Bethe-Heitler production is dominated by hadronic final states with low mass m_X which can give the same experimental signature as truly elastic events. More details of the Monte Carlo simulation of Bethe-Heitler scattering are given in chapter 5.

3.4 Gauge Boson Production

The HERA experiments are the first to measure electron proton scattering at a high enough centre of mass energy for the production of real or on-shell W and Z bosons. They can be produced in neutral and charged current processes, for example in the case of positron

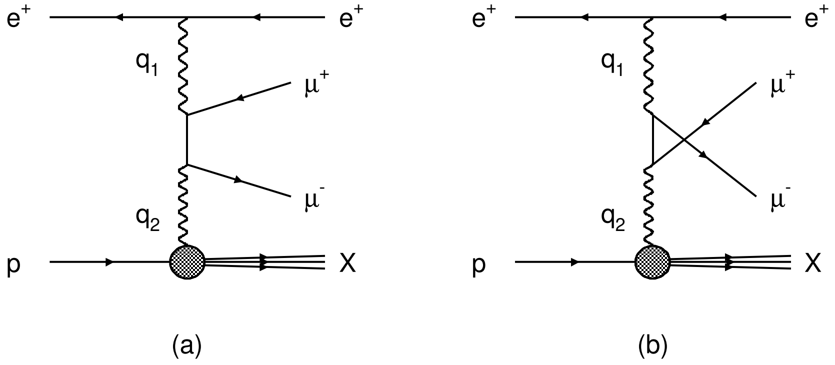

Figure 3.4: *Bethe-Heitler diagrams for lepton pair production in* e^+p *collisions.*

proton scattering :

$$e^+ + p \to e^+ + W^{\pm}/Z^0 + X \ , \tag{3.19}$$

$$e^+ + p \to \bar{\nu} + W^{+}/Z^0 + X \ , \tag{3.20}$$

and, in the case of neutral current scattering, are produced in regions of phase space corresponding to both photoproduction and deep inelastic scattering. The hard scale for the evaluation of both the proton and photon structure functions is provided by the gauge boson mass itself rather than the four-momentum transfer to the scattered lepton. The soft Q^2 spectrum in turn means that only the decay products of the gauge boson itself, together with the hadronic system X, are usually visible in the main ZEUS detector. Many more details concerning the mechanisms of gauge boson production and the expected characteristics of W and Z production events are provided in chapter 4.

In many respects the production of gauge bosons in ep collisions may be regarded as the electroweak radiation of a W or Z from the lepton or quark, analogous to the QED radiation familiar at lower energies. Since the W and Z are fairly heavy on the scale of the available centre of mass energy at HERA, the cross sections are correspondingly small compared, say, to the cross sections for s-channel W and Z production in $p\bar{p}$ or e^+e^- collisions. The highest cross section encountered, namely that for the production of W bosons in neutral current ep scattering, is of $O(1)$ pb. W and Z production is nevertheless an important process to consider for two main reasons. Firstly, the cross section for W production is sensitive to the couplings at the $WW\gamma$ triple gauge boson vertex, the subject of the next section. In general the cross section is enhanced for anomalous, or non-Standard Model values for these couplings and so limits may be placed on any such couplings by measuring the W production cross section. Secondly, W and Z production is the most serious Standard Model background to many of the signals for new physics that may be present at HERA. Such processes can themselves involve W and Z production in the decays of new heavy particles or give rise to the generic signature of high p_T leptons, perhaps with large missing p_T in addition. Such scenarios are outlined in more detail in the last section of this chapter.

3.5 Gauge Boson Self-Couplings and the $WW\gamma$ Vertex

3.5.1 The Effective Lagrangian Approach

The theory of electroweak interactions is a non-Abelian gauge theory, and consequently predicts self-couplings amongst the force carrying particles themselves - namely the W, Z and the photon. Despite the fact that these couplings are uniquely determined by the $SU(2)_L \times U(1)_Y$ gauge structure of the theory, they are relatively poorly constrained by low energy electroweak measurements. One of the tasks of high energy collider experiments is to directly measure these couplings and in so doing either confirm the basic structure of the electroweak interaction or uncover evidence of new physics at comparatively large energy scales [27].

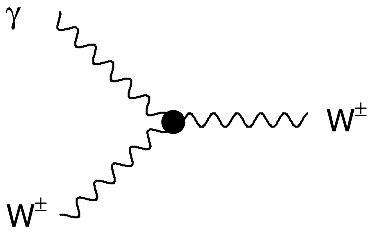

Figure 3.5: *The $WW\gamma$ vertex, parameterised in its most general form by the effective Lagrangian $\mathcal{L}^{eff}_{WW\gamma}$ (see text).*

At HERA, both single W production and radiative charged current DIS $(e^+p \to \bar{\nu}\gamma X)$ [4] are sensitive to the couplings at the $WW\gamma$ vertex, illustrated in fig. 3.5. In order to search for deviations from the Standard Model a so-called effective Lagrangian [5] is constructed that expresses the most general $WW\gamma$ vertex consistent only with Lorentz invariance [28] :

$$\mathcal{L}^{eff}_{WW\gamma} = - ie\,[\,g_1^\gamma(W^\dagger_{\mu\nu}W^\mu A^\nu - W^\dagger_\mu A_\nu W^{\mu\nu}) + \kappa_\gamma W^\dagger_\mu W_\nu F^{\mu\nu}$$

---

[4] Discussed in detail in chapter 5.

[5] For example the Lagrangian describing Fermi's four-point interaction is an effective Lagrangian. It is the low energy expression of a complete high energy theory, valid up to the scale of the new physics (in the case of Fermi's theory, for $q^2 \ll m_W^2$). See [27] and references therein.

$$
\begin{aligned}
&+ \quad \frac{\lambda_\gamma}{m_W^2} W^\dagger_{\lambda\mu} W^\mu{}_\nu F^{\nu\lambda} + i g_4^\gamma W^\dagger_\mu W_\nu (\partial^\mu A^\nu + \partial^\nu A^\mu) \\
&- \quad i g_5^\gamma \epsilon^{\mu\nu\rho\sigma} (W^\dagger_\mu (\partial_\rho W_\nu) - (\partial_\rho W^\dagger_\mu) W_\nu) A_\sigma + \tilde{\kappa}_\gamma W^\dagger_\mu W_\nu \tilde{F}^{\mu\nu} \\
&+ \quad \frac{\tilde{\lambda}_\gamma}{m_W^2} W^\dagger_{\lambda\mu} W^\mu{}_\nu \tilde{F}^{\nu\lambda} \,] \ , \qquad (3.21)
\end{aligned}
$$

where W^μ and A^μ are the W boson and photon fields, $W_{\mu\nu} = \partial_\mu W_\nu - \partial_\nu W\mu$ and $F_{\mu\nu} = \partial_\mu A_\nu - \partial_\nu A_\mu$ are the respective field strength tensors and $\tilde{F}_{\mu\nu} = \frac{1}{2}\epsilon_{\mu\nu\rho\sigma}F^{\rho\sigma}$ denotes the dual of F. Electromagnetic gauge invariance requires for on-shell photons that $g_4^\gamma = g_5^\gamma = 0$ and $g_1^\gamma = 1$. If one furthermore assumes CP conservation, then the couplings g_4^γ, $\tilde{\kappa}_\gamma$ and $\tilde{\lambda}_\gamma$ must equal zero. Hence, only the couplings κ_γ and λ_γ remain to be determined. In the Standard Model at tree level, they are given by

$$\kappa_\gamma = 1 \ \ , \ \ \lambda_\gamma = 0 \ . \qquad (3.22)$$

The terms in $\mathcal{L}^{eff}_{WW\gamma}$ multiplying the couplings κ_γ and λ_γ in fact correspond to terms in the multipole expansion of the W-photon interaction. Then the charge Q_W, magnetic dipole moment μ_W and the electric quadrupole moment q_W of the W^+ are given by [29, 30]

$$Q_W = e \ , \qquad (3.23)$$

$$\mu_W = \frac{e}{2m_W}(1 + \kappa_\gamma + \lambda_\gamma) \ , \qquad (3.24)$$

$$q_W = -\frac{e}{m_W^2}(\kappa_\gamma - \lambda_\gamma) \ . \qquad (3.25)$$

Deviations from the Standard Model are then expressed as non-zero values for the anomalous coupling constants [6]

$$\Delta\kappa_\gamma = \kappa_\gamma - 1 \ \ , \ \ \lambda_\gamma \ . \qquad (3.26)$$

Generally speaking, experimental determinations of the coupling strength at the $WW\gamma$ vertex are used to place limits on $\Delta\kappa_\gamma$ and λ_γ, the remaining couplings taking their Standard Model values. However, since the new physics parameterised by $\mathcal{L}^{eff}_{WW\gamma}$ could presumably violate CP, limits are sometimes also placed on couplings $\tilde{\kappa}_\gamma$ and $\tilde{\lambda}_\gamma$.

3.5.2 Existing Experimental Constraints

The constraints on anomalous triple gauge boson couplings from precision electroweak data are surprisingly weak, essentially due to the possibility of anomalous contributions cancelling

---

[6] Strictly speaking they are not constants. As in the case of Fermi theory, anomalous terms in $\mathcal{L}^{eff}_{WW\gamma}$ violate unitarity constraints at sufficiently high energy. In order to calculate finite anomalous cross sections the anomalous couplings are given a form-factor behaviour, often of the form $\Delta\kappa_\gamma(q^2) = \Delta\kappa^0_\gamma/(1+q^2/\Lambda^2_{FF})^2$ where the form factor scale Λ_{FF} is related to the scale of the new physics. It is important to compare different experimental constraints on anomalous couplings computed at the same value of Λ_{FF}.

when more than one coupling is allowed to deviate from its Standard Model value. Even to claim that anomalous couplings must be at most of $O(1)$ requires certain theoretical assumptions to be made [27].

Turning to direct measurements, the $WW\gamma$ vertex can be probed by a number of different reactions in high energy $p\bar{p}$ and e^+e^- collisions. Figures 3.6(a) and (b) are examples of Feynman diagrams contributing to radiative W production and W^+W^- production respectively. Although the measurement of W^+W^- production at LEP II will soon provide comparable limits, the most stringent limits currently available are provided by measurements made at the Tevatron $p\bar{p}$ collider. An additional advantage of measurements made in $p\bar{p}$ collisions is that the $WW\gamma$ vertex can be probed, through radiative W production, independent of any assumptions about the WWZ vertex. In contrast W^+W^- production is mediated by both s-channel photon and Z boson exchange and the two triple gauge boson couplings cannot be separately measured. In general limits are only obtained by assuming either $\Delta\kappa_\gamma = \Delta\kappa_Z$ and $\lambda_\gamma = \lambda_Z$, or by assuming that the anomalous $WW\gamma$ and WWZ couplings are related as prescribed in the $SU(2)_L \times U(1)_Y$ motivated 'HISZ' scenario [31].

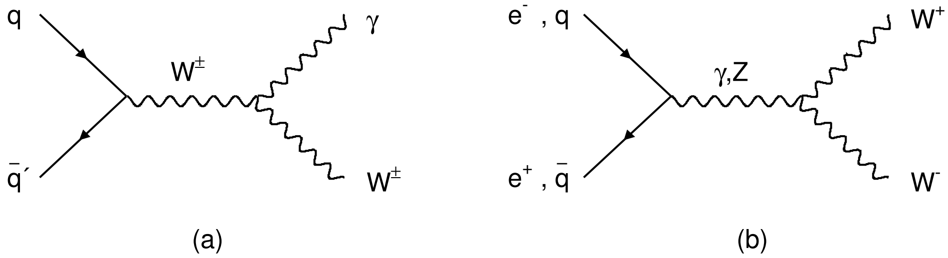

Figure 3.6: *Examples of Feynman diagrams for (a) radiative W production and (b) W^+W^- production in $p\bar{p}$ and e^+e^- collisions.*

The current limits on $\Delta\kappa_\gamma$ and λ_γ are summarised in fig. 3.7 [32]. Also shown are the regions allowed by a recent CLEO measurement of the process $b \to s\gamma$ [33]. More details of the measurement of radiative W production giving rise to the latest limits may be found in [34]. The 95% confidence level limits, based on 93 pb^{-1} of $p\bar{p}$ data taken at $\sqrt{s} = 1.8$ TeV and assuming a form factor scale of 1.5 TeV, are

$$-0.93 \ < \ \Delta\kappa_\gamma \ < \ 0.94 \quad (\lambda_\gamma = 0) \ , \tag{3.27}$$

$$-0.31 \ < \ \lambda_\gamma \ < \ 0.29 \quad (\Delta\kappa_\gamma = 0) \ . \tag{3.28}$$

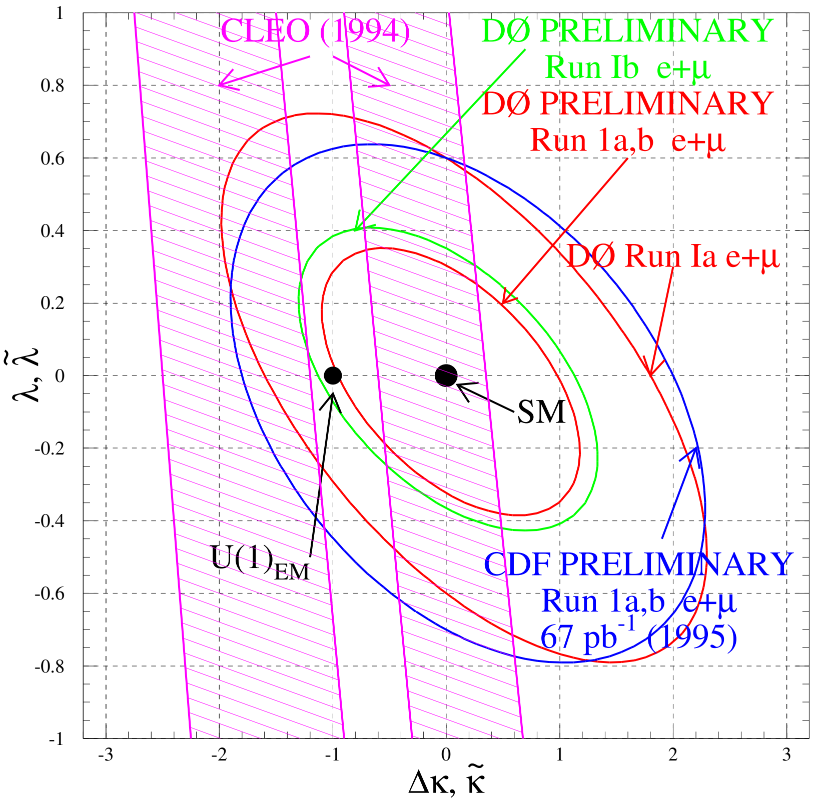

Figure 3.7: *Recent limits on anomalous couplings at the $WW\gamma$ vertex (see text). Note that the interpretation of the results as constraints on the CP violating couplings $\tilde{\kappa}$ and $\tilde{\lambda}$ is not considered here.*

Better limits on $\Delta\kappa_\gamma$ have been obtained from an analysis of W^+W^- production, but only on the assumption of identical $WW\gamma$ and WWZ couplings [35, 36].

The present limits on the anomalous couplings at the $WW\gamma$ vertex are particularly interesting in that they exclude for the first time the case $\kappa_\gamma = 0$ (indicated by $U(1)_{\rm EM}$ in fig. 3.7) and are comparable to the $O(1)$ limits on the anomalous couplings that can be extracted under reasonable assumptions from the electroweak precision data. Given the integrated luminosities delivered to date, the HERA experiments cannot match the sensitivity to $\Delta\kappa_\gamma$ and λ_γ currently achieved at the Tevatron and LEP II experiments. With the high luminosities anticipated for the future, however, the HERA limits, particularly on $\Delta\kappa_\gamma$, should complement those obtainable at other colliders [37].

Given the current limits on $\Delta\kappa_\gamma$ and λ_γ, any anomalous W production observed in the current HERA data would therefore more likely have a different source than a non-Standard Model coupling at the $WW\gamma$ vertex. Some of these are discussed next.

3.6 Beyond the Standard Model

HERA is the natural place to look for certain signatures for new or non-Standard Model physics. Since the *ep* system has both non-zero lepton and baryon numbers, leptoquarks [38, 39] with masses up to $\sqrt{s} \simeq 300$ GeV may be singly produced in s-channel electron-quark fusion. Furthermore, non-resonant exchange may increase the sensitivity to even higher leptoquark masses. Deep inelastic scattering at the highest available Q^2 values probes distance scales of $O(10^{-16})$ cm and neutral current cross sections are sensitive to contact terms of $O(1)$ TeV [40, 41], enabling stringent limits to be placed on quark compositeness and the existence of new electron-quark interactions.

Many types of new physics at HERA involve the production of W or Z bosons or have similar event topologies. One example is the resonant production and decay of excited fermions, illustrated in fig. 3.8. With the energy of the scattered lepton in neutral and charged current *ep* scattering extending up to a few hundred GeV, HERA is a natural place to search for such heavy leptons and quarks [42] and limits already extend beyond those obtainable at LEP I and II [43, 44]. Search channels include both the hadronic and leptonic decays of the W and Z that can be produced in the decay of the excited fermion, as well as the purely electromagnetic decays $e^*, \nu^*, q^* \to e, \nu, q + \gamma$. Standard Model W production is a particular background in those decay channels involving high p_T leptons in addition to large missing transverse momentum. As will be discussed in chapter 4, W production events are usually characterised by comparatively low hadronic transverse momenta and this is equally true of e^* production and decay, which can even be elastic in the sense that the beam proton emerges unscathed [44].

The HERA experiments also have a unique sensitivity to signals for supersymmetry in certain regions of MSSM (Minimal Supersymmetric Standard Model) parameter space [45, 46]. Fig. 3.9 shows examples of R_P conserving and R_P violating SUSY processes in *ep* collisions [7]. The first diagram shows neutralino current scattering, the supersymmetric analogue of neutral current scattering. In general all four neutralino species χ_i^0 can be exchanged, and the decays of both squarks and selectrons are assumed to involve the lightest neutralino species χ_1^0 only. Since, in addition, the lightest neutralino is assumed to

---

[7] $R_P = (-1)^{3B+L+2S}$, where S denotes the spin, B the baryon number and L the lepton number of the particle. Therefore $R_P = 1$ for ordinary particles and -1 for their supersymmetric partners, which differ only by half a unit of spin. If R_P is multiplicatively conserved then supersymmetric particles, or sparticles, must be produced in pairs. If R_P is violated, single sparticle production can take place. A further consequence is that the lightest supersymmetric particle (LSP) must be stable if R_P is conserved. For a general introduction to SUSY see, for example, H.P.Niles, *Phys. Rep.* **110**, 1 (1984).

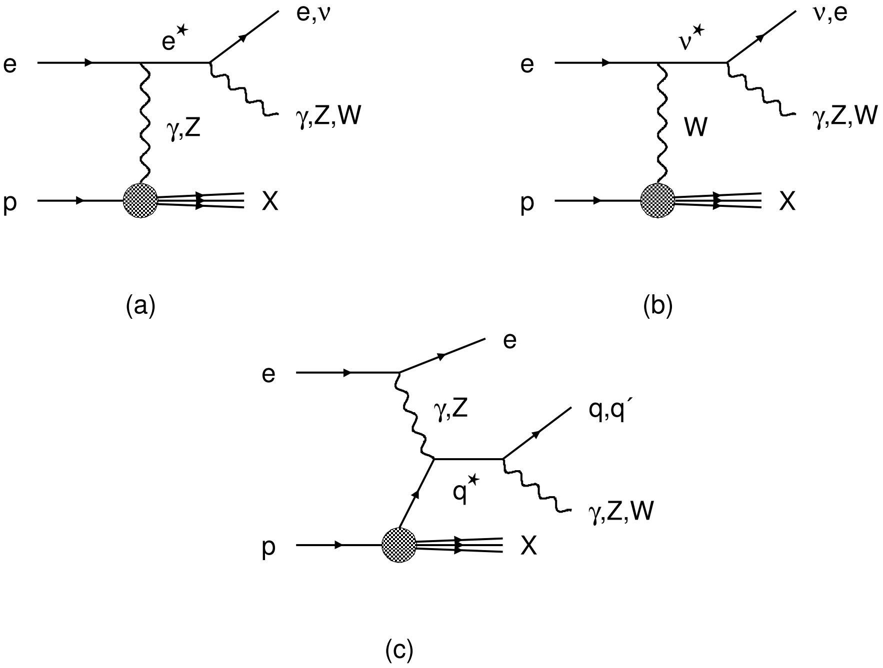

(a) (b)

(c)

Figure 3.8: *Feynman diagrams for the resonant production and decay of excited leptons and quarks in high energy ep collisions.*

be the LSP, it escapes undetected [47]. The characteristic signature of such events is therefore a single scattered electron, generally with large p_T and acoplanar with the scattered quark. This is similar to the event topology for real W production and decay $W \to e\nu$ (see chapter 4). Fig. 3.9(b) is an example of an s-channel diagram for R_P violating squark production. In general many decay channels exist for the produced squark, the simplest being the decay back to an electron and quark. In this case a squark of R_P violating SUSY behaves exactly as a scalar leptoquark. However the squark may also decay as indicated into a chargino χ_1^+, which may subsequently decay into a W^+ and a neutralino. Depending on the fate of the neutralino and the decay of the W, such events may contain high p_T leptons in addition to missing energy or large jet multiplicities. A table of event signatures and a discussion of Standard Model backgrounds, including that arising from W production, may be found in [48].

Many more scenarios for physics beyond the Standard Model at HERA exist than those discussed here. In general, striking event topologies such as high p_T leptons accompanied by missing energy are common to many discovery channels. It is clearly important, therefore, to understand the main Standard Model background to such signals, namely real W and Z

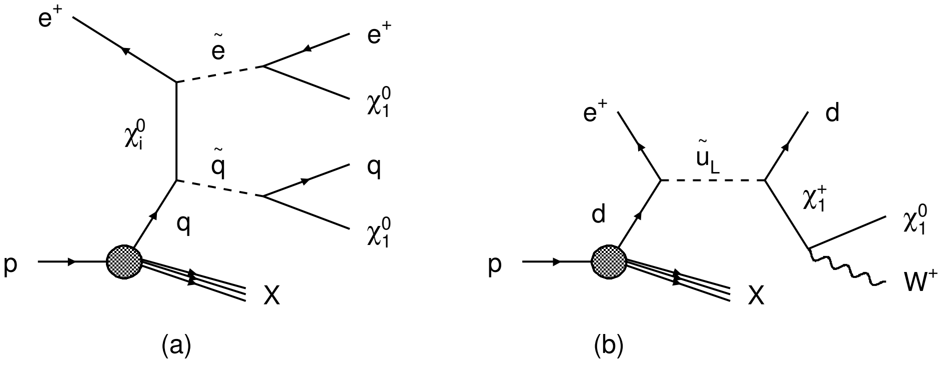

Figure 3.9: *Examples of (a) R_P conserving and (b) R_P violating SUSY processes at HERA.*

production, and to compare the measured high p_T lepton spectrum with the expectations from the Standard Model.

Chapter 4

W and Z Production at HERA

In this chapter the mechanisms and event signatures for the production of real W and Z gauge bosons in ep collisions are discussed. The Monte Carlo generator EPVEC is introduced and the assumptions that underly its treatment of W and Z production examined. A parameterisation of the total W production cross section as a function of anomalous couplings $\Delta\kappa$ [1] and λ is presented, that will eventually allow upper limits to be placed on these couplings. In addition, some Monte Carlo generator level distributions that show the important characteristics of W and Z production events are presented and discussed.

4.1 W Production

4.1.1 Cross Section Calculation

W production can occur in principle through either neutral current like or charged current like interactions :

$$e^+p \rightarrow e^+W^\pm X \quad , \tag{4.1}$$

$$e^+p \rightarrow \bar{\nu}\, W^+X \quad , \tag{4.2}$$

where X denotes the hadronic final state that, in the case of 4.2, can just be the elastically scattered incoming proton but in general is a higher mass state. In the treatment of the process $e^+p \rightarrow e^+W^\pm X$ by the authors of the Monte Carlo generator EPVEC, eight distinct Feynman graphs are considered [49]. These diagrams are shown in fig. 4.1(a) to (g).

Diagrams (a) and (b) represent the emission of a W^+ or a W^- from the initial and final state quarks respectively. Diagram (f) represents the emission of a W^+ from the incoming positron and diagram (g) the emission of a W^- from a scattered anti-neutrino. Diagrams (a) and (b) dominate the amplitude, since (f) and (g) are suppressed by the existence

---

[1] Unless otherwise stated, $\Delta\kappa \equiv \Delta\kappa_\gamma$ and $\lambda \equiv \lambda_\gamma$.

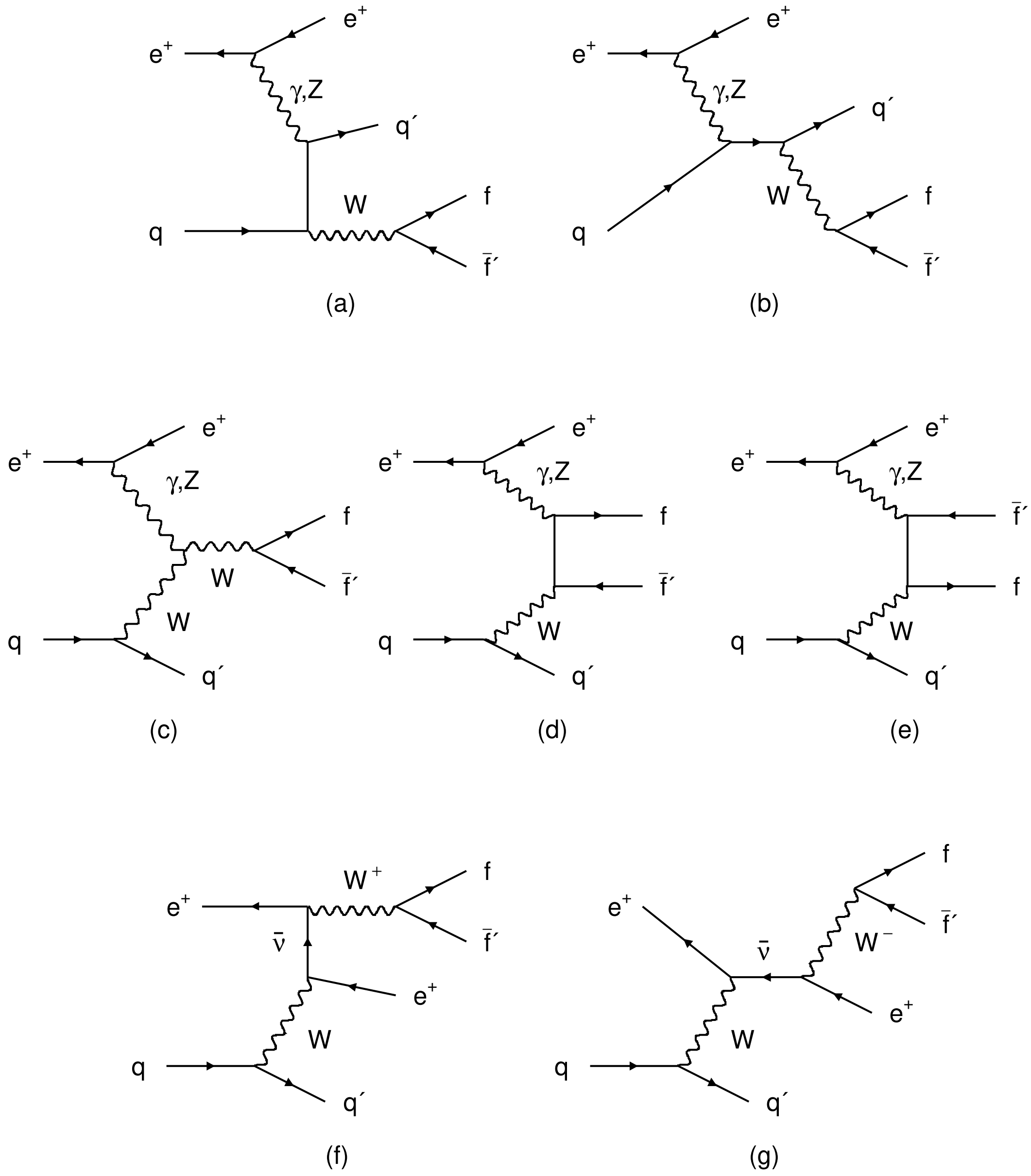

Figure 4.1: *Leading order Feynman diagrams for the process* $e^+p \rightarrow e^+W^\pm X$.

of an extra heavy propagator. Diagram (c) contains a $WW\gamma$ vertex while diagrams (d) and (e), containing off-shell W's, are required to ensure electromagnetic gauge invariant results [49, 50]. Corresponding Feynman diagrams may be drawn for process 4.2 with, for example, the photon propagator in (a) replaced by a W boson propagator. For this and other reasons the cross section for reaction 4.2 is expected to be roughly an order of magnitude smaller than 4.1 and the following discussion is limited to the neutral current process only.

The cross section for the process $e^+p \to e^+W^\pm X$ is calculated by splitting the phase space into two regions :

$$\sigma = \sigma(|u| > u_{cut}) + \int^{u_{cut}} d|u| \frac{d\sigma}{d|u|} \tag{4.3}$$

where

$$u = (p_q - p_W)^2 \tag{4.4}$$

and p_q and p_W are the four momenta of the incoming quark and final state W boson respectively. For the region $|u| > u_{cut}$ the matrix elements for the complete process $eq \to eWq', W \to \mathrm{f\bar{f}'}$ are calculable. In following sections this region will be called the deep inelastic or DIS region. Near the u-channel pole the approach is to fold a flux of on-shell photons from the incoming positron with the differential cross section $d\sigma/d|u|$ for the process $\gamma q \to Wq', W \to \mathrm{f\bar{f}'}$. The photon flux is calculated in the Weizäcker-Williams approximation (WWA) [51, 52]. Furthermore the bulk of the cross section for $\gamma q \to Wq', W \to \mathrm{f\bar{f}'}$ is calculated in the photon structure function approach, in which one envisages W production to be occuring via the annihilation of an anti-quark inside a resolved photon with a quark inside the proton. Accordingly, the cross section is calculated by multiplying the probability of finding an anti-quark of longitudinal momentum fraction z in the photon by the differential cross section for $q\bar{q}' \to W \to \mathrm{f\bar{f}'}$. The region of phase space for W production defined by $u < u_{cut}$ will be referred to as the photoproduction or PHP region. Note that photons in the WWA may still couple directly to the W as in diagram (c), a process which is manifestly not a resolved photon type process. Thus, even the cross section for W photoproduction exhibits a small but significant dependence with the assumed couplings at the $WW\gamma$ vertex (see section 4.1.4).

In all the above, the final state W is assumed to be exactly on shell. Finite-width effects are simulated by multiplying every amplitude by the Breit-Wigner factor :

$$\frac{p_W^2 - m_W^2}{p_W^2 - m_W^2 + im_W\Gamma_W} \quad . \tag{4.5}$$

4.1.2 Cross Section Uncertainties

u_{cut} Dependence

The Monte Carlo generator EPVEC can take as an input any value for the parameter u_{cut}. Although the cross sections for deep inelastic W production and W photoproduction are themselves strong functions of the chosen value of u_{cut}, the total W production cross section is roughly independent of this parameter. This statement remains true also in the case of any anomalous couplings assigned to the $WW\gamma$ vertex (see section 4.1.4). Fig. 4.2 shows that the uncertainty in the total W production cross section arising from the choice of u_{cut} is $\simeq 5\%$.

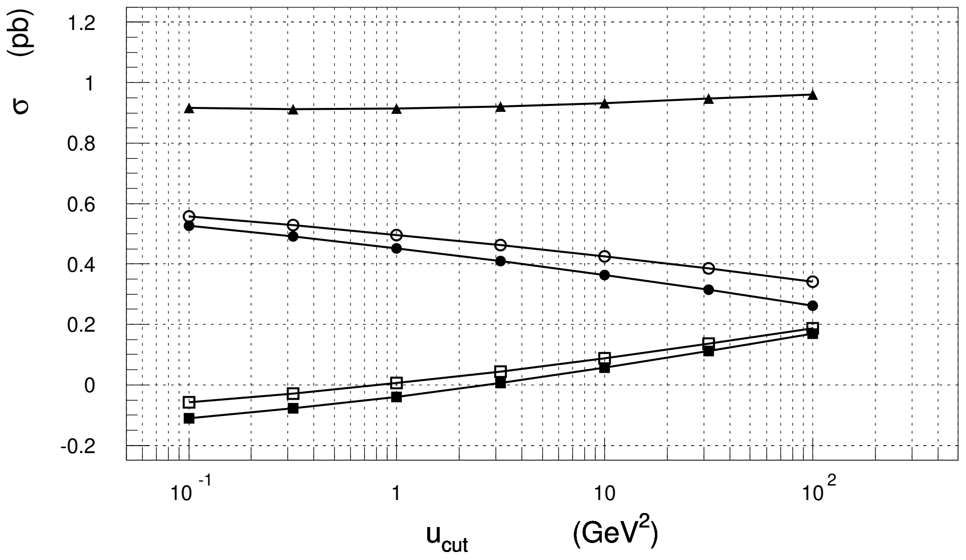

Figure 4.2: *The u_{cut} dependence of the W production cross section. The open and full circles show the W^+ and W^- deep inelastic cross sections respectively, while the open and full squares give the cross sections for W^+ and W^- photoproduction. The triangles give the total W production cross section for different values of u_{cut}.*

Since the W^+ and W^- photoproduction cross sections are not identical, a value for u_{cut} for which both vanish cannot be chosen. Therefore subsequent results, unless otherwise stated, are obtained with a value for u_{cut} of 25 GeV^2. For this value of u_{cut}, chosen also by the authors of [49], the W^+ and W^- photoproduction cross sections are both positive though fairly small. A more important source of uncertainty in the W production cross section is that arising from the choice of structure functions employed and is discussed in the next section.

Structure Functions

In the deep inelastic region the amplitudes are calculated for the parton level sub-process $eq \to eWq', W \to f\bar{f}'$ and in the photoproduction region for the process $\gamma q \to Wq', W \to f\bar{f}'$. Thus, for both regions of phase space the density of quarks in the proton is required to calculate the full $e^+p \to e^+W^\pm X$ cross section. In addition, the density of quarks and anti-quarks inside the photon is required to calculate the resolved-photon processes that dominate W photoproduction.

A new version of the generator EPVEC has been prepared for which built-in structure function parameterisations were replaced by an interface to PDFLIB [53]. This has allowed the calculation of W production cross sections for a range of more recent proton and photon structure functions. Table 4.1 shows a comparison of W^+ and W^- production cross sections for selected parton distribution functions. It can be seen that the total W production cross section varies by up to 5% depending on the choice of proton structure function and around 10% depending on the choice of photon structure function.

Structure Function		W^+ DIS	W^- DIS	W^+ PHP	W^- PHP	Total
p	γ	(pb)	(pb)	(pb)	(pb)	(pb)
GRV94 HO	GRV-G(LO)	0.393	0.319	0.128	0.100	0.940
CTEQ 2pM	GRV-G(LO)	0.418	0.328	0.133	0.100	0.979
MRS(G)	GRV-G(LO)	0.394	0.325	0.126	0.100	0.945
MRS(G)	WHIT-G 6	0.394	0.325	0.072	0.087	0.877
MRS(G)	LAC-G 3	0.394	0.325	0.137	0.114	0.969

Table 4.1: *The W^+ and W^- production cross sections in the deep inelastic and photoproduction regions for different proton and photon structure function parameterisations.*

As well as the choice of structure function, a considerable uncertainty arises from the choice of Q^2 scale for the partons in the proton and photon. Qualitatively the scales are set by the W boson mass itself, but in general they can be written $Q_p^2 = m_W^2/m$ and $Q_\gamma^2 = q_W^2/n$ where m and n are not expected to be too large. All the above cross sections have been calculated with $m = 1$ and $n = 10$. Table 4.2 shows that uncertainties of around 10% arise from considering alternative scales at which to evaluate the proton or photon structure functions.

All results that follow have been obtained with Monte Carlo ensembles of W production

Q^2 Scale Factor		W^+ DIS	W^- DIS	W^+ PHP	W^- PHP	Total
m	n	(pb)	(pb)	(pb)	(pb)	(pb)
1	1	0.394	0.325	0.087	0.056	0.861
1	100	0.394	0.325	0.166	0.144	1.03
1	10	0.394	0.325	0.126	0.100	0.945
0.1	10	0.355	0.293	0.114	0.091	0.853
10	10	0.445	0.366	0.142	0.112	1.06

Table 4.2: *The W^+ and W^- production cross sections in the deep inelastic and photoproduction regions for proton structure functions evaluated at a scale $Q_p^2 = m_W^2/m$ and photon structure functions evaluated at a scale $Q_\gamma^2 = q_W^2/n$.*

events prepared using the MRS(G) [54] parameterisation of the parton densities in the proton, evaluated at a scale m_W^2, and the GRV-G(LO) [55] parameterisation of the parton densities in the photon, evaluated at a scale $q_W^2/10$. Combining the above uncertainties from the choice of u_{cut}, structure functions and scales results in an overall uncertainty on $\sigma(e^+p \to e^+W^\pm X)$ of around 20% [2]. One extra theoretical error that should be combined with those listed here is that arising from the possible effect of as yet uncalculated QCD corrections to the leading order W production cross section. A rough estimate of the possible size of these corrections is $20-30\%$ of the leading order cross section [56]. A conservative estimate of the total uncertainty on the cross section for $e^+p \to e^+W^\pm X$ is therefore 35%, a 'theoretical' error of sufficient magnitude to make the measurement of the W production cross section an important one in itself. Note that this error estimate is somewhat smaller than that quoted in [49], again due to the use here of comparatively recent proton and photon structure functions. A less restrictive range of parton distribution functions might give rise to an uncertainty in the total W production cross section as large as 50%.

4.1.3 Event Characteristics

The transverse energy flows in Standard Model W production events are dominated by the W decay products. The scattered beam positron is scattered at small angles with respect to the incoming positron direction, as indicated in fig. 4.3. In only ~ 20% of W

---

[2] The uncertainty on the W production cross section arising from the choice of proton and photon structure functions does not itself depend on the value of u_{cut}, despite the change in the photoproduction fraction of the total cross section with this parameter.

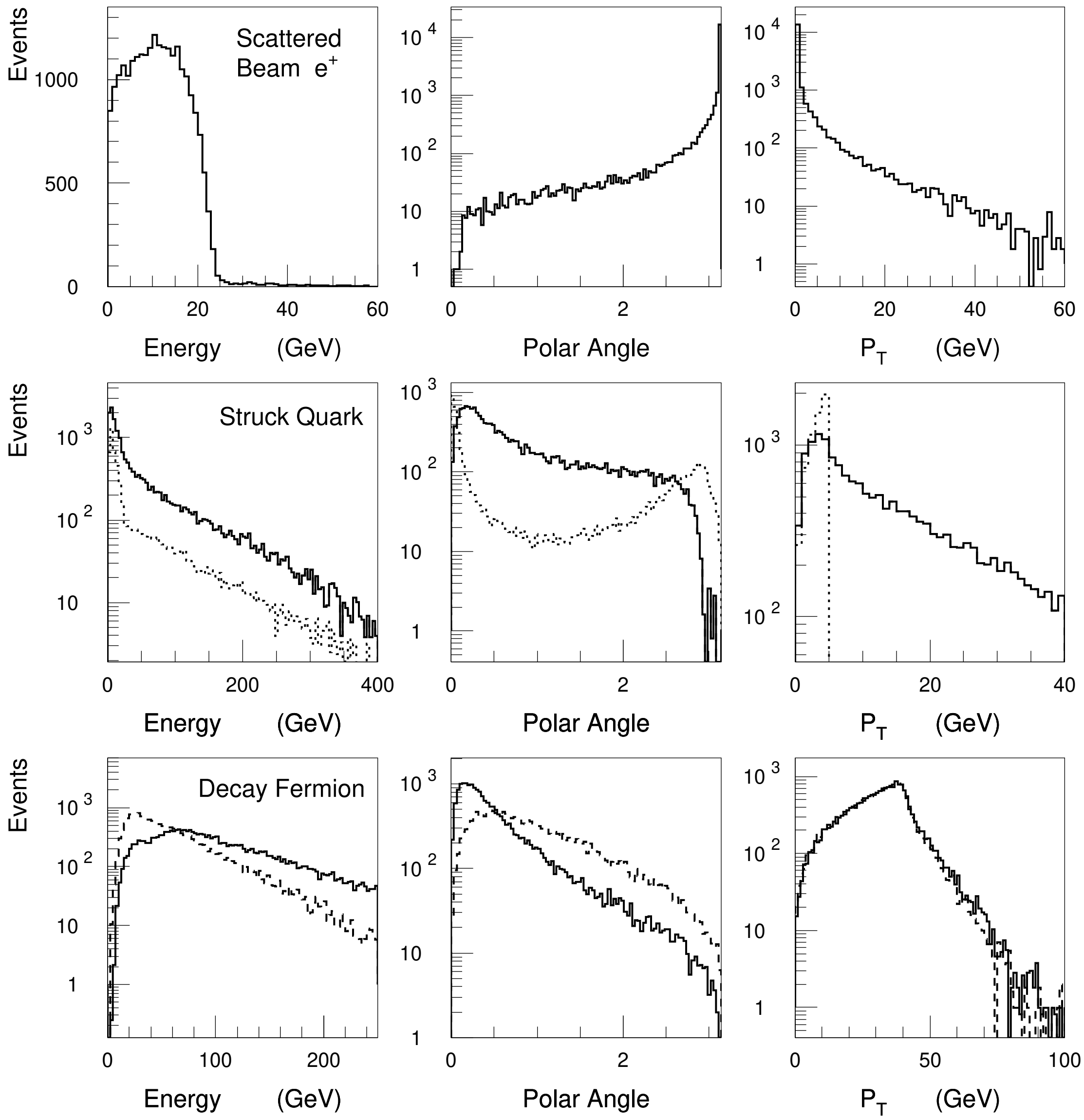

Figure 4.3: *The energy, polar angle and* p_T *distributions for the scattered beam positron, struck quark and decay fermion in* $e^+p \to e^+W^\pm X$ *events. The distributions in the first row are for all W production channels combined, while the solid and dotted lines in the second row correspond to the DIS and photoproduction phase space regions respectively. The solid and dashed lines in the last row give the distributions for charged particles and anti-particles from W decay respectively. Overall normalisation is arbitrary; relative normalisation is accurate.*

production events is the beam positron deflected by more than 5°, corresponding roughly to the edge of the RCAL acceptance. In the simulation of photoproduction events the beam positron is undeflected and so this fraction is composed entirely of deep inelastic type events. Similarly, the scattered quark from the proton emerges at small polar angles and with a very soft p_T spectrum in the case of Standard Model $WW\gamma$ couplings. In the case of W photoproduction the angular distribution of the struck quark is more peaked in the forward and rear directions. The peak close to 180° can be thought of as the photon remnant and will give rise to low transverse energy hadronic activity in the RCAL distinctive of resolved photon processes at HERA. Finally, fig. 4.3 shows the distributions of the W decay products themselves. It can be seen that the fermions from W decay are produced at small polar angles and with a large energy range, as expected for W's produced with large longitudinal boosts. The transverse momentum distribution shows the familiar Jacobian peak structure at $p_T \sim 1/2 \times m_W$, smeared by the intrinsic p_T of the produced W. The solid and dashed lines correspond to charged particles ($e^-, \mu^-, \ . \ . \ etc.$) and anti-particles ($e^+, \mu^+, \ . \ . \ etc.$) respectively. The different angular distributions can be understood as a consequence of the likely W polarisation in ep collisions at $\sqrt{s} \simeq 300$ GeV. Since the production of on-shell W's requires $\sqrt{x_{BJ} \times s} > m_W$, where x_{BJ} is the fraction of the incoming proton's momentum carried by the struck quark [3], W production is dominated by the valence quarks inside the proton. The mean W polarisation is therefore biased towards the incoming proton direction, giving rise to the different angular distributions for particles and anti-particles from W decay visible in fig. 4.3. Since there are inevitably efficiency limitations in the very forward direction close to the edge of the central tracking acceptance, the different particle and anti-particle angular distributions give rise to different W^+ and W^- tagging efficiencies. This effect is particularly noticeable in the $W \to \mu\nu$ decay channel, as described in chapter 9.

4.1.4 Anomalous Couplings

The generator EPVEC allows the CP conserving and Lorentz invariant anomalous couplings at the $WW\gamma$ vertex, $\Delta\kappa$ and λ, to take arbitrary values (see chapter 3). Fig. 4.4 shows the variation of the W^+ and W^- deep inelastic and photoproduction cross sections with the value of each of these anomalous couplings, the other being set to zero. The cross section dependence in all cases is quadratic, reflecting the presence of Standard Model

---

[3] This is not the same as the x that, for example, might be determined from the scattered electron using equations 3.4 to 3.6, since W production is a radiative process.

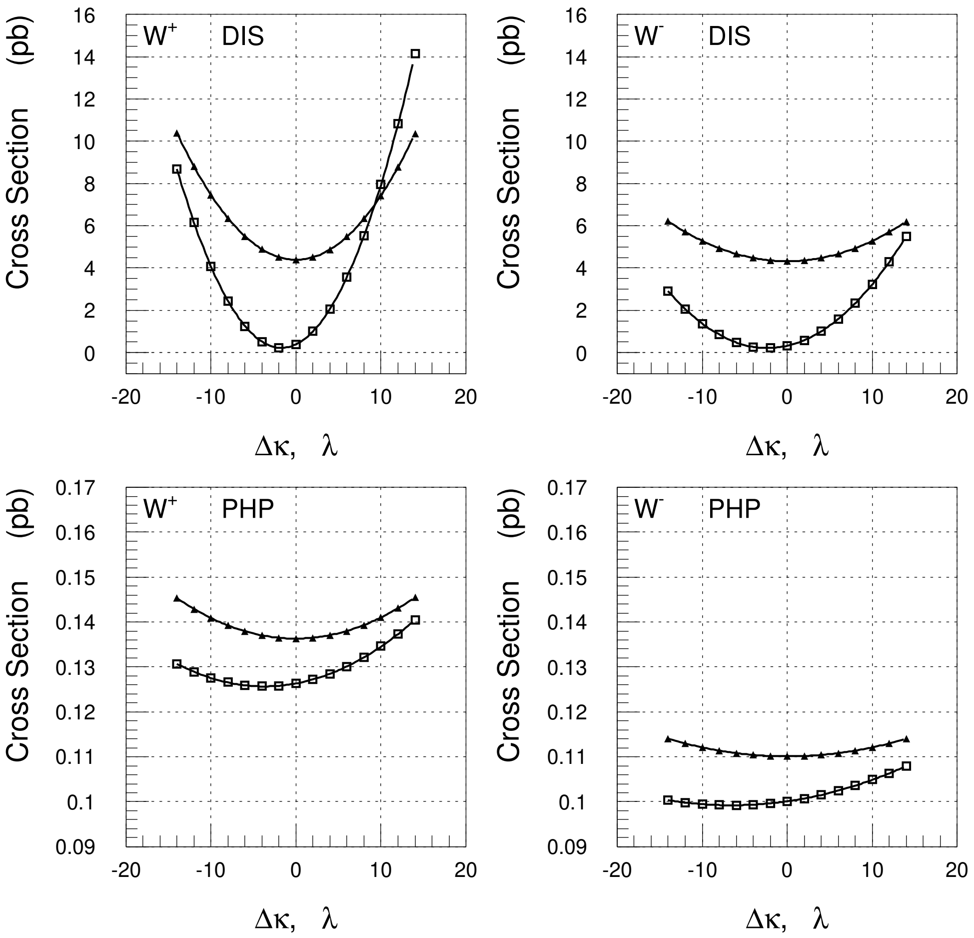

Figure 4.4: *The squares denote the* W^+ *and* W^- *production cross sections for values of the anomalous coupling* $\Delta\kappa$ $(\lambda = 0)$. *The triangles give the corresponding cross sections for values of* λ $(\Delta\kappa = 0)$. *The* λ *points are shifted by* 4 pb *for the DIS and* 0.1 pb *for the PHP phase space regions for clarity.*

terms (constant), anomalous terms ($\propto \Delta\kappa^2$ or λ^2) and interference terms ($\propto \Delta\kappa$ or λ).

With a value of $u_{cut} = 25$ GeV^2 the W^+ and W^- photoproduction cross sections exhibit a very small dependence on the anomalous couplings. Adding the separate contributions, fig. 4.5 shows the total W production cross section as a function of $\Delta\kappa$ and λ. The cross section shows a steeper dependence on $\Delta\kappa$ than λ, ensuring that for positive couplings W production is more sensitive to non-Standard Model values of $\Delta\kappa$ than λ. However, the cross section for W production falls for small negative values of $\Delta\kappa$, reaching a minimum at $\Delta\kappa \approx -2$. Thus, obtainable limits on $\Delta\kappa$ are asymmetric, while those on λ are symmetric about their Standard Model values $\Delta\kappa = \lambda = 0$.

Although the sensitivity to anomalous values for the couplings $\Delta\kappa$ and λ resides almost

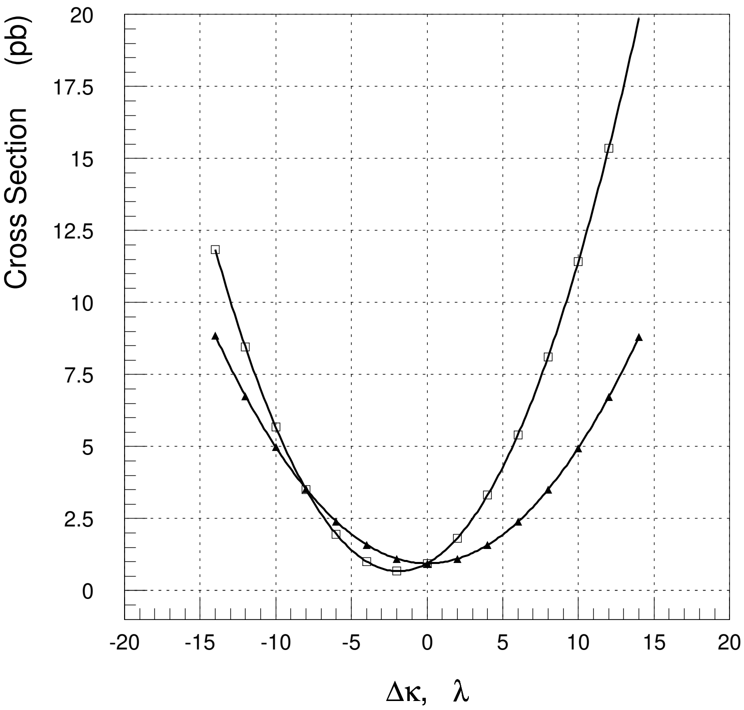

Figure 4.5: *The total W production cross section as a function of anomalous coupling* $\Delta\kappa$ *(open squares) and* λ *(triangles).*

entirely in the deep inelastic part of the W production cross section, the curves plotted in fig. 4.5 do not depend upon the value chosen for u_{cut}. This is due to the residual dependence of the photoproduction cross sections on the anomalous couplings, which becomes more pronounced as u_{cut} is increased. Fig. 4.6 shows, for three different values of u_{cut}, the variation of the W production cross section with positive values of $\Delta\kappa$ and λ.

One final important property of the anomalous couplings $\Delta\kappa$ and λ is that their contributions to the W production cross section are largely independent [4]. Fig. 4.7 shows the variation of the cross section with $\Delta\kappa$ for two distinct values of λ and, similarly, variations with λ for two distinct values of $\Delta\kappa$. In effect, anomalous coupling contributions to the total cross section take the form :

$$\sigma_W(\Delta\kappa,\lambda) \;\approx\; \sigma_{SM} + a\Delta\kappa + b\Delta\kappa^2 + c\lambda + d\lambda^2 \qquad (4.6)$$

where parameters a, b, c, d can be taken from the fits to the cross sections of fig. 4.5. This property implies the simple form for the ellipses in the $\{\Delta\kappa,\lambda\}$ plane that define an allowed region for a given W production cross section upper limit (see chapter 11).

---

[4] This is an approximation. Terms in the squared amplitude proportional to $\Delta\kappa \times \lambda$ do exist, but are found to be small.

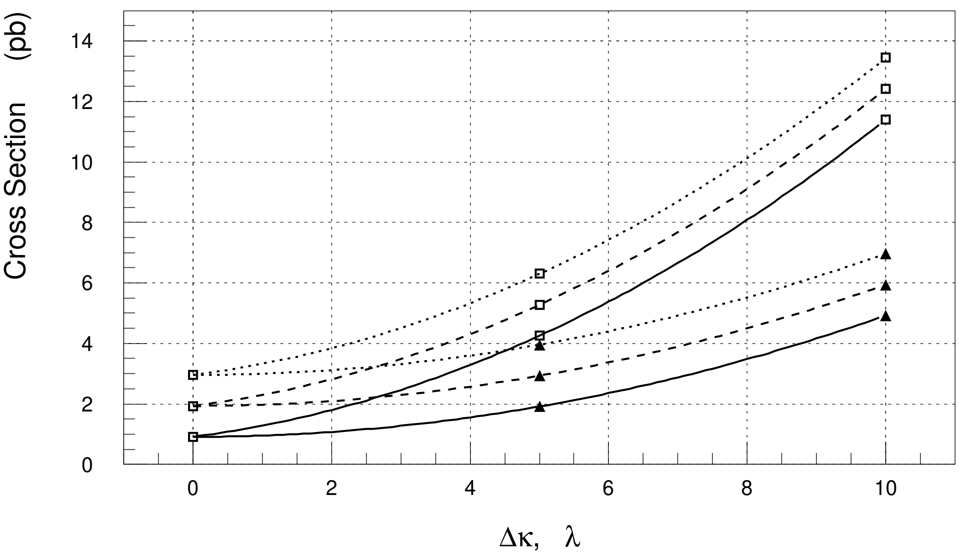

Figure 4.6: *The open squares and triangles denote the total W production cross section at different values of $\Delta\kappa$ and λ respectively. The values for $u_{cut} = 10$ GeV^2 (dashed) are shifted upwards by* 1 pb *and the values for $u_{cut} = 100$ GeV^2 (dotted) by* 2 pb *with respect to the values for $u_{cut} = 1$ GeV^2 (full line).*

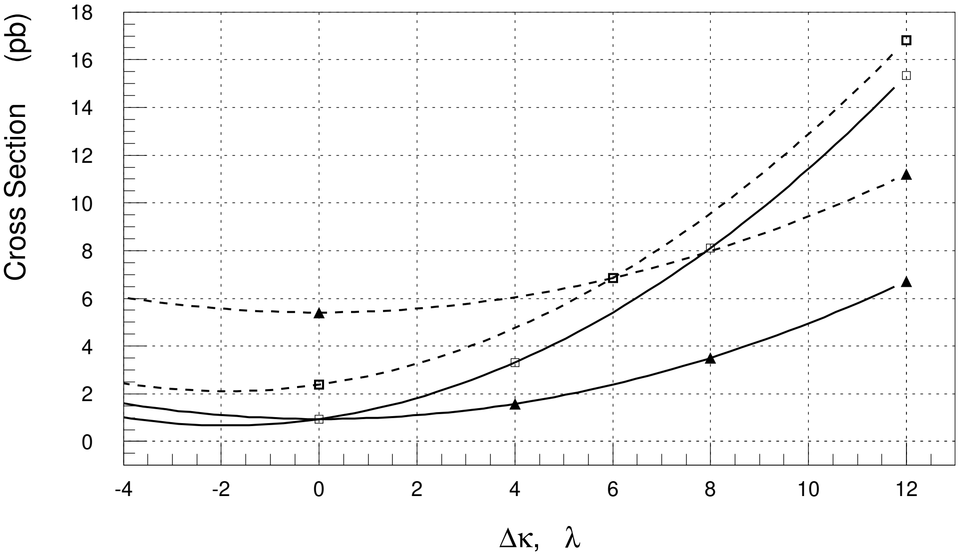

Figure 4.7: *The open squares denote the total W production cross section at different values of the coupling $\Delta\kappa$ for $\lambda = 0$ (full) and $\lambda = 6$ (dashed line). The triangles denote the cross section at different values of λ for $\Delta\kappa = 0$ (full) and $\Delta\kappa = 6$ (dashed line).*

In almost all respects, W production events with anomalous couplings are expected to have similar event characteristics to Standard Model W production events. One important exception, however, is the transverse momentum carried by the struck quark. As shown in fig. 4.8, the spectrum is much harder for events generated with anomalous $WW\gamma$ couplings. The excess cross section is located at large values of the quark p_T and is thus confined almost entirely to the DIS phase space region. With high luminosities and assuming that the struck quark gives rise to an observable jet in the final state, the sensitivity to W production in the presence of anomalous couplings is enhanced by demanding that the event have $p_T^{jet} > 5$ GeV in addition to other requirements [50]. Using the shape of the quark p_T distribution to place limits on anomalous couplings will also reduce the systematic uncertainties arising from the structure function dependency of the total cross section. However, given the current integrated luminosity the main task is to identify W production events with maximum efficiency and it is enough to note here that any events with large hadronic transverse momenta in addition to the W decay products are particularly interesting.

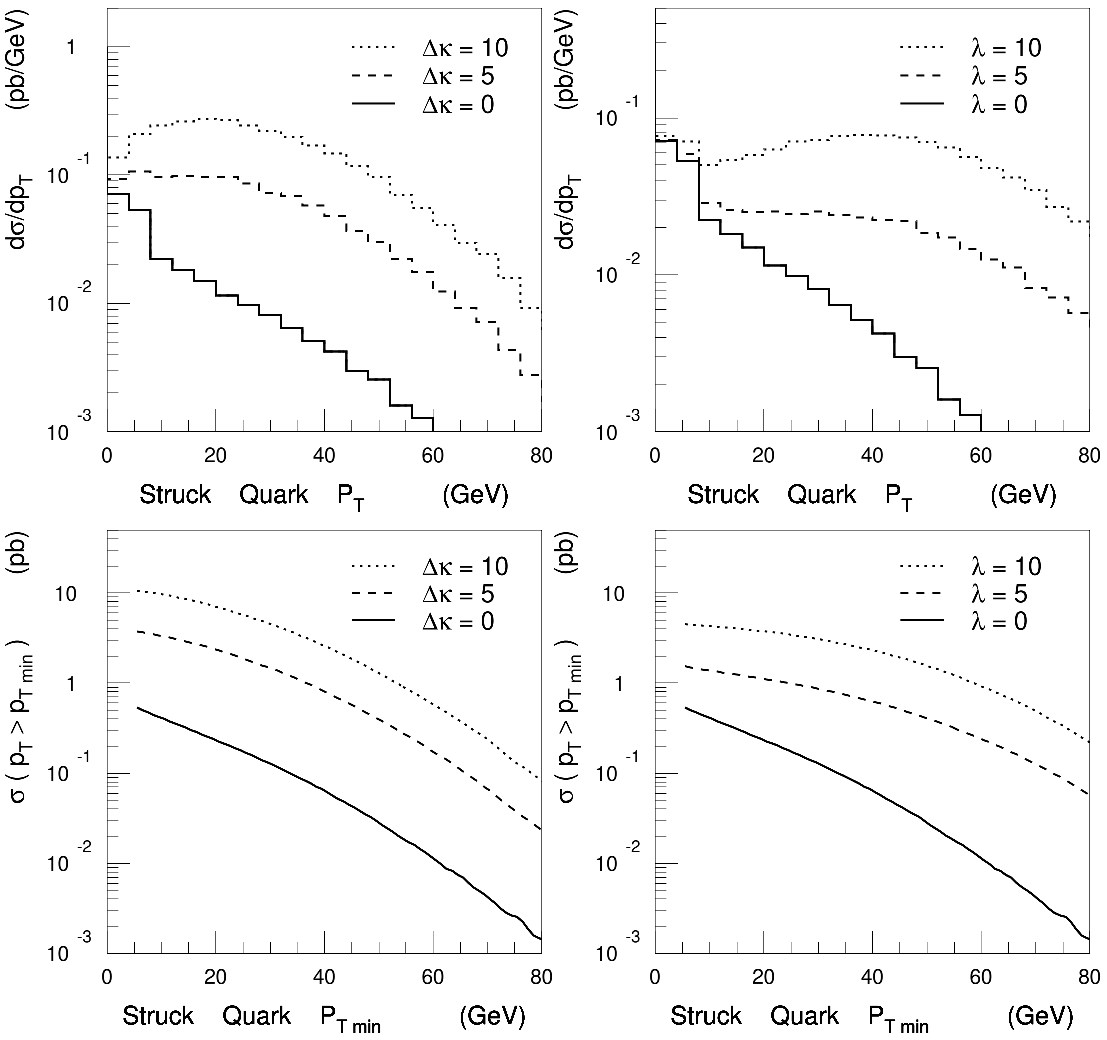

Figure 4.8: *The differential and integrated* W *production cross sections versus the struck quark* p_T. *The solid lines correspond to Standard Model values for the* $WW\gamma$ *couplings* κ *and* λ. *The cross sections corresponding to anomalous values for these couplings are indicated. The integrated cross sections are plotted for* $p_{T,min} > 5$ GeV *only.*

4.2 Z Production

4.2.1 Cross Section Calculation

As in the case of W production, two distinct Z production channels exist in e^+p collisions :

$$e^+p \to e^+Z^0X \ , \tag{4.7}$$

$$e^+p \to \bar{\nu}Z^0X \ . \tag{4.8}$$

For similar reasons to the W production scenario, the second of these reactions is expected to be much suppressed with respect to the first. The four Feynman diagrams considered in the calculation of the cross section for reaction 4.7 are shown in fig. 4.9 [49].

Diagrams (a) and (b), involving the emission of a Z boson from the initial and final state quark lines, are analogous to diagrams (a) and (b) for the process $e^+p \to e^+W^{\pm}X$. The same u-channel pole necessitates the division of phase space into deep inelastic and photoproduction regions. Diagrams (c) and (d), involving the emission of a Z from the initial and final state lepton lines, also contribute to deep inelastic Z production. However, the momentum transfer squared to the hadronic system, $|t|$, can also take very small values for which the parton model is not expected to be applicable. This requires the further division of phase space into elastic (ELA) and quasi-elastic (QEL) regions. In the first region a proton form factor method is employed to calculate the cross section for elastically scattering the beam proton and in the second region a fit for the electromagnetic proton structure function in the low mass resonance region is used to calculate the cross section for the beam proton to emerge as a low mass (few GeV) state. A cut at $|t| = 4$ GeV^2 separates the quasi-elastic from the deep inelastic scattering region.

Similar uncertainties relating to the choice of u_{cut} and proton and photon structure function scales and parameterisations affect the calculation of the Z production cross section. Overall uncertainties are comparable to those in the case of W production [49]. Table 4.3 shows the breakdown of the total cross section for the reaction $e^+p \to e^+Z^0X$ into the different phase space regions. As for the final W production Monte Carlo samples, a value for u_{cut} of 25 GeV^2 is chosen. Once again, the MRS(G) parameterisation is chosen for the proton and the GRV-G(LO) for the photon, evaluated at scales m_Z^2 and $q_Z^2/10$ respectively.

4.2.2 Event Characteristics

Z production events have somewhat different event characteristics to W production events, largely due to the presence of elastic and quasi-elastic production channels. Fig. 4.10 shows

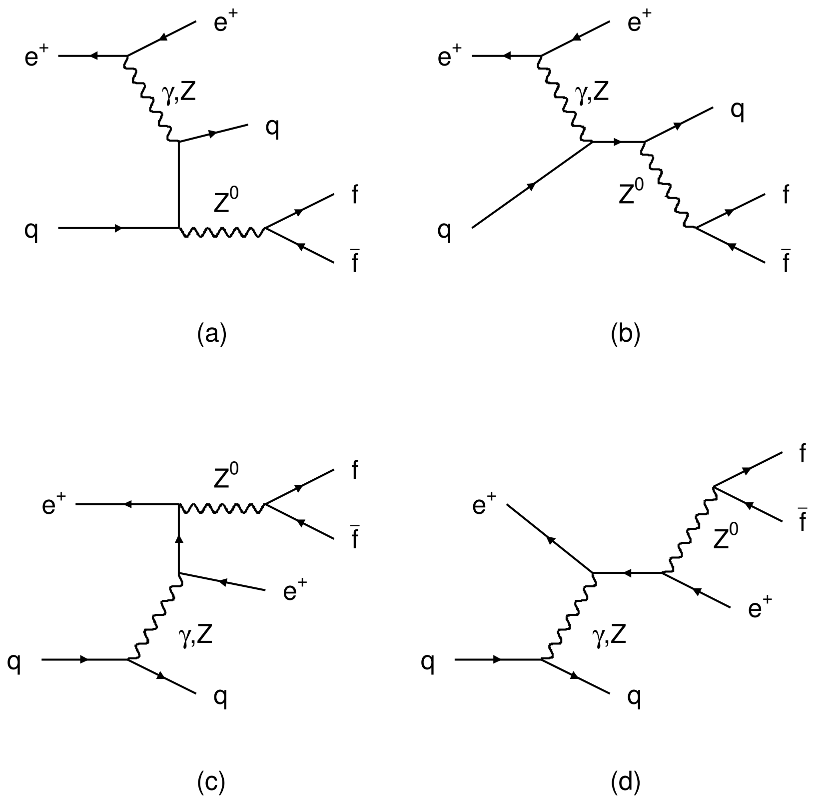

Figure 4.9: *Leading order Feynman diagrams for the process* $e^+p \to e^+Z^0X$.

Phase Space Region				
DIS (pb)	PHP (pb)	ELA (pb)	QEL (pb)	Total (pb)
0.138	0.056	0.100	0.037	0.330

Table 4.3: *The cross sections for Z production in the four different phase space regions.*

that the energy and angular distributions of the scattered beam positron are quite different for combined DIS and photoproduction channels (solid line) and combined elastic and quasi-elastic channels (dashed line). In the latter case there is a probability of around 50% for the scattered beam positron to be visible in the central detector. Elastically and quasi-elastically produced Z's also have much smaller longitudinal boosts than DIS or photoproduced Z's. As a consequence the decay lepton ($l^{\pm}$) energy spectrum is very much narrower and the angular distribution less forward peaked than that for Z production in the DIS and photoproduction regions. The lepton p_T spectrum, sensitive only to transverse boosts, is very similar for the different production channels. Unlike W production events, the distributions for decay leptons and anti-leptons are very similar and are combined in fig. 4.10.

In general the leptonic decays of Z bosons give rise to spectacular 2 or 3-lepton final states. In the case of elastic or quasi-elastic Z production the outgoing proton or low mass hadronic final state can escape detection through the forward beam pipe, giving rise to a fraction of Z production events with no hadronic activity visible in the detector. At some level events with the scattered beam positron in the detector in combination with the decay $Z^0 \to \nu\bar{\nu}$ can give rise to events with missing p_T plus an electron, so constituting a background to the signal for $W \to e\nu$. This is examined further in chapter 8.

4.3 Limitations of EPVEC

Most of the uncertainties in the W and Z production cross sections, for example arising from the choice of parameters such as u_{cut} and different parton distributions, can be addressed with the current version of EPVEC. More fundamentally, EPVEC does not attempt to include any QCD corrections or final state effects into its description of gauge boson production. As mentioned above, uncalculated QCD corrections to the leading order cross section for $e^+p \to e^+W^{\pm}X$ could be as large as $20-30\%$ of the leading order cross section. In terms of the QCD final state, quarks from the decays of the gauge bosons, as well as

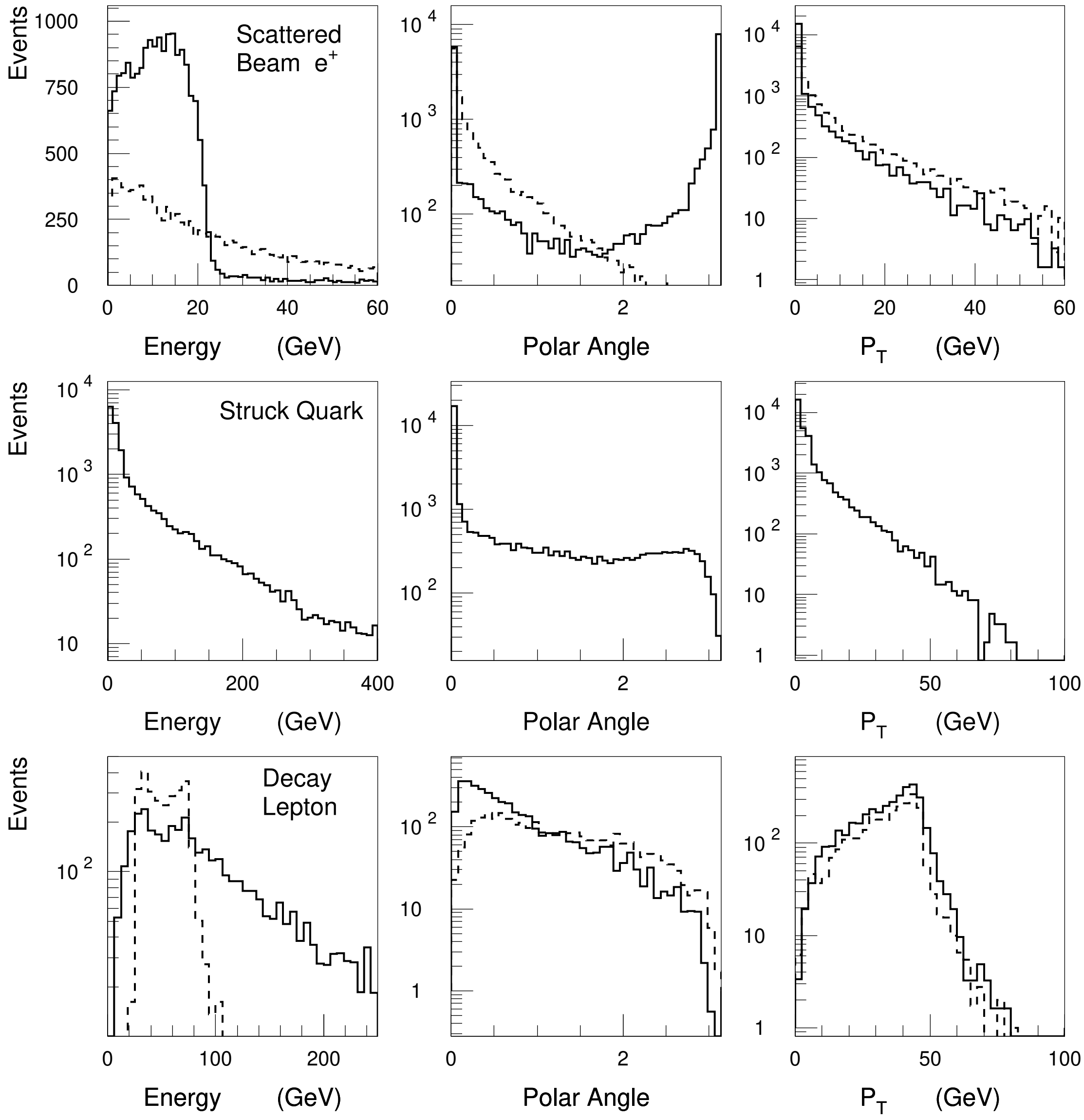

Figure 4.10: *The energy, polar angle and p_T distributions for the scattered beam positron, struck quark and decay lepton ($l^{\pm}$) in $e^{+}p \rightarrow e^{+}Z^{0}X$ events. In the top and bottom rows the solid lines correspond to the combined DIS and photoproduction phase space regions and the dashed lines correspond to combined elastic and quasi-elastic Z production. Overall normalisation is arbitrary; relative normalisation is accurate.*

the struck quark and proton remnant, are currently passed directly to JETSET for string fragmentation and hadronisation. Although QCD effects such as hard gluon radiation are important mainly in understanding the hadronic decays of W's and Z's, they could in principle alter the description of the hadronic final state even in events with leptonic decays. The possible effect on selection efficiencies estimated using Monte Carlo remains unknown.

Electroweak radiative corrections are also not included in EPVEC. For the most part these should be relatively small, but in principle could have a small effect on calculated selection efficiencies. For example, lepton matching track p_T distributions will not have the radiative tails down to smaller transverse momenta that are observed, for example, in the case of neutral current scattering. The sensitivity to such limitations is reduced by using only the calorimeter energy measurements in the case of $W \rightarrow e\nu$ and $Z^0 \rightarrow e^+e^-$ decays.

Finally, it is important to bear in mind the limitations arising from the division of the available phase space for W production into DIS and photoproduction regions. One consequence is that the hadronic transverse momentum spectrum is not well described at low p_T's, which is clear from the discontinuity visible in the struck quark p_T distribution in fig. 4.3. For hadronic transverse momenta greater than around 10 GeV, described entirely by DIS type W production, the prediction for the p_T spectrum is far more reliable [56].

To summarise, W and Z production in ep collisions is a phenomenologically complex process to describe. Large uncertainties affect the cross section predictions and to a lesser extent the event characteristics. Importantly, recent work by independent authors has confirmed the general results obtained using EPVEC [57].

The leptonic decays of W and Z bosons give rise to the distinctive signature of high p_T lepton(s), with additional missing p_T in the case of W production. However, since the cross sections for W and Z production are so small, serious backgrounds arise from other processes. These are discussed extensively in following chapters.

Chapter 5

Monte Carlo Simulation

A number of different computer programs exist to simulate and evaluate the cross sections for different physics processes that are considered in this work. The important features of these Monte Carlo programs are outlined in this chapter. Most of the programs discussed are also event generators, producing arrays of four vectors of the final state particles that can be passed to a detailed detector simulation. This detector simulation is described briefly in section 5.7. A more detailed account of the Monte Carlo generator for W and Z production was given in chapter 4.

5.1 Deep Inelastic Scattering

Deep inelastic scattering is the most important process to accurately describe and simulate in the context of HERA physics. The Monte Carlo event generator described, DJANGO [58], is an interface to an array of packages designed to simulate various parts of the deep inelastic neutral and charged current scattering processes.

The fact that in the leading-logarithm approximation QED and QCD corrections to the Born-level scattering cross section can be factorised or treated separately is reflected in the structure of the program. DJANGO is therefore an interface to HERACLES [59], which incorporates electroweak radiative corrections to $O(\alpha)$ including real photon Bremsstrahlung, and LEPTO [60] which allows the simulation of leading-logarithmic QCD cascades and includes in addition matrix elements describing specific perturbative QCD effects to $O(\alpha_S)$. QCD cascades can alternatively be implemented according to the colour dipole model of ARIADNE [61]. Finally, the program JETSET [62] uses the LUND string model to generate the observed hadronic final state consisting of mesons and baryons from the quarks and gluons that constitute the QCD final state.

5.1.1 Born-level Cross Sections

The event generator DJANGO is based on the Quark Parton Model. In the naïve QPM the cross section for deep inelastic lepton-nucleon scattering can be calculated by folding the cross section for the $2 \to 2$ sub-process $lq \to l'q'$ by the number density of partons of type i carrying momentum fraction x of the nucleon, $f_i(x)$. For example, in the case of neutral current scattering in which single photon exchange is assumed and the contribution from Z exchange is neglected, the cross section for the process $eq \to eq$ is given by :

$$\frac{d\sigma(eq \to eq)}{dy} = \frac{2\pi\alpha^2 e_q^2 \widehat{s}}{Q^4}\left[1 + (1-y)^2\right] \ , \tag{5.1}$$

where $\widehat{s}$ is the eq centre of mass energy. Then the resulting electron-proton scattering cross section can be written :

$$\frac{d^2\sigma(ep)}{dxdy} = \frac{2\pi\alpha^2 s}{Q^4}\left[(1 + (1-y)^2)\right]F_2(x) \ , \tag{5.2}$$

where

$$F_2(x) = \sum_i e_i^2 x f_i(x) \ . \tag{5.3}$$

Electroweak radiative corrections modify the form of the $2 \to 2$ parton level sub-processes for neutral and charged current scattering and simulate radiative processes such as $eq \to eq\gamma$. Leading logarithmic QCD corrections lead to the scale dependence of the parton distributions, $f_i(x) \to f_i(x, Q^2)$, and can be simulated using QCD cascades, described below. Non-logarithmic corrections of $O(\alpha_s)$ are explicitly included.

5.1.2 QED and Weak Corrections

Fig. 5.1 shows some of the $O(\alpha)$ electroweak radiative corrections to the neutral current process $eq \to eq$. Diagrams (a) and (b) represent real photon Bremsstrahlung from the incoming and scattered electron. The kinematics of the radiative process are completely specified by the four momenta of the scattered electron (or quark) and photon :

$$e(l) + q(p) \to e(l') + q(p') + \gamma(k) \ . \tag{5.4}$$

All other electroweak and QCD correction are simply applied to the reduced process :

$$e'(l) + q(p) \to e'(l') + q(p') \ , \tag{5.5}$$

where the incoming (outgoing) electron is now highly virtual in the case of hard initial (final) state radiation. The radiative cross section becomes large for photons emitted close

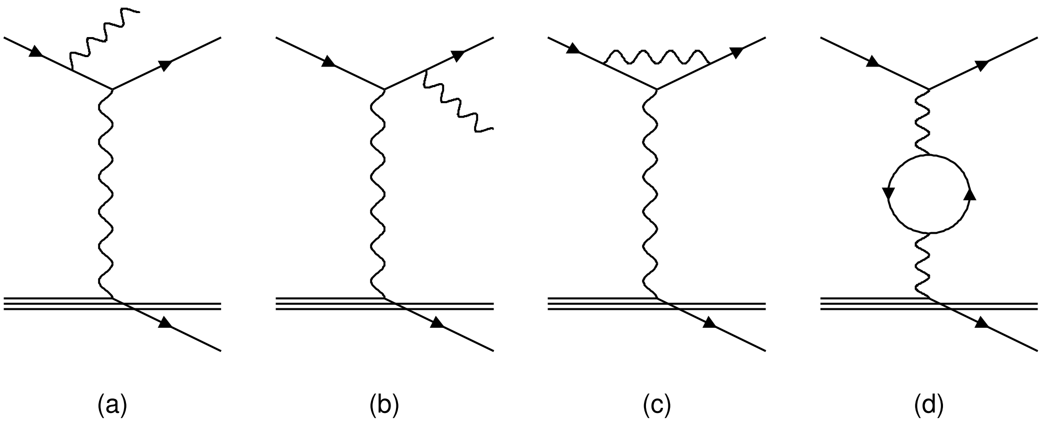

Figure 5.1: *Feynman diagrams for some of the $O(\alpha)$ electroweak corrections to the neutral current process $eq \to eq$.*

to the incoming or scattered electron directions and for events with a hard radiated photon but very small momentum transfer to the proton.

Diagrams (c) and (d) represent vertex and propagator corrections to the scattering process respectively. Note that the squared amplitudes corresponding to these diagrams would constitute $O(\alpha^2)$ corrections to the Born level cross section. Hence, $O(\alpha)$ corrections correspond to the interference between these and the tree level amplitudes.

The emission of Bremsstrahlung photons from the incoming or scattered quark is not implemented in the current version of DJANGO. By virtue of the larger quark masses and fractional electric charges the effect of quarkonic radiation on the cross section is expected to be comparatively small, at most a few percent [59]. In the case of charged current scattering no gauge invariant separation into leptonic and quarkonic radiation is possible. The dominant contribution to the Bremsstrahlung cross section, however, still comes from terms in the amplitude proportional to the lepton charge while those that enter with the quark charge are neglected. The resulting 'leptonic' Bremsstrahlung distributions nevertheless contain a significant contribution from photons emitted close to the direction of the scattered quark. This is illustrated in fig. 5.2, where at small polar angles the photon is emitted with a small azimuthal separation from the struck quark. At large polar angles, close to the direction of the incident lepton, there is a large peak visible in the radiative cross section for photons that are essentially uncorrelated with the struck quark direction. The important point is that the separation into leptonic and quarkonic initial and final state radiation for charged current scattering does not correspond to a separation based on the angle of the

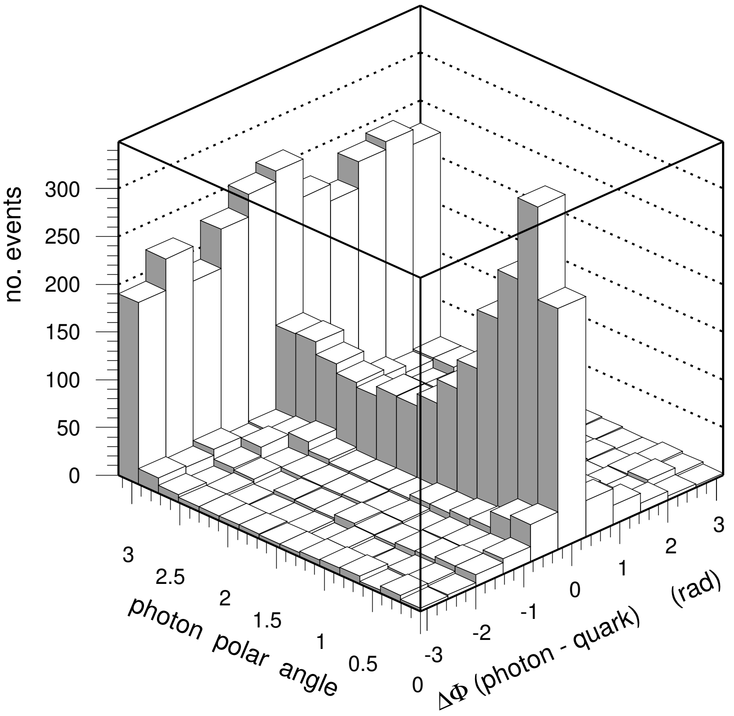

Figure 5.2: *The distribution of photons with* $E > 2$ GeV *in radiative charged current events generated by DJANGO. For most polar angles the photon is emitted close to the direction of the struck quark. The radiative cross section also becomes large at polar angles close to the direction of the incoming lepton with the photons in this case showing little correlation with the struck quark direction.*

radiated photon with respect to the incoming or scattered particles.

5.1.3 QCD Corrections

As mentioned above, QCD corrections are divided into exact $O(\alpha_s)$ corrections and higher order effects, the latter being included only up to leading logarithms. Explicit (i.e. non-logarithmic) $O(\alpha_S)$ corrections include matrix elements for boson-gluon fusion and gluon emission processes, depicted in fig. 5.3. Both of these processes would be expected to produce final states that include 2 jets in addition to the proton remnant, in contrast to the single current jet expected at leading order.

Higher order QCD effects are taken into account in the leading logarithm approach using QCD cascades. One approach is the parton shower model implemented in LEPTO which simulates the multiple Bremsstrahlung-like emission of partons by both initial and final state quarks. ARIADNE employs an alternative approach based on the radiation of

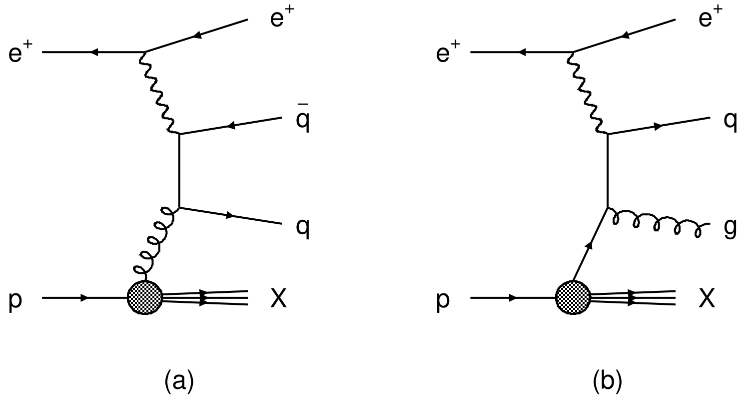

Figure 5.3: *$O(\alpha_S)$ QCD corrections to neutral current e^+p scattering. Diagram (a) corresponds to boson-gluon fusion and diagram (b) to hard gluon emission.*

soft gluons by the colour dipole formed by the struck quark and the proton remnant. This gives rise to further colour dipoles, and the process is iterated to form a full QCD cascade.

For the best possible simulation of DIS events the combination of QCD cascades with $O(\alpha_s)$ matrix elements is possible, with care taken to avoid any possible double counting.

5.1.4 Parton Distributions

Sets of parton distribution functions are taken from the library PDFLIB [53], to which the generator DJANGO is fully interfaced. The particular sets employed are stated explicitly in subsequent chapters.

5.1.5 Generator Level Cuts

The neutral current Monte Carlo samples employed here were generated with different Q^2 cuts, detailed in chapter 8, to give high Monte Carlo statistics in the region where neutral current scattering forms a serious background to W and Z production. With a much smaller total cross section, the charged current Monte Carlo was generated with a Q^2 cut of only 10 GeV^2, corresponding to very low neutrino transverse momenta.

5.2 Radiative Charged Current Scattering

The cross section calculation program WWGAMMA [63] includes all four diagrams, shown in fig. 5.4, that contribute to radiative charged current scattering. Diagrams (a), (b) and (c) constitute initial and final state radiation from the lepton and quark lines. Diagram (d)

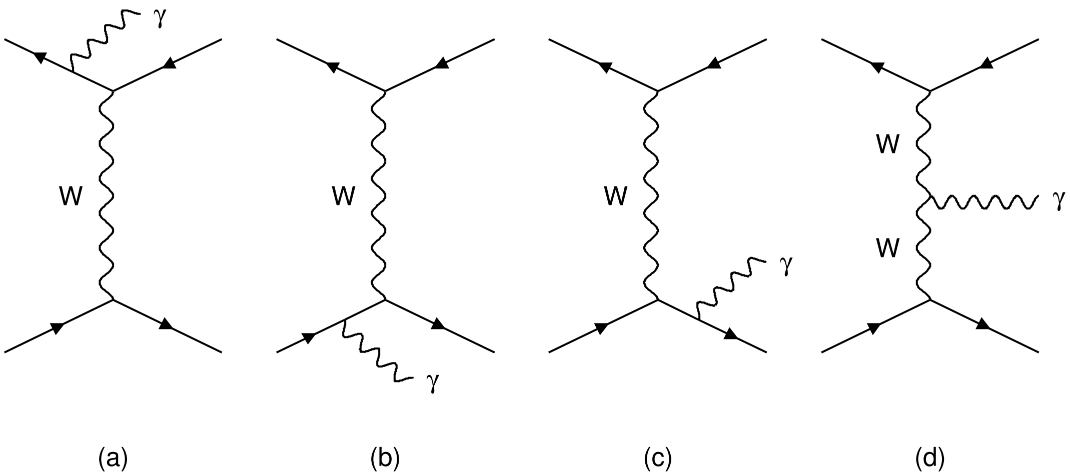

Figure 5.4: *The leading order diagrams for the radiative charged current process* $e^+p \rightarrow \bar{\nu}\gamma X$.

corresponds to the emission of a photon from the W propagator, the amplitude for which is clearly sensitive to the coupling of the photon to the W boson. The program includes a full parameterisation of the $WW\gamma$ vertex in terms of the anomalous couplings $\Delta\kappa$ and λ introduced in chapter 2, and had been adapted to calculate e^+p as well as e^-p radiative cross sections.

A comparison of the WWGAMMA and DJANGO descriptions of Standard Model radiative charged current scattering, showing generally good agreement between the two programs, is presented in fig. 5.5. Events were generated requiring the following :

1. $p_T^\gamma > 2$ GeV ; $5^\circ < \theta(\gamma) < 175^\circ$,
2. $p_T^{q'}$ = scattered quark $p_T > 10$ GeV ,
3. $p_T^{\bar{\nu}}$ = missing $p_T > 15$ GeV ,
4. $R_{\eta\phi}(\gamma, q')$ [1] > 1.0 ,

where the final cut on the proximity of the radiated photon to the scattered quark is required by WWGAMMA, along with the cuts on the polar angle and energy of the radiated photon, to avoid collinear and infrared singularities in the full radiative cross section. In addition it is well isolated photons that carry information about $WW\gamma$ couplings and such a cut mimics that required to separate photons from hadrons in the final state [63]. Since

---

[1] $R_{\eta\phi} = \sqrt{\Delta\eta^2 + \Delta\phi^2}$, where the pseudorapidity variable $\eta = -\ln(\tan\theta/2)$.

DJANGO generates complex QCD final states consisting in principle of several quarks and gluons, the struck quark variables correspond in this case to the net p_T and direction of the hadronic system balancing the scattered neutrino and photon. Nevertheless, the last plot of fig. 5.5 shows good agreement between WWGAMMA and DJANGO calculated values for the photon-quark separation. The fact that WWGAMMA contains no QCD or other corrections required for a precise cross section estimate partly accounts for the $\sim 5\%$ discrepancy with respect to DJANGO in the value for the total radiative cross section after the above cuts. Moreover, since the choice of parton density functions which WWGAMMA can employ is at present rather limited, this comparison is based on MRS B0-235 structure functions [64] for WWGAMMA and MRS(A) low Q^2 structure functions [65] for the DJANGO generated events.

Although the event generator DJANGO must be used to compare the expected rate of radiative charged current DIS with the data, only WWGAMMA contains photon radiation from the W propagator and the corresponding dependence on the couplings κ and λ. Fig. 5.6(a) shows the p_T distribution of radiated photons for Standard Model and anomalous radiative charged current scattering, from which it can be seen that the extra cross section in the case of anomalous couplings manifests itself primarily as an excess of radiated photons with large transverse momenta. The sensitivity to anomalous couplings is therefore enhanced by requiring that p_T^γ be greater than some minimum p_T. For example. fig. 5.6(b) shows the total radiative charged current cross section for different values of the anomalous couplings $\Delta\kappa$ and λ for $p_T^\gamma > 10$ GeV.

The dependence of the radiative charged current cross section on anomalous couplings $\Delta\kappa$ and λ displayed in fig. 5.6(b) can be compared with that of fig. 4.5 for single W production. In general the sensitivity to anomalous couplings is expected to be considerably better for the latter process, although with different dependencies on $\Delta\kappa$ and λ the two measurements are complementary (see chapter 11).

5.3 Photoproduction

Both direct and resolved photoproduction events generated with the Monte Carlo program HERWIG [66] have been used in this analysis. In the case of direct photoproduction the complete matrix elements including the $e\gamma e$ vertex are used, while for resolved events the Weizsäcker-Williams approximation is used to calculate the photon flux entering the hard scatter. In addition to matrix elements for the particular hard subprocesses, HERWIG

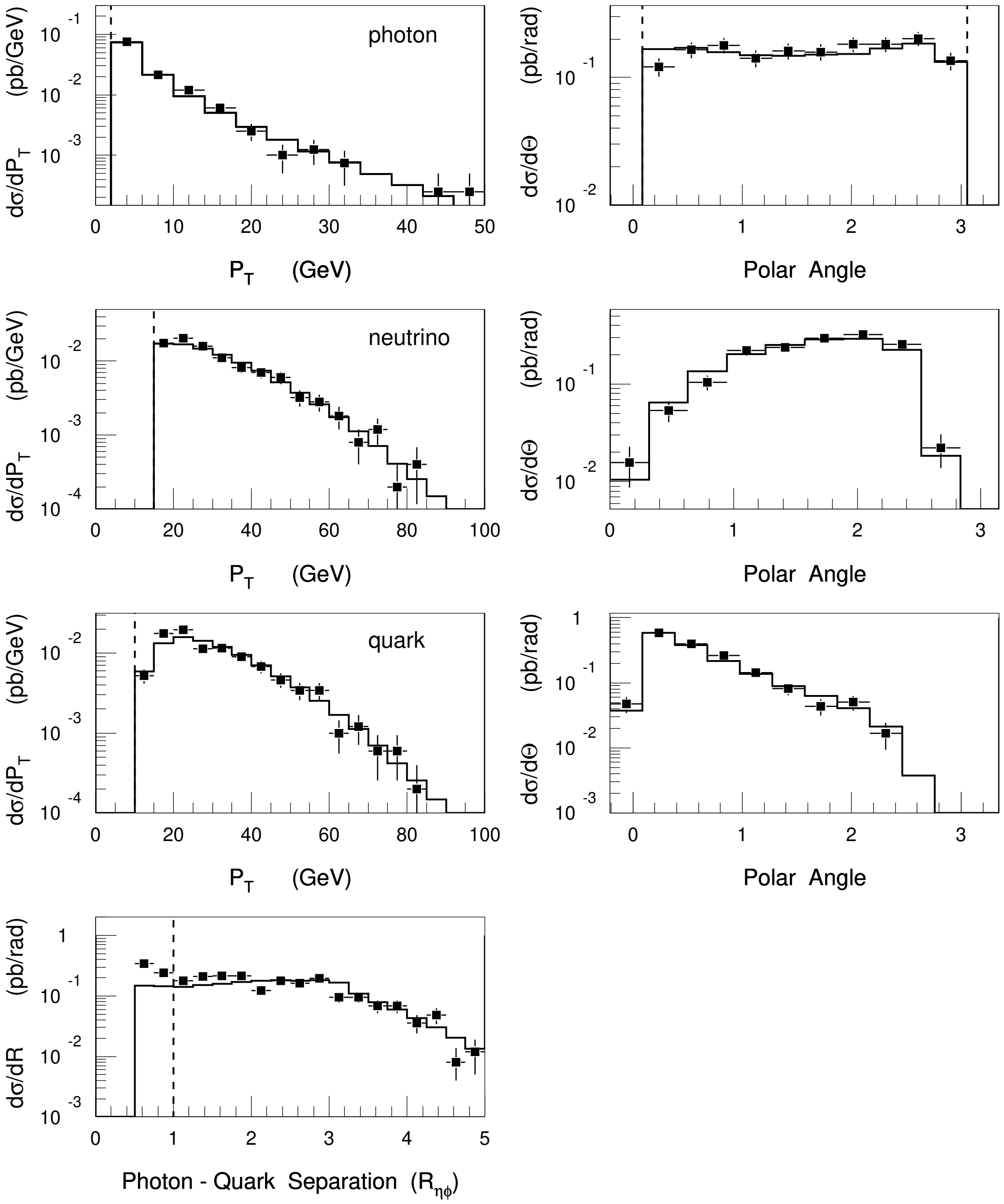

Figure 5.5: *A comparison of radiative charged current scattering described by the cross section program* WWGAMMA *(solid line) and the event generator* DJANGO *(points), with cuts as described in the text and indicated by the dashed lines. There is some discrepancy between the two programs at smaller values for the photon-quark separation variable* $R_{\eta\phi}$*. The photon polar angle distribution is much flatter than in fig. 5.2 due to the photon angular and* p_T *cuts imposed here.*

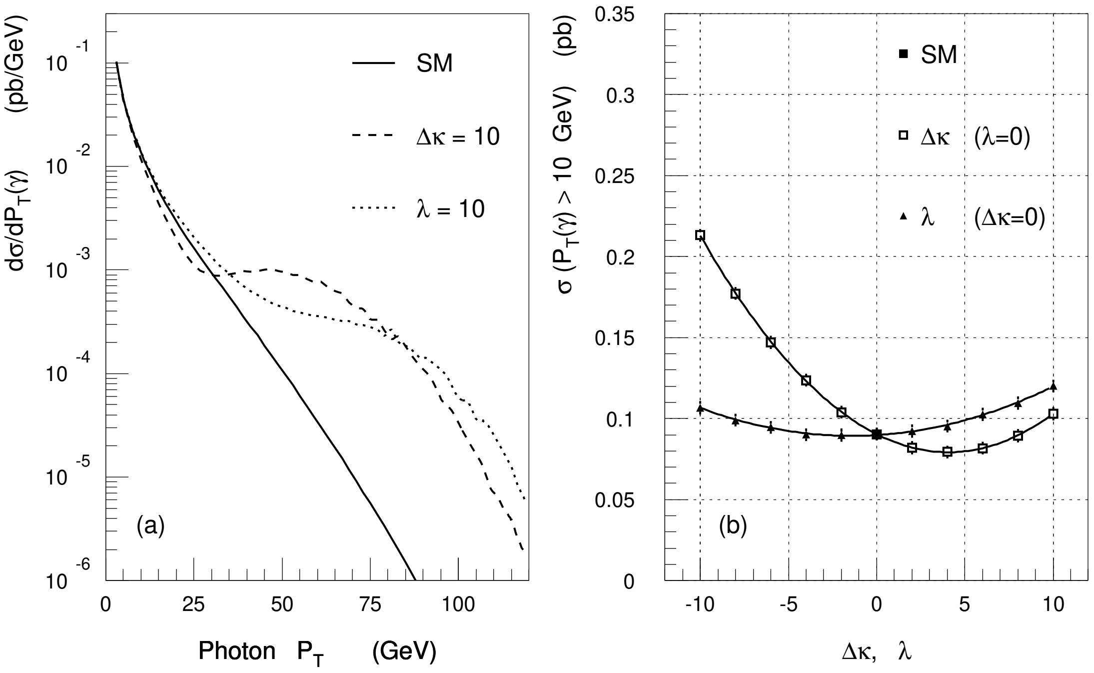

Figure 5.6: *(a) The photon p_T spectrum for radiative charged current scattering in the Standard Model and in the presence of anomalous $WW\gamma$ couplings $\Delta\kappa$ and λ. The dependence of the cross section on $\Delta\kappa$ and λ for $p_T^\gamma > 10$ GeV is plotted in (b). Remaining cuts are described in the text.*

implements an extensive simulation of initial and final state parton showers as a means of incorporating higher order QCD effects. Electroweak corrections are, however, not included. Hadronisation is performed by a cluster fragmentation model rather than the more conventional string fragmentation.

Photon as well as proton parton distributions can be selected from PDFLIB in a similar manner to the simulation of DIS events.

5.3.1 Generator Level Cuts

The events were generated with the standard $Q^2_{max} = 4$ GeV, corresponding roughly to the lowest Q^2 for which the scattered beam electron can be measured in the main detector. The bulk of the photoproduction cross section is at very low transverse energies. Since the interest here is in processes with large E_T, events generated with $p_T^{hard} > 8$ GeV were used, where this determines the minimum p_T of each outgoing parton in the hard scatter. Events generated with these cuts are then selected by requiring that the generator level total E_T exceed 28 GeV, reducing the number of events passed through the detector simulation by a factor of three. However, reducing the p_T^{hard} cut to 4 GeV increases the direct cross section by around 20%. This is a measure of the uncertainty in the predicted high E_T photoproduction cross section arising from the choice of this parameter.

5.4 Bethe-Heitler Process

As discussed in chapter 3, two photon processes are the most important source of high invariant mass lepton pairs in *ep* collisions. Bethe-Heitler scattering, which gives the dominant contribution, has been implemented in the event generator LPAIR [67]. Exact matrix elements are calculated for the process $ep \to eX\mu^+\mu^-$, where for elastic scattering $X = p$, and are extended to the case of e^+e^- and $\tau^+\tau^-$ production simply by the substitution of the corresponding lepton masses. Additional terms that appear in the matrix element for the production of lepton pairs with the same flavour as the beam lepton are therefore neglected.

Since inelastic Bethe-Heitler scattering is dominated by low masses for the hadronic final state (see chapter 3), the approach taken in LPAIR is the use of form factors for the photon-proton vertex. The form factor used here is an average through the very low mass resonance region, but is less accurate at higher momentum transfers than a parton model approach. LPAIR is interfaced to JETSET for the final state hadronisation.

The angular distribution of the scattered beam lepton in Bethe-Heitler events is plotted is fig. 5.7(a) for $\mu^+\mu^-$ events generated with $p_T^\mu > 2$ GeV and $5^\circ < \theta_\mu < 175^\circ$. The approximate limit of the central detector acceptance is indicated by the dashed line. In only $5 - 6\%$ of events is the scattered beam lepton expected to be observed in addition to the leptons from the two photon sub-process. The angular distribution of the muons, plotted in fig. 5.7(b), is peaked in the forward and rear directions for both elastic and inelastic scattering. The solid lines in fig. 5.7(c) and (d) indicate the integrated cross sections for $15^\circ < \theta < 165^\circ$, roughly the angular acceptance of the central tracking detector. For masses above 40 GeV the cross section is computed for events with $p_T^\mu > 10$ GeV, indicated by the dotted lines. The distributions in both cases are steeply falling, with a combined elastic and inelastic di-muon production cross section for invariant masses greater than 80 GeV of only 7×10^{-3} pb. This can be compared with a cross section for $Z^0 \to \mu^+\mu^-$ of around 10^{-2} pb before cuts.

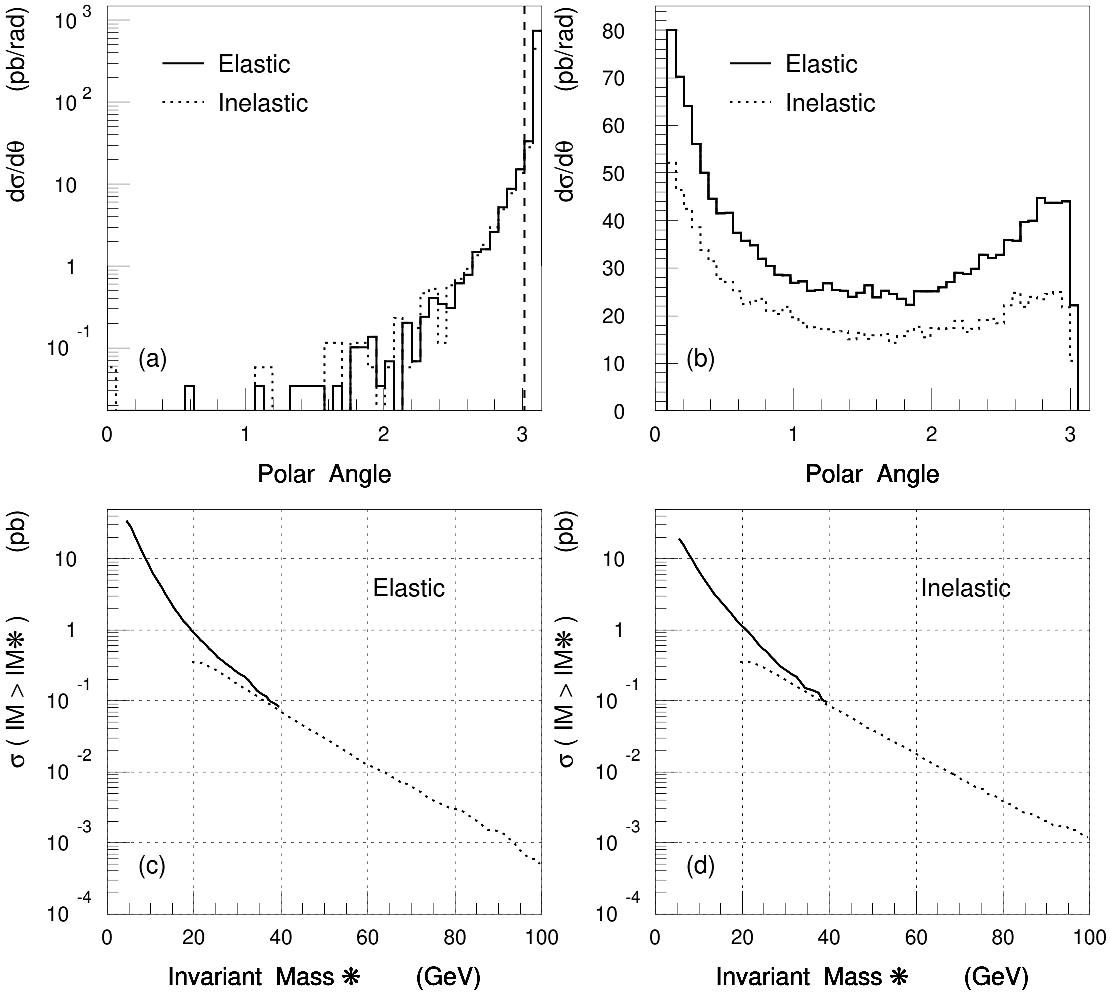

Figure 5.7: *The polar angle distributions for (a) the scattered beam lepton in Bethe-Heitler* $\mu^+\mu^-$ *events and (b) the muons from the two photon sub-process. The integrated cross sections for elastic and inelastic scattering are plotted in (c) and (d) for cuts given in the text.*

5.5 Vector Meson Production

In the study of muon chamber triggered events, and in particular for the measurement of muon finding efficiencies using elastic di-muon events (see chapter 9), an important process to consider is vector meson production with subsequent decay to muons. The two channels explicitly considered here are the elastic production and decays $J/\Psi \rightarrow \mu^+\mu^-$ and $\Upsilon \rightarrow \mu^+\mu^-$. The events used were generated with the DIPSI Monte Carlo program [68] with a cut $Q^2 < 4$ GeV. For the J/Ψ production $y < 0.5$ was also imposed. It must be noted that the cross sections are anyway rather poorly determined theoretically and the samples described here provide only a rough estimate of the contribution from these processes. This is further discussed in section 9.1.

5.6 QED Compton Events

Radiative neutral current events with very small momentum transfers to the hadronic system but both the electron and photon visible in the main detector are called QED Compton events. They are of interest here primarily due to the possibility that photon conversions in the material of the beam pipe may simulate multi-electron final states at relatively high invariant masses. QED Compton Monte Carlo events also provide a suitable sample of relatively high p_T isolated photons to evaluate the photon finding efficiencies using electromagnetic cluster finding algorithms (see section 6.2.5). Elastic and inelastic QED Compton scattering occurs at a similar rate, with a small admixture of resonant or quasi-elastic scattering similar to that described for Z production in section 4.2. Events in all three production channels were generated with the Compton 2.0 Monte Carlo program [69] for electrons and photons with $E > 4$ GeV and $3^\circ < \theta < 135^\circ$. Smaller luminosity samples with a polar angle coverage $3^\circ < \theta < 173^\circ$ have also been used.

In the current QED Compton event generator no attempt is made to simulate the hadronic final state. This means, for example, that background estimates cannot readily be divided into elastic and inelastic contributions on the basis of energy flows in the region of the proton remnant (see section 8.3.2). In addition the net calorimeter p_T distribution is not well simulated without hadrons to balance the final state $e-\gamma$ pair and, since the cross sections involved are tiny compared to those for other processes with high p_T electrons [2], the QED Compton background is assumed to be negligible in the search for events with missing p_T in addition to a high p_T electron.

5.7 Detector Simulation

The output from each event generator, including the generator for W and Z production described in the previous chapter, consists of arrays of four vectors for the final state particles. These four vectors are passed to a detailed simulation of the ZEUS detector, MOZART [7], based on the detector simulation package GEANT [70]. As well as tracking the passage of stable particles through the detector and simulating the development of electromagnetic and hadronic showers, MOZART can decay long lived particles such as heavy quark states

---

[2] For example 7.55 pb for the $3^\circ < \theta < 135^\circ$ polar angle range.

passed to it by the event generator.

An important aspect of the treatment of Monte Carlo events is the simulation of the ZEUS trigger, performed by a separate program ZGANA [71]. The accuracy of the trigger simulation is checked by running ZGANA on real data and comparing the on-line and simulated trigger responses.

There is evidence of a small miscalibration of the calorimeter energy scale for the ZEUS running period covered in this work. This 5% shift in the barrel calorimeter response and 2.5% shift in the rear calorimeter response is explicitly corrected for in the real data only [72]. In all other respects and unless otherwise stated, real and Monte Carlo data are treated identically in the analysis presented here.

Chapter 6

Lepton Identification

6.1 Introduction

In this chapter the basic techniques for the identification of high p_T electrons and muons are introduced. The cuts used to select electron and muon candidates are tuned using suitable Monte Carlo data samples. However the resulting efficiencies and purities are checked wherever possible against the data, as described in subsequent chapters.

6.2 Electron Identification

Many different algorithms exist to identify electromagnetic showers in the ZEUS calorimeter. The group of calorimeter cells containing energy deposits that such algorithms identify as forming an electromagnetic shower are together called an electromagnetic *cluster*. Further stages in the selection of a pure electron sample include the matching of CTD tracks to calorimeter energy deposits and cuts on the isolation of the electron candidate. These are described in more detail below.

A major background to $W \to e\nu$ decay arises from charged current events with an electromagnetic cluster in addition to missing energy from the outgoing neutrino. This electromagnetic cluster can correspond to a real electron from heavy quark decay or a photon from radiative charged current scattering but is more likely, particularly at high energies, to be a 'fake' electron. Such fake electrons can arise, for example, from $\pi \to e$ misidentification or π^0 decay. The cuts introduced below are designed to minimise this contamination while preserving a high overall efficiency for identifying true electrons.

6.2.1 The SINISTRA Electron Finder

SINISTRA is a neural network based algorithm for the identification of electromagnetic clusters, described in detail in [73]. The first stage consists of the grouping together of calorimeter cells into larger scale logical structures called *islands*, consisting of clusters of cells around local energy maxima [74]. The photomultiplier signals from the cells in a 3×3 window around the island centre [1] are partially summed to form 54 separate inputs to the neural network. The neural network was trained on separate, equally sized Monte Carlo samples of electromagnetic and hadronic clusters, with the final parameters in the neural network function chosen so as to minimise the misidentification probability for true electromagnetic and hadronic showers. In this analysis the standard probability cut of 0.9 is used to select electron candidates [75].

Fig. 6.1 shows the number of cells combined into a single electromagnetic cluster and the electromagnetic fraction for SINISTRA electron candidates in $W \to e\nu$ (solid line) and charged current Monte Carlo events (dotted line). The electromagnetic fraction is defined as the summed energy in EMC cells assigned to the cluster divided by the total cluster energy. The peak at smaller cell multiplicities for the charged current Monte Carlo is primarily due to the softer energy spectrum for the electron candidates. A fraction of the candidates also consist of much larger numbers of cells than the average for $W \to e\nu$ events and correspond to collimated jets being misidentified as electrons. Such electron candidates can be removed by imposing an upper limit on the cluster size as described in chapter 8. The lower average electromagnetic fraction is also an indication that many of the clusters are correlated with hadronic activity in charged current Monte Carlo events.

In fig. 6.2(a) the electron finding efficiency, defined as :

$$efficiency = \frac{\#electrons\ correctly\ identified}{\#electrons} \tag{6.1}$$

is plotted as a function of the true electron energy for electrons in the angular region $10^\circ < \theta < 170^\circ$. The low energy region is populated by electrons from elastic Bethe-Heitler Monte Carlo events and the high energy region by $W \to e\nu$ events. The SINISTRA efficiencies, plotted as closed squares, are compared to the efficiencies for a conventional electron finder called ELEC5, denoted by open squares. ELEC5 combines angularly adjacent cells into clusters and calculates a probability based on the size and composition of the clusters for them to be electromagnetic in origin [76]. It can be seen that particularly at low energies but also at high energies the neural network based electron finder gives better results. In figs 6.2(b) and (c) the efficiencies are plotted as a function of polar and azimuthal angles for electrons in elastic Bethe-Heitler events with $E > 8$ GeV (SINISTRA) and $E > 13$ GeV (ELEC5), corresponding roughly to the energies at which the two finders

---

[1] Here the centre simply denotes the island cell with the highest energy.

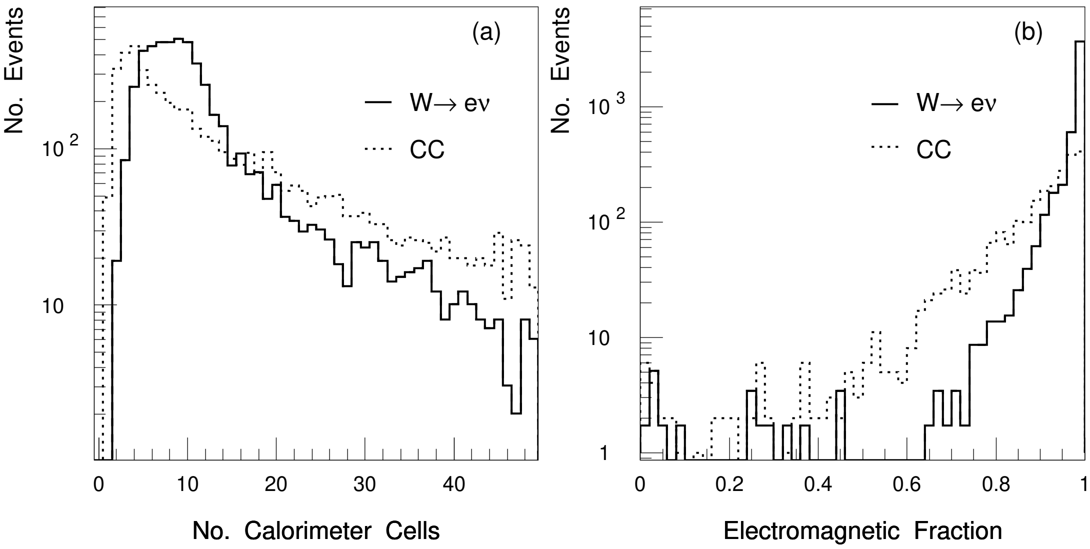

Figure 6.1: *(a) The number of calorimeter cells making up SINISTRA electron candidates in $W \rightarrow e\nu$ (solid line) and charged current Monte Carlo events (dotted line). The electromagnetic fraction for the same candidates is plotted in (b).*

become maximally efficient. The polar angles in fig. 6.2(c) are once again restricted to the region $10^\circ < \theta < 170^\circ$. Both electron finders suffer from small efficiency losses at the F/BCAL and B/RCAL boundaries where non-neighbouring cells must be combined into islands and clusters but otherwise exhibit no angular dependences.

6.2.2 Electron Position Determination

The electron position reconstruction routine ELECPO [77] is used to obtain the best estimate of the electromagnetic shower position in the calorimeter. One transverse coordinate (for example the x coordinate in the F or RCAL) is accurately determined by comparing the left and right photomultiplier signals. The relationship between this imbalance and the electron position has been parameterised from test beam data and by using the position reconstructed by the ZEUS hadron-electron separator (HES), a device consisting of silicon diode planes mounted in gaps in the F and RCAL electromagnetic sections at a depth of around 3 radiation lengths. The perpendicular transverse component (the y coordinate in F/RCAL) is determined from the distribution of energy deposits in neighbouring electromagnetic cells. The resulting resolution with which the electron position can be reconstructed is of the order of 1 cm in both transverse directions.

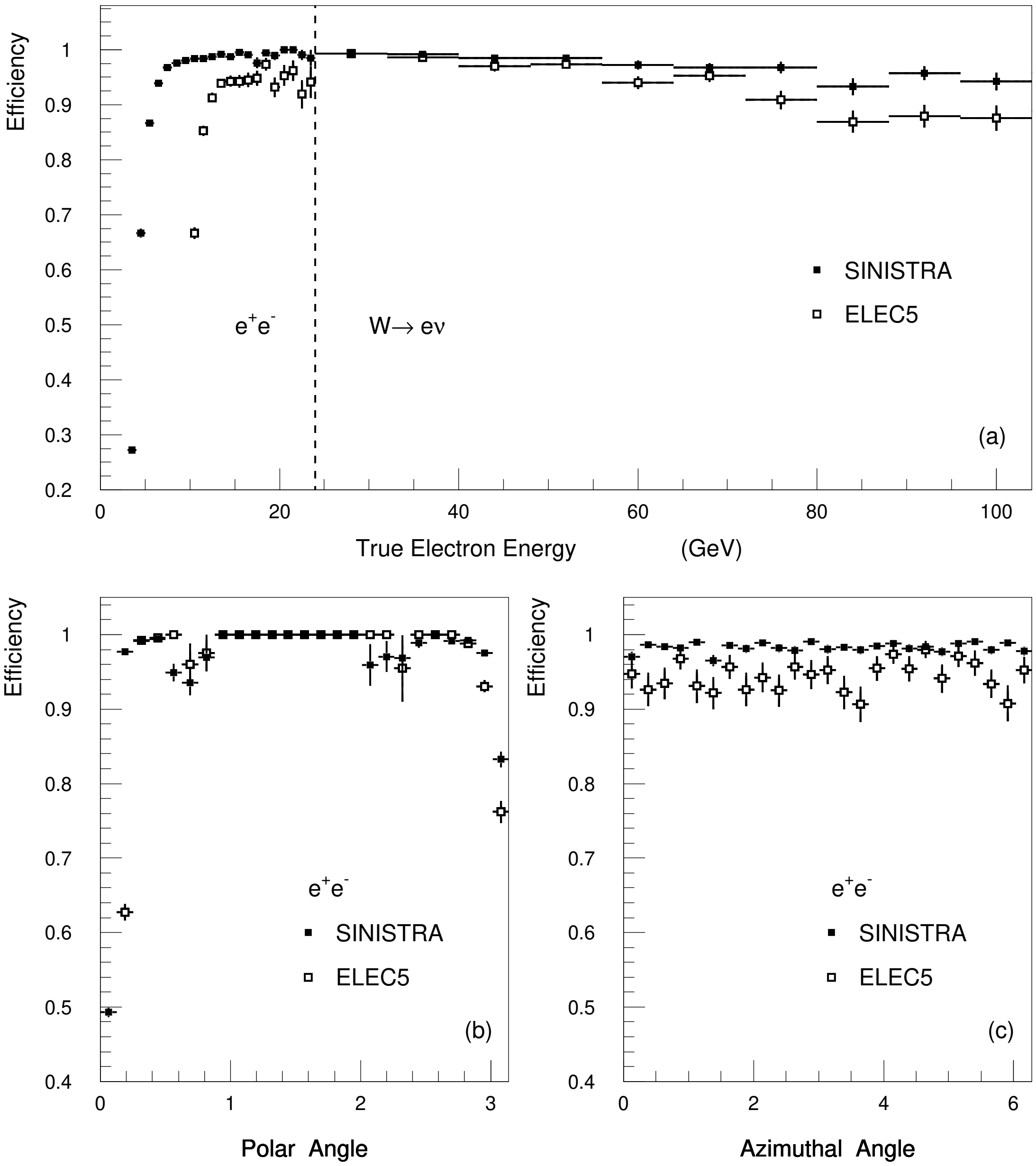

Figure 6.2: *The electron finding efficiency versus energy, polar and azimuthal angles for a neural net based electron finder (SINISTRA) and a conventional electron finder (ELEC5). More details are given in the text.*

6.2.3 Track Matching Requirements

In order for an electromagnetic cluster to be considered an electron candidate, it must have a matching CTD track. The ZEUS tracking reconstruction swims tracks using a modified Runge Kutta routine from the point at which the track leaves the CTD to the roughly cylindrical inner surface of the calorimeter. From the point of entry into the calorimeter a straight line extrapolation is performed and the distance of closest approach in three dimensions to a specified object calculated [78].

The mean distance of closest approach (DCA) of the nearest matching CTD track to the electromagnetic cluster is plotted as a function of polar angle for $W \to e\nu$ and charged current Monte Carlo events in fig. 6.3(a). The DCA is degraded at small polar angles by the deterioration in the accuracy of the track reconstruction at the edge of the CTD acceptance and the increased length of the track extrapolation through the material and inhomogeneous magnetic field in the region of the FDET. For polar angles less than 0.4 rad the cut on the DCA is therefore relaxed to 15 cm from the 10 cm at larger angles, as indicated by the dashed line. This results in an overall efficiency in excess of 80% for W decay electrons identified by SINISTRA to pass the matching track cuts. It can also be seen from fig. 6.3(a) that electron candidates in charged current events have comparatively much poorer matching tracks, which is expected if a large fraction of the electromagnetic clusters are arising from hadron misidentification or decay.

6.2.4 Electron Isolation Requirements

An important method of reducing the fake electron background is to require that candidate electrons are well isolated from other activity in the event. The measure used is the isolation energy, defined as

$$E_{iso} = \sum_i E^i_{non-elec} \qquad \forall \quad R_{\eta\phi}\,(i, elec) \ < \ R_0 \ , \tag{6.2}$$

where the summation extends over all calorimeter cells not assigned by SINISTRA to the electromagnetic cluster that lie with an $\{\eta, \phi\}$ cone of radius R_0 centred about the electron direction. It has been found that $R_0 = 0.6$ units allows an effective separation of isolated and non-isolated electrons, as illustrated in fig. 6.3(b). Elastic Bethe-Heitler events contain very little non-electron energy while W decay electrons, produced at small angles near the proton remnant and current jet regions, can have significant values for E_{iso}. Nevertheless, requiring $E_{iso} < 4$ GeV rejects fewer than 2% of $W \to e\nu$ events while removing many fake electrons in charged current events occupying the tail towards very high isolation energies.

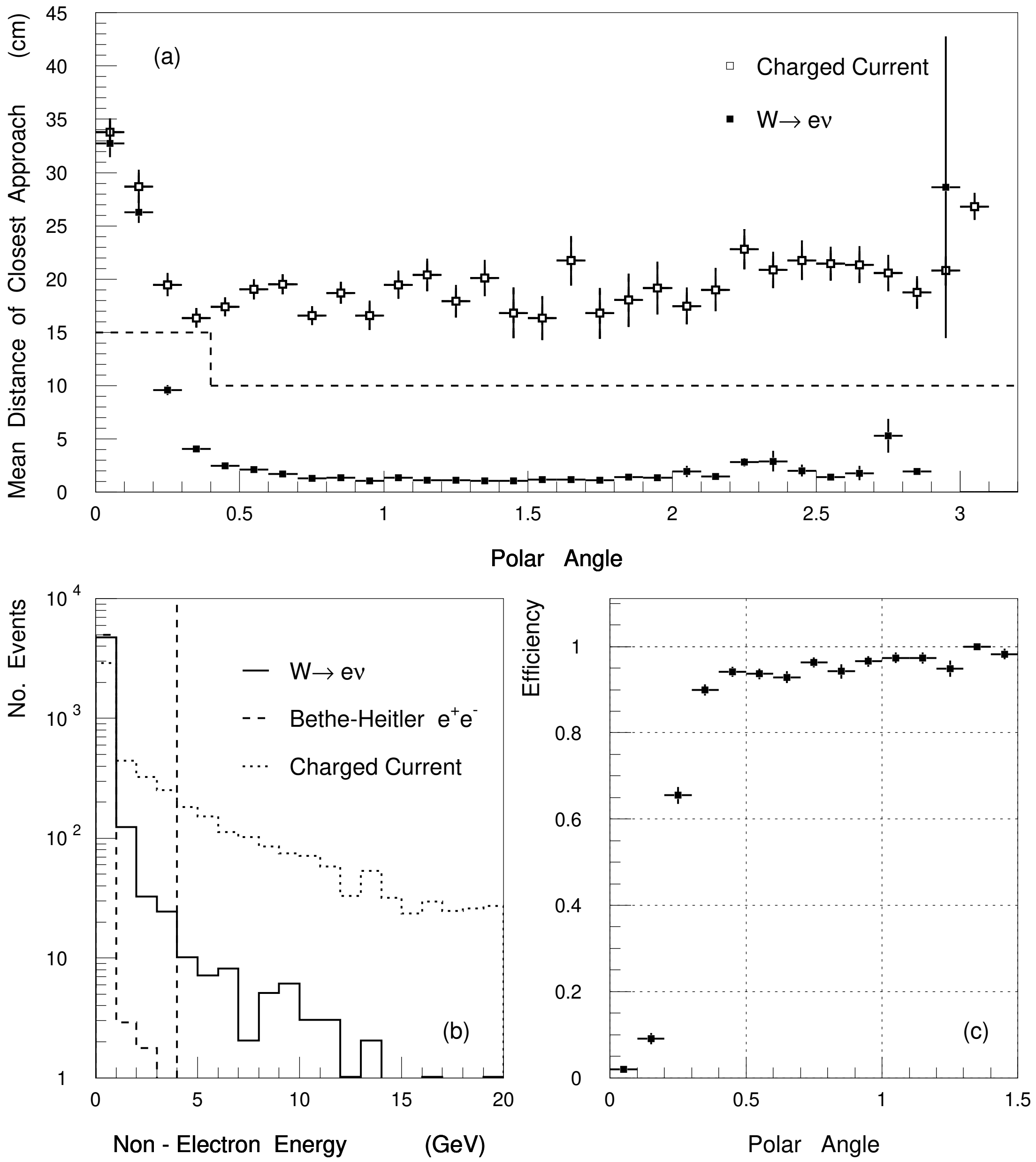

Figure 6.3: *(a) The mean value for the distance of closest approach of the matching CTD track for W decay electrons and electromagnetic clusters in charged current events. Their isolation energy is shown in (b) in addition to that for electrons in elastic Bethe-Heitler events. The combined efficiency for electromagnetic cluster finding, track matching and isolation requirements, with cuts indicated by the dashed lines in (a) and (b), is shown for W decay electrons in (c). Histograms in (b) have the same overall normalisation.*

The combined efficiency for electromagnetic cluster finding, track matching and requiring the electron candidate to be isolated is plotted in fig. 6.3 for $W \rightarrow e\nu$ events. A minimum bias W production sample [2] yields an overall efficiency of 77% for tagging electrons from the decay $W \rightarrow e\nu$. Note that this is somewhat lower than the corresponding efficiency for high Q^2 neutral current events, due mainly to the different angular distributions of the electrons in both cases. In addition the electron from $W \rightarrow e\nu$ decay need not be back-to-back with respect to the recoiling hadronic system, making it more likely that W decay electrons are less well isolated from other particles in the event.

Note that in order to improve the signal to background ratio in the final selection of $W \rightarrow e\nu$ candidate events, the given cuts on the DCA and electron isolation energy are eventually tightened, as described in detail in chapter 8.

6.2.5 Photon Identification

The electromagnetic clusters produced by high energy photons are found with high efficiency by the same algorithms described above for electrons. This efficiency is plotted as a function of energy and polar angle in fig. 6.4 for photons in elastic QED Compton events where, for the angular distributions, only photons with $E > 8$ GeV (SINISTRA) and $E > 13$ GeV (ELEC5) are considered. Turn on curves similar to those plotted in fig. 6.2 are visible, as are the calorimeter boundaries in the polar angle distributions. The single important requirement in the selection of photons is that there is no track matching the electromagnetic cluster within some distance of closest approach. However, the placing of this track isolation cut depends strongly on the type of events under investigation and will be different for, say, elastic QED Compton events and high track multiplicity radiative charged current events. These issues are returned to in chapter 8.

6.3 Muon Identification

Muons have been searched for in events with large missing p_T and events triggered on the basis of muon detector activity. The basic calorimeter and tracking requirements for muon candidacy are the same in both event classes and are discussed in the following subsections. In order to maximise the muon finding efficiency, muon candidates in events that are triggered by large missing p_T are not required to match muon chamber hits in addition. This eliminates geometrical and detector acceptance losses associated with the ZEUS muon

---

[2] That is, all W^+ and W^- production channels in proportion to their calculated cross sections.

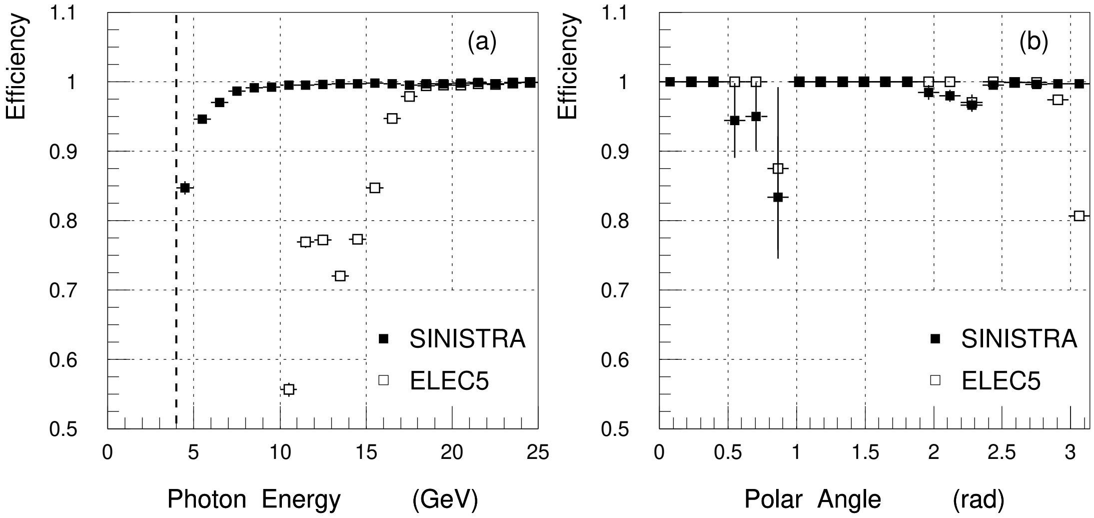

Figure 6.4: *The photon finding efficiency versus (a) energy and (b) polar angle for the neural net based electron finder (SINISTRA) and a conventional electron finder (ELEC5). Cuts are described in the text.*

detectors. If an event has been triggered on the basis of muon detector activity, however, the presence of a matching muon chamber track segment is an additional requirement.

6.3.1 Calorimeter Requirements

Muons with energies above a few GeV are penetrating enough to travel through the entire depth of the ZEUS calorimeter. The characteristic deposits of energy in the electromagnetic and hadronic sections of the calorimeter that indicate the passage of a muon are together called a MIP. Since the energy deposited by a muon in a single calorimeter cell can be very small, MIP finding algorithms are run before calorimeter noise suppression routines are applied.

MIP finding, like electron identification, starts with the organisation of calorimeter cells into islands. In order to maximise the chance that single energy deposits, for example due to isolated hadrons, are reconstructed as a single island, diagonally adjacent cells are considered neighbours as well as those sharing an edge. However, since muons deposit comparatively small energies over long path lengths, a further combination of islands into super-islands or *archipelagoes* is required. This combination proceeds on the basis of the angular separation of existing islands [79]. Finally, a MIP is defined to be any archipelago satisfying the the following requirements :

1. $1 \leq$ No. EMC Cells ≤ 6
2. $1 \leq$ No. HAC Cells ≤ 8
3. $0.0 \leq$ Summed EMC Energy ≤ 3.0 GeV
4. $0.5 \leq$ Summed HAC Energy ≤ 8.0 GeV

where EMC and HAC denote the electromagnetic and hadronic calorimeter sections respectively. Fig. 6.5 shows the distributions of these four quantities for reconstructed MIP's in elastic Bethe-Heitler Monte Carlo events for muon energies greater than 5 GeV. Note that the mean energy deposited by the muon depends on the depth of the active material and so is different for muons traversing the forward, barrel and rear calorimeters.

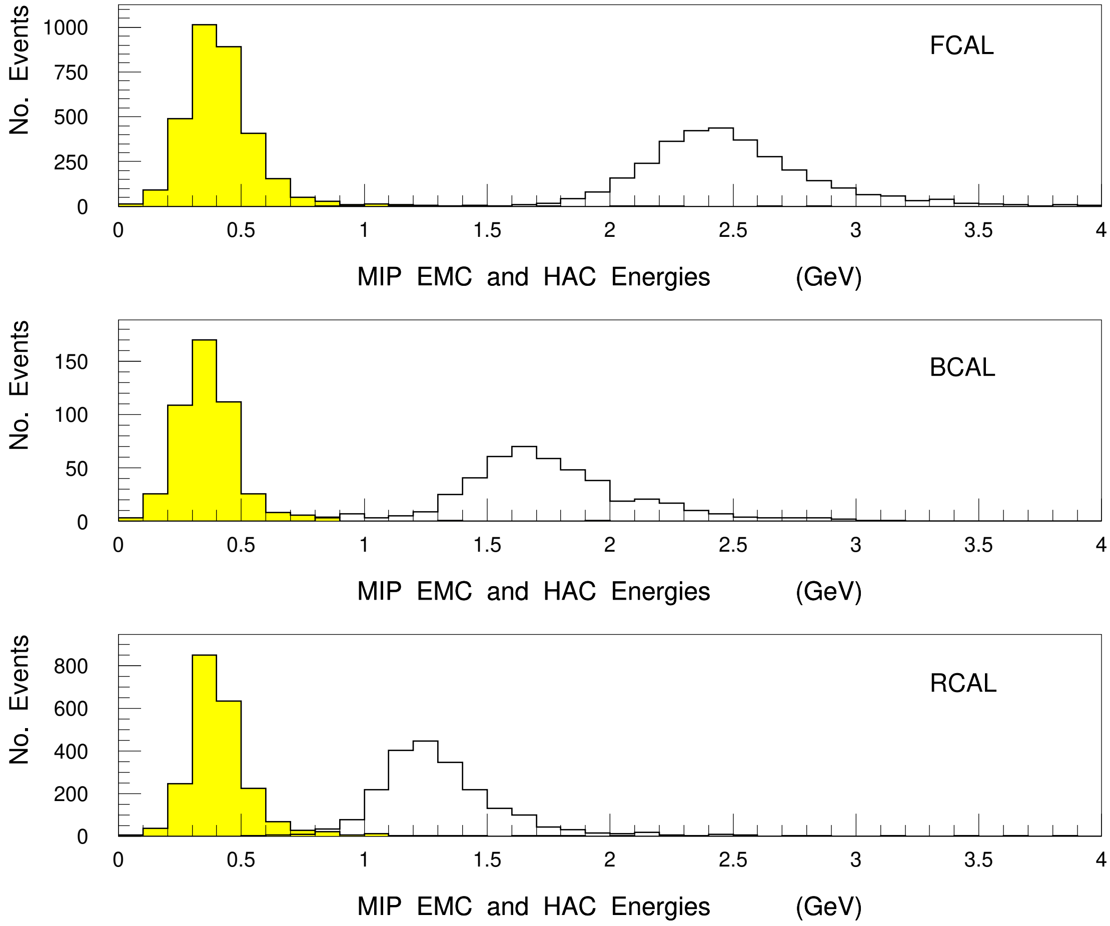

Figure 6.5: *The summed EMC energies (shaded histogram) and HAC energies (open histogram) for MIP's reconstructed in elastic Bethe-Heitler Monte Carlo events.*

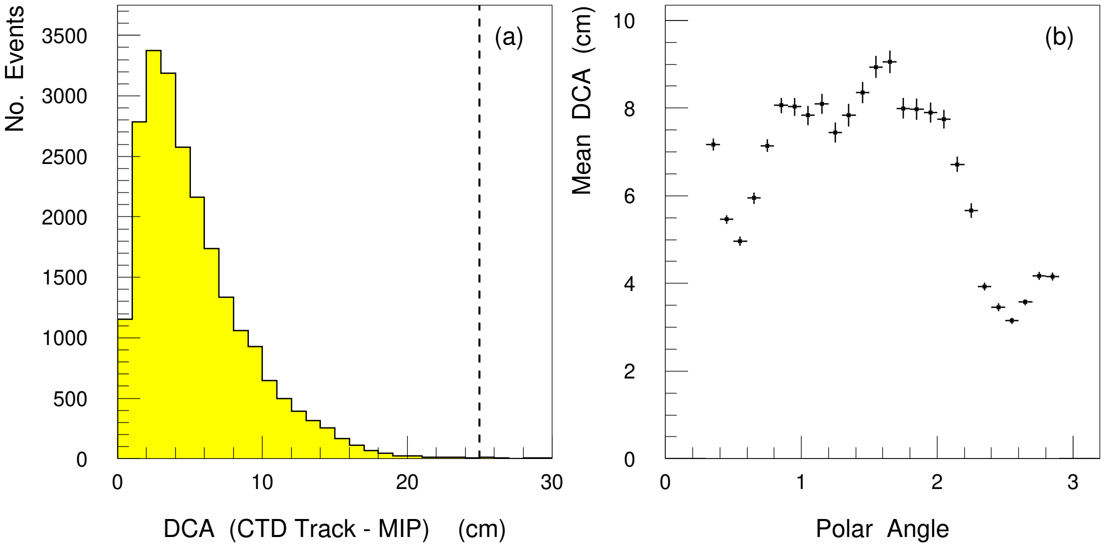

Figure 6.6: *(a) The DCA of CTD tracks to calorimeter MIP's for elastic Bethe-Heitler Monte Carlo events and (b) the mean value of the DCA as a function of polar angle. The standard cut of* 25 cm *is indicated.*

6.3.2 Tracking Requirements

Muon candidates are required to have a CTD track matching the calorimeter MIP. The same track extrapolation technique used in the identification of electron candidates is used. Distances of closest approach are calculated from the MIP centre, defined here as the energy weighted mean position of all the cells combined into the calorimeter archipelago. Geometric cell centres are used for the position of each individual cell. Fig. 6.6(a) shows the distribution of the distance of closest approach of CTD tracks to calorimeter MIP's in a sample of elastic Bethe-Heitler Monte Carlo events. In fig. 6.6(b), the mean value of the DCA is plotted as a function of the polar angle. In the central region the mean DCA is significantly less than the typical dimension of the BCAL module faces, which have a width of some 24 cm at their innermost point. Muons traversing the forward and rear calorimeters can cross several modules or towers and the resulting improvement in the polar angle reconstruction of the MIP lowers the mean value of the DCA. At polar angles near the edge of the central tracker acceptance the DCA is degraded by the poor quality of the matching CTD track.

Unless otherwise stated a cut of 25 cm is placed on the distance of closest approach of the track to the reconstructed MIP, which safely selects muon candidates at all polar angles. Since the main interest in this work is to identify well isolated muons, any further

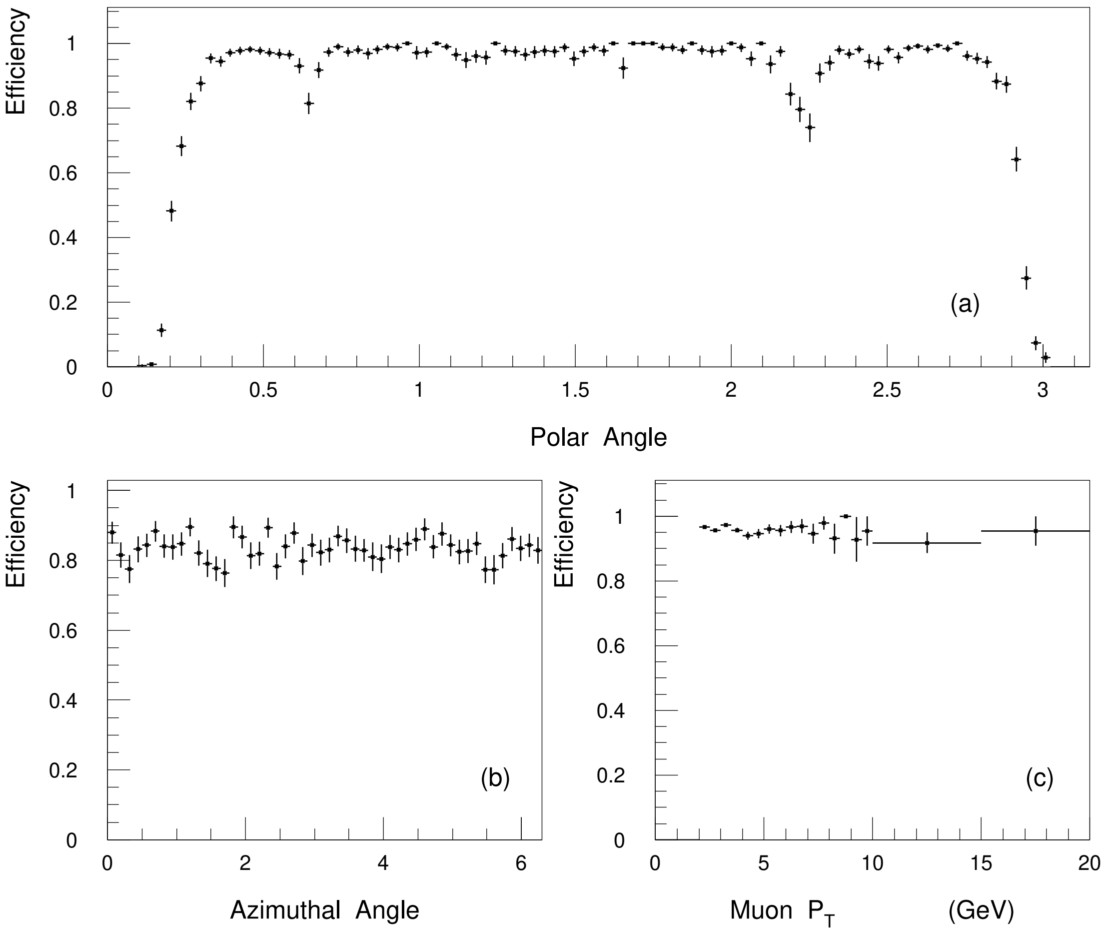

Figure 6.7: *(a) The CTD-MIP match finding efficiency as a function of polar angle and (b) as a function of azimuthal angle. Plotted in (c) is the match finding efficiency as a function of the muon p_T, for which central polar angles only are considered.*

track that matches the MIP must have a DCA $>$ 50 cm. This suppresses the number of events in which the muon candidate is found close to a jet or other hadronic activity.

In order to estimate the efficiency of the combined MIP finding and track matching, well isolated muons with $p_T > 2$ GeV are selected in Monte Carlo Bethe-Heitler events. Fig. 6.7(a) shows the efficiency for a CTD-MIP match to be reconstructed along the true direction of a muon in the event, as a function of the muon polar angle. It can be seen that the probability of reconstructing a well matching track falls away rapidly towards the edge of the central tracker acceptance. Dips are also visible at polar angles around 0.65 and 2.25, due to inefficiencies in combining cells and islands into archipelagoes across the F/BCAL and B/RCAL boundaries respectively. It can be seen from fig. 6.7(c), for which muons well inside the tracking acceptance only are considered, that there is no significant dependence of the efficiency on the p_T of the muon.

The purity of a muon finder may be defined analogously to the efficiency as

$$purity = \frac{\#muons\ correctly\ identified}{\#muon\ candidates} \tag{6.3}$$

where the number of correctly identified muons can, for Monte Carlo events, be calculated by comparing the parameters of the muon candidate with the parameters of generated muons. The purity is more strongly dependent on the type of event under investigation than the muon finding efficiency. For example photoproduction events can have high track multiplicities and relatively isolated hadrons, which are the most serious background to genuine MIP signals. The purity of the CTD-MIP match based muon finder has been calculated to be around 50% for high E_T direct photoproduction Monte Carlo events, which is to be compared to purities of 100% for elastic Bethe-Heitler di-muon events. These results, together with the muon finding efficiencies for the different types of event, are summarised in fig. 6.10.

6.3.3 Barrel and Rear Muon Chambers

The barrel and rear muon detectors, described in chapter 3, consist of inner and outer muon chambers that lie inside and outside of the iron return yoke respectively. Each chamber itself consists of four planes of limited streamer tubes, or LST's. The first stage of the barrel and rear muon reconstruction involves looking for combinations of hits amongst each set of four LST planes and thus forming track segments, each with a position and direction [80]. A further stage of the reconstruction seeks matches between inner and outer muon chamber track segments, yielding an independent momentum measurement for muons traversing the magnetised iron yoke.

For this analysis it is sufficient that a muon candidate is aligned with a single inner muon chamber track segment [3]. Therefore an independent momentum measurement is not always available. Furthermore, for the high p_T muons under consideration the matching CTD track provides the best momentum estimate. The main requirement of muons entering the barrel and rear regions of the detector is therefore that a CTD track matches the muon chamber track segment. Fig. 6.8(a) shows the distance of closest approach of the CTD track to the barrel or rear muon track segment or BMU segment for short. In fig. 6.8(b) the

---

[3] Or a single outer muon chamber track segment in the negative y direction not covered by inner muon chambers.

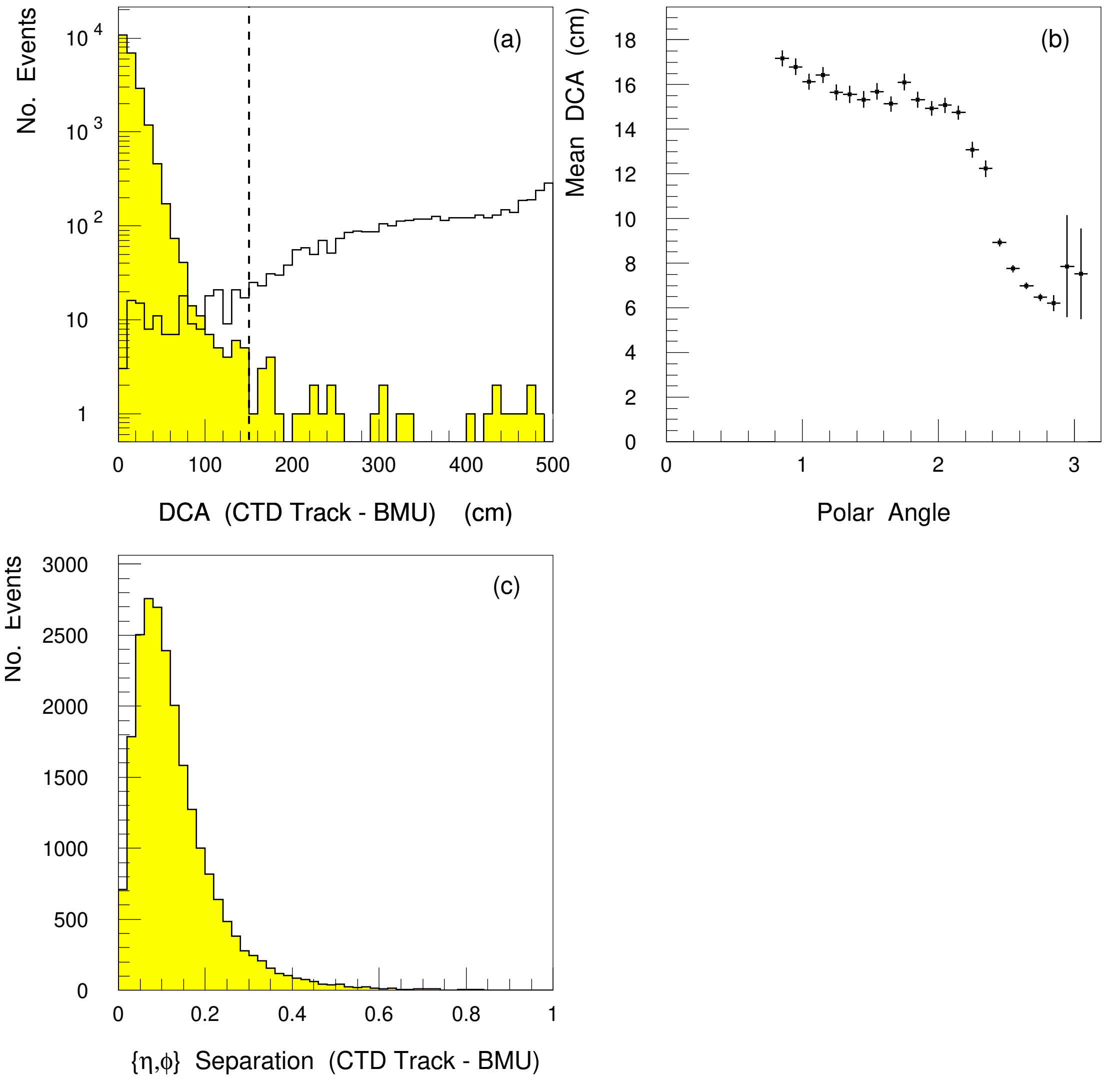

Figure 6.8: *(a) The distance of closest approach of CTD tracks to barrel and rear muon chamber segments (shaded histogram) for muons in Bethe-Heitler Monte Carlo events with* $p_T > 3$ GeV*. The open histogram shows the DCA distribution for incorrectly matched tracks in such events and the dashed line indicates the standard cut at* 150 cm*. In (b) the mean DCA is plotted as a function of polar angle and in (c) the* $\{\eta, \phi\}$ *separation of the CTD track and BMU segment directions is plotted.*

mean value of the DCA is plotted versus the muon polar angle. Unless otherwise stated, the DCA must be less than 150 cm and the DCA of any second matching track must be greater than 50 cm. The angular separation of the CTD track and BMU segment in $\{\eta, \phi\}$ space, showing the clear correlation between the two measured directions, is plotted in fig. 6.8(c) but is not cut on in this analysis.

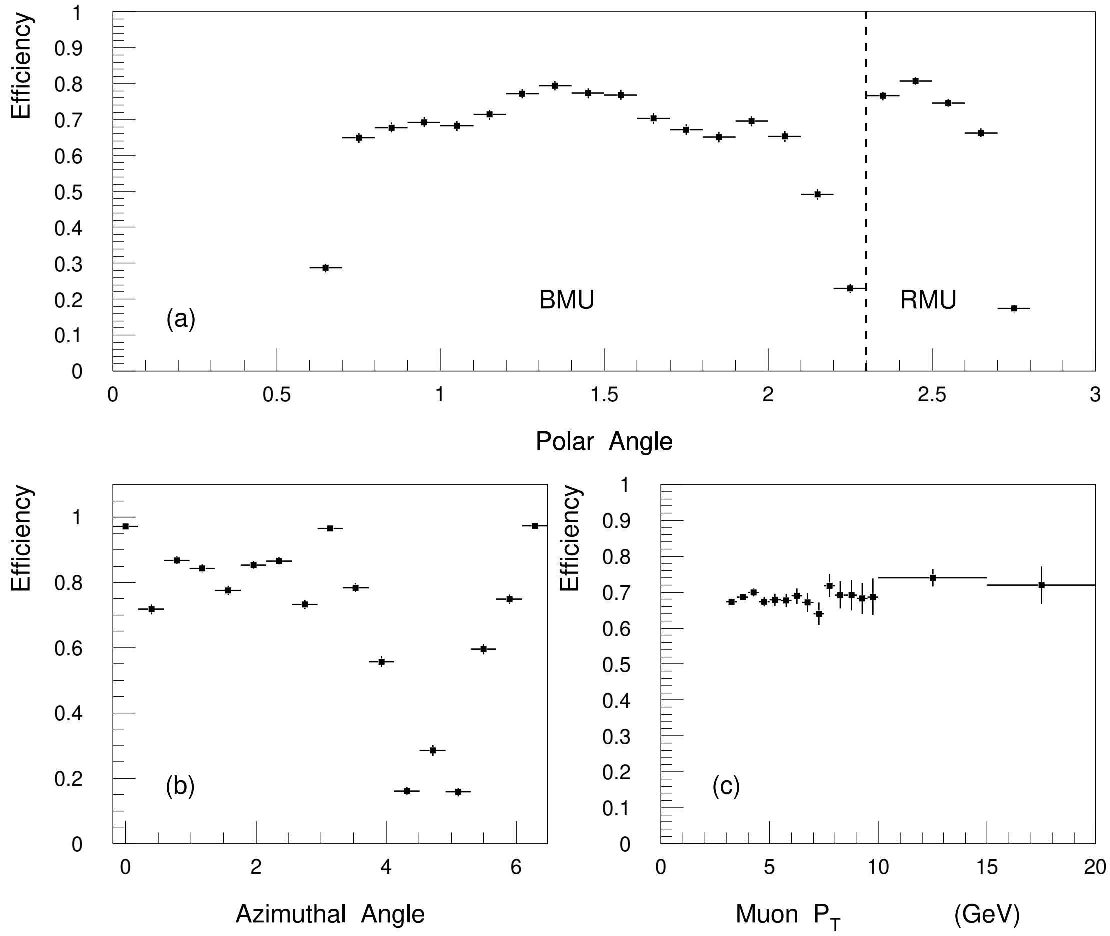

Figure 6.9: *(a) The efficiency for muons to be reconstructed as a CTD-MIP-BMU match as a function of polar angle and (b) as a function of azimuthal angle. The division between barrel muon (BMU) and rear muon (RMU) detectors is indicated. The efficiency versus muon* p_T *is plotted in (c). In (b) and (c), barrel muons with* $\theta > 0.8$ rad *only are considered.*

One final requirement of muon candidacy is that the same CTD track matches both the calorimeter MIP, as described above, and the BMU segment. The efficiency of this CTD-MIP-BMU match is plotted as a function of the polar and azimuthal angles in fig. 6.9(a) and (b). The important features are the loss in efficiency associated with the gap between barrel and rear muon detectors at $\theta \simeq 2.3$ rad and the dips in the efficiency at values of ϕ close to boundaries between the eight barrel muon sectors [80]. The presence of mechanical support structures severely limits the barrel muon coverage in the negative y direction between ϕ of around 4.1 and 5.3 rad.

The efficiencies and purities for the CTD-MIP and CTD-MIP-BMU based muon finders are plotted in fig. 6.10 for both photoproduction and elastic Bethe-Heitler di-muon events. The purities for both muon finders are expected to be close to 100% for di-muon type events and the efficiencies, in particular for the CTD-MIP based muon finder, are high. The situation is very different, however, if muons are searched for in high E_T photoproduction events. Firstly the efficiencies are markedly lower, due mainly to muons being produced close to jets where a calorimeter MIP signal cannot be separated from the other hadronic activity in the event and matching tracks will in general not be well isolated. Secondly the purities are significantly lower for photoproduction events, indicating that fake muon signals are more prolific in events with many final state hadrons and tracks than in clean $\mu^+\mu^-$ events. Many such fake muons are removed by demanding a barrel muon chamber track in addition to a CTD-MIP match, as indicated by the much higher purity for the second type of muon finder. The decays $W \to \mu\nu$ and $Z^0 \to \mu^+\mu^-$ give rise to isolated muons for which the muon finding efficiencies should be comparatively high. However, both correctly identified and fake muon candidates from other physics processes provide a serious background to the search for these decays. These issues are returned to in chapter 9.

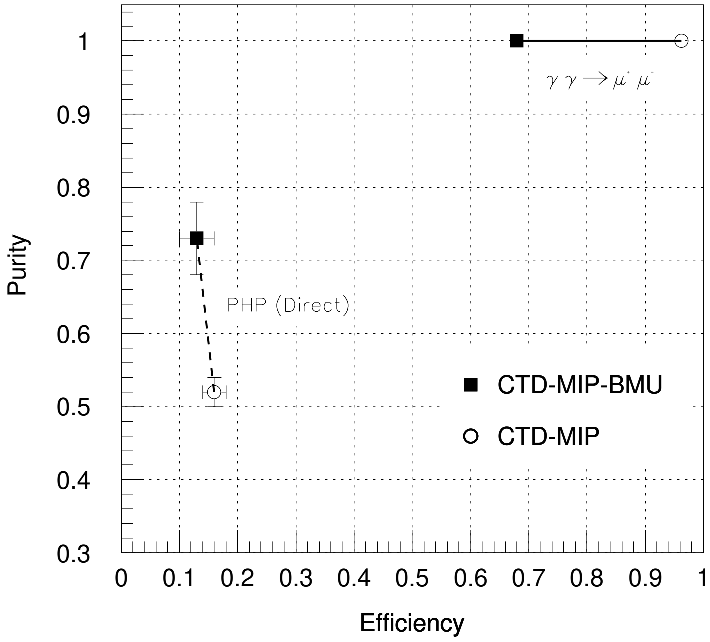

Figure 6.10: *The efficiency and purity of the CTD-MIP and CTD-MIP-BMU match based finders for muons in elastic Bethe-Heitler events (solid line) and high E_T direct photoproduction events (dashed line).*

6.4 Tau Identification

No explicit identification of tau leptons is attempted in this analysis. The background to the hadronic decay modes of the tau lepton from isolated hadrons and low multiplicity jets makes it difficult to reliably estimate a purity for any tau finding algorithm. However, the decays $\tau \rightarrow \nu_\tau \, e \, \nu_e$ and $\tau \rightarrow \nu_\tau \, \mu \, \nu_\mu$ do give rise to events in the electron and muon event samples. Moreover the cascade decays $W \rightarrow \tau \rightarrow e, \mu$ enhance the sensitivity to W production and leptonic decay and are taken into account. However, the branching ratio for both τ's in $Z^0 \rightarrow \tau^+\tau^-$ events to decay to the same flavour lepton is too small to significantly enhance the sensitivity to Z production in the e^+e^- and $\mu^+\mu^-$ event samples.

Chapter 7

The Data Samples

The classes of event considered in this work are selected on the basis of missing p_T, high transverse energy or by activity in the ZEUS muon detectors consistent with the passage of a minimum ionising particle. The following sections describe in more detail the selection of events with these signatures and the general features of the resulting event samples. The selection of specific event topologies and detailed comparisons with Standard Model predictions are described in subsequent chapters.

7.1 Events with Missing p_T

7.1.1 Trigger Requirements

Trigger slots exist at each stage of the ZEUS three-level trigger system to select events with missing p_T and transverse energy, E_T, defined by :

$$p_T = \sqrt{(\sum_i p_{x,i})^2 + (\sum_i p_{y,i})^2} \ , \tag{7.1}$$

$$E_T = \sum_i \sqrt{(p_{x,i})^2 + (p_{y,i})^2} \ , \tag{7.2}$$

where $p_{x,i} = E_i \sin\theta_i \cos\phi_i$ and $p_{y,i} = E_i \sin\theta_i \sin\phi_i$. Polar and azimuthal angles are calculated assuming a primary vertex at the nominal interaction point ($x = y = z = 0$ cm) at the first and second level triggers. At the third level trigger, as in offline event processing, the vertex position is measured from tracks in the CTD. At the first level trigger the E_i's correspond to the energies in each of the sixteen trigger regions of the calorimeter [81], while at the second and third level triggers the above summations are over individual calorimeter cells.

First Level Trigger

An event in the missing p_T sample must have one of several global first level trigger (GFLT) bits set, the definitions of which vary slightly for the 1994, 1995 and 1996 running periods. They can be split broadly into two classes :

- Missing p_T. In 1996 both p_T and E_T were required to be greater than 5.1 GeV, in addition to at least one CTD vertex track [1]. The tracking requirements are relaxed if $p_T > 8$ GeV. The corresponding p_T thresholds in 1995 were 6 and 8.9 GeV respectively. In 1994 $p_T > 8$ GeV and $E_T > 5.1$ GeV were required for the corresponding bit to be set without any additional tracking requirements.
- Regional and global energy sums. If the total calorimeter energy is greater than 15 GeV in an event with at least one CTD vertex track then the event passes the first level trigger. If the electromagnetic energy is greater than 15 GeV then an event is accepted without any tracking requirements. Remaining slots accept events with BCAL and RCAL energies above certain low energy thresholds.

Second Level Trigger

A single global second level trigger (GSLT) slot is designed to accept events with missing p_T. As for the first level trigger slots described above the definitions vary slightly between different running periods. This GSLT trigger bit is set if $p_T > 9$ GeV and $p_T[-1\mathrm{ir}] > 8$ GeV, where the latter quantity is calculated without including the first ring of calorimeter cells in the FCAL immediately neighbouring the beam pipe. This ensures that the missing p_T has not arisen from a small mismeasurement of the large energies surrounding the forward beam pipe in the region of the proton remnant. In addition, the total FCAL energy must exceed 20 GeV for 1995 and 1996 running.

The same GSLT trigger bit is also set for values of p_T as low as 7 GeV in 1995 and 1996. However, the E_T calculated excluding two inner FCAL rings must exceed 7 GeV (6 GeV in 1996) and tracking requirements are also made. A full description of the second level trigger operation may be found in [82].

Third Level Trigger

Two third level trigger slots select events with missing p_T. They are :

---

[1] For this as for other trigger bits a track veto is applied in addition, which is designed to reject beam gas events with a large fraction of non-vertex tracks.

- Missing p_T with good track. The vertex-corrected p_T must be greater than 7 GeV and there must be at least one good track, passing certain quality cuts and with $p_T > 0.5$ GeV (1.0 GeV in 1994), in addition.
- Missing p_T. The basic p_T cut for this slot is 9 GeV. However, no tracking requirements are made over and above those specifically designed to cut out beam-gas and cosmic ray topologies.

A more detailed description of the third level trigger operation may be found in [83].

7.1.2 Missing p_T + Electron Sample

Events that pass the trigger requirements outlined above are required to have an offline reconstructed calorimeter p_T greater than 10 GeV, where this quantity is calculated after calorimeter noise suppression and PMT spark rejection. Demanding in addition that $p_T[-1\text{ir}] > 9$ GeV means that both these offline cuts are more stringent than the corresponding trigger level cuts for any given year. Events are required to have at least one good track, defined as a vertex fitted track with $15^\circ < \theta < 164^\circ$ and $p_T > 0.2$ GeV, and to contain no pattern of CTD tracks consistent with the passage of a cosmic ray muon. Standard cuts select good electron candidates, namely

1. $E_e > 8$ GeV and $p_T^e > 2$ GeV ,
2. A vertex fitted matching track with DCA < 10 cm (15 cm for $\theta < 0.4$ rad),
3. Isolation Energy $(R_{\eta\phi} = 0.6) < 4$ GeV ,

thereby ensuring that the neural network based electron finder is efficient and reducing the fake electron background (see chapter 6). Finally, since the interest is in identifying electrons from the decays of heavy objects and not from neutral current scattering at relatively low Q^2, only electron candidates with $\theta < 2$ rad are accepted.

The vertex z-position for the 1996 preselected data is shown in fig. 7.1. The solid histogram is the measured vertex distribution for this period [2], with arbitrary normalisation relative to the data points. There is little indication of any contamination from non-ep physics backgrounds, characterised by flatter vertex distributions, and only a handful of cosmic muon events are removed at a later stage of the event selection. The final preselection

---

[2] An average over the whole running period, this vertex distribution is sampled in the generation of Monte Carlo events for the 1996 detector configuration.

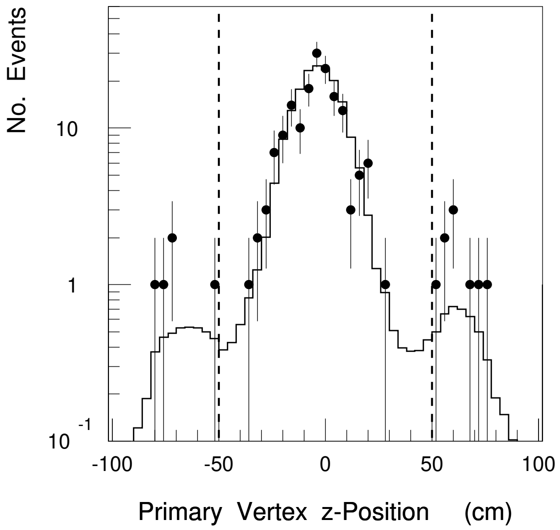

Figure 7.1: *The z-position of the primary vertex for the preselected 1996 data in the missing p_T plus electron sample (points), plotted against the measured 1996 vertex distribution (solid histogram). The final allowed range for the vertex position is indicated by the dashed lines.*

requirement, indicated in fig. 7.1, is that the vertex position lie between -50 and 50 cm, reducing uncertainties due to the understanding of the satellite structure of the beams [3].

An example of an event in the missing p_T + electron sample is shown in fig. 7.2. The event has a missing p_T of around 12 GeV and a high p_T positron is clearly visible in the BCAL. The event is almost certainly a relatively high Q^2 neutral current DIS event in which some energy has been lost in the direction of the recoiling jet of hadrons. The fact that a muon has been reconstructed in the barrel muon system in the direction of the jet supports this hypothesis. Monte Carlo studies indicate that neutral current events dominate this event sample and, as discussed in detail in the next chapter, constitute the most serious background to W production and decay $W \to e\nu$.

7.1.3 Missing p_T + Muon Sample

The first stage of the event selection is to run the muon finding algorithms described in chapter 6. The distance of closest approach of the nearest track to the calorimeter MIP must be less than the default 25 cm and the standard isolation requirement, namely that any further MIP matching track must have a DCA > 50 cm, is also made. The closest MIP

---

[3] Satellite bunches are protons leading the main bunch by 4.8 ns and therefore giving rise to ep collisions at $z \simeq +70$ cm, outside the range allowed here.

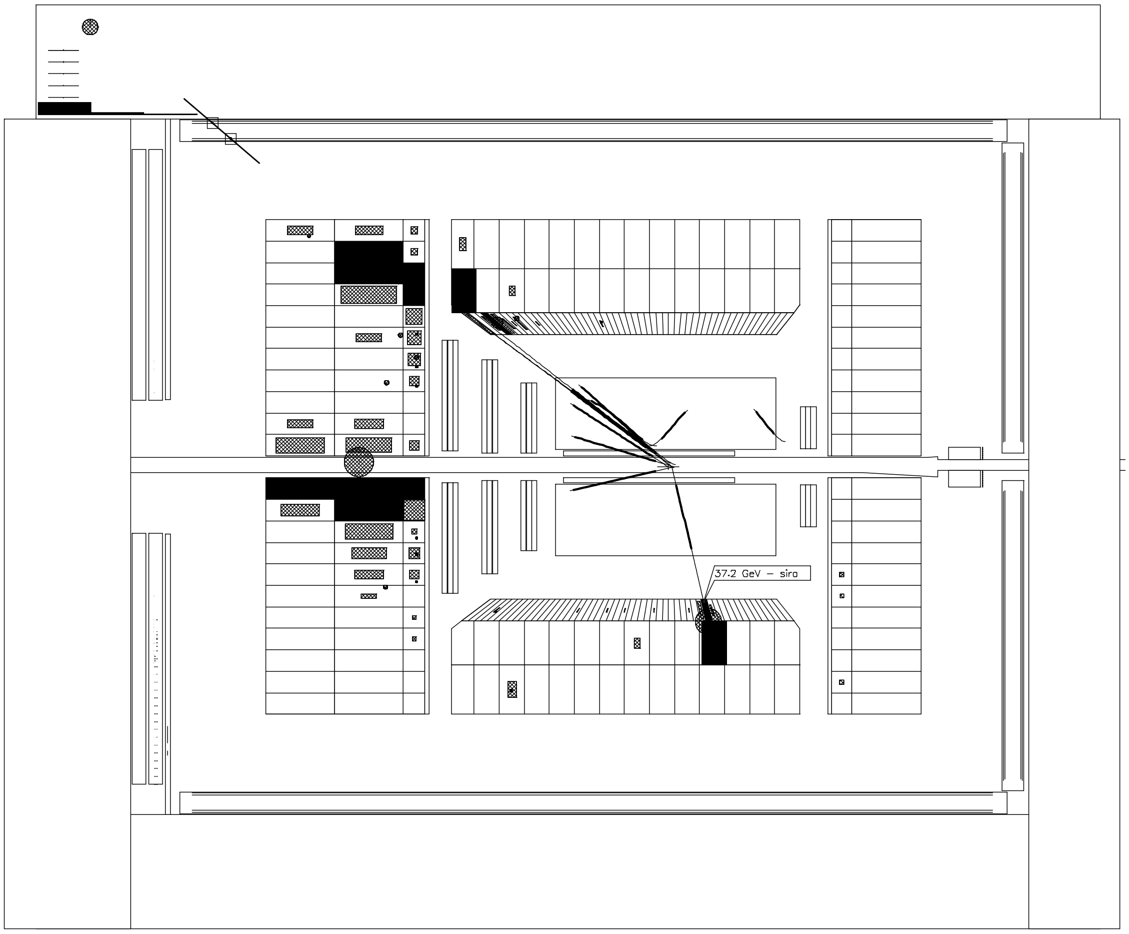

Figure 7.2: *An example of an event with missing* $p_T \simeq 12$ GeV *and a high* p_T *positron at a polar angle of* 105°. *See text for more details.*

matching track must in addition be fitted to the primary vertex and have $p_T > 2$ GeV.

Although cosmic ray identification algorithms have already been run at the trigger level and in the initial stage of offline event selection, they still constitute the main background to muon production in ep collisions. In order to suppress further the contribution from cosmic ray muons, events with more than one CTD track must in addition satisfy the requirement that :

$$\left[\cos\theta_{\mathrm{OPEN}} = \max\left(\cos\theta_{ij} = \frac{\mathbf{p}_i \cdot \mathbf{p}_j}{\mid \mathbf{p}_i \mid\mid \mathbf{p}_j \mid}\right)\right] \; > \; -0.99 \; , \tag{7.3}$$

where all track combinations $\{i, j\}$ are considered subject to one of the tracks being the MIP matching track. This cut removes almost all the remaining cosmic ray muons, which have two track opening angles close to 180°. This is shown in fig. 7.3(a), for which all preselected events with calorimeter $p_T > 10$ GeV and $p_T[-1\mathrm{ir}] > 9$ GeV are plotted. The cosmic ray

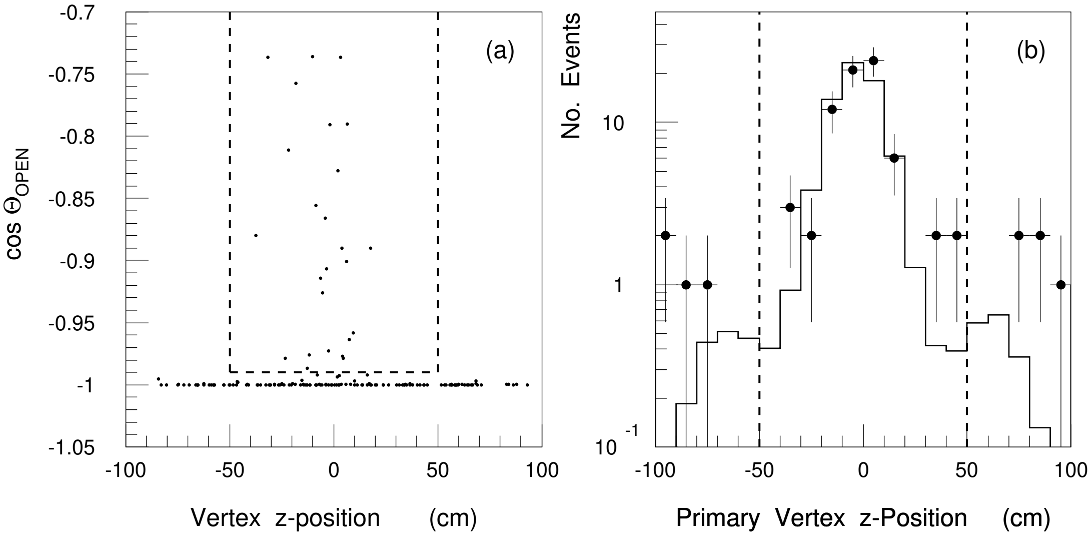

Figure 7.3: *(a) The vertex z-position and cosine of the opening angle for preselected events in the missing* p_T + μ *sample from 1994-96. The indicated box cut removes most of the cosmic ray muon background at opening angles close to* 180°. *The vertex position after the cut on the opening angle is shown in (b) for all the data (points), compared to the measured 1996 vertex distribution (solid histogram).*

background gives rise to the band of events at $\cos\theta_{\mathrm{OPEN}}$ close to -1 and distributed across all vertex z-positions. The box cut incorporates the cut on the cosine of the opening angle as well as the final cut on the z-coordinate of the reconstructed vertex. Fig. 7.3(b) shows the vertex distribution for all years after only the cut on the opening angle, showing reasonable agreement with the measured 1996 vertex distribution. The last few cosmic ray background events are removed by visual scanning at a later stage of the event selection. They may survive the above cut by having a poorly measured second track or by being measured in coincidence with a genuine ep event that gives rise to all the measured CTD tracks.

An example of an event with a high p_T muon and missing p_T is displayed in fig. 7.4. With a calorimeter p_T of approximately 36 GeV resulting from the scattered positron [4], this event also falls into the high E_T event sample described in the next section. A pair of muons are also clearly visible, with transverse momenta of around 31 GeV (BCAL) and 2.4 GeV (RCAL). No proton remnant activity is visible in the forward region of the detector, and the event is probably an example of elastic Bethe-Heitler di-muon production at very high Q^2 (see chapter 9).

---

[4] That is, the missing p_T measured in the calorimeter arises solely from the escaping muons. In chapter 9 events are searched for with missing p_T in the form of neutrino(s) in addition to a high p_T muon.

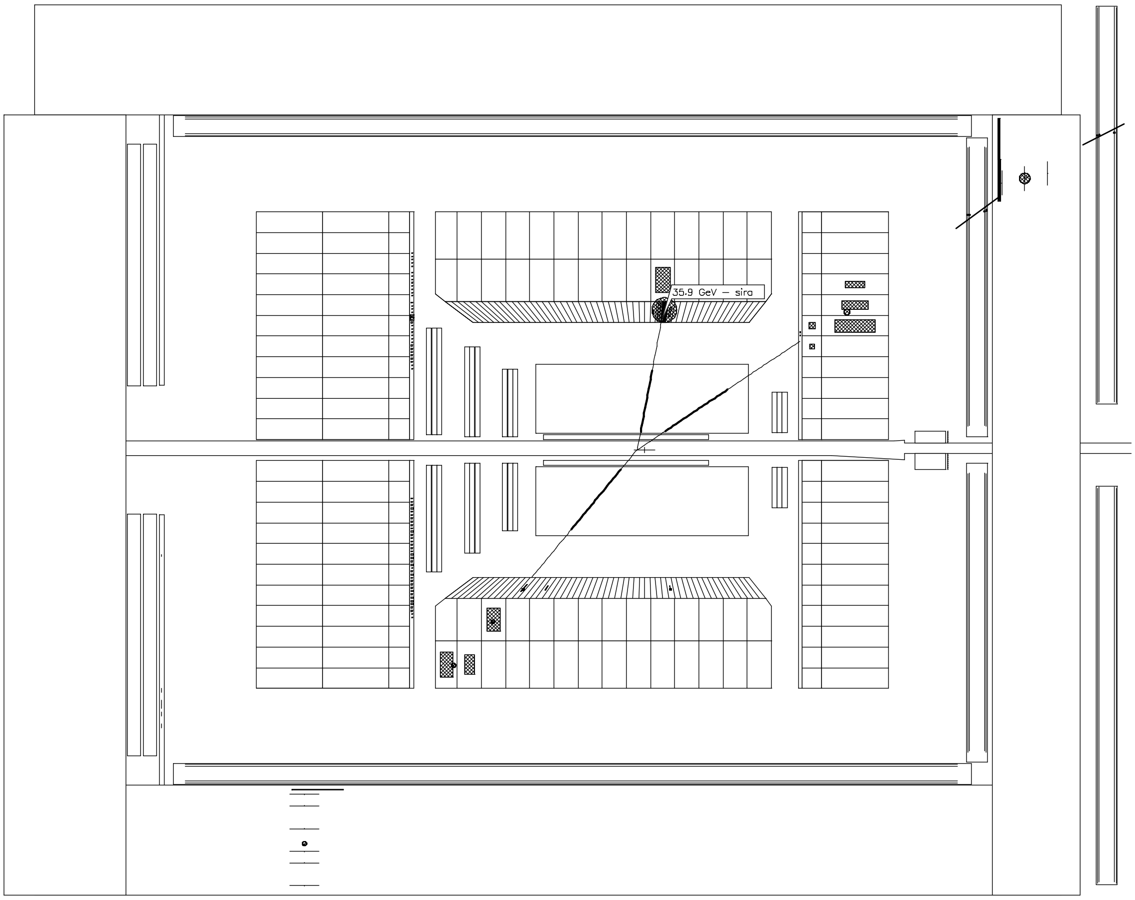

Figure 7.4: *An example of an event with calorimeter* $p_T \simeq 36$ GeV *and high* p_T *leptons. The beam positron is scattered at an angle of almost* 90° *and muons are clearly visible traversing the barrel and rear calorimeters. See text for more details.*

7.2 Events with High Transverse Energy

7.2.1 Trigger Requirements

First Level Trigger

As for events with missing p_T, several GFLT trigger slots exist to tag events with high transverse energies. An event is accepted if one or more of the following GFLT bits is set :

- Calorimeter E_T. Events with a first level trigger E_T in excess of 15.1 GeV (30.1 GeV in 1996) are accepted. The E_T threshold is reduced to 11.6 GeV for all three years if CTD tracks consistent with originating from an event vertex are also present.

- Regional and global energy sums. These slots are identical to those used to trigger events with missing p_T.

Second Level Trigger

One of two second level trigger bits must be set for an event with high transverse energy to be considered in this analysis :

- Very high E_T. If $E_T[-2\text{ir}] > 35$ GeV then this trigger bit is set. The $[-2\text{ir}]$ indicates that the first two rings of calorimeter cells around the FCAL beam pipe are excluded from the E_T sum. In 1994 only the first ring was excluded.
- Medium E_T. $E_T[-2\text{ir}] > 25$ GeV ($E_T[-1\text{ir}] > 20$ GeV in 1994) is required, but in addition $E - p_Z$ must be greater than 15 GeV. The second requirement suppresses the beam-gas background peaked at low values of $E - p_Z$.

Third Level Trigger

The main extra requirement at the third level trigger is that an event with high transverse momentum must have a well reconstructed tracking vertex.

7.2.2 High E_T Event Sample

In addition to the trigger bit requirements, events in the high E_T sample must have at least one good track, with the same definition used above for the missing p_T event sample. More importantly, cuts are made on the offline reconstructed transverse energy that are tighter than the trigger level cuts for any given year :

- $E_T[-2\text{ir}] > 40$ GeV , or
- $E_T[-2\text{ir}] > 30$ GeV and $E - p_Z > 18$ GeV .

This ensures a high conditional trigger efficiency (that is, fraction of events satisfying the offline E_T requirements that in addition pass all three trigger levels) and thereby reduces uncertainties resulting from the simulation of the trigger efficiency. Fig. 7.5 shows the vertex distribution for the 1996 high E_T preselected data in which at least one electron candidate, with cuts as described in section 7.1.2, has been identified. There is good agreement with the measured vertex distribution and very little background from non-*ep* interactions in this sample. The shaded histogram is the component of the data in which at least 2 electron candidates have been identified, forming the subset of the high E_T sample used in the search for high mass multi-electron events in chapter 8.

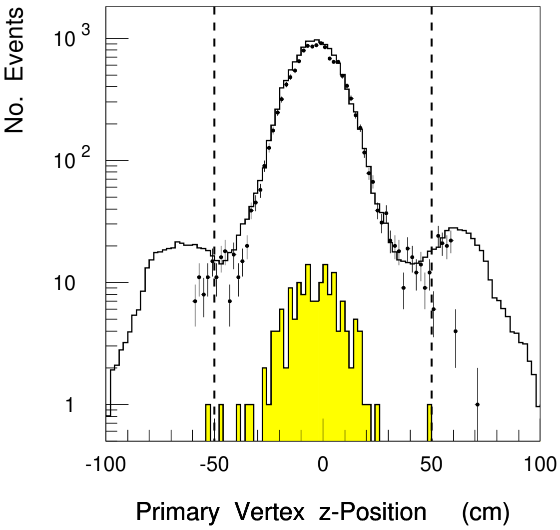

Figure 7.5: *The z-position of the primary vertex for the preselected 1996 data in the high E_T plus electron sample (points) plotted against the measured 1996 vertex distribution (solid histogram). The shaded histogram is the component of the data in which more than one electron candidate is identified. The final allowed range for the vertex position is indicated by the dashed lines.*

7.3 Muon Triggered Events

This section deals in particular with events triggered on the basis of muons reconstructed in the barrel and rear muon detectors. The combined barrel and rear muon sample is sometimes referred to simply as the barrel muon sample, with the main interest here in events with relatively forward going muons.

7.3.1 Trigger Requirements

First Level Trigger

Crude hit information from the barrel and rear muon detectors is available at the first level trigger. Events with hits in the barrel and rear muon chambers consistent with the passage of a muon pass the first level trigger, provided certain track and calorimeter requirements are also met. Standard vetoes reject non-*ep* backgrounds such as beam gas events and proton beam related (so-called 'halo') muons.

Second Level Trigger

At the SLT, barrel calorimeter timing cuts are imposed to reduce the rate of cosmic rays in the barrel and rear muon trigger slots. A requirement that $p_Z/E < 0.96$ removes events, such as beam gas background events, with a large fraction of their energy in the very forward direction in addition to barrel or rear muon chamber hits.

Third Level Trigger

At the third level trigger the barrel and rear muon detectors are fully reconstructed. Events are selected on the basis of matches found between muon detector tracks, CTD tracks and calorimeter MIP signals in a similar way to the offline identification of muons described in chapter 6.

7.3.2 Barrel Muon Sample

As well as a match between a CTD track and a calorimeter MIP, events in the barrel muon sample must have a matching barrel muon chamber segment in addition. The matching procedure is described in detail in chapter 6. A loose cut on the distance of closest approach of the MIP matching track and the muon chamber segment of 150 cm is applied. Fig. 7.6(a) shows the distribution of the vertex z-position and $\cos\theta_{\mathrm{OPEN}}$ for events in this sample in which a single muon is identified (dots) and events in which more than one muon is identified (open squares), where any second muon need only consist of a standard CTD-MIP match. The vertex distribution for the events after the requirement that $\cos\theta_{\mathrm{OPEN}} > -0.99$ is shown in fig. 7.6(b).

It should be noted that the cut on the opening angle is quite safe for selecting the highest mass multi-muon events at HERA. Fig. 7.6(c) shows the true opening angle distribution for $Z^0 \to \mu^+\mu^-$ Monte Carlo events for which both muons are in the central detector ($10^\circ < \theta_{\mu^+}, \theta_{\mu^-} < 170^\circ$). Longitudinal momentum conservation ensures that both muons from the decay of heavy objects are likely to be travelling forward in the laboratory frame with an opening angle considerably less than 180°, and the presence of the $\cos\theta_{\mathrm{OPEN}}$ cut has a negligible impact on the final efficiency for selecting $Z^0 \to \mu^+\mu^-$ events.

An example of an event in the barrel muon sample is shown in fig. 7.7. The match between a CTD track, calorimeter MIP and barrel muon chamber segment at around 70° is clearly visible. The event also contains a muon reconstructed in the forward muon system that matches a low angle CTD track fitted to the event vertex. The momentum of the low angle track is undetermined by the fit to hits in the CTD alone. However, the p_T is measured by the forward muon toroid to be around 6 GeV, similar to the p_T of the larger angle muon.

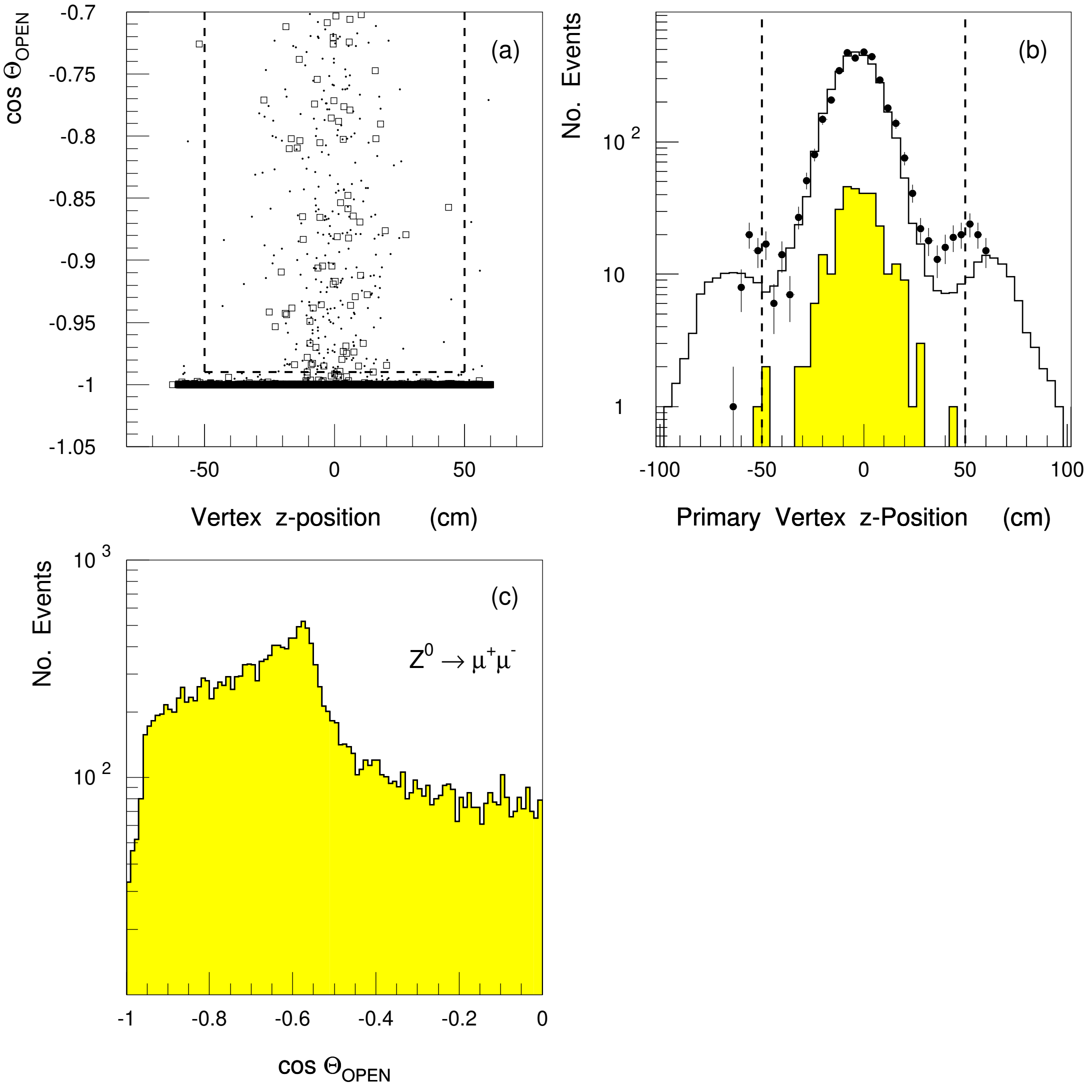

Figure 7.6: *(a) The vertex z-position versus the cosine of the opening angle for single muon events (dots) and multi-muon events (open squares) in the 1996 barrel and rear muon sample. The vertex distribution for the events (points) after the cut on* $\cos\theta_{\mathrm{OPEN}}$ *is compared to the measured vertex distribution (solid histogram) in (b), with the multi-muon component of the data given by the shaded histogram. The true opening angle for the* $\mu^+\mu^-$ *pair in* $Z^0 \to \mu^+\mu^-$ *events in which both muons are in the central detector is shown in (c).*

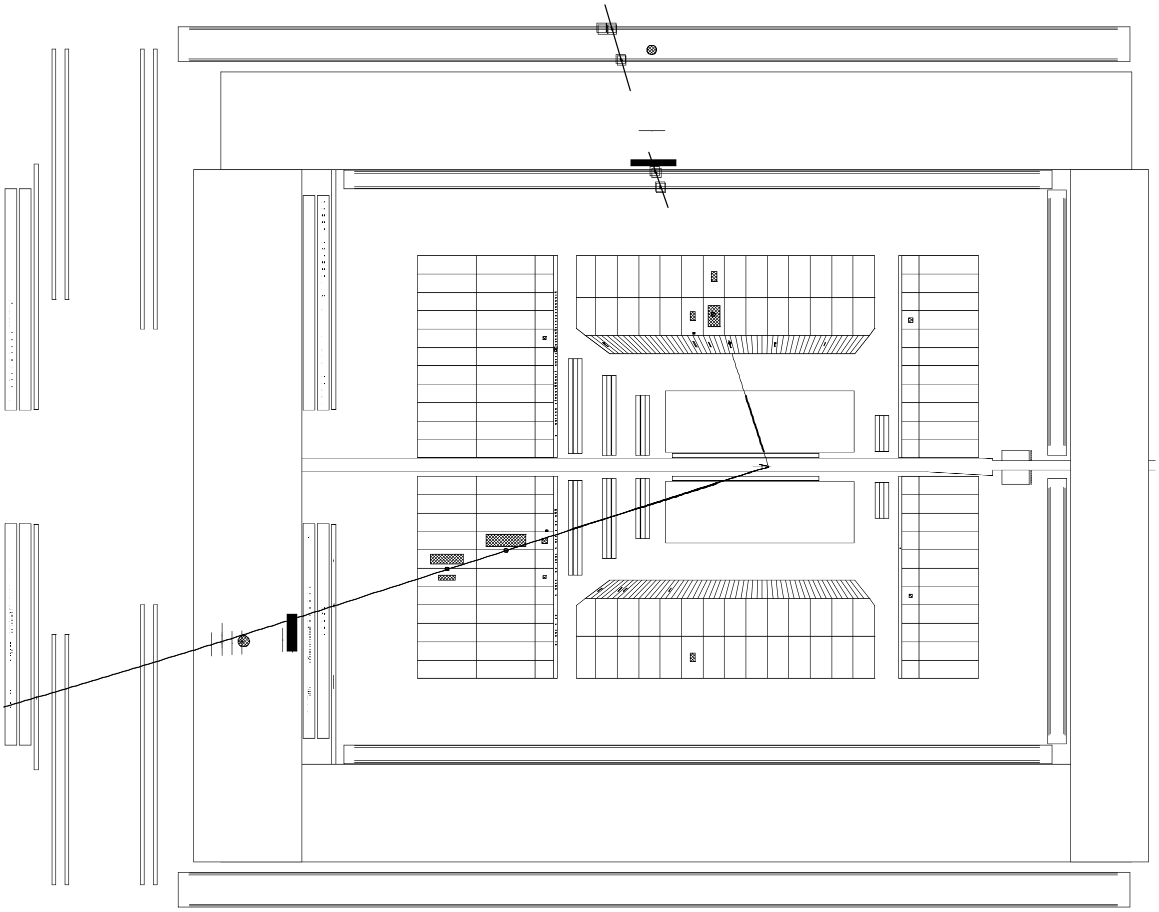

Figure 7.7: *An example of an event in the barrel muon event sample. The barrel muon chamber segment is represented by the short lines on either side of the iron return yoke. In addition the event contains a muon reconstructed in the forward muon system that matches a low angle CTD track, indicated by the continuous solid line.*

Chapter 8

High p_T Electrons

The main analysis presented in this chapter is of events with high p_T electrons in addition to missing p_T. The final event selection is optimised primarily for selecting $W \to e\nu$ events. A separate search for radiated photons in charged current events with large missing p_T is presented in section 8.2. Finally, a subsequent section looks at multi-electron events in the high E_T event sample, with cuts optimised for the search for $Z^0 \to e^+e^-$ events.

8.1 Electrons in Events with Missing p_T

Many different physics processes in *ep* collisions can give rise to the the signature of a high p_T electron in addition to missing p_T. For example fake electrons can be reconstructed in charged current and photoproduction events and missing p_T can arise, in the case of photoproduction and neutral current scattering, from the mismeasurement of energy or the leakage of energy from jets in the form of muons and neutrinos.

The various Monte Carlo samples used to estimate these contributions are listed in table 8.1. More details of the generators themselves may be found in chapters 4 and 5.

- W production. Only $e^+p \to e^+W^\pm X$ is considered. As well as $W \to e\nu$, the decay $W \to \tau\nu$ gives rise to events with high p_T electrons in the final state. The generator cuts and structure functions used are outlined in detail in chapter 4.

- Z production. Again, only the neutral current process $e^+p \to e^+Z^0X$ that dominates the real Z production cross section is considered. More details of the generator level cuts are given in section 4.2.

- Neutral Current DIS. Two samples with different lower Q^2 cuts, listed in table 8.1, have been used. Both were generated with the CTEQ4 set of parton density functions [84] and use ARIADNE to model the hadronic final state (see section 5.1.3).

Alternative samples for $Q^2 > 400$ GeV^2, generated with both matrix elements and parton showers (MEPS) and ARIADNE options, are used in the analysis of the 1997 data in chapter 11.

Since Q^2 is related to the hadronic p_T via the expression $Q^2 = (p_T^{had})^2/1 - y$, the lowest Q^2 cut of 100 GeV^2 ensures that all events with $p_T^{had} = p_T^{elec} > 10$ GeV are included. The most common source of large missing p_T in neutral current events is the mismeasurement of either the scattered electron or hadronic final state energies. Since in addition W decay leptons have an angular distribution strongly peaked in the forward direction, the dominant background from neutral current DIS should be concentrated at high Q^2. This issue is addressed further in section 8.1.3.

- Charged Current DIS. A sample of charged current events generated with $Q^2 > 10$ GeV^2 and $W > 3$ GeV is used, where the latter cut is on the invariant mass of the hadronic final state. MRS(A) parton density functions are employed [65] and MEPS used in the simulation of the hadronic final state.

- Photoproduction. Both direct and resolved events generated with $Q^2 < 4$ GeV^2 have been used. MRS(A) and GRV-G(L-HO) [55] parton distributions were used for the proton and photon respectively. As described in section 5.3 the events were generated with a cut of $E_T > 28$ GeV. Although such events are likely to dominate the photoproduction background in the missing p_T samples, events with lower transverse momenta can in principle contribute. An excess of data over the Monte Carlo at low missing p_T's would result. It should be noted, however, that when an isolated high p_T lepton is required in addition to missing p_T, the backgrounds from photoproduction processes are found in general to be very small.

- Bethe-Heitler di-lepton production. Although the dominant background is from e^+e^- production, the small contributions from $\tau^+\tau^-$ production and $\gamma\gamma \to \mu^+\mu^-$ are also estimated using suitable Monte Carlo samples. Note that the cuts listed in table 8.1 are required of a single lepton from the $\gamma\gamma$ sub-process only.

For most of the physics processes listed the cross sections are small and the effective luminosities of the Monte Carlo samples are thus large. Even for the high cross section photoproduction and neutral current samples the Monte Carlo luminosity is larger by at least a factor of 1.5 than that of the data. Unless otherwise stated the Monte Carlo samples are always normalised to the data luminosity.

Generator	Process	Important Cuts	Cross Section After Cuts	Effective Luminosity
EPVEC	$e^+p \to e^+W^\pm X$	$u_{cut} = 25$ GeV^2	0.95 pb	50 fb^{-1}
	$e^+p \to e^+Z^0X$	$u_{cut} = 25$ GeV^2 $\lvert t \rvert$ (DIS) > 4 GeV^2	0.33 pb	100 fb^{-1}
DJANGO	$e^+p \to e^+X$ (NC DIS, ARIADNE)	$Q^2 > 100$ GeV^2	7.5 nb	59 pb^{-1}
		$Q^2 > 800$ GeV^2	367 pb	292 pb^{-1}
	$e^+p \to \bar{\nu}X$ (CC DIS, MEPS)	$Q^2 > 10$ GeV^2	40 pb	1.0 fb^{-1}
HERWIG	γp (Direct)	$E_T > 28$ GeV	2.0 nb	111 pb^{-1}
	γp (Resolved)		7.0 nb	34 pb^{-1}
LPAIR	$\gamma\gamma \to e^+e^-$ (Elastic)	$10^\circ < \theta < 170^\circ$ $E_e > 5$ GeV	172 pb	291 pb^{-1}
	$\gamma\gamma \to e^+e^-$ (Inelastic)		291 pb	171 pb^{-1}
	$\gamma\gamma \to e^+e^-$ (Elastic)	$5^\circ < \theta < 175^\circ$ $p_T^e > 20$ GeV	96 fb	104 fb^{-1}
	$\gamma\gamma \to e^+e^-$ (Inelastic)		320 fb	31 fb^{-1}
	$\gamma\gamma \to \mu^+\mu^-$ (Elastic)	$5^\circ < \theta < 175^\circ$ $p_T^\mu > 2$ GeV	108 pb	141 pb^{-1}
	$\gamma\gamma \to \mu^+\mu^-$ (Inelastic)		185 pb	108 pb^{-1}
	$\gamma\gamma \to \tau^+\tau^-$ (Elastic)	none	106 pb	565 pb^{-1}
	$\gamma\gamma \to \tau^+\tau^-$ (Inelastic)		71 pb	840 pb^{-1}

Table 8.1: *The Monte Carlo samples used in the analysis of events with a high p_T electron and missing p_T. More details of the event generators can be found in chapters 4 and 5.*

The starting point for this analysis is the preselected data sample described in chapter 7. With an integrated luminosity of 20.1 pb^{-1} for 1994-96 and applying the same trigger requirements and selection cuts, the combined Monte Carlo expectation of 245 events is significantly below the 292 events observed in the data. The data and combined Monte Carlo samples are compared in fig. 8.2, with the contribution from W production given by the shaded histogram. The background is dominated by neutral current DIS at this stage of the selection, indicated by the steeply falling missing p_T spectrum and the concentration

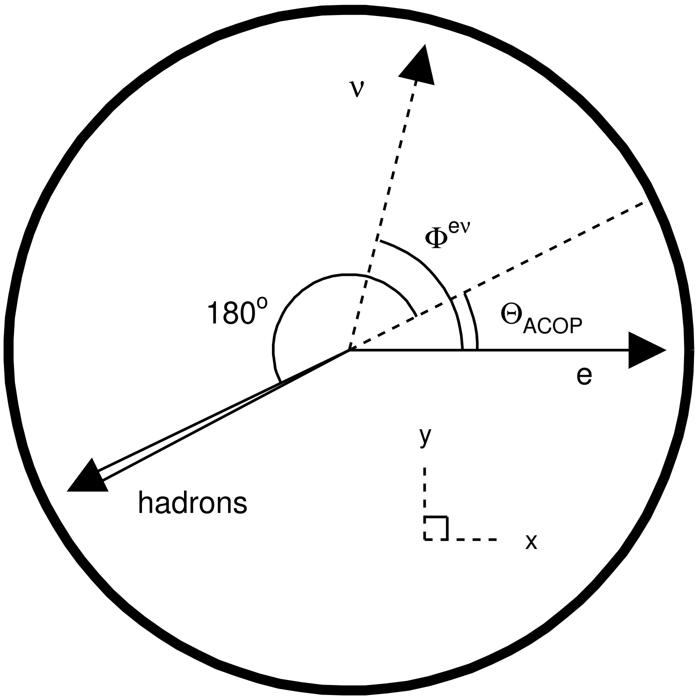

Figure 8.1: *The definition of the acoplanarity angle,* Θ_{ACOP} *and the azimuthal separation of the neutrino and electron,* $\Phi^{e\nu}$*, for an event. See text for more details.*

of events with high values of $E - p_Z$ [1]. Charged current DIS and di-electron production also contribute. An important quantity in separating the signal from the neutral current background, plotted in fig. 8.2(e), is the *acoplanarity angle* for an event. Defined in fig. 8.1 it is, in effect, a measure of the deviation of an event from the usual back-to-back configuration and is therefore strongly peaked at small values for neutral current events. A meaningful calculation of the acoplanarity angle, however, requires the direction of the hadronic system to be well reconstructed and this quantity is therefore only determined for events with a total hadronic p_T in excess of 4 GeV. For W production the direction of the decay electron is essentially uncorrelated with the recoiling hadronic system and the acoplanarity distribution is almost flat. A small excess at low acoplanarities is due to the transverse boost that the W can receive from the recoiling hadrons and scattered beam positron, producing a small bias towards the neutral current back-to-back configuration.

A closely related quantity is the transverse mass for an event, defined as [85] :

$$M_T = \sqrt{2\, p_T^e\, p_T^\nu\, (1 - \cos\Phi^{e\nu})} \ , \tag{8.1}$$

---

[1] See chapter 3. A fully contained event has $E - p_Z \simeq 55$ GeV.

where the neutrino direction and transverse momentum correspond to the direction and magnitude of the measured missing p_T. For $W \to e\nu$ events the Jacobean peak structure visible in fig. 8.2(a) is heavily smeared by the transverse momentum of the produced W and resolution effects, giving rise in addition to the broad transverse mass distribution visible in fig. 8.2(f).

The excess of the data over the Monte Carlo is concentrated at low acoplanarity angles, which is dominated by neutral current scattering. This is consistent with the excess at large electron polar angles and high $E-p_Z$ values. At higher acoplanarity angles the Monte Carlo prediction is similar to or above the data (see section 10.1). One reason for the overall excess could be a discrepancy between the data and Monte Carlo missing p_T distributions. This can arise if, for example, certain detector inactive material distributions and inefficiencies giving rise to misreconstructed p_T's are not adequately described by the Monte Carlo detector simulation. This issue is addressed in a following sub-section describing the analysis of the neutral current control sample.

8.1.1 Selecting $W \to e\nu$ Events

A cut on the electron p_T of 10 GeV, as indicated in fig. 8.2(a), efficiently selects electrons from W decay and reduces the background from sources of low energy electrons such as Bethe-Heitler di-lepton production. The most important cut in reducing the neutral current background is, however, on the acoplanarity angle. It can be seen from fig. 8.2(e) that requiring $\Theta_{\mathrm{ACOP}} > 0.2$ rad (for events with hadronic p_T greater than 4 GeV) removes the bulk of neutral current events but only a small fraction of $W \to e\nu$ events.

In order to further reduce the neutral current background the cut on the missing p_T is increased and use is made of the separation of the signal and background in the $E - p_Z$ distribution. In fact these cuts are optimised by making a 2-dimensional cut in the $\{\text{missing } p_T, E - p_Z\}$ plane, as illustrated in figure 8.3. The minimum requirements are missing $p_T > 15$ GeV and $E - p_Z < 55$ GeV.

After the above cuts the data is reduced to 12 events against an expectation of around 14 from the combined Monte Carlo samples. The remaining events are plotted in figure 8.4. It can be seen that the signal is still concentrated at small polar angles and large missing p_T's with respect to the remaining background. These cuts are therefore tightened with respect to their preselection values to the following :

1. $\theta^e < 1.5$ rad ,

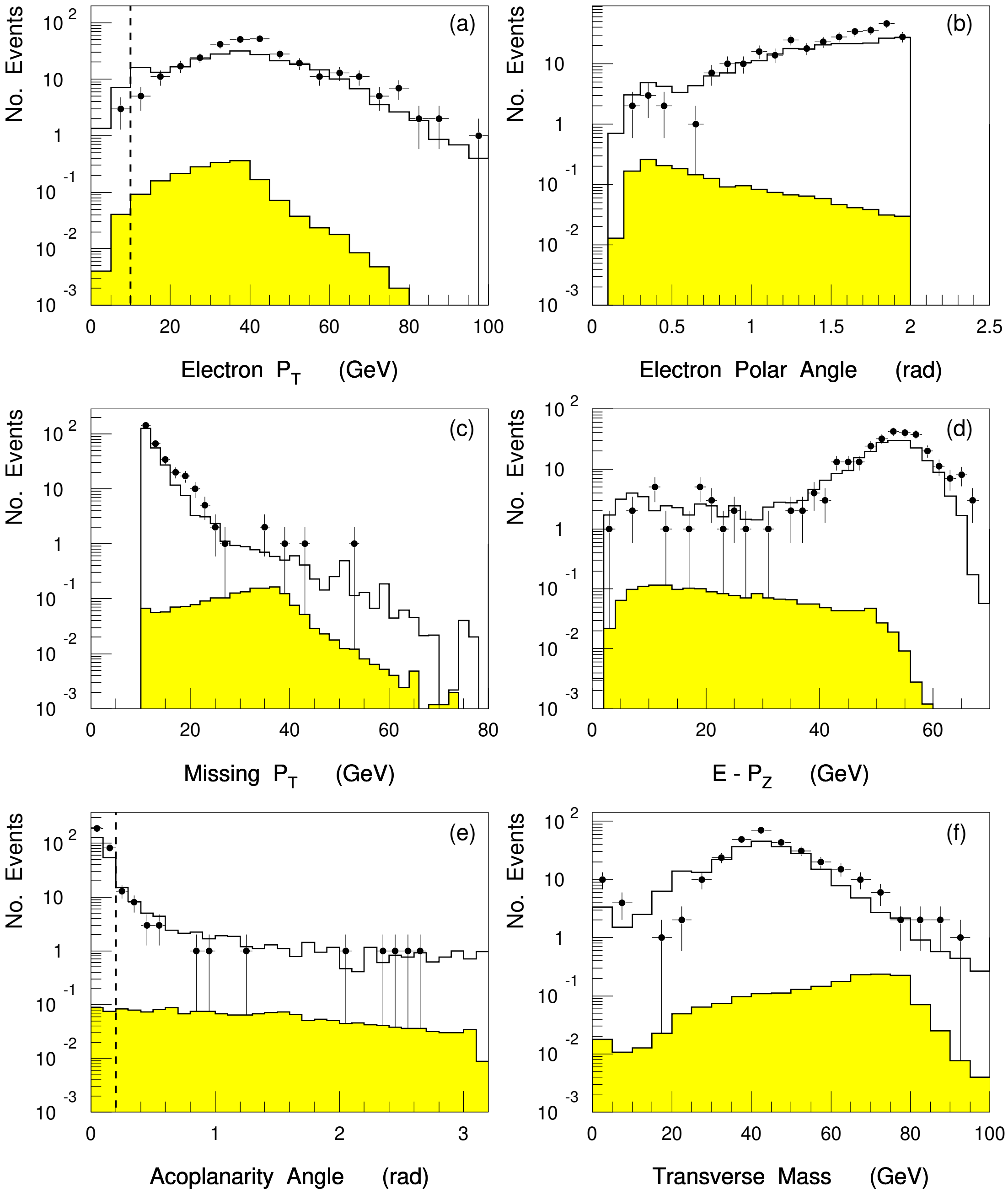

Figure 8.2: *A comparison of the preselected missing p_T plus electron data from 1994 to 1996 (points) with the combined Monte Carlo sample (solid histogram). The contribution from W production and decay is given by the shaded histogram.*

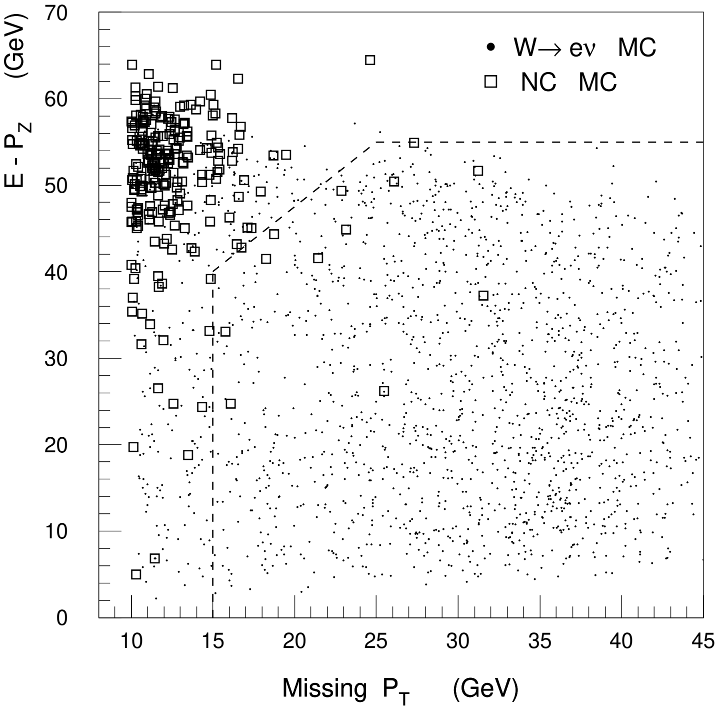

Figure 8.3: *The cut made in the $\{$missing $p_T, E - p_Z\}$ plane in order to separate the signal from the neutral current background. The points and open squares depict preselected $W \rightarrow e\nu$ and neutral current (NC) Monte Carlo events respectively. The relative normalisation of the two Monte Carlo samples is arbitrary.*

2. Missing $p_T > 20$ GeV.

At this stage in the event selection the background from charged current DIS, at first small compared to that from neutral current scattering, is the most significant. As discussed in previous sections this background arises mainly from the presence of fake electrons close to hadronic activity in charged current events. Three further cuts, illustrated in fig. 8.4(e)-(g), are introduced primarily to reduce the remaining charged current background. The first cut is on a track isolation variable, defined to be the distance of closest approach of the second closest matching track to the electron candidate. From fig. 8.4(e), where electrons with no second matching track enter by default the last bin of the histogram, it can be seen that the charged current component of the background, indicated by the wide hatched histogram, is concentrated at low values for the track isolation. A cut at 30 cm removes a large component of the charged current background. The second cut utilises the fact that fake electrons can pass the track matching cuts due to the presence of low momentum charged hadrons in the vicinity of the electromagnetic cluster. A demand is therefore made

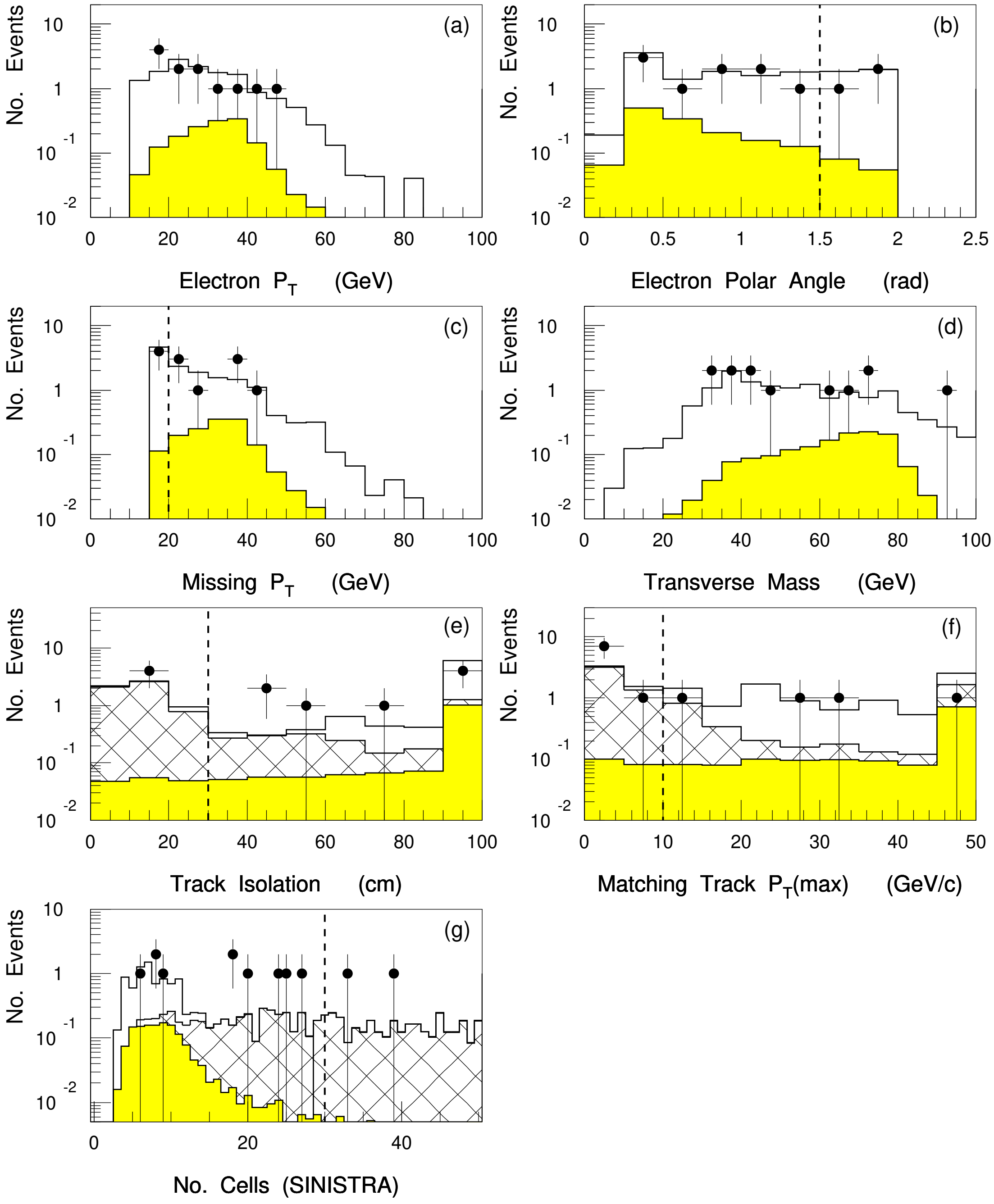

Figure 8.4: *A comparison of the missing p_T plus electron data from 1994 to 1996 (points) with the combined luminosity weighted Monte Carlo sample (solid histogram) after the cuts described in the text. The contribution from W production is given by the shaded histogram and from charged current DIS by the wide hatched histogram.*

that the closest matching track is consistent with having a transverse momentum in excess of 10 GeV. That is

$$p_{T,trk}^{max} = \frac{1}{(1/p_{T,trk}) - \sigma(1/p_{T,trk})} > 10 \text{ GeV} \quad , \tag{8.2}$$

where $\sigma(1/p_{T,trk})$ is directly related to the error on the radius of curvature of the track measured in the CTD. Finally, fake electrons in charged current events are on average 'larger' than electromagnetic showers from electrons and photons. The number of calorimeter cells included in the cluster is plotted in fig. 8.4(g), from which it can be seen that a cut requiring this number to be ≤ 30 removes a negligible fraction of signal events. These three cuts combined remove over 90% of the remaining charged current background, although with some cost in efficiency for selecting $W \to e\nu$ events.

The effect of all the cuts described on the expected signal and background is summarised in table 8.2. It can be seen from the second to last column that the expected signal to background ratio is still somewhat less than 1. The final stage in the event selection therefore consists of a tightening of certain previous cuts :

- Distance of Closest Approach ($\theta > 0.4$ rad) : 10 cm → 8 cm ,
- Distance of Closest Approach ($\theta < 0.4$ rad) : 15 cm → 10 cm ,
- Isolation Energy ($R_{\eta\phi} = 0.6$) : 4 GeV → 2 GeV .

The effect is to significantly reduce the remaining charged current background to the W production signal. Finally, the neutral current background is more than halved by raising the cut on the acoplanarity angle to 0.3 rad (for events with hadronic p_T greater than 4 GeV) and demanding $E - p_Z < 50$ GeV in addition to the previous requirements. The results of the final cuts are presented in the last column of table 8.2. The subsequent value for the signal to background in excess of 1 ensures that in principle an observation of W production and decay to electrons can be made (see chapter 10).

It is interesting to note the potential background to W production from real Z production, which persists even after hard cuts have been applied. These events are genuine lepton plus missing p_T events originating mainly from $Z^0 \to \nu\bar{\nu}$ decays in which the beam positron is scattered at small polar angles, with contributions also from $\tau^+\tau^-$, $\mu^+\mu^-$ and heavy quark decays of the Z. In principle an anomalous rate of Z production at HERA might show up at high luminosities as an excess in the background to W production, providing a useful cross check to the direct $Z^0 \to l^+l^-$ searches. This, like many other backgrounds

	Cut						
Background Process	$p_T^e >$ 10 GeV	$\Theta_{\mathrm{ACOP}} >$ 0.2 rad	{missing p_T, $E - p_Z$}	$\theta^e <$ 1.5 rad	missing $p_T >$ 20 GeV	CC Rejection	Final Cuts
$e^+p \rightarrow e^+X$ (NC DIS)	214	36.8	4.36	1.95	0.86	0.86	0.40
$e^+p \rightarrow \bar{\nu}X$ (CC DIS)	6.95	6.93	6.63	5.96	5.28	0.30	0.20
γp (Direct)	0.73	0.36	< 0.2	< 0.2	< 0.2	< 0.2	< 0.2
γp (Resolved)	0.59	< 0.7	< 0.7	< 0.7	< 0.7	< 0.7	< 0.7
$\gamma\gamma \rightarrow e^+e^-$ (Elastic)	< 0.08	< 0.08	< 0.08	< 0.08	< 0.08	< 0.08	< 0.08
$\gamma\gamma \rightarrow e^+e^-$ (Inelastic)	11.0	9.52	1.24	0.98	0.02	0.02	0.02
$\gamma\gamma \rightarrow \mu^+\mu^-$ (Elastic)	< 0.2	< 0.2	< 0.2	< 0.2	< 0.2	< 0.2	< 0.2
$\gamma\gamma \rightarrow \mu^+\mu^-$ (Inelastic)	0.74	0.37	0.19	< 0.2	< 0.2	< 0.2	< 0.2
$\gamma\gamma \rightarrow \tau^+\tau^-$ (Elastic)	0.18	0.18	0.07	< 0.04	< 0.04	< 0.04	< 0.04
$\gamma\gamma \rightarrow \tau^+\tau^-$ (Inelastic)	0.60	0.38	0.14	0.07	0.02	0.02	0.02
$e^+p \rightarrow e^+Z^0X$	0.22	0.18	0.12	0.10	0.08	0.06	0.06
Signal Process							
$W \rightarrow e\nu$ (Efficiency)	1.34 (65%)	1.26 (61%)	1.21 (58%)	1.12 (54%)	1.07 (52%)	0.92 (45%)	0.86 (41%)
$W \rightarrow \tau\nu$	0.29	0.27	0.23	0.21	0.16	0.08	0.07
Other Channels	0.13	0.09	0.06	0.04	0.04	0.02	0.02
Total	237	56.4	14.2	10.4	7.53	2.29	1.65
Data							
94-96	289	37	12	9	5	1	1

Table 8.2: *The expected number of background and signal events at each stage in the selection of events with missing p_T in addition to a high p_T electron. The efficiency with which $W \rightarrow e\nu$ events are selected and the number of surviving data events are recorded at the bottom of the table. See text for more details of the cuts applied.*

Production Channel	W^+ DIS	W^- DIS	W^+ PHP	W^- PHP	Combined
Efficiency	45 ± 1 %	37 ± 1 %	50 ± 1 %	45 ± 1 %	43 ± 1 %

Table 8.3: *The efficiency for selecting $W \to e\nu$ events in the different W production channels, calculated using the 1995 Monte Carlo detector configuration. The combined value assumes the mixture of deep inelastic and photoproduction type W production given in chapter 4. Statistical errors only are given.*

in this analysis, should be largely absent from the $W \to \mu\nu$ channel, again indicating the usefulness of comparing at least two decay channels in the search for W production at HERA.

The expected number of W production events in the final sample is around 1 event, composed almost entirely of $W \to e\nu$ and $W \to \tau \to e$ decays. The few percent of the signal associated with other W decay channels consists overwhelmingly of $W \to \mu\nu$ decays in which the beam positron is scattered at high Q^2, mimicking an electron from the decay of the W boson itself. The overall efficiency is broken down by production channel in table 8.3. Deep inelastic W production is associated with larger hadronic p_T's, increasing the chance that the W decay lepton is not well isolated in the detector, while the difference between W^+ and W^- efficiencies is accounted for by the different angular distributions for positively and negatively charged leptons from W decay. These features of W production have been discussed in more detail in chapter 4. Note that efficiencies for selecting $W \to e\nu$ events calculated using the 1996 Monte Carlo (that is, Monte Carlo that simulates the 1996 detector configuration and running conditions) are systematically $2-3\%$ smaller in absolute terms than the same efficiencies calculated using 1995 Monte Carlo. This is mainly due to differences in the vertex distribution in 1995 and 1996 and in particular the larger satellite contribution [2] in 1996. The efficiencies listed in table 8.2 and in chapter 10 represent luminosity weighted averages of the 1995 and 1996 Monte Carlo calculated efficiencies [3].

8.1.2 The Final Event Sample

The single remaining event from 1994-1996 is displayed in fig. 8.5. The electromagnetic cluster at a polar angle of 37° has a transverse momentum of 21 GeV and, from the well measured matching track, is determined to be a positron. There is little activity in the detector apart from the positron and proton remnant activity in the forward beam pipe

---

[2] See section 7.1.2.

[3] The 1995 Monte Carlo is used for the 1994 contribution to the total integrated luminosity.

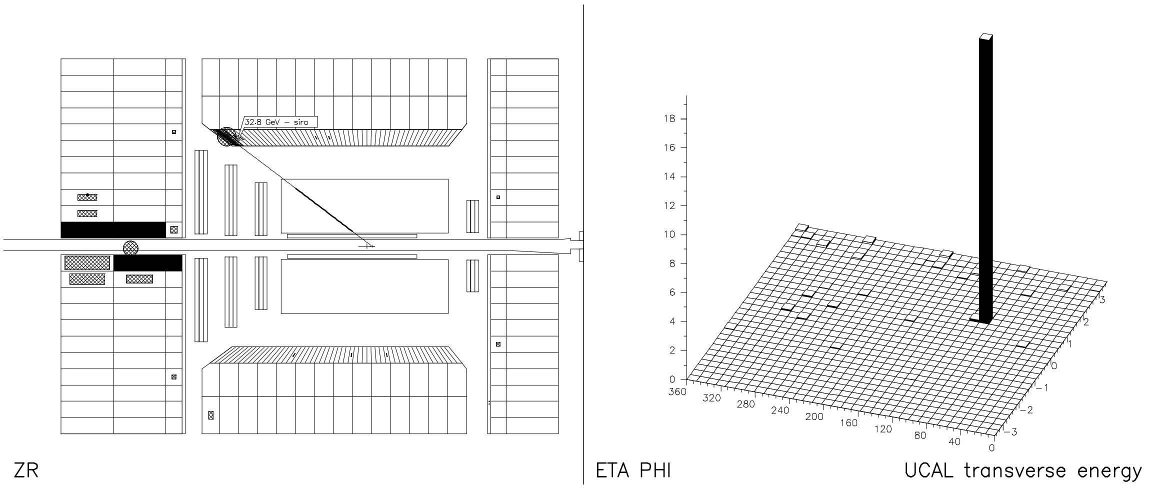

Figure 8.5: *The surviving event in the search for W production and decay $W \to e\nu$ in the 1994-1996 data. The scattered positron is clearly visible in the upper half of ZR view of the detector. The right hand plot shows the transverse energy in bins of pseudo-rapidity (η) and azimuthal angle (ϕ). Only the electromagnetic cluster, denoted by the vertical column, carries any significant transverse momentum in this event. See text for more details.*

region, which is typical of low hadronic p_T W production. Correcting the energies of the positron and hadrons on the basis of the amount of inactive material between the primary vertex and face of the calorimeter, a procedure described in more detail in section 10.2, gives a corrected positron p_T and transverse mass for the event of 22 and 44 GeV respectively. This makes the event kinematically unlikely to be a $W \to e\nu$ event. In addition, the fact that proton remnant activity around the beam pipe is visible makes an event of this topology unlikely to originate from the $Z^0 \to \nu\bar{\nu}$ background to the W production signal. More properties of the event and comparisons with Monte Carlo may be found in section 10.2.

8.1.3 Neutral Current Control Sample

Table 8.2 indicates reasonable agreement between the number of events expected from Monte Carlo and found in the data. Nevertheless it is important to check whether the Monte Carlo is providing an accurate estimate of the efficiency with which $W \to e\nu$ events can be selected, since this number in particular will determine the limit that may be placed on any anomalous W production. A suitable class of event is neutral current DIS events at high E_T. Such events are a source of high p_T electrons at relatively small polar angles and can be selected using largely independent trigger slots from the missing p_T sample.

In addition to the preselection cuts outlined in chapter 7 for events with high transverse energy, neutral current events are selected by requiring :

1. $E_T[-2\mathrm{ir}] > 30$ GeV,
2. $20 < E - p_Z < 65$ GeV,
3. $\theta^e < 2.5$ rad,
4. $p_T^e > 10$ GeV,

where the first two cuts are above the on-line trigger cuts and designed to ensure a high trigger efficiency for the control sample. Almost 9000 events are selected from the 1996 data, within 2% of the Monte Carlo expectation. The purity of the sample is in excess of 98%, with only a few events at small polar angles and low electron p_T's due to photoproduction and other background processes. From fig. 8.6(a)-(e) it can be seen that the various data and Monte Carlo distributions are in good overall agreement. The broader peak in the $E - p_Z$ distribution for the data might indicate a poorer energy resolution than for the Monte Carlo events and the discrepancy in the region of large acoplanarity angles is discussed with larger statistics samples in chapter 10. One important respect in which the data and Monte Carlo differ, however, is in the detailed shape of the missing p_T spectrum. The fraction (DATA/MC) is plotted as a function of missing p_T in fig. 8.6(f), for which the Monte Carlo has been normalised to the number of data events. There is clearly some shift in the data towards higher values for the missing p_T, which could explain the excess of the data over the Monte Carlo after the missing p_T plus electron preselection. This discrepancy must also be considered in the evaluation of the error on the estimate of the background to W production that enters the limit setting procedure.

The neutral current control sample confirms that fake SINISTRA electrons are larger on average than true scattered positrons, as shown in fig. 8.7. It can be seen that the background Monte Carlo, given by the shaded histogram, is concentrated at much larger cell multiplicities and that, despite possible discrepancies between the neutral current data and Monte Carlo for small electromagnetic clusters, a cut at 30 cells is quite safe.

In addition to providing information on one of the major backgrounds to W production, the neutral current control sample provides a large number of events that can be compared to Monte Carlo in order to evaluate systematic uncertainties affecting the estimate of the $W \to e\nu$ selection efficiency. These are considered next.

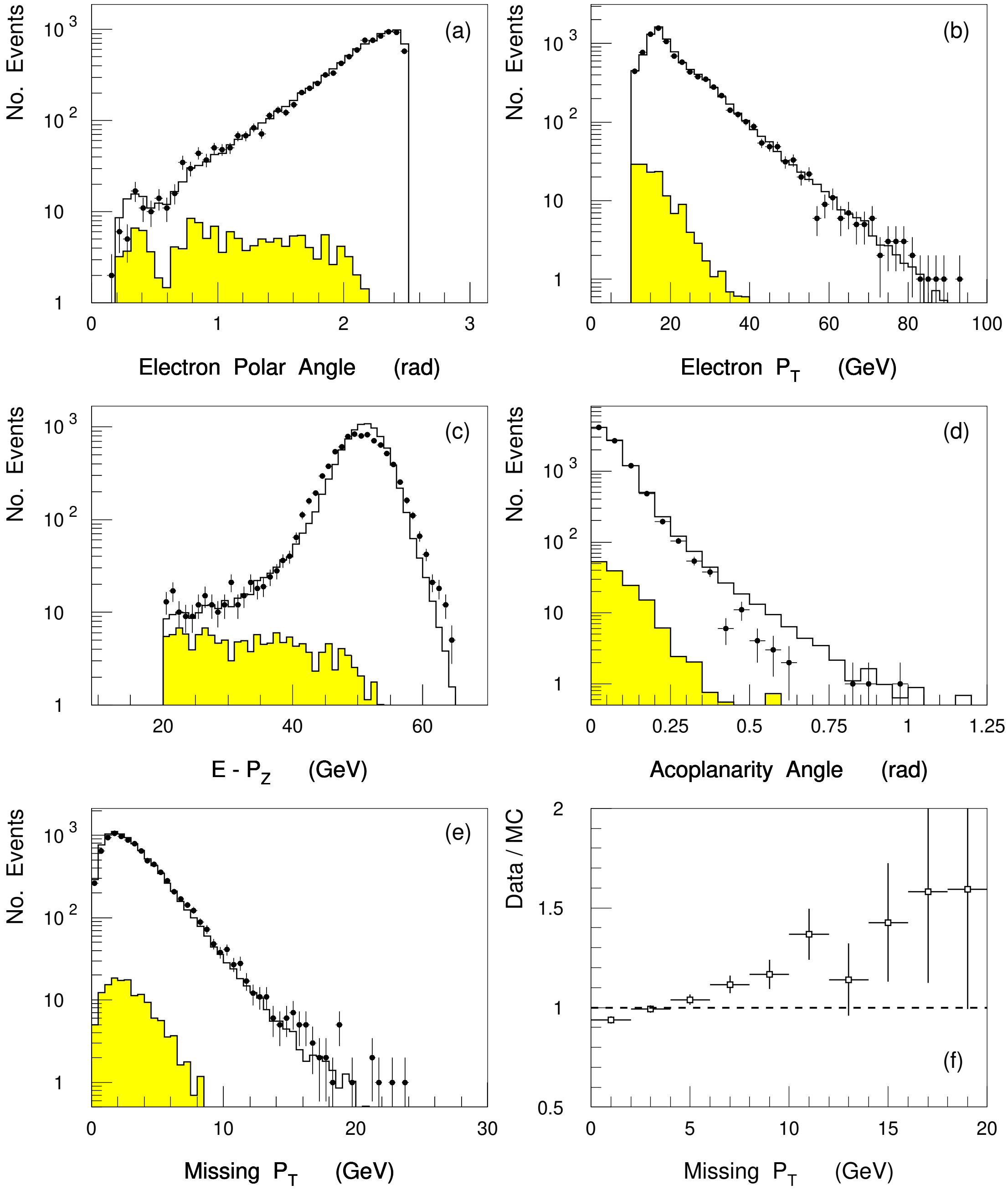

Figure 8.6: *A comparison of the data (points) and Monte Carlo expectation (open histogram) for the high E_T neutral current control sample. The shaded histogram shows the contribution to the sample from physics processes other than high Q^2 neutral current DIS. Plot (f) is described in the text.*

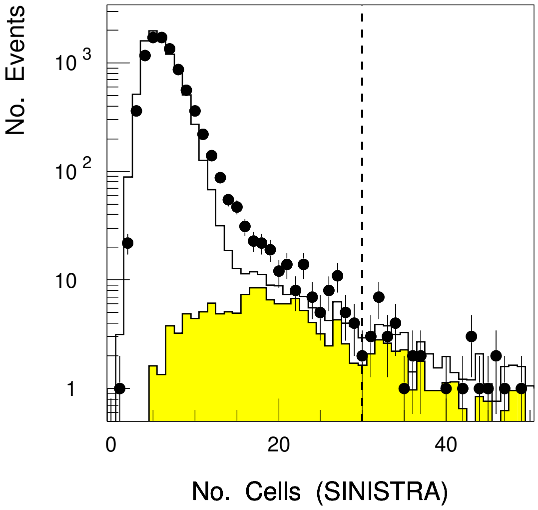

Figure 8.7: *A comparison of the number of calorimeter cells making up the electromagnetic cluster that forms the electron candidate in the data (points) and Monte Carlo (solid histogram) of the neutral current control sample. The background Monte Carlo contribution to the total is indicated by the shaded histogram and the cut of* ≤ 30 *cells is indicated by the dashed line.*

8.1.4 Systematic Uncertainties in the Selection Efficiency

The most important systematic uncertainty is that associated with the electron finding. The uncertainty in the electromagnetic cluster identification efficiency is considered first, followed by the uncertainties that arise from the track matching and isolation requirements that are made of a good electron candidate. Uncertainties in the description of the vertex and acoplanarity angle distributions also give rise to systematic error contributions. Finally, the trigger and knowledge of the absolute calorimeter energy scale are considered as further sources of systematic uncertainty.

Electron Finding Efficiency

As discussed in chapter 6, different electromagnetic cluster finding algorithms become fully efficient at different energies and can exhibit different behaviours at, for example, calorimeter boundaries. A naïve estimate of the uncertainty in the electron finding efficiency is therefore obtained simply by comparing the results of different electron finding algorithms. Requiring only that the event have a true electron p_T greater than 20 GeV, corresponding to the final cut in the analysis described above, it is found that 98% of W decay electrons are correctly identified by the neural network based electron finder against 94% by the conventional electron finder ELEC5. A systematic error of 4% is therefore attached to the electromagnetic cluster finding efficiency.

Track Matching and Energy Isolation

In order to evaluate the uncertainty arising from the cut on the distance of closest approach of the CTD track to the electromagnetic cluster, the high E_T selection is relaxed to accept all candidates with DCA < 25 cm. The resulting comparison between data and Monte Carlo is shown in fig. 8.8(a). Around 97% of Monte Carlo events pass the final DCA cut of 8 cm (10 cm for $\theta^e < 0.4$ rad) indicated on the plot, compared to 96% of data events. A systematic error of 1% is therefore attributed to this requirement.

A similar technique allows the investigation of the effect of the isolation energy requirement on the electron finding efficiency. The loosened requirement $E_{iso} < 10$ GeV gives the distributions plotted in fig. 8.8(b). The effect of the final $E_{iso} < 2$ GeV cut differs by less than 0.5% between data and Monte Carlo, however, and is a negligible contribution to the total systematic error.

Finally, figures 8.8(c) and (d) compare the matching track p_T and error for the neutral current control sample data and Monte Carlo. The transverse momentum distribution is very well described by the Monte Carlo, but the mean value for $\sigma(1/p_T)$ is around 40% higher in the data than the Monte Carlo. Correcting the Monte Carlo values by this factor before applying the $p_{T,trk}^{max}$ cut results in a 1% absolute change in the overall efficiency.

Calorimeter Scale Uncertainty

As mentioned in section 5.7 the data is rescaled with respect to the Monte Carlo by as much as 5% depending on the calorimeter section and running period. This figure is used as an indication of the uncertainty in the knowledge of the absolute calorimeter energy scale. In the analysis presented here this uncertainty enters primarily through the missing p_T, $E - p_Z$ and electron energy cuts. In order to estimate the effect of this uncertainty the whole analysis chain is repeated for Monte Carlo events that are rescaled by an additional $\pm 5\%$. The net effect is only a 1% absolute variation in the $W \to e\nu$ selection efficiency.

Acoplanarity Requirement

The acoplanarity distribution for the signal could in principle depend on features of the event simulation, in particular of the hadronic final state. Clearly QCD effects such as multi-jet hadronic final states might reduce the acoplanarity angle resolution with respect to the leading order Monte Carlo. In order to test the sensitivity of the selection efficiency

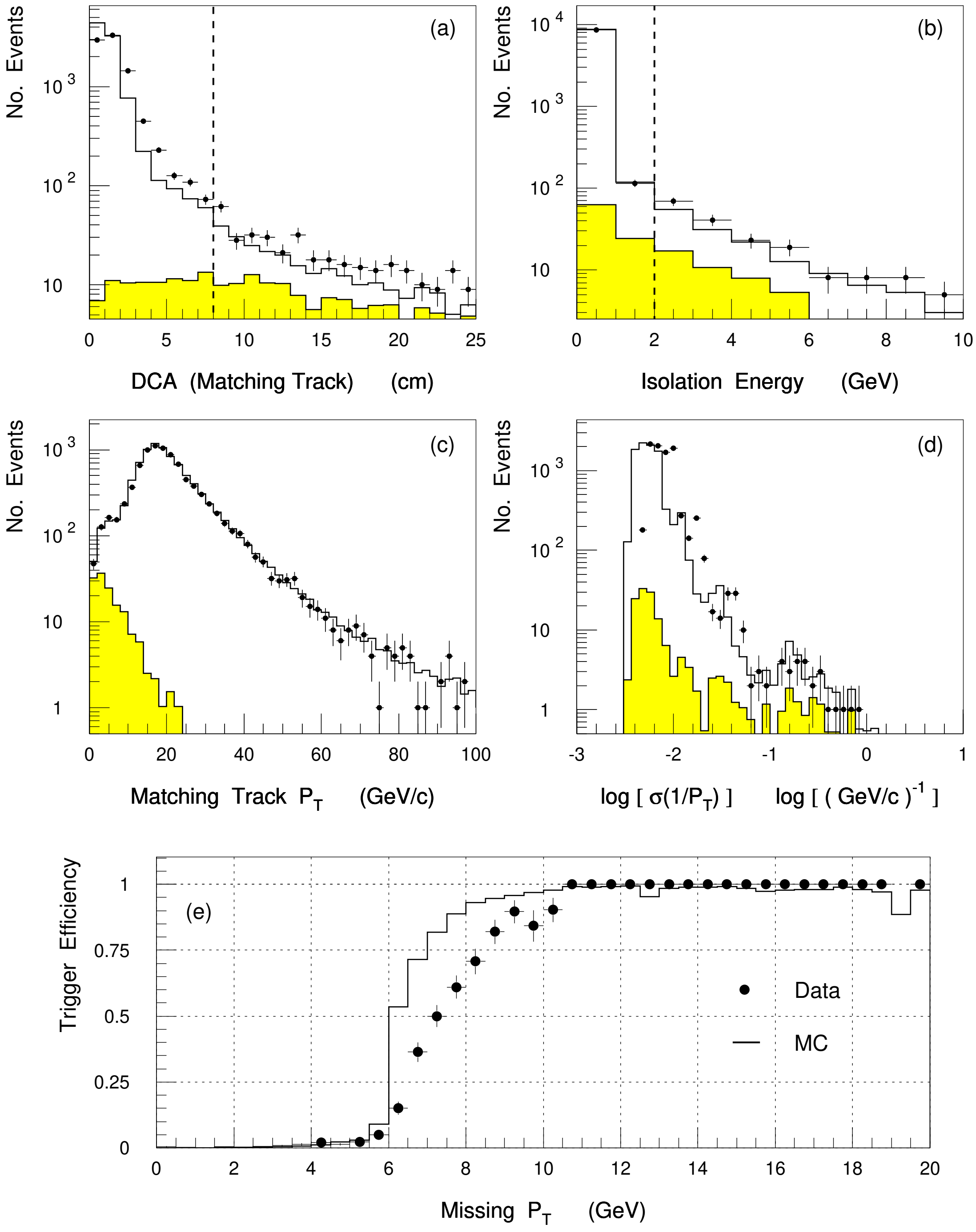

Figure 8.8: *Plots used in the estimate of the systematic uncertainty in the selection efficiency for $W \rightarrow e\nu$. The data (points) are compared to Monte Carlo (solid line) for relaxed selection cuts, with the final $W \rightarrow e\nu$ cuts indicated by the dashed lines. Non-neutral current Monte Carlo is given by the shaded histogram. Further details are given in the text.*

to the distribution of this quantity for signal events, the final cut of 0.3 rad is varied by ±0.05 rad with the same requirement that the hadronic p_T be greater than 4 GeV. The selection efficiency for $W \to e\nu$ events is found to be rather insensitive to the placing of this cut, with fractional changes of at most 2%.

Vertex Distribution

It was mentioned above that there are differences between the selection efficiencies calculated for Monte Carlo events incorporating the 1995 and 1996 detector simulations. In fact the variation of around 2.5% is mainly due to the different vertex distributions employed in the two versions. Although the two sets of Monte Carlo data are combined according to the relevant luminosity ratio in the calculation of overall efficiencies and event rates, the difference is used here as a conservative estimate of the error introduced into the efficiency calculation from uncertainties in the vertex distribution.

Trigger

With neutral current events selected on the basis of high E_T it is possible to calculate the fraction that would fire the missing p_T trigger slots for a given offline reconstructed missing p_T. This is plotted in fig. 8.8(e) for both data and Monte Carlo. It is noticeable that the data trigger efficiency turns on somewhat slower than predicted by Monte Carlo, which could be due to inaccuracies in the complex simulation of the calorimeter trigger system. Nevertheless the efficiency appears to saturate well before the final 20 GeV cut required in the analysis and the conditional trigger efficiency is therefore expected to be high. Indeed, it is found from $W \to e\nu$ Monte Carlo that around 99% of events passing all other cuts have the required trigger slots set. The systematic uncertainty arising from the understanding of the trigger efficiency is therefore estimated to be around 1%.

Combined

Combining the above sources of systematic error in quadrature gives an overall fractional uncertainty in the selection efficiency for $W \to e\nu$ events of 8%.

8.1.5 Error on the Background Estimate

There are systematic and statistical sources of error on the background estimate. Firstly, fig. 8.6(e) showed a discrepancy between data and Monte Carlo missing p_T distributions. At the cut value of 20 GeV the data is consistent with being twice the Monte Carlo expectation and an error of 100% is therefore assigned to the neutral current contribution to the background. The other main sources of background suffer from large statistical uncertainties, for example $\sim$ 30% in the case of the charged current background estimate. Combining these sources of error in quadrature, the overall uncertainty on the number of events expected from Monte Carlo is around 0.4 events or $\sim$ 55%. Remaining sources of systematic uncertainty in the background estimate are assumed to be small compared to this number.

8.1.6 Error on the Integrated Luminosity

The luminosity is determined to within 1-2% depending on the running period, with the main uncertainties arising from such sources as the luminosity monitor acceptance correction and background subtraction [12]. There is an additional uncertainty arising from the size and effect of the satellite bunches on the luminosity measurement and Monte Carlo acceptance estimate. The overall systematic error on the integrated luminosity is assumed for the purposes of this analysis to be be 2%.

8.1.7 Cross Section Upper Limit

A method for calculating cross section upper limits in the presence of uncertainties in the selection efficiency, background estimate and luminosity has been developed and is presented in appendix A. Using the above calculated efficiencies, background estimates and data from 1994-96, a 95% confidence level upper limit can be placed on the W production cross section in e^+p collisions at HERA :

$$\sigma(e^+p \rightarrow e^+W^\pm X) \;\times\; BR(W \rightarrow e\nu) \;\;<_{95\%}\;\; 0.52 \;\; \text{pb} \;. \tag{8.3}$$

Assuming a value for the branching ratio of 10.8%, then

$$\sigma(e^+p \rightarrow e^+W^\pm X) \;\;<_{95\%}\;\; 4.8 \;\; \text{pb} \;. \tag{8.4}$$

This upper limit has so far neglected the contribution to the signal sensitivity from the fraction of $W \rightarrow \tau\nu$ decays that are selected. Computing an average efficiency for the two channels of around 22% and taking the combined branching ratio for $W \rightarrow e\nu\,,\,\tau\nu$ results in an improved 95% confidence level constraint of 4.4 pb.

This result can, under certain assumptions, be interpreted as a limit on anomalous couplings at the $WW\gamma$ vertex. This is discussed further in chapter 11.

8.2 Radiative Charged Current Scattering

Radiative charged current scattering is, through photon radiation from the W propagator, sensitive to the same couplings at the $WW\gamma$ vertex as single W production (see chapter 5). The first stage in the analysis of radiative charged current scattering is the selection of a relatively pure charged current sample. This is achieved using a cut scheme similar to that described in [25] :

1. $\mid z - \text{vertex} \mid < 50$ cm ,
2. Good track requirement (see section 7.1.2) and cosmic muon rejection ,
3. Missing $p_T > 15$ GeV and $p_T[-1\text{ir}] > 9$ GeV ,
4. $E - p_Z < 45$ GeV ,
5. (missing-$p_T/E_T) > 0.4$,
6. $p_T^{trk}/p_T^{cal} > 0.1$,
7. $\Delta\phi\ (trk,\ cal) < 1.0$ rad ,

where the missing p_T cut corresponds, via equation 3.10, to a cut on the uncorrected Q^2 value for the event.

The last three cuts in particular are important in selecting charged current events. The requirement that the fraction (missing-p_T/E_T) is greater than 0.4 rejects events, such as high E_T photoproduction events, for which a small mismeasurement or escape of energy gives rise to a net missing p_T. The final two cuts require that the momentum imbalance measured from the CTD tracks, p_T^{trk}, is also significant and matches the direction of the missing p_T measured in the calorimeter. This also helps to remove events for which the calorimeter measured missing p_T, due to hadrons entering regions of inactive material or energy leakage from jets, is unreliable. The data and luminosity weighted Monte Carlo is compared in fig. 8.9, where only the cut corresponding to each distribution has not been applied and is indicated by the dashed line. The contribution to the Monte Carlo total from non-charged current processes is illustrated by the shaded histogram and is concentrated overwhelmingly at small missing p_T's. All Monte Carlo samples used in the estimate of the background to W production have been used here.

In general there is good agreement between data and Monte Carlo, with the total number of events predicted statistically consistent with the number observed. The large excess of

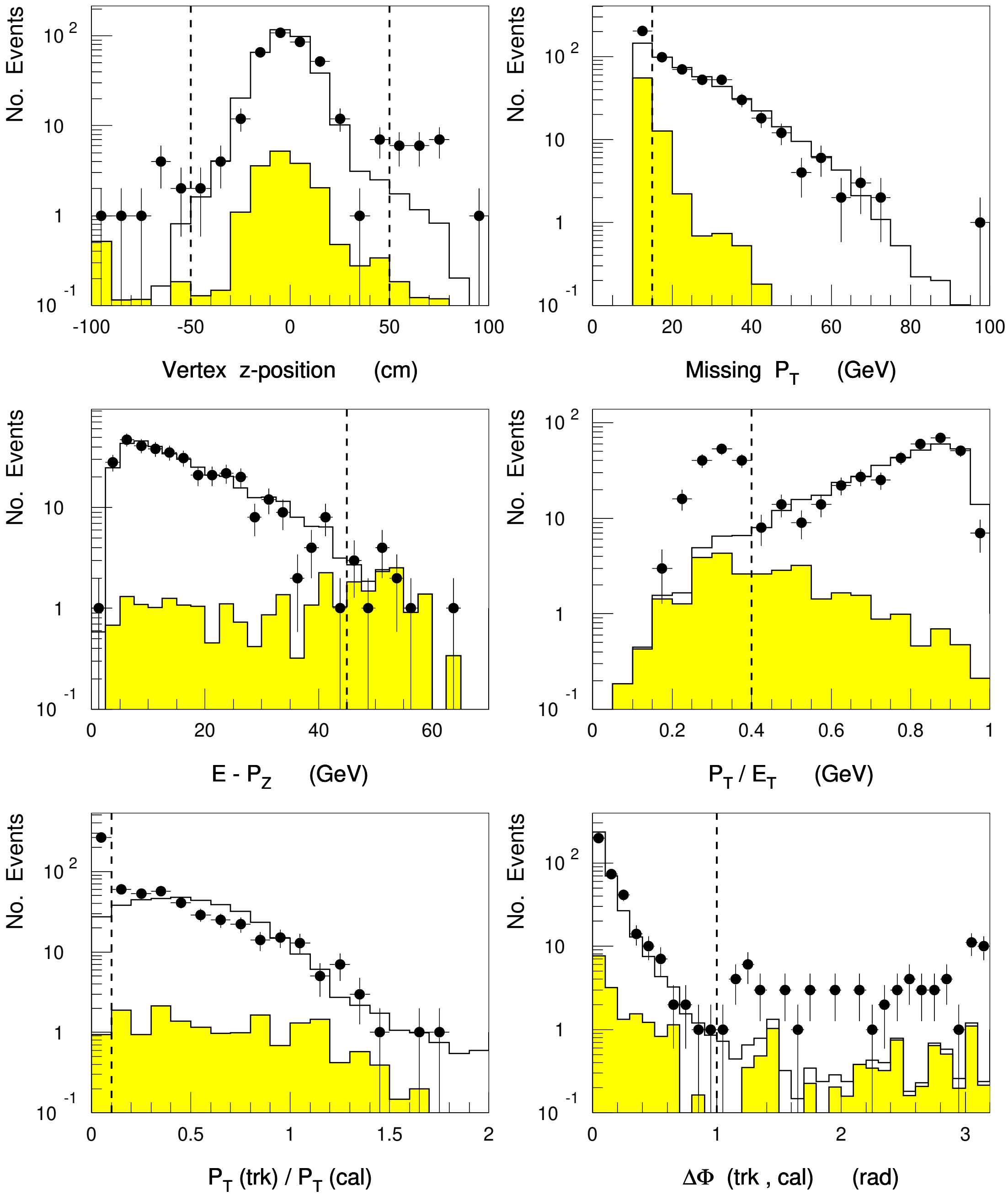

Figure 8.9: *The selection of charged current events. The data (points) are compared to Monte Carlo (solid line), with the non-charged current Monte Carlo contribution given by the shaded histogram. Only the cut corresponding to each distribution has not been applied and is indicated by the dashed line in each case (see text).*

events at small values for (missing-p_T/E_T) and p_T^{trk}/p_T^{cal} are mainly proton beam gas and cosmic muon overlay events respectively. The final sample has been visually scanned to remove any remaining such events. The slightly different shape of the p_T^{trk}/p_T^{cal} distribution in the data compared to the Monte Carlo would clearly give rise to a systematic uncertainty in the selection efficiency. However the object here is simply the efficient selection of a high purity sample of charged current events and the above cuts, primarily that on the missing p_T, ensure a purity estimated from the Monte Carlo in excess of 95%.

8.2.1 Radiative Event Selection

As described in section 6.2.5, electromagnetic showers produced in the calorimeter by photons are efficiently identified by the same neural network based algorithm used to identify electrons. In order to identify as many radiative events as possible given a steeply falling photon energy spectrum the minimum electromagnetic cluster energy is reduced to 5 GeV. The only subsequent requirement is that the electromagnetic cluster, if it has a matching track at all, must have a distance of closest approach for the nearest track in excess of 20 cm. This is very much larger than the mean DCA for electrons over almost all polar angles (see section 6.2.3) and ensures a purity determined using charged current Monte Carlo of around 50%. That is, half of the photon candidates selected in this manner correspond to photons from the radiative sub-process $e^+q \to \bar{\nu}\gamma q'$ and half are photons from hadron decay or are themselves misidentified hadrons. The efficiency with which events containing a radiated photon with $E > 5$ GeV , $p_T > 2$ GeV and $5^\circ < \theta < 175^\circ$ are selected is 28%. An example of a radiative charged current candidate is shown in fig. 8.10, with a clear photon candidate in the RCAL at a polar angle of 160° and with an energy of 13 GeV. The missing p_T for the event of 55 GeV ensures that the event is in a region free from non-charged current backgrounds.

The 17 radiative charged current candidate events from 1994-96 are plotted against the luminosity weighted combined Monte Carlo sample in fig. 8.11 where, for events with more than one photon candidate, the highest p_T electromagnetic cluster is selected. The expected number of events is 16.7 (charged current) + 0.8 (background), where the latter is composed mainly of W production and Bethe-Heitler events. The matching track DCA distribution is plotted in fig. 8.11(a), where events for which the photon has no close matching track enter the last bin of the distribution. Although fig. 8.11(b) indicates a number of events with large photon isolation energies, defined as for electrons by equation 6.2, a large fraction of such events are nonetheless radiated photons close to the scattered quark and are retained

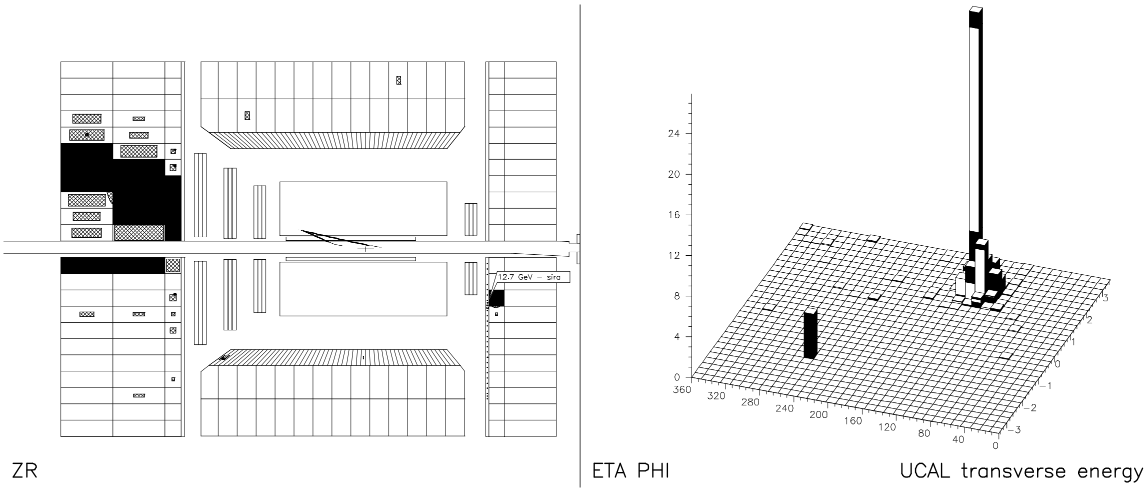

Figure 8.10: *An event in the radiative charged current sample. A collimated jet is visible in the FCAL and a* 13 GeV *electromagnetic cluster is visible in the RCAL at a polar angle of* 160°. *The net missing* p_T *for the event is* 55 GeV. *Note that the photon and jet are not back-to-back in the plane perpendicular to the beam line, with an acoplanarity angle of around* 50°.

in this analysis.

As discussed in section 5.2, the sensitivity to anomalous $WW\gamma$ couplings is found primarily in the high p_T end of the photon spectrum. The cuts indicated in fig. 8.11(c)-(f) by the dashed lines, not only on the photon p_T but also polar angle, isolation and hadronic p_T, correspond to the cuts with which radiative charged current scattering has been simulated using the cross section calculation program WWGAMMA. The hadronic p_T and photon isolation, defined as the $\{\eta, \phi\}$-separation of the photon and net hadron flow, are used as estimators of the struck quark p_T and photon-quark separation respectively. Photons in events passing these hard cuts are here called WWGAMMA photons.

The radiative charged current results are summarised in table 8.4, which compares the expected number of charged current and background Monte Carlo events after the initial charged current event selection, photon selection and finally the WWGAMMA selection. Note that the comparison here, like that in fig. 8.11, is between the data and DJANGO description of radiative charged current scattering. Photon radiation from the W propagator, not included in DJANGO, forms a very small part of the Standard Model radiative cross section with the cuts described. In addition it was shown in section 5.2 that the DJANGO description of radiative charged current scattering agreed closely, within a few percent, to that of the cross section program WWGAMMA. This comparison was made using the

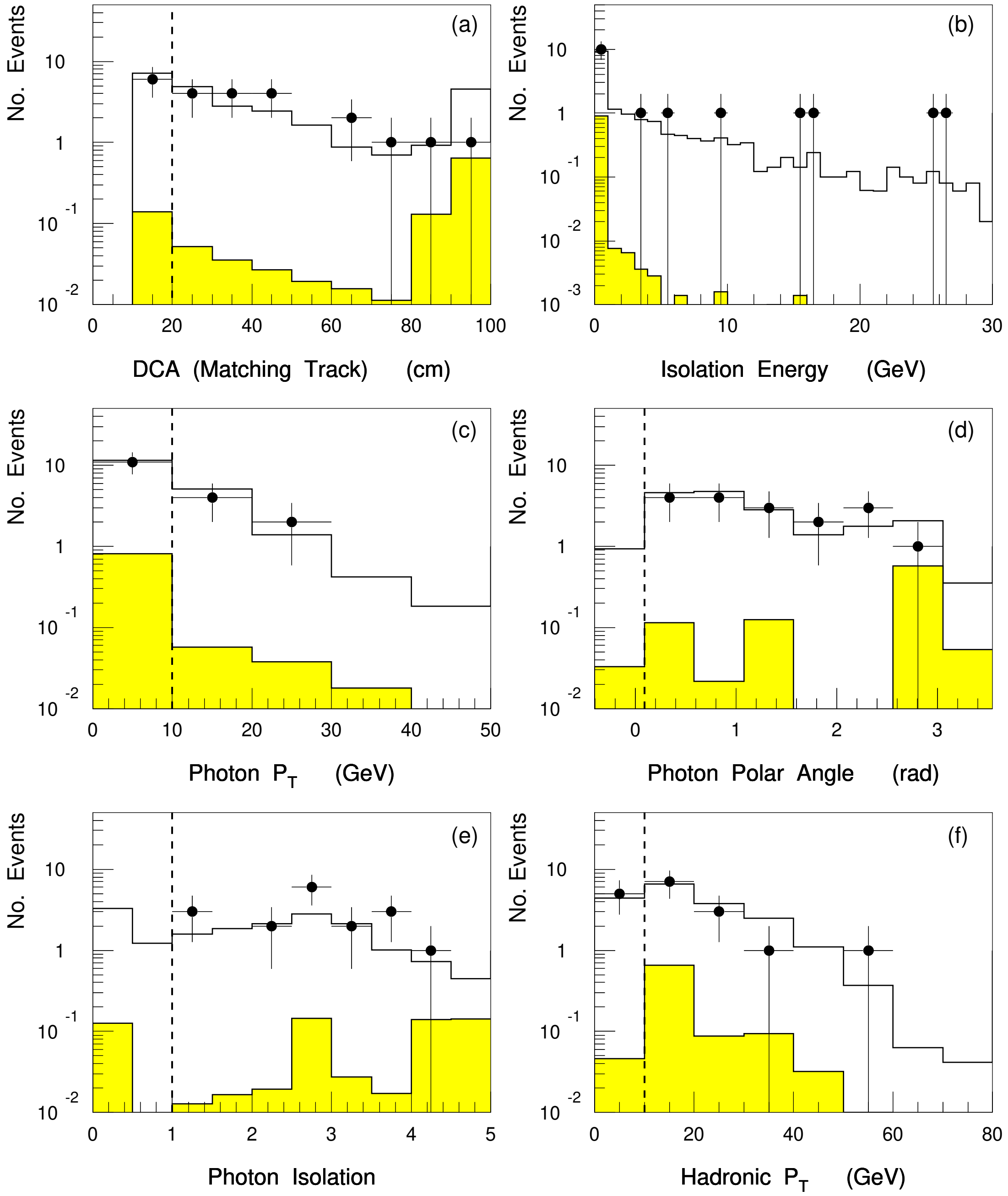

Figure 8.11: *A comparison of radiative charged current data (points) and Monte Carlo (solid line). Non-charged current Monte Carlo is given by the shaded histogram. All cuts have been applied except in (a), where the final DCA cut of* 20 cm *has not been applied and is indicated by the dashed line. The WWGAMMA photon cuts are indicated by the dashed lines in (c)-(f).*

Cut	Monte Carlo				Data 94-96
	CC [WWGAMMA]		Background	Total	
CC selection	345	[1.1]	17	362	348
Loose photon	16.7	[1.0]	0.8	17.5	17
WWGAMMA	2.9	[0.9]	0.1	3.0	1

Table 8.4: *The numbers of events expected and observed after each stage of the radiative charged current event selection. The numbers in square brackets indicate the charged current Monte Carlo events that pass WWGAMMA cuts at the generator level (see text).*

four vectors generated by DJANGO before any detector simulation, and the numbers in square brackets in table 8.4 indicate the number of charged current events that pass the WWGAMMA cuts at the generator level. Dividing this number by the total before any event selection therefore yields an efficiency based on Monte Carlo for selecting events that pass the WWGAMMA cuts, listed in full in section 5.2. The final efficiency is estimated to be $46 \pm 5\%$, where the comparatively large statistical error reflects the tiny cross sections involved (~ 0.1 pb) and the correspondingly limited number of Monte Carlo events even in a large 1 fb^{-1} sample.

8.2.2 Systematic Error on the Photon Finding Efficiency

There are three main sources of systematic uncertainty that affect the efficiency for selecting WWGAMMA photons.

Electron Finding Algorithm

With no other cuts applied, it is found that $93 \pm 3\%$ of true WWGAMMA photons are correctly identified by the neural network based electron finder. The corresponding efficiency is $95 \pm 3\%$ for a conventional electron finder. Adding the difference and the statistical error in quadrature gives a systematic uncertainty of 4% arising from the choice of electron finder.

Track Isolation Cut

The distribution of the distance of closest approach of the nearest matching track to the photon candidate, plotted in fig. 8.11(a) for the loose photon selection, shows reasonable agreement between the data and Monte Carlo. Varying the cut by ±10 cm only changes the Monte Carlo calculated efficiency for selecting WWGAMMA photons by 2%.

Calorimeter Scale Uncertainty

Varying the calorimeter energy scale for Monte Carlo events by ±5% gives rise to as much as a 9% fractional change in the high p_T photon radiative charged current selection efficiency. This is comparatively large due to a steeply falling photon energy spectrum combined with the sensitivity of the overall charged current selection efficiency to the absolute calorimeter energy scale.

Combined

Combining the above sources of systematic error in quadrature with the statistical error gives a total error on the WWGAMMA photon finding efficiency of 15%. This is significantly larger than the uncertainty calculated for the $W \to e\nu$ selection efficiency, again due to the larger statistical and calorimeter energy scale related uncertainties.

8.2.3 Error on the Background Estimate

For the purposes of setting an upper limit on anomalous high p_T photon production in charged current scattering, all Standard Model sources are here included as backgrounds. The same ±10 cm change in the track isolation cut used to evaluate the systematic error on the photon finding efficiency gives rise to as much as a 40% change in the number of background events expected from Monte Carlo.

8.2.4 Cross Section Upper Limit

Using the errors calculated above on the photon finding efficiency and background estimate, together with the error on the integrated luminosity quoted in section 8.1.6, an upper limit may be placed on the anomalous production of isolated photons with $p_T > 10$ GeV and $5^\circ < \theta < 175^\circ$ in charged current events with missing $p_T > 15$ GeV and hadronic $p_T > 10$ GeV :

$$\sigma_{anom}(e^+p \to \bar{\nu}\gamma X) \quad <_{95\%} \quad 0.41 \ \ \text{pb} \ , \tag{8.5}$$

which, adding the Standard Model radiative cross section for these cuts, gives :

$$\sigma(e^+p \to \bar{\nu}\gamma X) \ = \ \sigma_{anom}(e^+p \to \bar{\nu}\gamma X) \ + \ \sigma_{SM}(e^+p \to \bar{\nu}\gamma X) \ <_{95\%} \ 0.51 \ \ \text{pb} \ . \tag{8.6}$$

The significance of such an upper limit and a comparison with the radiative charged current cross section calculated in the presence of anomalous couplings is discussed in chapter 11.

8.2.5 Relaxing the Cuts

From fig. 8.11 it can be seen that radiative charged current scattering is well described by Standard Model Monte Carlo. However, certain cuts in the initial selection of charged current events implicitly reject events of a certain topology. In particular, the cuts on (missing-p_T/E_T) and $\Delta\phi$ (trk,cal) could remove events in which a very high p_T photon has a large azimuthal separation from the current jet, similar to the known bias of such cuts against multi-jet final states. The comparatively high radiative event selection efficiency then reflects the fact that high p_T photons in Standard Model charged current scattering are radiated at small angles with respect to the struck quark. Radiation in the presence of anomalous couplings or other non-Standard Model process giving rise to events with high p_T photons and missing p_T can have larger photon-quark angular separations.

It is interesting, therefore, to relax both these cuts and compare the data to the Monte Carlo, as shown in fig. 8.12. The non-charged current Monte Carlo component, given by the shaded histogram, is clearly more significant once background rejection cuts are relaxed, but there is nevertheless good agreement with the data. The efficiency for selecting WWGAMMA photons with the same cuts described above increases to around 55% which, with 2 data events surviving against an expectation of around 4.8 from all Monte Carlo sources, results in an almost identical anomalous radiative cross section limit to that given in equation 8.5. This number is therefore not too sensitive to assumptions about the distribution of photons in events with missing p_T, a fact which is important in converting a cross section upper limit into anomalous coupling constraints as described in chapter 11.

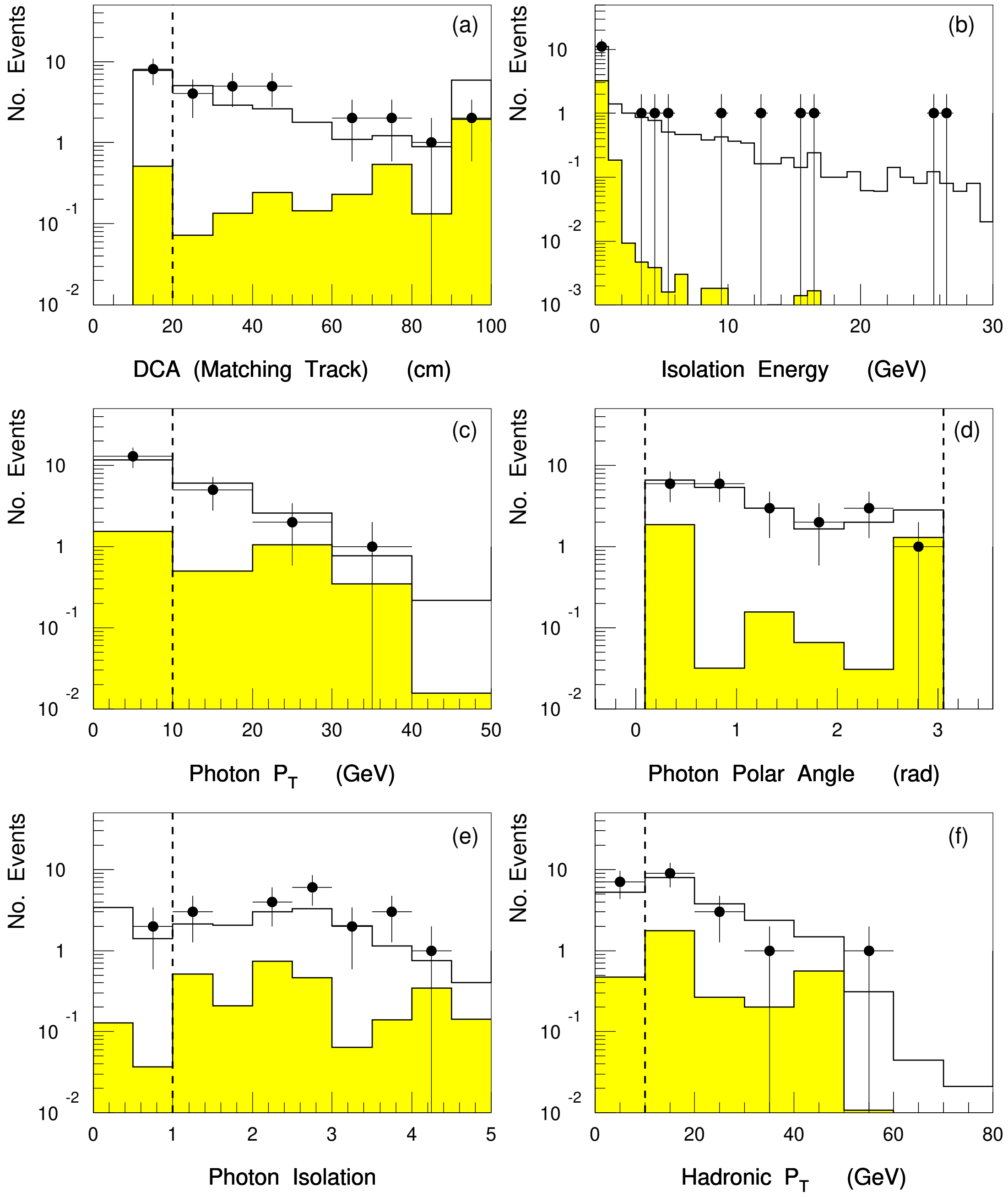

Figure 8.12: *A comparison of radiative charged current data (points) and Monte Carlo (solid line) with relaxed topological cuts (see text). Non-charged current Monte Carlo is given by the shaded histogram. All cuts have been applied except in (a), where the final DCA cut of* 20 cm *has not been applied and is indicated by the dashed line. The WWGAMMA photon cuts are indicated by the dashed lines in (c)-(f).*

8.3 Multi-Electron Events at High E_T

Events are searched for in the high E_T sample that have at least two good electron candidates, with standard good electron and preselection cuts described in chapters 6 and 7 respectively. Fig. 8.13 shows some kinematic distributions for events in which at least two of the electron candidates have $p_T > 10$ GeV and polar angles less than 2.0 rad, with the combined Monte Carlo background indicated by the solid histogram and the contribution from Z production given by the shaded histogram. Note that since a significant fraction of Z production events have the scattered beam positron inside the main detector (see section 4.2.2), the invariant mass is formed from the two highest p_T electron candidates only. There is good agreement between data and Monte Carlo, the latter being composed almost entirely of neutral current events in which a second fake electron is identified in addition to the true scattered positron. This can be seen from the $E - p_Z$ distribution, with a clear peak visible close to twice the lepton beam energy. Unlike the case for $W \to e\nu$ decays, however, the signal is concentrated in a similar region of $E - p_Z$ and this quantity cannot be cut on here. Extracting a clear multi-lepton signal therefore demands stricter good electron and electron isolation cuts.

Fig. 8.13(e) shows the distance of closest approach distribution for any second track that extrapolates close to an electron candidate. Requiring that this quantity be greater than 30 cm removes a fraction of neutral current events in which the electron candidate is close to a high track multiplicity jet. Fig 8.13(f) shows the number of cells that make up the electromagnetic cluster for each electron in the sample. The background Monte Carlo is flatter than the signal, as observed for electron candidates in charged current events in section 8.1.1, due to the fake electron being ‘larger’ on average than the true scattered positron in neutral current events. Requiring that each electron candidate be composed of ≤ 30 calorimeter cells has a negligible effect on the selection efficiency for $Z^0 \to e^+e^-$. Since the signal for $Z^0 \to e^+e^-$ is so small compared to the background coming mainly from neutral current scattering, the standard good electron cuts are tightened further than in the missing p_T plus electron analysis :

- Distance of Closest Approach ($\theta > 0.4$ rad) : 10 cm → 5 cm ,
- Distance of Closest Approach ($\theta < 0.4$ rad) : 15 cm → 10 cm ,
- Isolation Energy ($R_{\eta\phi} = 0.6$) : 4 GeV → 2 GeV .

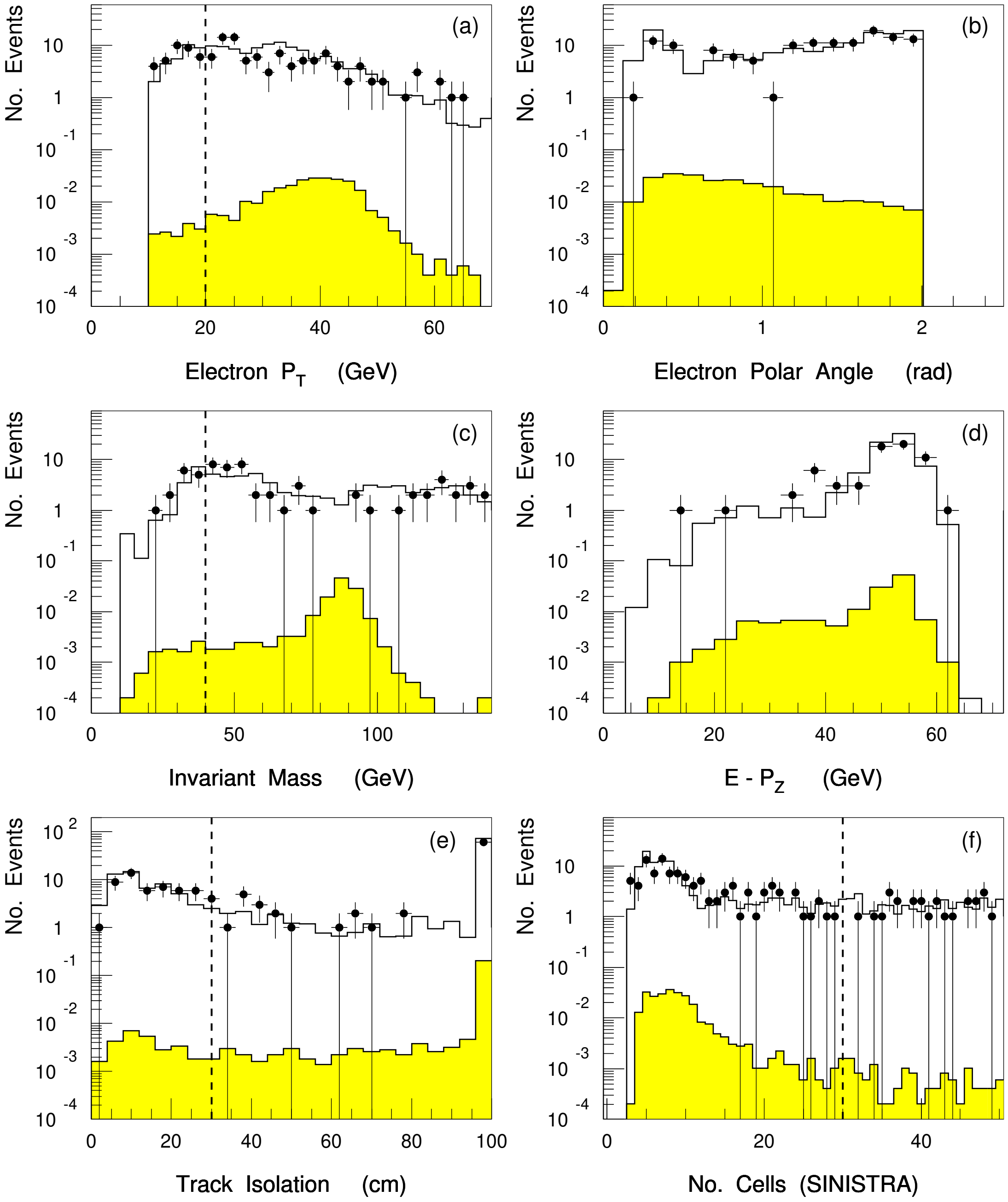

Figure 8.13: *Events in the 1994-96 high E_T sample which contain at least two electron candidates with $p_T > 10$ GeV and $\theta < 2.0$ rad. The combined Monte Carlo expectation is given by the solid histograms with the contribution from Z production indicated by the shaded part. Subsequent selection cuts are indicated by the dashed lines and described in more detail in the text.*

8.3.1 Selecting $Z^0 \to e^+e^-$ Events

After applying the extra quality cuts described above, the data and Monte Carlo are compared in fig. 8.14 for events in which at least two candidates have $p_T > 20$ GeV and form an invariant mass greater than 40 GeV. Fig. 8.14(c) shows the invariant mass distribution for the $Z^0 \to e^+e^-$ signal after all cuts, on the basis of which an invariant mass window $75 < \mathrm{IM} < 100$ GeV is chosen. The electron p_T cut is raised to 30 GeV at the same time. It can be seen that no data events survive in the invariant mass window, against an expectation of only 0.08 $Z^0 \to e^+e^-$ and 0.29 background events. The numbers of events expected and observed at each stage in the event selection are summarised in table 8.5.

The final signal to background ratio is around 30%, although with a significant uncertainty on the background estimate (see below). The overall selection efficiency is around 36% and is broken down by Z production channel in table 8.6. The efficiency is enhanced for the elastic and quasi-elastic channels due to the more central angular distributions for the Z decay products (see section 4.2.2) and the reduced probability for one of the decay leptons to be poorly isolated from hadrons in the event. With such a small signal to background ratio, any prospect for isolating a $Z^0 \to e^+e^-$ signal at HERA will require the highest luminosities and tighter selection cuts. For example, the specific selection of events containing 3 electrons might enhance the signal to background ratio at the cost of a reduced selection efficiency. Future Z searches at HERA are discussed briefly in section 9.5.5 and in chapter 11.

8.3.2 High Mass Multi-Electron Events

Although no events fall inside the narrow invariant mass window for the $Z^0 \to e^+e^-$ search, there are high invariant mass multi-electron events in the event sample. Fig. 8.15 shows the highest mass event, containing two electromagnetic clusters with p_T in excess of 50 GeV and a corrected [4] invariant mass of 133 GeV. The event is interesting in that it is also an elastic event, for which the neutral current background is negligible. The forward matching track consists of relatively few hits, and the possibility that the electromagnetic cluster in the FCAL originates from a high energy photon cannot be ruled out [5]. The expectation from Bethe-Heitler e^+e^- production (elastic and inelastic) and QED Compton Monte Carlo

---

[4] Only the electromagnetic cluster energies are corrected using the dead material and calorimeter non-uniformity correction described in chapter 10.

[5] An asymmetric conversion in the dead material of the beam pipe might give one stiff and one low momentum track, which is consistent with the pattern of hits in the CTD.

Background Process	**Cut**		
	Pre-selection	$p_T^e > 20$ GeV ; IM > 40 GeV	$p_T^e > 30$ GeV ; $75 <$ IM < 100 GeV
$e^+p \to e^+X$ (NC DIS)	68.7	2.64	0.13
γp (Direct)	0.6	< 0.21	< 0.21
γp (Resolved)	< 0.68	< 0.68	< 0.68
$\gamma\gamma \to e^+e^-$ (Elastic)	1.8	0.64	0.07
$\gamma\gamma \to e^+e^-$ (Inelastic)	2.0	0.58	0.06
$\gamma\gamma \to \tau^+\tau^-$ (Elastic)	0.04	< 0.04	< 0.04
$\gamma\gamma \to \tau^+\tau^-$ (Inelastic)	0.12	< 0.03	< 0.03
QED Compton	1.3	0.20	0.02
$e^+p \to e^+W^\pm X$	0.1	0.02	0.
Signal Process			
$Z^0 \to e^+e^-$ (Efficiency)	0.11 (50%)	0.10 (43%)	0.08 (36%)
$Z^0 \to \tau^+\tau^-$	0.01	0.01	0.
Other Channels	0.02	0.	0.
Total	74.6	4.17	0.37
Data			
95-96	66	5	0

Table 8.5: *The expected and observed numbers of events in the 1994-96 high E_T multi-electron event sample. See text for more details.*

Production Channel	Z^0 DIS	Z^0 PHP	Z^0 ELA	Z^0 QEL	Combined
Efficiency	30 ± 2 %	34 ± 2 %	42 ± 2 %	40 ± 2 %	36 ± 1 %

Table 8.6: *The efficiency for selecting $Z^0 \to e^+e^-$ events in the different Z production channels, calculated using the 1995 Monte Carlo detector configuration. The combined value assumes the mixture of DIS, photoproduction, elastic and quasi-elastic type Z production given in chapter 4. Statistical errors only are given.*

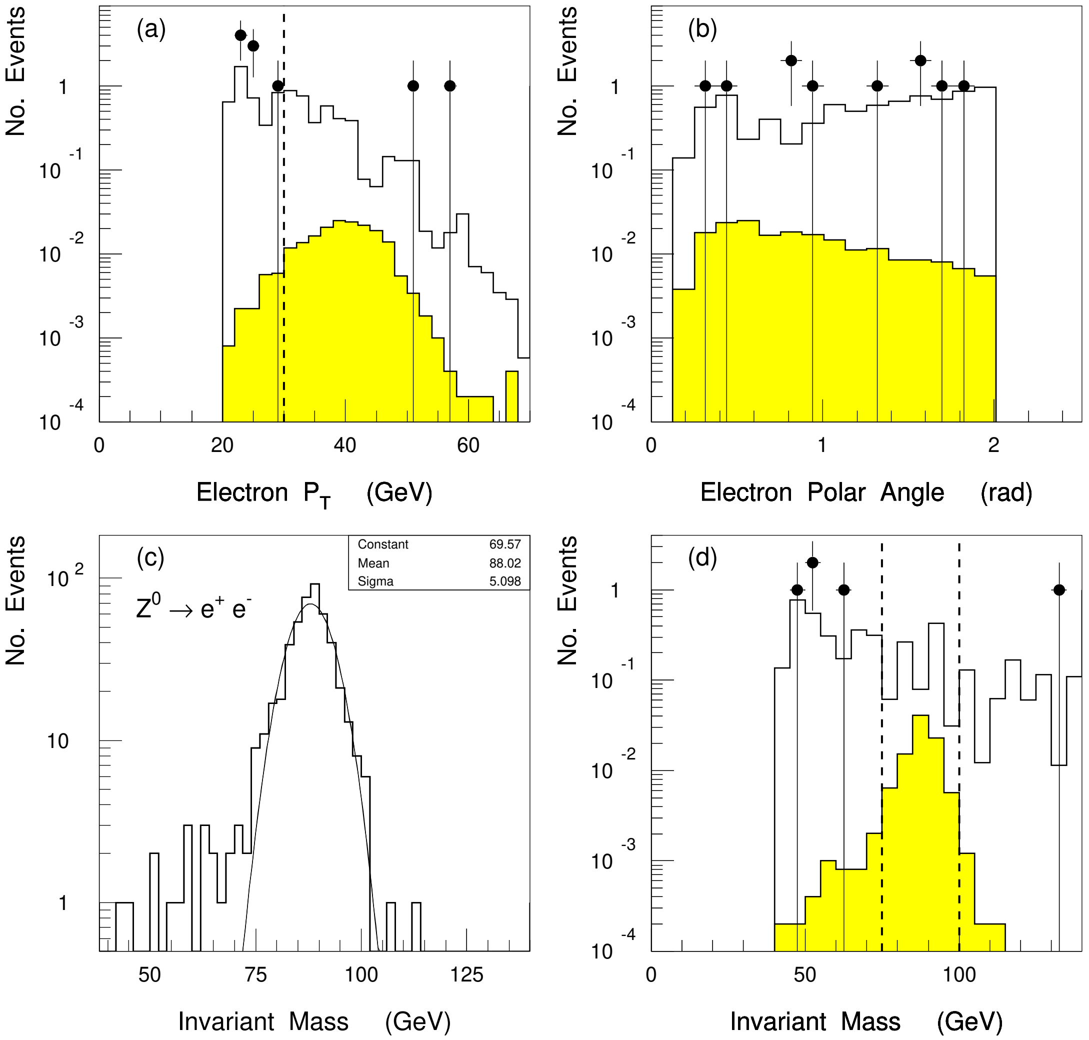

Figure 8.14: *Events in the 1994-96 high* E_T *sample which contain at least two electron candidates with* $p_T > 20$ GeV *that have an invariant mass greater than* 40 GeV*. The combined Monte Carlo expectation is given by the solid histograms with the contribution from Z production indicated by the shaded part. The signal invariant mass distribution is plotted in (c) and subsequent selection cuts are indicated by the dashed lines.*

is only 0.017 and 0.006 events respectively [6] for invariant masses greater than 130 GeV and other cuts described above for fig. 8.14. However, this estimate is based on QED Compton Monte Carlo which is known not to simulate such quantities as the total E_T correctly due to the lack of any simulation of the hadronic final state. Clearly more luminosity will be required to establish the presence or otherwise of events at large invariant masses above the

---

[6] No attempt is made to split the expected number of events into elastic and inelastic detector level events for the reasons given in section 5.6.

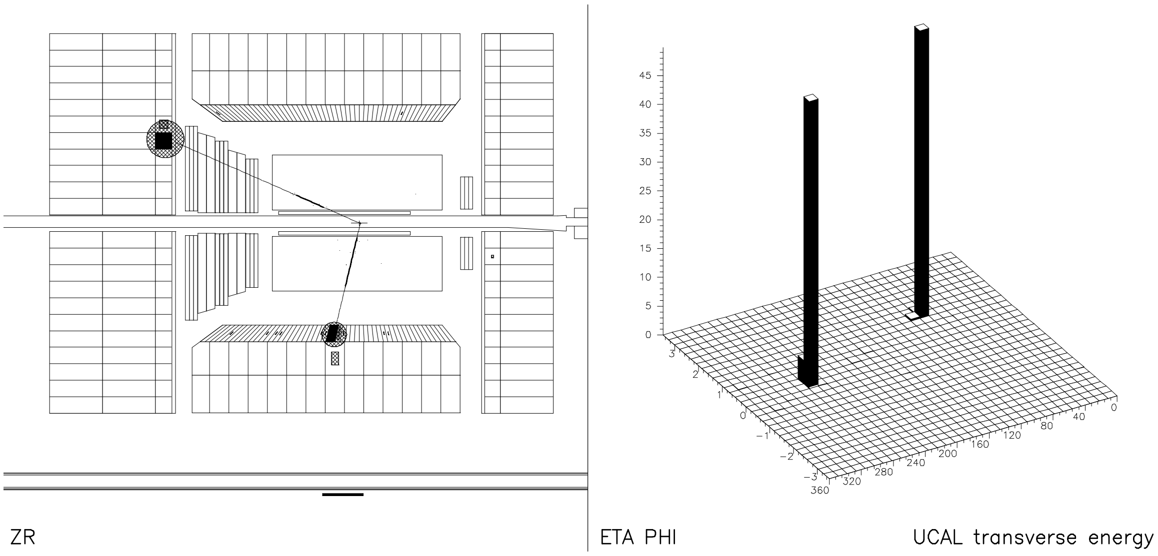

Figure 8.15: *The highest invariant mass multi-electron event in the 1994-96 high E_T sample. Two high p_T electrons are well isolated in $\{\eta, \phi\}$ and have a corrected invariant mass of* 133 GeV*. See text for more details.*

rate expected from Monte Carlo.

8.3.3 Systematic Error on the $Z^0 \to e^+e^-$ Selection Efficiency

Since the selection of $Z^0 \to e^+e^-$ events hinges on the identification of high p_T electron candidates, the electron finding efficiency and calorimeter scale uncertainty are expected to dominate the systematic uncertainties. Possible trigger inefficiencies are briefly considered but found to be negligible.

Electron Finding Efficiency

The conventional electron finder ELEC5 is compared to SINISTRA for $Z^0 \to e^+e^-$ Monte Carlo events in which the electron and positron from the Z decay have true transverse momenta above the final cut value of 30 GeV. With no other cuts applied the efficiency is $92 \pm 1\%$ for ELEC5 and $99 \pm 1\%$ for SINISTRA, resulting in a 7% fractional systematic uncertainty from the electron finding algorithm.

The track matching requirement was found to give rise to a 2% systematic uncertainty in the electron finding efficiency in the analysis of the neutral current control sample above. It is therefore assumed to contribute 4% to the systematic uncertainty in the selection efficiency for events with two or more high p_T electrons.

Calorimeter Scale Uncertainty

The selection efficiency is rather sensitive to the calorimeter energy scale due to the hard cuts on the E_T and electron p_T and from the shift of the invariant mass peak within the window of allowed values. The overall effect of varying the energy scale by $\pm 5\%$ is as much as a 9% fractional variation in the selection efficiency.

Trigger

Significantly harder cuts are placed on the offline reconstructed E_T than are used in the trigger (e.g. $E_T[-2\text{ir}] > 40$ GeV without an $E - p_Z$ requirement, compared to 35 GeV at the trigger level) in order to minimise the possible impact of any discrepancy between the data and Monte Carlo turn on curves similar to that in fig. 8.8. With a conditional trigger efficiency calculated from Monte Carlo of 100%, any systematic uncertainty arising from poorly described trigger efficiencies is therefore assumed to be small.

Combined

Combining the above sources of systematic error in quadrature results in an overall uncertainty of 12% in the efficiency for selecting $Z^0 \to e^+e^-$ events. This is clearly higher than that for selecting $W \to e\nu$ events due to the greater dependence of the selection procedure on the electron finder and because events of a specific invariant mass are being selected in the presence of an uncertainty in the absolute calorimeter energy scale.

8.3.4 Error on the Background Estimate

The statistical error on the estimate of the background from Bethe-Heitler e^+e^- production is small and that on the neutral current estimate is of order 50%. Since neutral current events in the multi-electron sample most likely have at least one fake electron, it might be expected that the number of events depends on the hadronic final state simulation. In fact, estimating the background using $Q^2 > 400$ GeV^2 ARIADNE Monte Carlo rather than MEPS results in a doubling of the background estimate. A systematic uncertainty of 100% is therefore attributed to the background estimate in this analysis.

8.3.5 Cross Section Upper Limit

Taking the above efficiency and estimate for the background results in the following 95% confidence level limit on Z production and decay to electrons :

$$\sigma(e^+p \to e^+Z^0X) \times BR(Z^0 \to e^+e^-) \quad <_{95\%} \quad 0.42 \text{ pb} . \tag{8.7}$$

Given a branching ratio to charged leptons of 3.36% the constraint on the total Z production cross section is therefore 12.6 pb. Unlike the limit derived above for W production in e^+p collisions, this upper limit is not of the same order as the Standard Model cross section. The sensitivity afforded by the current HERA data is therefore limited to large anomalous Z production cross sections only.

In general there is good agreement between the data and Monte Carlo in the high p_T lepton channels considered in this chapter. This has allowed upper limits to be placed on the W and Z production cross sections and the high p_T photon radiative charged current cross section. In the case of W production the sensitivity is to cross sections of the same order as the Standard Model cross section, making the preliminary inclusion of the 1997 data particularly interesting. Before that, however, the search for W and Z production in the 1994-96 data is extended to include the muon in addition to the electron decay channels.

Chapter 9

High p_T Muons

This chapter deals with the analysis of events with high p_T muons. The first part describes how the efficiency of the muon finders described in chapter 6 has been checked using data and compared to the results obtained using Monte Carlo events. Specific event selections are then described and comparisons made with Standard Model expectations. In particular, events consistent with being the muon decays of W or Z bosons are searched for.

9.1 Muon Finder Efficiencies

It is important to be able to determine the efficiency for identifying high p_T muons with as little reliance as possible on the Monte Carlo simulation of the ZEUS detector. For example it is known that there are dead or inefficient barrel muon limited streamer tubes that are not implemented in the Monte Carlo, although in general the agreement between the data and Monte Carlo is good [86]. One of the main effects of these dead LST's, namely the impact on the first level trigger efficiency, is simulated throughout the analysis of barrel and rear muon chamber events with a special routine applied to Monte Carlo events only [87].

A suitable class of event to study the muon identification efficiency in the data is a clean di-muon sample. Events from the barrel muon sample are selected that have two muons present with $p_T > 3$ GeV [1] where a muon is defined to be a CTD-MIP match described in chapter 6. At least one of these two muons must match a barrel muon chamber segment in addition. The 1997 data is included here in order to maximise the statistics available for the efficiency measurement, giving a total 1995-97 integrated luminosity of 43.6 pb^{-1}. 'Clean' di-muon events are also required to have

- Exactly 2 vertex tracks with $p_T > 2$ GeV,

---

[1] This slightly higher p_T cut than the 2 GeV preselection requirement ensures that muons in the events selected are penetrating enough to have a high probability of detection in the barrel and rear muon chambers.

- B and RCAL EMC energies less than 2 GeV each.

These two requirements together ensure that there is little activity in the central detector apart from the two muon tracks and MIP energy deposits. The cut on the EMC energy in the barrel and rear calorimeters removes events where one of the high p_T tracks is in fact the scattered positron or a high p_T hadron. The cuts do not remove inelastic events with large energy deposits in the inner rings of the FCAL close to the incident proton direction, for reasons mentioned below. Finally all remaining events in the sample are visually scanned, removing a small number of cosmic ray background events. There is no evidence from the visual scanning of any contamination of the sample from physics sources other than di-muon production. This confirms the high muon finder purities reported in chapter 6.

Fig. 9.1 shows a comparison between the di-muon data from 1995-97 and luminosity normalised Monte Carlo, where the latter is dominated by Bethe-Heitler elastic and inelastic $\mu^+\mu^-$ production. It can be seen that there is general agreement in the shapes of the basic kinematic distributions between the data and Monte Carlo. Furthermore, it is evident from fig. 9.1 that a significant contribution from inelastic di-muon production is required to obtain agreement between the data and Monte Carlo, despite the selection of low track multiplicity events.

Other possible sources of high p_T leptons that have been considered are elastically and inelastically produced $\tau^+\tau^-$ pairs, and the elastic production of J/ψ and Υ vector mesons. The expected numbers of events in the clean di-muon sample from these sources are summarised in table 9.1. Although there is qualitative agreement between the data and Monte Carlo distributions in fig. 9.1, there are in total 341 data events against a Monte Carlo expectation of 383 events. One important difference between the data and Monte Carlo, evident in fig. 9.1(e), is the smaller fraction of data events that have little or no energy in the FCAL inner ring compared to Monte Carlo. That is, fewer events are ‘elastic’ at the detector level in the data than the Monte Carlo. It is also clear that the inelastic contribution to the number of events with little proton remnant activity visible in the main detector is significant, due to inelastic di-lepton production being dominated by events with small hadronic final state masses. The discrepancy in the FCAL inner ring energy distribution may be due to limitations in the simulation of the hadronic final state for inelastic Bethe-Heitler di-lepton production that were mentioned in section 5.4.

In order to investigate whether the difference in the expected and observed number of events in the clean di-muon sample can be attributed to different muon finding efficiencies

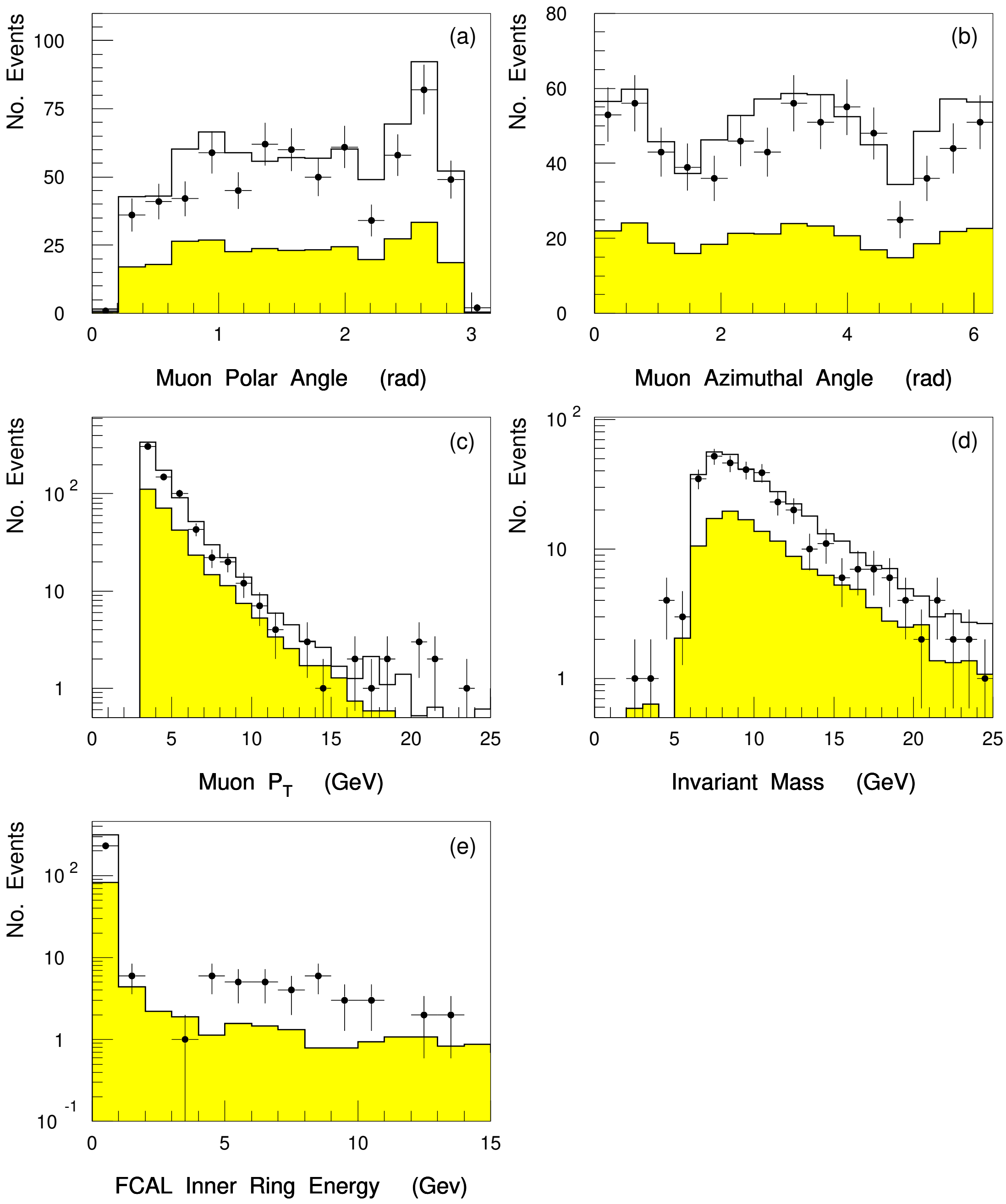

Figure 9.1: *A comparison of data from 1995-97 (points) with luminosity weighted Monte Carlo (open histogram) in the clean di-muon sample. The shaded histogram indicates the contribution from inelastic* $\gamma\gamma \rightarrow \mu^+\mu^-$ *events to the Monte Carlo total.*

Monte Carlo Process	Number of Events
$\gamma\gamma \to \mu^+\mu^-$ (Bethe-Heitler, Elastic)	228
$\gamma\gamma \to \mu^+\mu^-$ (Bethe-Heitler, Inelastic)	152
$\gamma\gamma \to \tau^+\tau^-$ (Bethe-Heitler, Elastic)	0.46
$\gamma\gamma \to \tau^+\tau^-$ (Bethe-Heitler, Inelastic)	0.36
$J/\Psi \to \mu^+\mu^-$ (Elastic)	0.13
$\Upsilon \to \mu^+\mu^-$ (Elastic)	2.30
Total	383
Data	
95-97	341

Table 9.1: *The number of events in the clean di-muon sample expected from Monte Carlo and observed in the 1995-97 data.*

for the data and Monte Carlo, the above selection criteria for elastic di-muon events are modified. Events are now considered that have at least one CTD-MIP-BMU match, exactly two good tracks and a total electromagnetic energy less than 2 GeV. In order to rule out the possibility that cosmic rays are entering this new sample, a tighter cut on the two track opening angle of $\cos\theta_{\mathrm{OPEN}} > -0.95$ is made. Once again, visual scanning removes a few remaining cosmic ray events and confirms the high purity of the sample. The electromagnetic energy cut, now covering the whole calorimeter, removes almost all inelastic events and events where the second track points to the scattered positron. However, due to the difference between the data and Monte Carlo FCAL energy distributions, the resulting number of events is around 40% lower in the data than expected from Monte Carlo.

Events selected in the manner described above, an example of which is shown in fig. 9.2, are in fact $\mu^+\mu^-$ events but with no requirement that more than one muon is identified. The second track is then *assumed* to be a muon and the muon finding efficiency can be calculated from the data by finding the probability that this track forms part of a second CTD-MIP or CTD-MIP-BMU match. Note that this method does not rely on the overall normalisation of the data for an efficiency measurement and is therefore insensitive to possible differences between the data and Monte Carlo that have been alluded to above. However, in order to ensure that the efficiency measurement for the data is not biased with respect to the identically performed Monte Carlo measurement, it is important that the

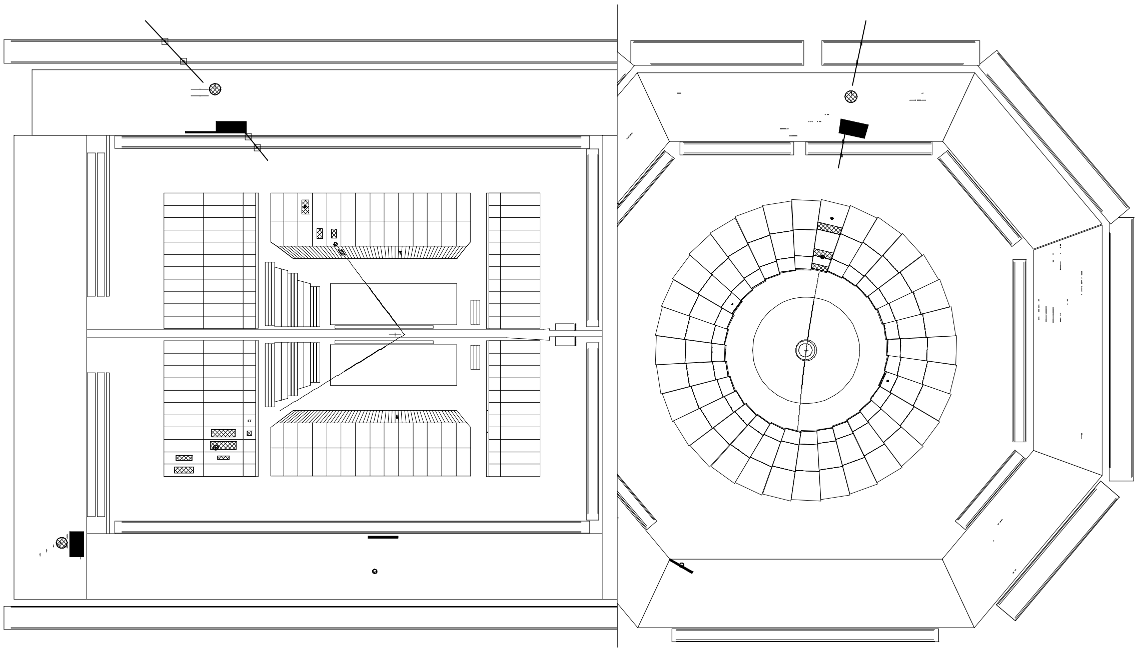

Figure 9.2: *A di-muon event used in the measurement of the muon finding efficiency. The event is selected on the basis of the upper muon, clearly matching a barrel muon chamber segment. In this example the forward going muon, outside the barrel muon acceptance, provides a test of the CTD-MIP match based muon finder in the FCAL region.*

angular and p_T distributions of the muon candidates are in qualitative agreement. This is confirmed in figs. 9.3(a)-(c) in which the muon polar angle and azimuthal angle structures and the steeply falling p_T spectrum are reasonably reproduced by the Monte Carlo.

The results of the efficiency determination are shown in fig. 9.3(d) and (e). The first plot shows the probability that tracks with $p_T > 3$ GeV are matched to an isolated calorimeter MIP for both data and Bethe-Heitler Monte Carlo events, as a function of the polar angle. There is no evidence within the limited data statistics for any deviation of the measured efficiency from the Monte Carlo calculated efficiency. Integrating over all polar angles the CTD-MIP match finding probability is found to be $97.5 \pm 1.1\%$ for the data, in agreement with the 96.3% found for the corresponding Monte Carlo sample. This efficiency is found not to be a strong function of the matching track p_T, giving confidence that the Monte Carlo estimate of the CTD-MIP match finding efficiency for muons from W and Z decay should be accurate.

Fig. 9.3(e) shows the probability that the selected muons match a barrel or rear muon chamber segment in addition to a calorimeter MIP, again for the data and Monte Carlo separately. It can be seen that there is good agreement between the data and Monte Carlo

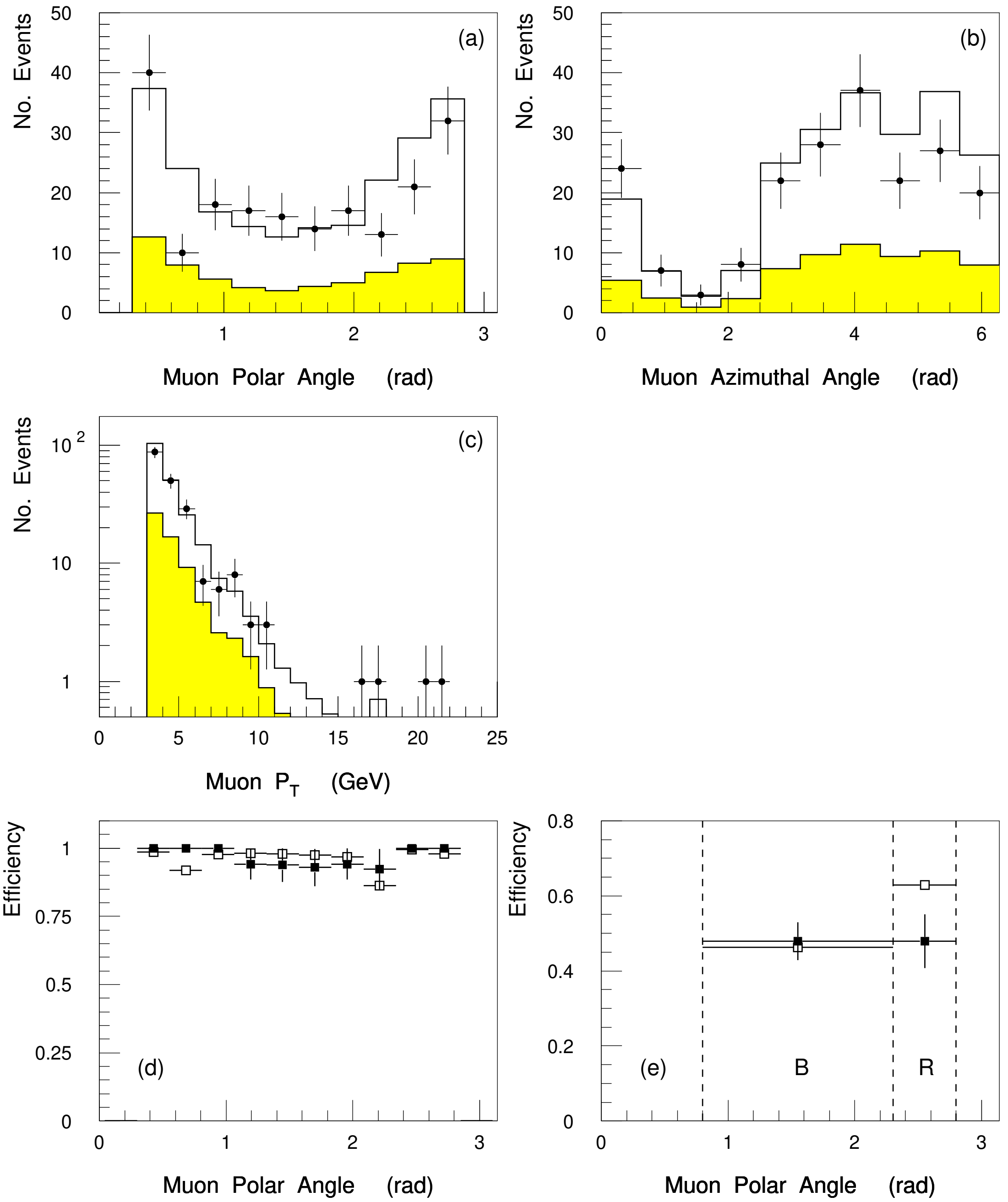

Figure 9.3: *The polar angle (a), azimuthal angle (b) and p_T distributions (c) for data events used in the muon finding efficiency measurement (points) and identically selected Monte Carlo events normalised to the data (open histogram). The shaded histogram is the inelastic Bethe-Heitler contribution to the Monte Carlo total. The resulting CTD-MIP match finding efficiency is plotted versus polar angle for data (closed squares) and Monte Carlo (open squares) in (d) and the CTD-MIP-BMU match finding efficiency in (e). The polar angle coverages of the barrel (B) and rear (R) muon chambers are indicated.*

in the barrel region, with the data efficiency lying somewhat below that calculated from Monte Carlo at larger polar angles, although with poor data statistics. Again integrating over all polar angles, the combined average efficiency is $48 \pm 4\%$ for the data and 53% for the Monte Carlo. There is no evidence, again given the limited statistics, of a p_T dependence of the efficiency deficit in the data.

Harder cuts have been applied to select a suitable sample of events for the measurement of muon finding efficiencies than for the original di-muon sample. It is therefore still possible that, due to discrepancies in the Monte Carlo description of such quantities as track multiplicities and FCAL inner ring energies, the comparison between data and Monte Carlo efficiencies is biased in some way. A simple check that can be made is to compare the number of double to single CTD-MIP-BMU matches for data and Monte Carlo using the original sample of clean di-muon events, the selection of which required only a single such match. Although two CTD-MIP matches were required, the above results indicate that this simpler muon finder is well described by the Monte Carlo. It is found that

$$\textit{Double Match Fraction} = \frac{\#\ \ \textit{Events with 2 CTD-MIP-BMU matches}}{\#\ \ \textit{Tagged}\ \mu^+\mu^-\ \textit{Events}} \tag{9.1}$$

is around 15% lower for the data events than the corresponding Monte Carlo events, again indicating a possible discrepancy between the data and Monte Carlo CTD-MIP-BMU match finding efficiencies. This is consistent with the difference observed in the direct measurement of the efficiency.

In summary, the high efficiency of the CTD-MIP match based muon finder has been confirmed by direct measurement using a sample of clean di-muon events. The data does, however, suggest a discrepancy at large polar angles between the data and Monte Carlo CTD-MIP-BMU match finding efficiencies. Since the comparison is, however, of limited statistical significance the approach adopted here is to take this difference as an indication of the likely systematic uncertainty on the Monte Carlo calculated muon finding efficiency. This systematic uncertainty is important in setting limits on the cross sections for $W \to \mu\nu$ and $Z^0 \to \mu^+\mu^-$ in following sections. With greater luminosity it will be possible to measure the muon finding efficiency using methods such as the above with much greater precision. In particular it should be possible to determine if such a discrepancy, should it persist, can arise from the small number of dead or inefficient muon chamber tubes not included in the Monte Carlo or if some other aspect of the detector understanding and simulation is responsible.

9.2 Transverse Momentum Measurements

9.2.1 Definitions

For events containing one or more muon candidate, a number of different transverse momenta can be calculated that have different interpretations and experimental significance. The four different transverse momenta referred to in subsequent sections are :

- *muon* p_T. The measured p_T of the CTD track that forms part of the CTD-MIP or CTD-MIP-BMU match.
- *calorimeter* p_T. The global transverse momentum using all calorimeter cells. The contribution from the muon is therefore limited to the typically small calorimeter MIP energies that enter the sum. It is this quantity, referred to simply as the missing p_T, that has been used to trigger and select the events in the missing p_T plus lepton samples described in chapter 7.
- *hadronic* p_T. The calorimeter p_T with the MIP contribution subtracted. This quantity is therefore a measure of the p_T of the system recoiling from the high p_T muon [2].
- *net* p_T. This is the transverse momentum calculated by combining the muon and hadronic p_T's, and is therefore an estimator of the missing or neutrino p_T in an event.

It is therefore the azimuthal separation of the muon and net transverse momenta, $\Phi^{\mu\nu}$, that enters the analogous expression to equation 8.1 defining the transverse mass for high p_T muon events and the acoplanarity angle measures how far the muon is from being back-to-back with respect to the hadronic p_T vector in the $\{x, y\}$ plane.

9.2.2 p_T Resolution

Since, even in the case of muon chamber triggered events, a second muon momentum measurement is not required in this analysis, the muon p_T determination relies entirely on the CTD track that forms part of the CTD-MIP or CTD-MIP-BMU match. It is important not only to select high p_T muons but also muon candidates for which the p_T is well measured. This ensures that the relevant kinematic quantities such as the net p_T and transverse mass are also well reconstructed and removes background events with poorly measured low p_T

---

[2] Note that no attempt is made in general to identify and subtract the scattered positron from the hadronic p_T calculation.

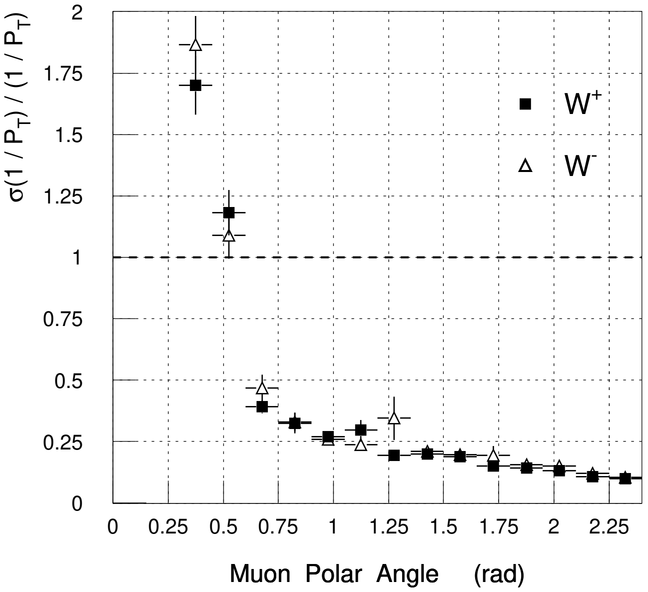

Figure 9.4: *The fractional error on* $1/p_T$ *as a function of polar angle for muon tracks in* $W^+ \to \mu^+\nu_\mu$ *(squares) and* $W^- \to \mu^-\bar{\nu}_\mu$ *(triangles) Monte Carlo events. The condition for the muon track to be well measured in the CTD is indicated by the dashed horizontal line.*

muons. The explicit requirement made is that :

$$\frac{\sigma(1/p_T)}{(1/p_T)} < 1 \ , \tag{9.2}$$

where $\sigma(1/p_T)$, introduced in section 8.1.1, is derived from the error on the track sagitta measured in the CTD. This is a comparatively weak constraint on the track quality, ensuring that the $1\,\sigma$ p_T interval extends downwards to values for the track p_T no smaller than half the measured central value. Inequality 9.2 also coincides with the requirement that a $1\,\sigma$ determination of the track charge is made, a quantity clearly of interest in the search for W production and decay $W \to \mu\nu$.

Despite the fact that condition 9.2 represents a fairly mild constraint on the quality of the MIP matching track it nevertheless represents an important acceptance limitation, particularly in the analysis of muons in events with missing p_T. From fig. 9.4, where the fractional error on $1/p_T$ is plotted for muon tracks in $W^+ \to \mu^+\nu_\mu$ and $W^- \to \mu^-\bar{\nu}_\mu$ Monte Carlo events separately, it can be seen that it in fact corresponds to an implicit cut on the polar angle of the muon at around 30°. This can clearly be substantially improved upon in the future when the full forward tracking information is available in the global track fit.

Finally, in order to understand the effect of cut 9.2 on the efficiency for selecting high

p_T muon events, the true CTD momentum resolution must be well produced by the Monte Carlo. This is addressed in more detail in section 9.3.1 dealing with systematic uncertainties.

9.3 Muons in Events with Missing p_T

The preselection of events with a CTD-MIP muon candidate in addition to missing p_T is described in chapter 7. The sample is subsequently visually scanned to remove some remaining cosmic ray background events and a small number of proton beam gas like events at low missing p_T.

In figures 9.5 and 9.6 the 1994-96 data is compared to the combined luminosity weighted Monte Carlo samples described in section 8.1. The first requirement in the search for W production and decay $W \to \mu\nu$ is that the muon candidate is relatively forward and a cut of $\theta^{\mu} < 2.0$ rad removes a fraction of the 2-photon background at large polar angles. It can be seen from fig. 9.5 that there is a slight excess of data over the Monte Carlo, mainly apparent at low calorimeter and net transverse momenta. The excess is probably due to relatively low E_T photoproduction events that are not included in the $E_T > 28$ GeV Monte Carlo sample. This is consistent with the excess at small acoplanarity angles visible in fig. 9.6(b) and the results of visually scanning the sample. Requiring a momentum imbalance $p_T^{net} > 10$ GeV improves the agreement between the data and Monte Carlo while only reducing the efficiency for selecting $W \to \mu\nu$ events by around 1%.

The acoplanarity angle distribution, plotted in fig. 9.6(b), is almost flat for the W production signal. Unlike the electron channel, however, the background is not strongly peaked at small acoplanarity angles. This is because a major background even in the single muon sample is from inelastic $\mu^+\mu^-$ production which, due to the presence of a second muon, does not display the same azimuthal correlation between the lepton and hadron transverse momenta that is characteristic of neutral current scattering. A cut on the acoplanarity angle is therefore not applied here.

In fig. 9.6(c) and (d) the cuts $\theta^{\mu} < 2.0$ rad and $p_T^{net} > 10$ GeV have already been applied. It can be seen that with respect to fig. 9.5(c) a large fraction of the high p_T muon background has already been removed. The signal to background ratio is enhanced by requiring finally that :

1. $p_T^{net} > 15$ GeV ,
2. $p_T^{\mu} > 15$ GeV .

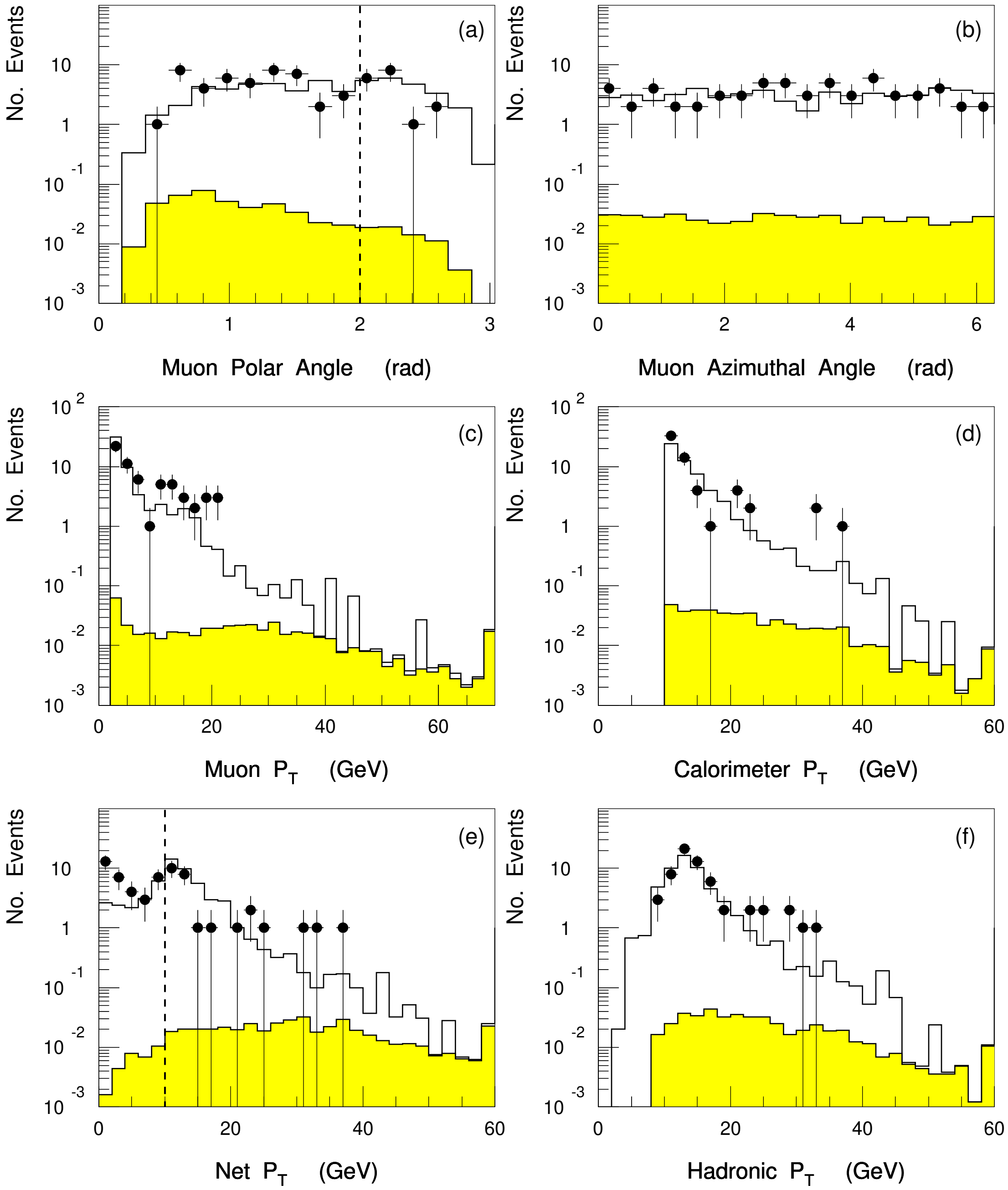

Figure 9.5: *A comparison of the preselected 1994-96 missing p_T plus muon data (points) with combined Monte Carlo (solid histogram). The W component of the Monte Carlo is given by the shaded histogram. The dashed lines in (a) and (e) indicate cuts made in the search for $W \to \mu\nu$.*

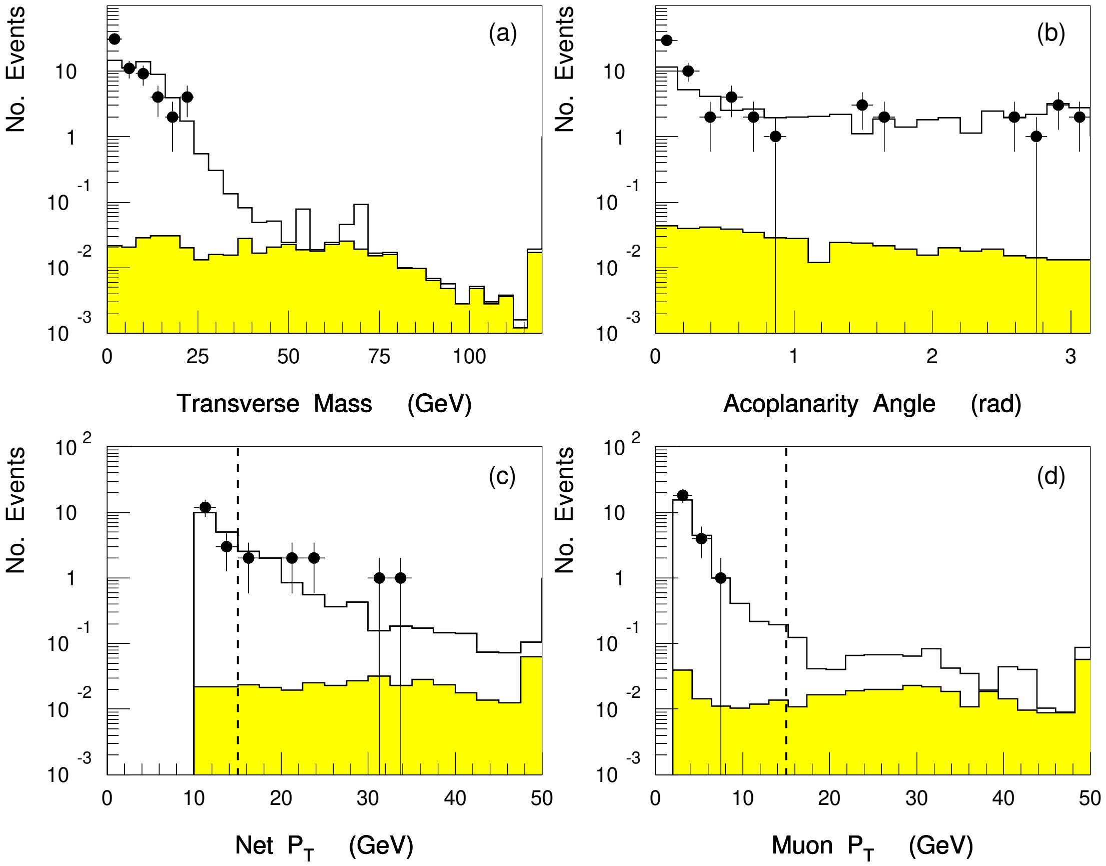

Figure 9.6: *A comparison of the 1994-96 missing p_T plus muon data (points) with combined Monte Carlo (solid histogram). The W component of the Monte Carlo is given by the shaded histogram. In plots (c) and (d) the cuts* $\theta^\mu < 2.0$ rad *and* $p_T^{net} > 10$ GeV *have already been applied.*

The number of events expected and observed at each stage of the selection is summarised in table 9.2 and the resulting efficiency is broken down by W production channel in table 9.3.

It is clear that we are only sensitive to DIS type W production when searching in the muon plus missing p_T sample, which is a direct consequence of the soft hadronic p_T spectrum for photoproduction type W production (c.f. fig. 4.3). Only if the struck quark has a large transverse momentum can the event have a large enough calorimeter p_T imbalance to be selected. This is discussed further in chapter 11. The difference between the W^+ and W^- selection efficiencies is also more striking than in the electron channel, reflecting the poorer acceptance at small polar angles due to the track momentum resolution requirement.

Background Process	**Cut**				
	Preselection	$\theta^\mu <$ 2.0 rad	$p_T^{net} >$ 10 GeV	$p_T^{net} >$ 15 GeV	$p_T^{\mu} >$ 15 GeV
$e^+p \rightarrow e^+X$ (NC DIS)	10.5	7.2	3.0	0.68	< 0.06
$e^+p \rightarrow \bar{\nu}X$ (CC DIS)	9.0	6.7	6.4	4.3	0.04
γp (Direct)	4.0	3.1	1.8	0.18	< 0.21
γp (Resolved)	3.6	3.0	1.8	0.6	< 0.7
$\gamma\gamma \rightarrow e^+e^-$ (Elastic)	< 0.08	< 0.08	< 0.08	< 0.08	< 0.08
$\gamma\gamma \rightarrow e^+e^-$ (Inelastic)	0.12	< 0.14	< 0.14	< 0.14	< 0.14
$\gamma\gamma \rightarrow \mu^+\mu^-$ (Elastic)	2.5	2.1	0.08	0.03	< 0.03
$\gamma\gamma \rightarrow \mu^+\mu^-$ (Inelastic)	23.3	11.1	8.5	1.5	0.20
$\gamma\gamma \rightarrow \tau^+\tau^-$ (Elastic)	0.39	0.39	0.14	0.04	< 0.04
$\gamma\gamma \rightarrow \tau^+\tau^-$ (Inelastic)	1.7	0.98	0.53	0.12	< 0.03
$e^+p \rightarrow e^+Z^0X$	0.06	0.05	0.04	0.03	0.02
Signal Process					
$W \rightarrow \mu\nu$ (Efficiency)	0.35 (17%)	0.32 (16%)	0.30 (15%)	0.28 (14%)	0.26 (12%)
$W \rightarrow \tau\nu$	0.10	0.08	0.08	0.06	0.02
Other Channels	0.04	0.02	0.02	0.02	0.
Total	55.6	35.0	22.7	7.82	0.54
Data					
94-96	61	45	23	8	0

Table 9.2: *The number of events expected from Monte Carlo compared with the 1994-96 data in the analysis of events with missing p_T and a high p_T muon. See text for more details of the cuts.*

Production Channel	W^+ DIS	W^- DIS	W^+ PHP	W^- PHP	Combined
Efficiency	21.3 ± 0.9 %	9.9 ± 0.6 %	0 %	0 %	12.0 ± 0.5 %

Table 9.3: *The efficiency for selecting $W \rightarrow \mu\nu$ events in the different W production channels in the analysis of events with missing p_T and a high p_T muon, calculated using the 1995 Monte Carlo detector configuration. The combined value assumes the mixture of deep inelastic and photoproduction type W production given in chapter 4. Statistical errors only are given.*

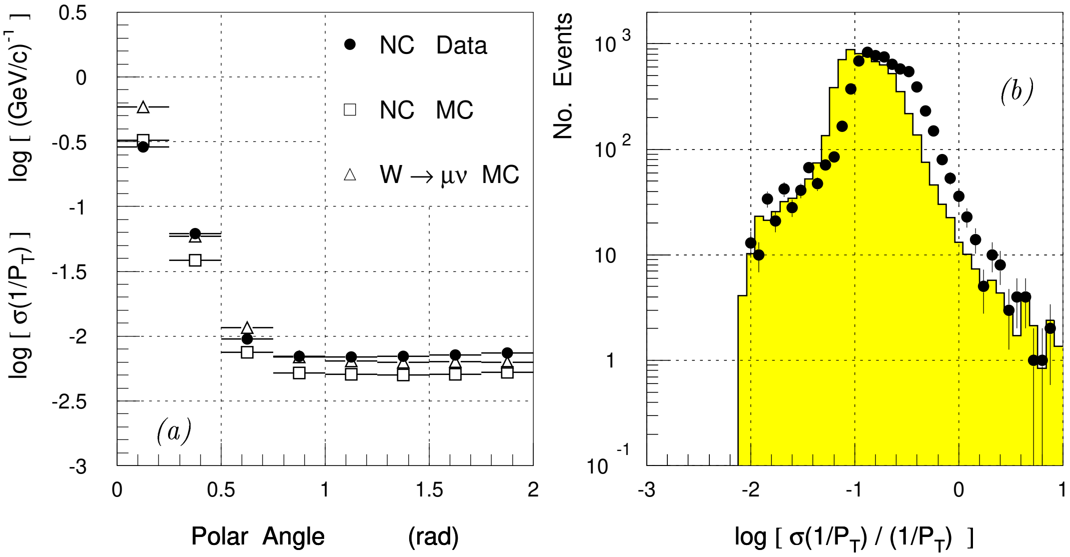

Figure 9.7: *(a) A comparison of the average track momentum resolution at different polar angles for neutral current data and Monte Carlo and $W \to \mu\nu$ Monte Carlo events. The fractional resolution is plotted in (b) for the neutral current data (points) and Monte Carlo (shaded histogram).*

9.3.1 Systematic Uncertainties in the Selection Efficiency

Momentum Resolution Requirement

As mentioned in section 9.2.2, the requirement that the fractional error on $1/p_T$ for the MIP matching track is less than 1 is the most important cut in this analysis. The track momentum resolution has already been checked in the context of systematic uncertainties in the efficiency for selecting $W \to e\nu$ events (see section 8.1.4) and was found to be some 40% higher on average in the data than Monte Carlo. In order to confirm this at the smallest possible polar angles a similar comparison is made for tracks that match electron candidates in the 1997 high E_T neutral current control sample described in section 10.1. In fig. 9.7(a) the mean value of $\sigma(1/p_T)$ is plotted for this sample as a function of the electron polar angle, indicating a systematic shift of the neutral current data with respect to the Monte Carlo that is relatively constant at around 0.15-0.20 in $\log(\sigma)$. Also plotted is the track resolution for muons in $W \to \mu\nu$ events, which is poorer on average than that for electrons in NC Monte Carlo events but within this systematic band. In fig. 9.7(b) the fractional resolution is plotted for the same tracks in the neutral current data and Monte Carlo. The shift in the mean value also corresponds to a 40% poorer resolution in the data which, applied to the W production Monte Carlo, gives rise to a 5% systematic uncertainty in the selection efficiency for $W \to \mu\nu$ events.

Muon Finding Algorithm

The difference between the data and Monte Carlo measured CTD-MIP match finding efficiencies is at most 2%, given the size of the statistical error on the measurement presented in section 9.1. This is used here as an estimate of the systematic error on the CTD-MIP matching efficiency calculated for $W \to \mu\nu$ Monte Carlo events.

Trigger

In the search for $W \to e\nu$ events with a final missing p_T cut of 20 GeV, the conditional trigger efficiency (that is, the Monte Carlo calculated probability that an event passes the trigger selection given that it passes all other cuts) was found to be around 99%. That the missing p_T trigger is fully efficient in this region was confirmed using the high E_T neutral current control sample. However, a calorimeter p_T cut of only 10 GeV is much closer to the turn on curve visible in fig. 8.8(e) and the conditional trigger efficiency for $p_T > 10$ GeV and $p_T[-1\text{ir}] > 9$ GeV calculated from W production Monte Carlo is 97.5%. Referring once again to the 1997 neutral current control sample the data and Monte Carlo efficiencies for the same offline reconstructed p_T cuts are 96% and 99% respectively. The 3% difference between data and Monte Carlo is used here as an estimate of the uncertainty on the trigger efficiency for selecting W production events with the same calorimeter p_T [3].

Calorimeter Scale Uncertainty

As discussed in section 8.1.4, varying the calorimeter energy scale by ±5% before the calculation of all calorimeter level quantities and before both electromagnetic cluster and MIP identification gives an estimate of the systematic uncertainty arising from the knowledge of the absolute energy scale of the calorimeter. Since the calorimeter p_T distribution is steeply falling in the vicinity of the $p_T > 10$ GeV cut this results in a slightly larger uncertainty in the selection efficiency, around 4%, compared to the electron channel.

Combined

Combining these sources of error in quadrature gives an overall systematic uncertainty in the efficiency for selecting $W \to \mu\nu$ events of around 7%. This is comparable to the error on the efficiency for selecting $W \to e\nu$ events, due to the smaller intrinsic lepton

---

[3] This is a conservative estimate of the error since the missing p_T distribution is more steeply falling in the case of neutral current DIS than W production and decay $W \to \mu\nu$.

finding uncertainty being combined with much larger errors resulting from the CTD track measurement and trigger thresholds.

9.3.2 Error on the Background Estimate

The error on the background estimate is dominated by the Monte Carlo statistical errors which, added in quadrature, give an overall 30% fractional error on the mean value of 0.26 events. Remaining systematic uncertainties are assumed to be small in comparison. Note that since all the neutral current Monte Carlo events that pass the cuts prior to the final cut on the muon p_T are at high Q^2, for which large luminosity Monte Carlo samples are available, the constraint on this contribution to the background is at the level of only 0.06 events.

9.3.3 Cross Section Upper Limit

Taking the above background and efficiency estimates and corresponding uncertainties, together with the 2% error on the integrated luminosity quoted in section 8.1.6, an upper limit can be placed on the cross section for W production and decay $W \to \mu\nu$:

$$\sigma(e^+p \to e^+W^\pm X) \ \times \ BR(W \to \mu\nu) \quad <_{95\%} \quad 1.2 \ \text{ pb} \ . \tag{9.3}$$

Assuming a value for the branching ratio of 10.8% and taking into account the small extra sensitivity due to $W \to \tau\nu$ decays gives an upper limit on the W production cross section of 10.3 pb at 95% confidence.

Clearly this upper limit is poorer than that obtained in the electron channel due to the lower overall selection efficiency. More importantly, the value for the efficiency obtained for W production in the presence of anomalous $WW\gamma$ couplings will be quite different to the Standard Model value, reflecting the fact that the selection of events with a high p_T muon and missing calorimeter p_T requires a large hadronic or struck quark transverse momentum. Therefore the upper limit quoted here cannot be translated directly into constraints on $\Delta\kappa$ and λ. Moreover the values for the calculated efficiencies even in the Standard Model case rely on the correct Monte Carlo parameterisation of the hadronic p_T spectrum. These issues are looked at in more detail in the analysis of the results in chapter 11.

9.4 Barrel and Rear Muon Events

Events containing only a CTD-MIP-BMU match with the default matching track p_T cut of 2 GeV can have small net transverse energies or E_T's. There is no hard cut, such as that required in the previous analysis that the calorimeter p_T be greater than 10 GeV, to define a high E_T scale. The data is therefore compared to the high E_T Monte Carlo after further preselection cuts on the muon and net p_T :

1. $p_T^\mu > 5$ GeV ,
2. $p_T^{net} > 5$ GeV ,
3. $\theta^\mu < 2$ rad ,
4. FCAL inner ring energy > 1 GeV .

The resulting angular and p_T distributions are plotted in fig. 9.8 where, in fig. 9.8(a), the tighter angular cut has not been made. The small excess of data at larger polar angles is again composed mainly of events with low E_T and low Q^2 neutral current events and, in fig. 9.8(b), the gap in the muon chamber coverage in the negative y direction is clearly visible. The cut on the FCAL inner ring energy suppresses the contribution from elastic di-muon processes that are not of interest here [4]. After these three preselection cuts the data and the combined, luminosity weighted Monte Carlo sample are in good agreement. Within the limited statistics the shapes of the four p_T distributions seem to be well reproduced by the Monte Carlo, dominated by inelastic $\mu^+\mu^-$ production. Figure 9.9 compares the transverse mass, acoplanarity angle and FCAL inner ring energy for the same data and Monte Carlo. As was found in the analysis of muons in events with missing p_T the background to $W \to \mu\nu$ has a rather flat acoplanarity angle distribution and no cut is made on this quantity. However, an excess in the data at small acoplanarity angles that persists in the 1997 data is already visible and is discussed further in section 10.5.2.

It can be seen in fig. 9.8(c) and (e) that the W production signal is well separated from the background at large muon and net transverse momenta, reflected also in the high transverse mass end of the spectrum. The signal distribution is much more like that of the background in the calorimeter and hadronic p_T distributions which, unlike in the previous

---

[4] In the search for Z production, where a significant fraction of the cross section is elastic or quasi-elastic, such a requirement cannot be made. The smaller cross section W production process $e^+p \to \bar{\nu}\ W^+X$ also has elastic ($X = p$) and quasi-elastic contributions but is not considered here.

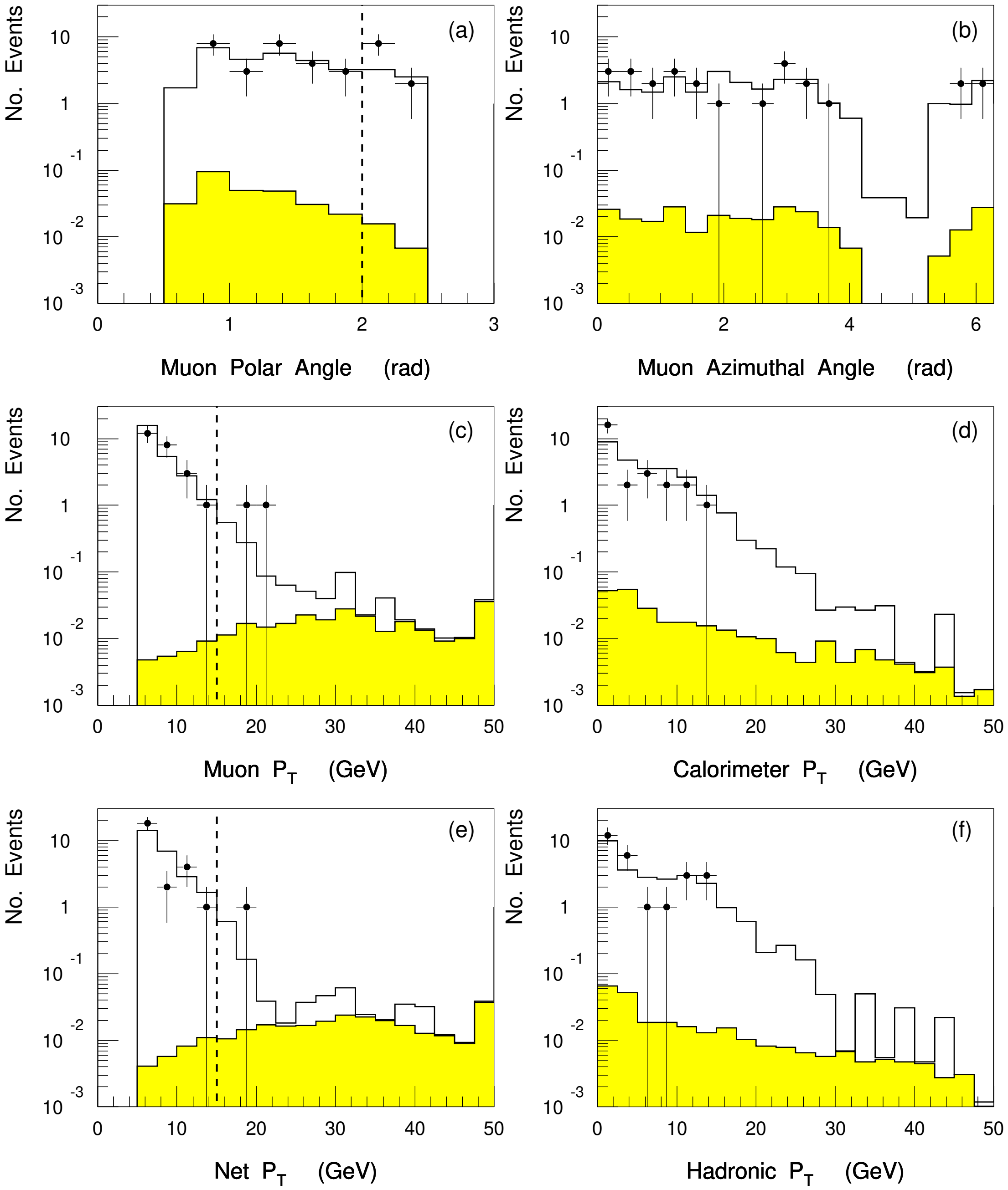

Figure 9.8: *A comparison of the preselected 1995-96 barrel muon data (points) with combined Monte Carlo (solid histogram). The W component of the Monte Carlo is given by the shaded histogram. Plots (b) to (f) are for* $\theta^{\mu} < 2.0$ rad *and the dashed lines in (c) and (e) indicate cuts made in the search for* $W \rightarrow \mu\nu$.

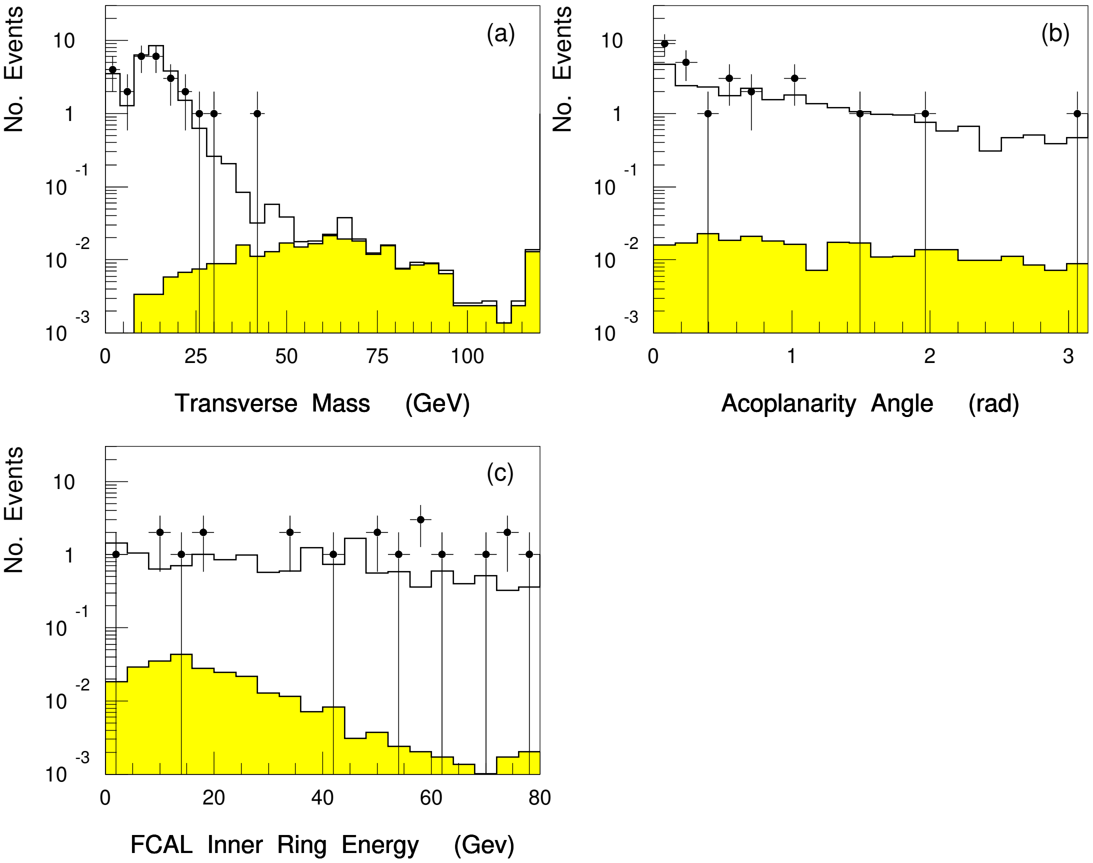

Figure 9.9: *A comparison of the 1995-96 barrel muon data (points) with combined Monte Carlo (solid histogram). The W component of the Monte Carlo is given by the shaded histogram.*

analysis, do not need to be cut on here. The final cuts in the analysis of barrel muon chamber triggered events, indicated by the dashed lines in fig. 9.8, are therefore :

1. $p_T^{\mu} > 15$ GeV ,
2. $p_T^{net} > 15$ GeV .

The numbers of events surviving after each cut in the data and Monte Carlo are compared in table 9.4 and the selection efficiencies summarised in table 9.5. With small numbers of expected events and in the context of setting upper limits on the W production cross section it is important to maintain as high a signal selection efficiency as possible. As a consequence the expected signal to background ratio is somewhat less than one with the above cuts, although with a substantial error on the background estimate (see below). With a larger data sample it would clearly be desirable to tighten the cuts. For example, with cuts on the muon and net p_T of 25 GeV the background is expected to be present at the level of just 10% with a selection efficiency of $\sim 9\%$.

The single surviving event is shown in fig. 9.10. A muon is clearly visible at a polar angle of 106° closely matching a track segment reconstructed in the barrel muon chambers. The muon p_T and the transverse mass for the event are :

$$p_T^{\mu} \;=\; 21.8\,^{+5.6}_{-3.7}\ \text{GeV} \quad ; \quad M_T \;=\; 41.3\,^{+11.1}_{-7.4}\ \text{GeV}\ ,$$

where the error on the transverse mass reflects the error on the measured track p_T only. The event is probably an example of inelastic $\mu^+\mu^-$ production in which the second muon, produced at a shallow polar angle, is not well isolated from the hadrons in the event. The presence of a single track besides that forming the muon candidate supports this hypothesis. The numbers in table 9.4 also indicate that this type of event forms the dominant background to $W \to \mu\nu$ with the cuts described here.

9.4.1 Systematic Uncertainties in the Selection Efficiency

Momentum Resolution Requirement

By virtue of the barrel muon chamber angular acceptance the tracks that form muon candidates in the barrel muon sample are more central and therefore better measured in the CTD. In fact, varying the track momentum resolution by the amount given in section 9.3.1 gives rise to only a 1% fractional systematic error on the selection efficiency.

Muon Finding Algorithm

The 10% difference between the data and Monte Carlo direct measurements of the CTD-MIP-BMU match finding efficiency is taken here as an indication of the systematic uncertainty in the efficiency for identifying muons in $W \to \mu\nu$ events in the barrel muon chamber sample.

Trigger

The missing p_T trigger was tested by making use of the fact that a subset of the events are triggered independently on the basis of large total E_T's. In addition the properties of these neutral current events are known to be generally well described by existing Monte Carlo simulations. Unfortunately a comparable sample of independently triggered muon events does not yet exist.

Background Process	**Cut**		
	Preselection	$p_T^\mu > 15$ GeV	$p_T^{net} > 15$ GeV
$e^+p \to e^+X$ (NC DIS)	2.8	< 0.3	< 0.3
$e^+p \to \bar{\nu}X$ (CC DIS)	0.07	0.05	0.05
γp (Direct)	1.4	< 0.2	< 0.2
γp (Resolved)	< 0.6	< 0.6	< 0.6
$\gamma\gamma \to e^+e^-$ (Elastic)	< 0.07	< 0.07	< 0.07
$\gamma\gamma \to e^+e^-$ (Inelastic)	< 0.1	< 0.1	< 0.1
$\gamma\gamma \to \mu^+\mu^-$ (Elastic)	0.71	0.09	0.07
$\gamma\gamma \to \mu^+\mu^-$ (Inelastic)	21.0	0.90	0.24
$\gamma\gamma \to \tau^+\tau^-$ (Elastic)	0.06	< 0.03	< 0.03
$\gamma\gamma \to \tau^+\tau^-$ (Inelastic)	0.12	< 0.03	< 0.02
$e^+p \to e^+Z^0X$	0.02	0.02	0.02
Signal Process			
$W \to \mu\nu$ (Efficiency)	0.25 (14%)	0.24 (13%)	0.23 (13%)
$W \to \tau\nu$	0.04	0.02	0.01
Other Channels	0.	0.	0.
Total	26.5	1.3	0.62
Data			
95-96	26	2	1

Table 9.4: *The number of events expected from Monte Carlo compared with the 1995-96 data in the analysis of barrel muon triggered events. See text for more details of the cuts.*

Production Channel	W^+ DIS	W^- DIS	W^+ PHP	W^- PHP	Combined
Efficiency	16.2 ± 0.8 %	7.1 ± 0.6 %	16.6 ± 0.8 %	7.4 ± 0.6 %	12.5 ± 0.5 %

Table 9.5: *The efficiency for selecting $W \to \mu\nu$ events in the different W production channels in the analysis of barrel muon triggered events, calculated using the 1995 Monte Carlo detector configuration. The combined value assumes the mixture of deep inelastic and photoproduction type W production given in chapter 4. Statistical errors only are given.*

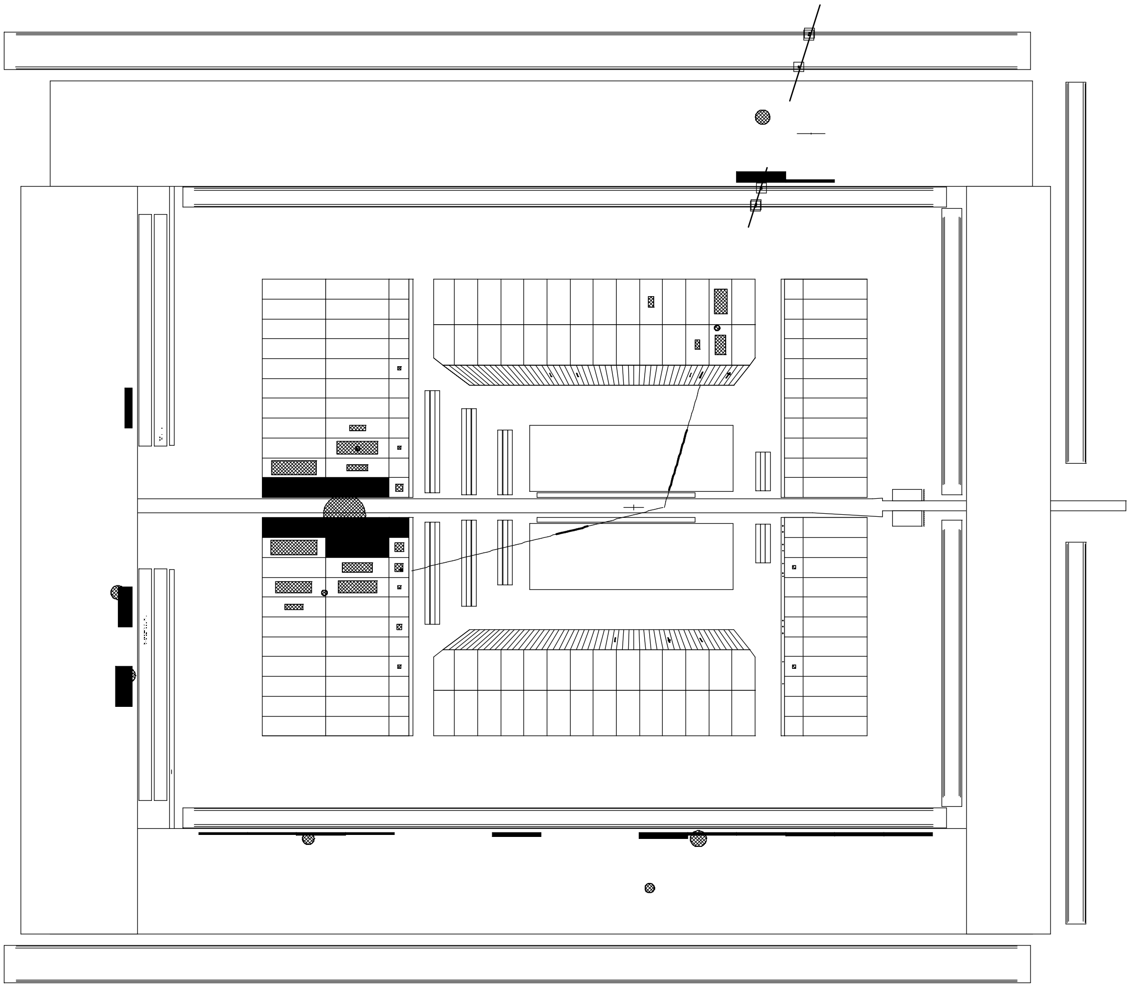

Figure 9.10: *The single surviving event in the missing p_T plus muon selection. The muon transverse momentum is* $21.8^{+5.6}_{-3.7}$ GeV *and the transverse mass is* $41.3^{+11.1}_{-7.4}$ GeV*.*

It is expected that the dominant contribution to any discrepancy between the muon trigger efficiency for the data and Monte Carlo will be due to dead or inefficient limited streamer tubes (LST's) that are not correctly treated in the Monte Carlo. As mentioned above, the routine [87] has been used here to simulate this effect, resulting in changes to the overall trigger efficiency for single muon processes such as $W \to \mu\nu$ at the level of 10%. Since at least part of the dead LST map is dynamic in nature and therefore the correction only approximate, this 10% variation in the trigger efficiency is taken here to be an estimate in addition of the systematic error on the corrected trigger efficiency.

Calorimeter Scale Uncertainty

Since almost all the cuts in the analysis of muon chamber triggered events are made on the basis of CTD track calculated quantities, the efficiency for selecting $W \to \mu\nu$ events is largely insensitive to the calorimeter energy scale. Varying the scale by the usual ±5% gives rise to only a 1% fractional variation in this efficiency.

Combined

The above sources of error, dominated by the trigger and muon finding uncertainties, combine to give an overall 14% error on the Monte Carlo calculated efficiency for selecting $W \to \mu\nu$ events in the barrel muon sample. This is around twice the value for the uncertainties that have been estimated for the $W \to e\nu$ and $W \to \mu\nu$ selection efficiencies in the calorimeter missing p_T samples. It was stressed above that the comparison of the di-muon data to Monte Carlo is rather statistically limited at present and given the current integrated luminosity there are few events with muon transverse momenta of the same order as that expected from W and Z decay. This is clearly one area where greater statistics will in future further constrain existing systematic uncertainties.

9.4.2 Error on the Background Estimate

Adding in quadrature the statistical errors on the charged current and di-muon background contributions gives an overall uncertainty on the background estimate of 25%, comparable with that in other search channels. Since no resolved photoproduction events pass even the preselection and no direct photoproduction or neutral current Monte Carlo events pass the penultimate hard p_T cut, the contributions from these sources are assumed here to be negligible.

9.4.3 Cross Section Upper Limit

Calculating an upper limit in the usual way, taking into account the contribution to the sensitivity from $W \to \tau\nu$ decays, gives an overall upper limit on the W production cross section of 18 pb. This is a poorer constraint than that obtained in the analysis of muons in events with missing p_T due to the single observed event and slightly lower integrated luminosity. The selection efficiencies and background estimates are, however, very similar for the two analyses. Moreover, the barrel muon selection is less sensitive to assumptions about the hadronic p_T spectrum for the process $e^+p \to e^+W^\pm X$. The overlap of the two $W \to \mu\nu$ searches and different sensitivities to anomalous W production are briefly discussed in chapter 11.

9.5 Multi-Muon Events

In addition to the analysis of events with a single high p_T muon candidate, events are searched for in the barrel and rear muon chamber sample that have two or more muon candidates. Although a muon candidate here means a CTD-MIP match, at least one of the muon candidates must in addition match a barrel muon segment. As discussed in section 9.4, a comparison of the data with high transverse energy Monte Carlo samples requires a hard p_T cut of some kind. Events are therefore considered in this section that have at least two candidates with $p_T^{\mu} > 5$ GeV, where the usual track momentum resolution requirement is made. The resulting comparison between data and Monte Carlo is shown in fig. 9.11, in which the various angular and transverse momentum distributions are plotted. In addition the invariant mass distribution is shown in fig. 9.11(g) and the FCAL inner ring energy, showing a large 'elastic' peak in the first bin, is plotted in fig. 9.11(h). Good agreement between the data and Monte Carlo is evident in all the distributions and it is clear that only in the muon p_T and invariant mass distributions is the $Z^0 \to \mu^+\mu^-$ signal, depicted by the shaded histogram, well separated from the predominant background from Bethe-Heitler $\mu^+\mu^-$ production. There is also a clear elastic peak in the signal, which is discussed further in the next section.

9.5.1 Selecting $Z^0 \to \mu^+\mu^-$ Events

In light of the above comparison of the data with the Monte Carlo, simple cuts are used to enhance the sensitivity to Z production and decay $Z^0 \to \mu^+\mu^-$:

1. p_T (two muons) > 20 GeV ,
2. Invariant Mass > 50 GeV ,

where the first requirement looks for any pair of muons satisfying this condition [5]. The resulting expected and observed numbers of events are summarised in table 9.6 and the final efficiencies in the different Z production channels in table 9.7. Note that the efficiencies considerably favour the elastic and quasi-elastic channels, due partly to the different angular distributions for the muons in these channels (see section 4.2.2) and partly to the enhanced muon finding efficiencies in the absence of final state hadrons in the central detector. The result is that the number of events at low FCAL inner ring energies visible in fig. 9.11(h) is

---

[5] In fact in the 1995-96 barrel and rear muon chamber sample there are no events with more than two high p_T muons.

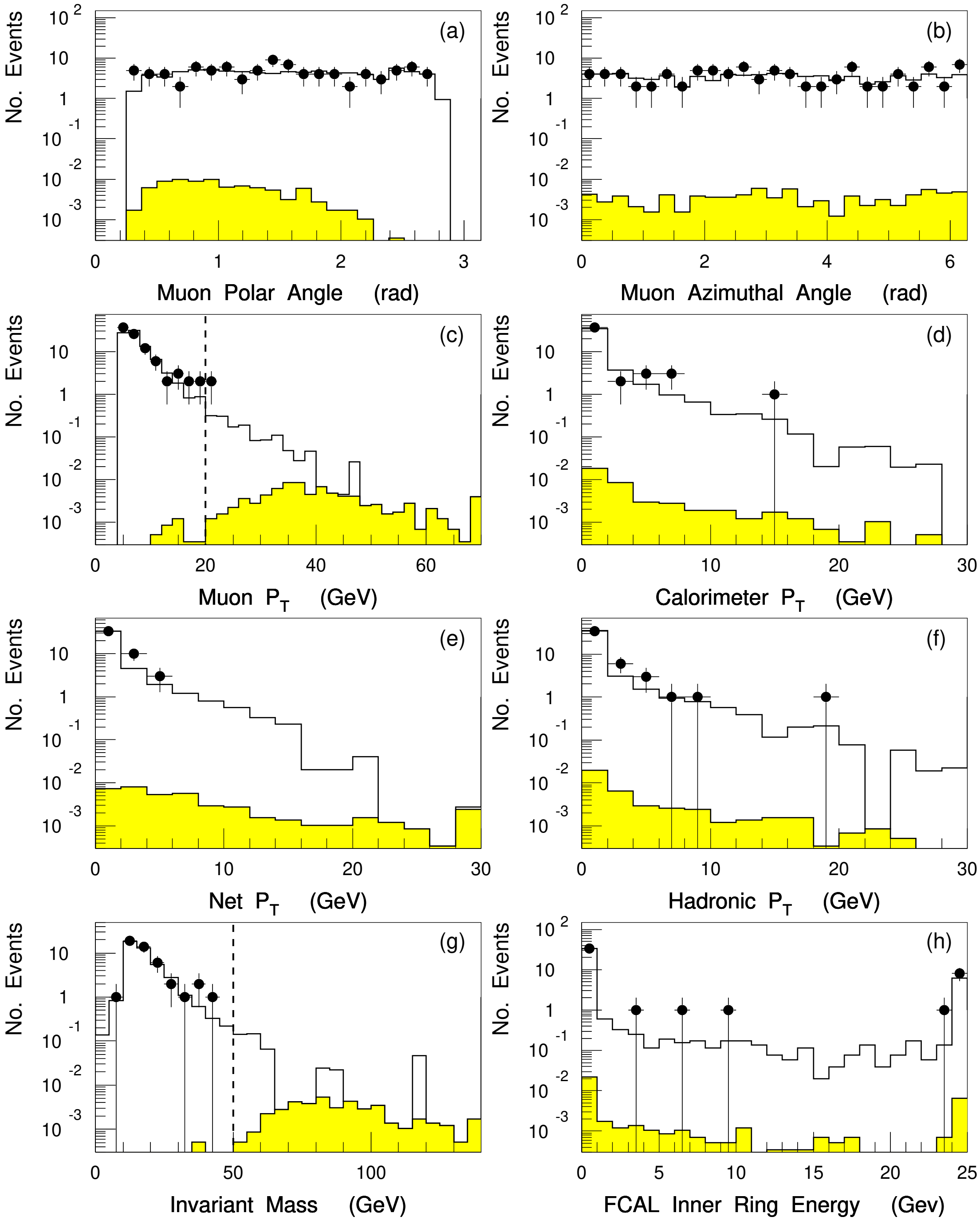

Figure 9.11: *A comparison of the 1995-96 di-muon data (points) with combined Monte Carlo (solid histogram). The Z component of the Monte Carlo is given by the shaded histogram and cuts in the selection of* $Z^0 \to \mu^+\mu^-$ *candidate events are given by the dashed lines in (c) and (g).*

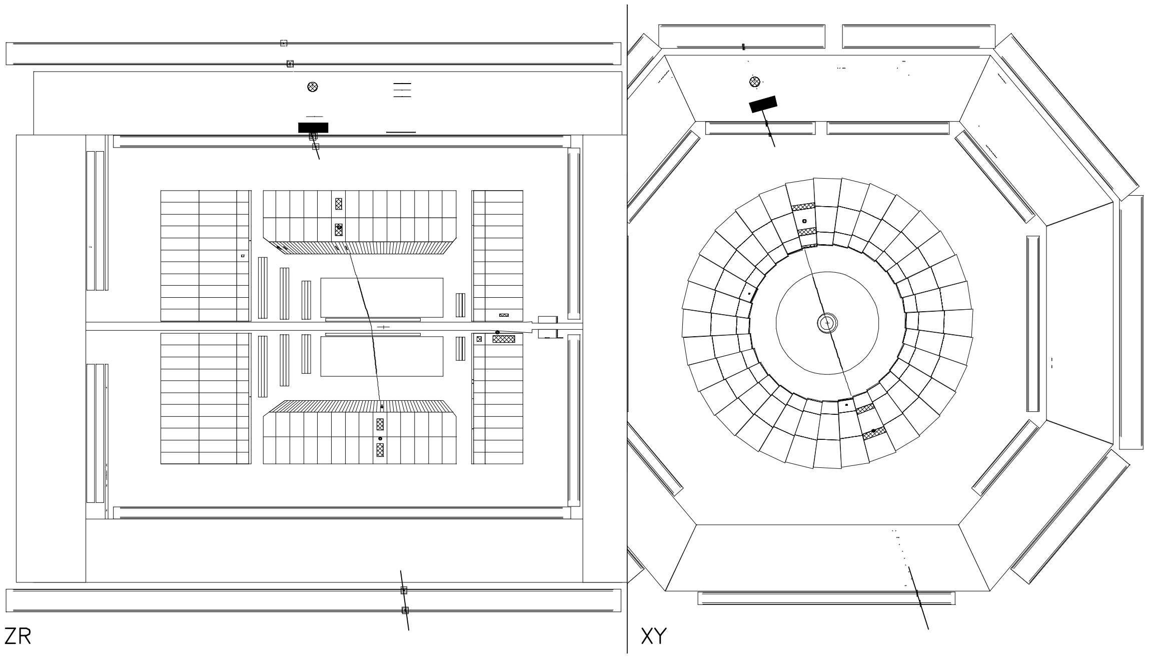

Figure 9.12: *The highest mass di-muon event in the 1995-96 barrel and rear muon chamber sample. The invariant mass is* 41^{+10}_{-7} GeV *and the muon pair has an opening angle of around* 170°. *See text for more details.*

greater than expected from the ratio of cross sections in the different production channels and in particular the signal to background ratio is not greatly enhanced by selecting either elastic or inelastic detector level events. The final selection efficiency of 21% is around twice the corresponding efficiency for selecting $W \to \mu\nu$ events due to the different muon polar angle distribution and the fact that either muon from Z decay in the barrel muon chamber acceptance region can trigger the event.

The single event surviving after the p_T^μ cut is the highest invariant mass di-muon event in 1995-96 and is shown in fig. 9.12. The two clearly visible muons, each of around 20 GeV p_T, combine to give an invariant mass of 41^{+10}_{-7} GeV. The opposite muon charges are determined with a significance of around 7σ each. The opening angle of the two muons, at around 170°, is sufficiently far from being back-to-back for muons of this p_T to rule out the possibility that the event is a cosmic ray muon.

9.5.2 Systematic Uncertainties in the Selection Efficiency

Momentum Resolution Requirement

Since one of the muons in the di-muon sample need not be confined to the angular

Background Process	**Cut**		
	Preselection	$p_T^\mu > 20$ GeV	Invariant Mass > 50 GeV
$\gamma\gamma \to \mu^+\mu^-$ (Elastic)	23.4	0.22	0.16
$\gamma\gamma \to \mu^+\mu^-$ (Inelastic)	19.7	0.19	0.12
$\gamma\gamma \to \tau^+\tau^-$ (Elastic)	0.03	< 0.03	< 0.03
$\gamma\gamma \to \tau^+\tau^-$ (Inelastic)	< 0.02	< 0.02	< 0.02
$J/\Psi \to \mu^+\mu^-$ (Elastic)	0.	0.	0.
$\Upsilon \to \mu^+\mu^-$ (Elastic)	0.02	0.	0.
Other (DIS, γp)	0.	0.	0.
Signal Process			
$Z^0 \to \mu^+\mu^-$ (Efficiency)	0.043 (22%)	0.040 (21%)	0.040 (21%)
$Z^0 \to \tau^+\tau^-$	0.	0.	0.
Other Channels	0.	0.	0.
Total	43.2	0.45	0.31
Data			
95-96	46	1	0

Table 9.6: *The numbers of events in the 1995-96 di-muon sample and after the cuts in the search for* $Z^0 \to \mu^+\mu^-$.

Production Channel	DIS	Elastic	Quasi-elastic	PHP	Combined
Efficiency	10 ± 1 %	36 ± 2 %	35 ± 2 %	9 ± 1 %	21 ± 1 %

Table 9.7: *The efficiency for selecting* $Z^0 \to \mu^+\mu^-$ *events in the different Z production channels in the analysis of di-muon events, calculated using the 1995 Monte Carlo detector configuration. The combined value assumes the mixture of Z production channels given in chapter 4. Statistical errors only are given.*

acceptance region of the barrel muon system, the requirement that both muons satisfy $\sigma(1/p_T)/(1/p_T) < 1$ does have an impact on the selection efficiency for $Z^0 \to \mu^+\mu^-$. Varying the track momentum resolution by the amount given in section 9.3.1 gives rise to as much as a 6% fractional systematic error on the selection efficiency.

Muon Finding Algorithm

Since at least one muon candidate in the multi-muon event selection is required to match a barrel or rear muon chamber segment, the main muon finding systematic error will derive from the 10% uncertainty on the CTD-MIP-BMU match finding efficiency calculated above. However, since around 40% of $Z^0 \to \mu^+\mu^-$ events have two such matches, the total error on the selection efficiency from the 10% match finding uncertainty is reduced to around 5% overall.

Trigger

Applying the same procedure described in section 9.4.1 to estimate the possible effect of dead LST's on the barrel muon trigger efficiency gives a 7% systematic error on the trigger efficiency for $Z^0 \to \mu^+\mu^-$ decays. This is lower than the corresponding number for single muon events since in a fraction of Z decay events both muons are in the muon chamber acceptance region and can trigger the event, reducing the effect of local barrel and rear muon chamber inefficiencies.

Calorimeter Scale Uncertainty

As was the case in the analysis of $W \to \mu\nu$ events in the barrel muon sample, the precise setting of the calorimeter energy scale has little impact on a selection that relies essentially only on tracking information. The effect of varying the calorimeter energy scale by ±5% is consequently less than 1% on the overall $Z^0 \to \mu^+\mu^-$ selection efficiency.

Combined

Combining the above sources of error gives an 11% overall systematic uncertainty on the selection efficiency for $Z^0 \to \mu^+\mu^-$, smaller than that quoted for $W \to \mu\nu$ decays simply due to the fraction of events with two muons in the barrel and rear muon chamber angular acceptance region.

9.5.3 Error on the Background Estimate

The statistical error on the estimate of the background from elastic and inelastic $\mu^+\mu^-$ production, at around 30%, is again assumed to dominate the total uncertainty on the background estimate. As in the search for W production in the muon chamber sample the contribution to the background from neutral current DIS and photoproduction can safely be assumed to be small, given that no Monte Carlo events in these samples pass even the preselection cuts.

9.5.4 Cross Section Upper Limit

The contribution from $Z^0 \to \tau^+\tau^-$ decays to the overall sensitivity is found to be negligible, given that both τ's must decay to muons and pass hard p_T cuts to be selected. The upper limit is then :

$$\sigma(e^+p \to e^+Z^0X) \ \times \ BR(Z^0 \to \mu^+\mu^-) \quad <_{95\%} \quad 0.85 \ \text{pb} \ . \tag{9.4}$$

The constraint on the cross section, like that obtained in the search for $Z^0 \to e^+e^-$, is far from the Standard Model value for $\sigma(e^+p \to e^+Z^0X)$. Moreover, the poorer invariant mass resolution in the case of $Z^0 \to \mu^+\mu^-$ decays will make it much harder even in the future to isolate a Z production signal in this channel, as discussed next.

9.5.5 $Z^0 \to \mu^+\mu^-$ Signal to Background Ratio

With poor Monte Carlo statistics in the high p_T, high invariant mass phase space region the question remains whether it is possible in principle to isolate a signal for Z production and decay $Z^0 \to \mu^+\mu^-$. To answer this question elastic and inelastic Bethe-Heitler $\mu^+\mu^-$ production events have been generated requiring both muons to have $p_T > 20$ GeV and $10^\circ < \theta < 170^\circ$ and compared with $Z^0 \to \mu^+\mu^-$ Monte Carlo with the same lepton cuts applied. The comparison is made at the generator level (that is, true particle four momenta) except that the di-muon invariant mass distribution is smeared in the case of Z production by a Gaussian of width 10 GeV as an optimistic detector resolution function [6]. The resulting combined distributions are indicated by the solid lines in fig. 9.13, with the Z components indicated by the dotted lines. It is clear that at most any signal will probably only be observed as a shoulder on the lepton p_T and invariant mass distributions. Harder cuts to enhance the signal come at the cost of reduced efficiency which, given the already small Z production cross section and branching ratio to leptons, will rule out any observation of

---

[6] The resolution on the reconstructed invariant mass is currently substantially worse than this.

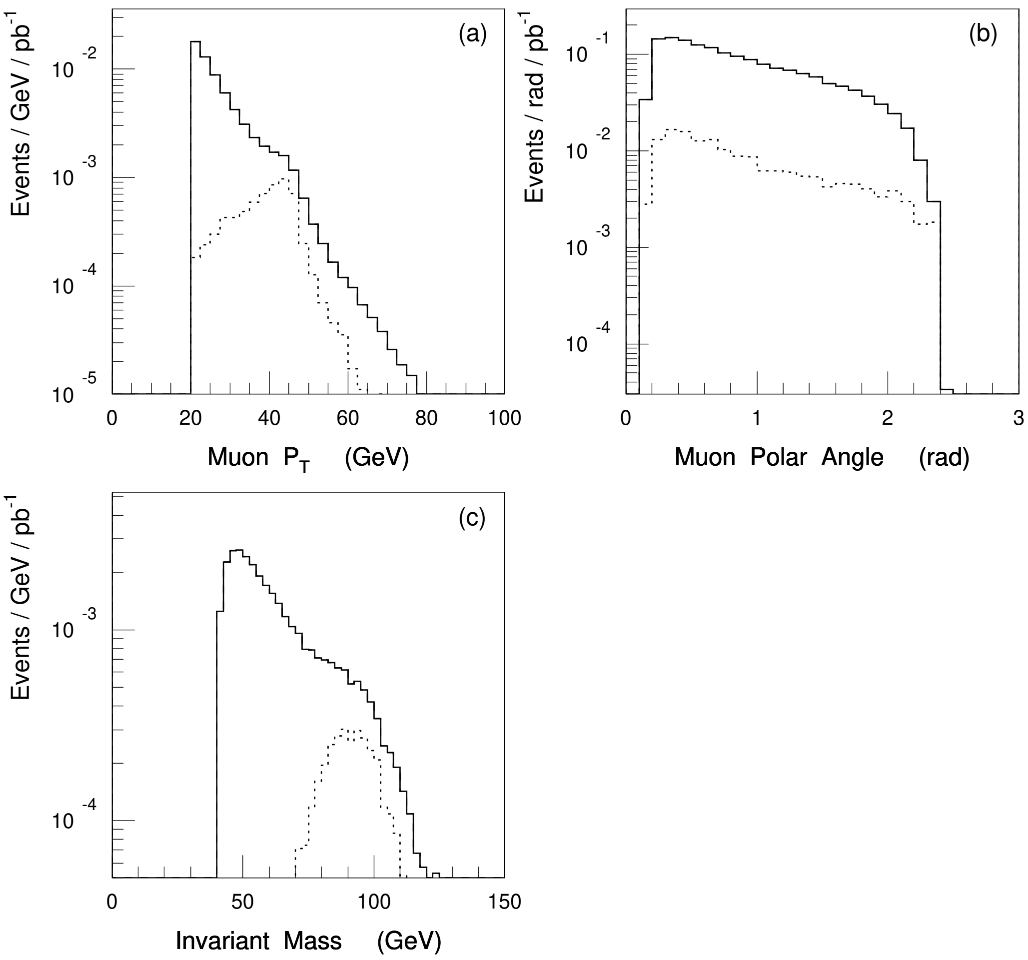

Figure 9.13: *Generator level distributions for Bethe-Heitler $\mu^+\mu^-$ production and $Z^0 \to \mu^+\mu^-$ at high lepton p_T, weighted by their respective cross sections. The solid lines indicate the combined numbers of events and the dotted line the contribution from Z production and decay to muons.*

Standard Model Z production except at the highest integrated luminosities. It should be noted here for completeness that other event properties [7] have not been considered, and the signal to background ratio may be more favourable in the hadronic decay channels.

---

[7] For example, the angular distribution of the scattered beam lepton is different for Bethe-Heitler scattering and Z production and no attempt has been made to separate the events into elastic and inelastic type events in this generator level analysis.

Chapter 10

The 1997 Data

A short accelerator shutdown over the winter of 1996-97 ensured that a large integrated luminosity was delivered by HERA during 1997 running (see section 2.1.2). In fact the 26.6 pb^{-1} collected by ZEUS more than doubles the previous data sample and it is natural to extend the main searches and analyses presented in chapters 8 and 9 to include the 1997 data. However, the results presented here must be considered preliminary since detector studies for the 1997 running period are not complete. Since few important changes were made to the detector in the short 1996-97 shutdown, it is simply assumed here that the 1997 data can be treated in the same way as that taken during 1996.

10.1 Neutral Current Backgrounds Revisited

The 1997 data offers the chance to construct a neutral current control sample at higher Q^2 than 1996 and hence in a region of the detector more relevant to W production and decay $W \to e\nu$. Events in the 1997 high E_T sample are selected that have $p_T^e > 15$ GeV and $\theta^e < 1.5$ rad [1] and compared with preliminary samples of 1997 neutral current Monte Carlo generated with the CTEQ4 structure functions [84] and with a minimum Q^2 of 400 GeV^2. Importantly, separate sets exist with both ARIADNE and MEPS models to simulate QCD effects (see chapter 5). Both Monte Carlo sets well describe the basic features and overall normalisation of the data.

It is particularly the cuts on the missing p_T and acoplanarity angle that suppress the neutral current background to the $W \to e\nu$ signal. It is therefore important for an estimate of the remaining background that the distributions of both these quantities are well described by the Monte Carlo. Figs. 10.1(a) and (b) show a comparison of the data and luminosity weighted MEPS Monte Carlo for events in the 1997 neutral current control sample, with the

---

[1] Compare with the final $W \to e\nu$ selection cuts of $p_T^e > 10$ GeV and $\theta^e < 1.5$ rad.

background (i.e. non-neutral current) contribution given by the shaded histograms. The dotted line in fig. 10.1(b) is the expectation from the ARIADNE Monte Carlo, which appears to be above that of the MEPS Monte Carlo at large acoplanarity angles. In fig. 10.1(c) and (d) the data is compared to the ARIADNE and MEPS samples in which the number of Monte Carlo events is normalised to the total number of data events. The clear trend in fig. 10.1(c) was observed in the analysis of the 1996 control sample. What is clearer in the 1997 sample, however, is that there are also possible discrepancies in the description of the acoplanarity angle distribution, particularly for the ARIADNE Monte Carlo. This might, for example, be due to different hadronic energy flows between the struck quark and proton remnant in the two Monte Carlos, although this is a matter for further investigation. The assumption is made here that, since the MEPS Monte Carlo better reproduces the acoplanarity angle distribution at high Q^2, it provides a better estimate of the neutral current background to W production to be used in the final cross section and upper limit calculations. A systematic error on the neutral current Monte Carlo background of 100% due to the discrepancy between the data and Monte Carlo missing p_T distributions is retained in the analysis of the 1997 data and is large compared to the difference between the expected background calculated using the 1997 MEPS and ARIADNE Monte Carlo sets.

10.2 $W \to e\nu$ Search

The same sequence of cuts described in section 8.1 is applied to the new data sample. Figure 10.2 shows some important distributions after all cuts up to and including the cut in the $\{\text{missing } p_T, E - p_Z\}$ plane, with the Monte Carlo normalised to the total 1994-97 integrated luminosity of 46.7 pb^{-1}. There is some discrepancy between the total number of events observed (24) and the number expected from Monte Carlo (33) after this stage in the selection, although after subsequent cuts the numbers are generally in good agreement. The expected number of events after all cuts is broken down in table 10.1, from which it can also be seen that 4 data events, including the single event from the 1994-96 data, are selected.

10.2.1 Properties of the Events

Table 10.2 lists some of the important properties of the 4 events passing the $W \to e\nu$ selection cuts. The electron energies have been corrected using a routine taking into account the amount of inactive material between the primary vertex and the entry point of the

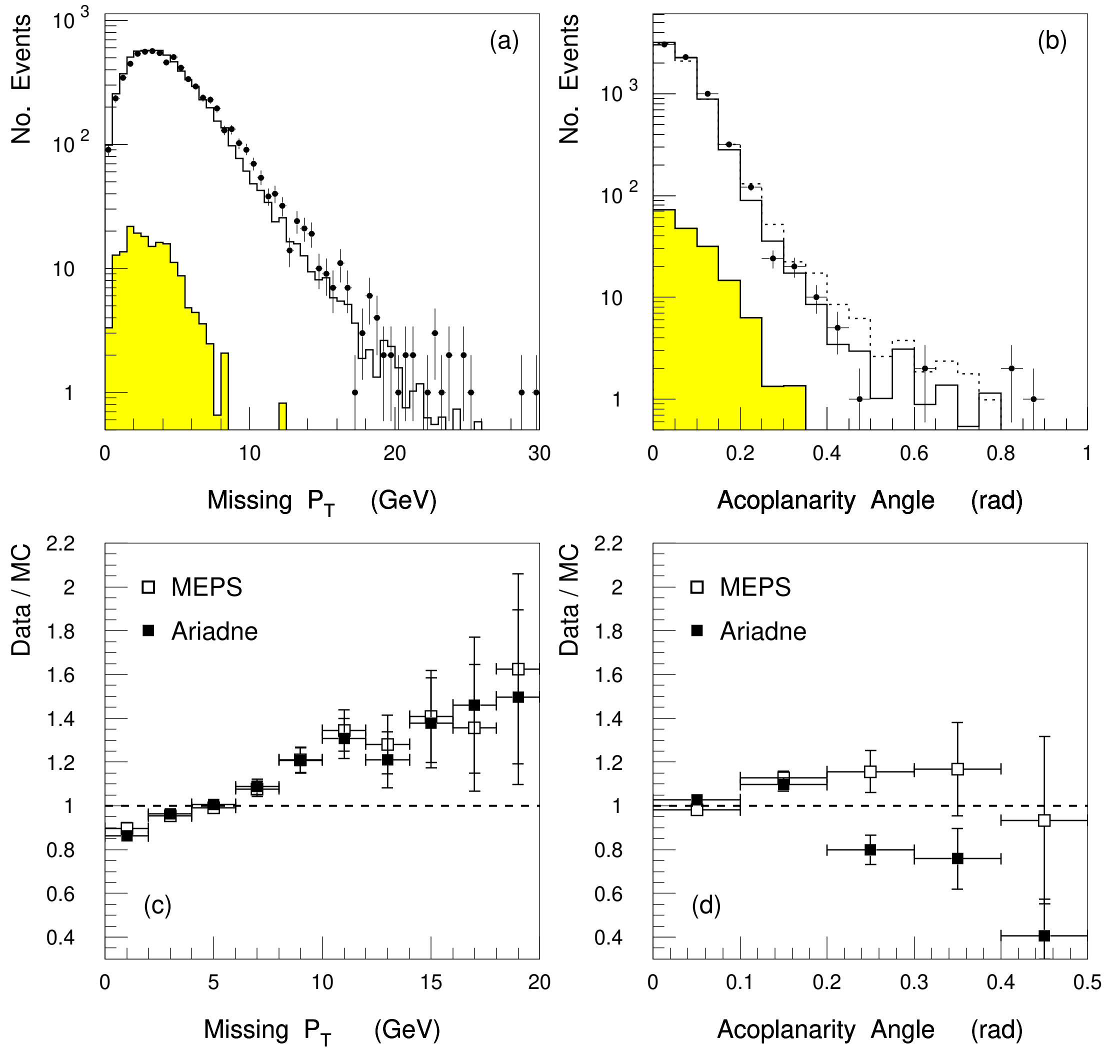

Figure 10.1: *The missing p_T and acoplanarity angle distributions for the data (points) and luminosity weighted MEPS Monte Carlo (solid line) in the 1997 neutral current control sample. The dotted line in (b) is the expectation from ARIADNE neutral current Monte Carlo. The ratio is plotted separately for MEPS and ARIADNE sets below, where the number of Monte Carlo events is normalised to the total number of data events in each case.*

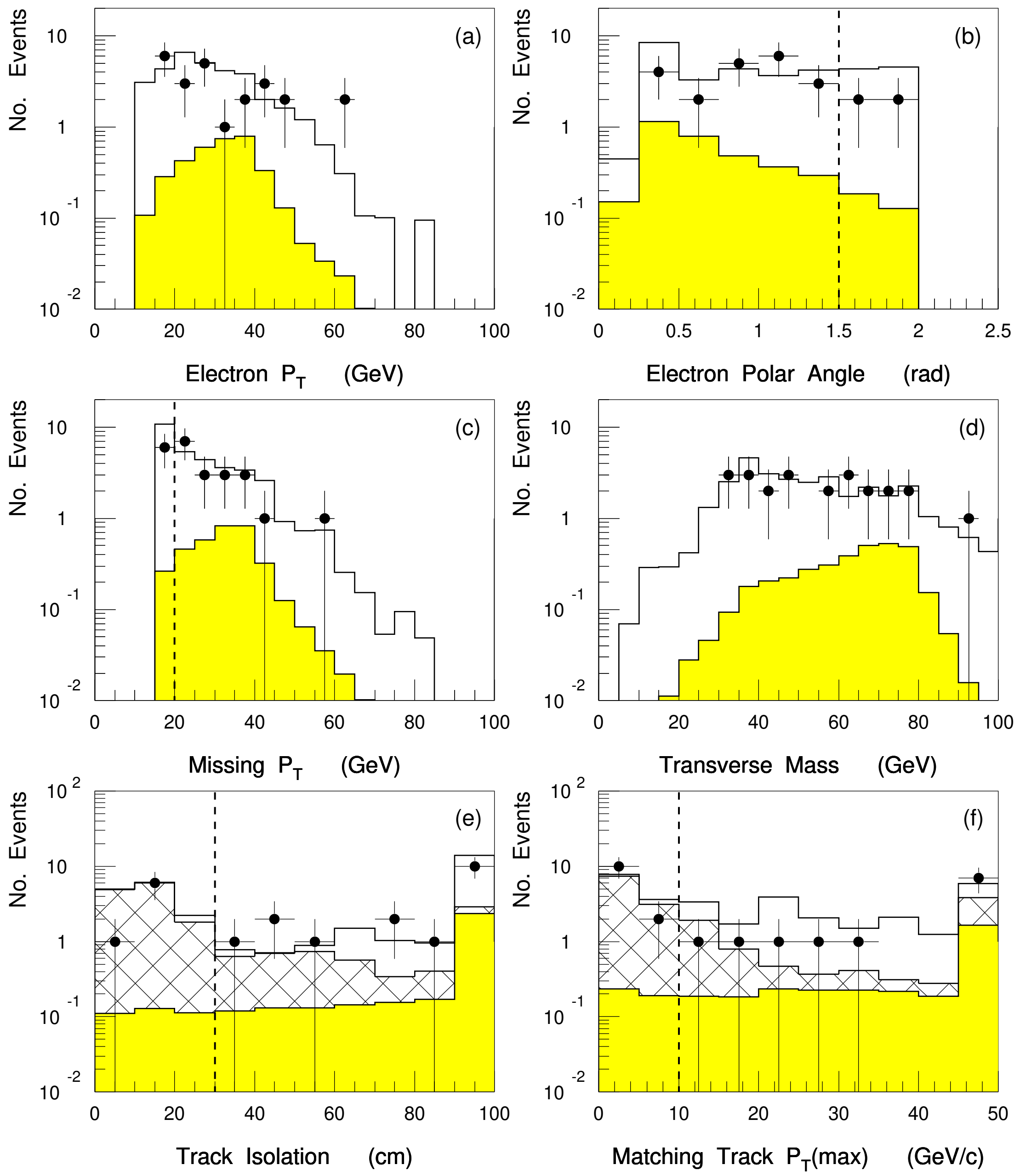

Figure 10.2: *The inclusive 1994-97 data (points) plotted against the luminosity weighted Monte Carlo (solid histogram). The contribution to the Monte Carlo total from W production is indicated by the shaded histogram and the charged current background by the wide hatched histogram. Some of the cuts in the final* $W \to e\nu$ *selection are indicated by the dashed lines.*

Background Process	Expected Number of Events
$e^+p \to e^+X$ (NC DIS)	0.44
$e^+p \to \bar{\nu}X$ (CC DIS)	0.47
$\gamma\gamma \to e^+e^-$ (Elastic and Inelastic)	0.03
$\gamma\gamma \to \tau^+\tau^-$ (Elastic and Inelastic)	0.06
$e^+p \to e^+Z^0X$ (All decay channels)	0.14
Signal Process	
$W \to e\nu$	1.96
$W \to \tau\nu$	0.17
Other decay channels	0.04
Total	3.31
Data	
1994-97	4

Table 10.1: *The expected and observed numbers of events in the search for W production and decay $W \to e\nu$ including the 1997 data. The neutral current background has been calculated using high Q^2 MEPS Monte Carlo.*

Candidate	1	2	3	4
Year	95	97	97	97
Corrected Electron p_T (GeV)	22.1 ± 1.0	48.8 ± 2.0	43.8 ± 1.9	37.1 ± 1.7
Electron Polar Angle	37°	58°	71°	54°
Corrected Hadronic p_T (GeV)	0.4 ± 0.1	18.9 ± 2.7	24.6 ± 1.5	18.6 ± 2.4
Corrected Missing p_T (GeV)	21.6 ± 1.0	35.0 ± 2.5	22.1 ± 2.1	32.9 ± 1.4
Corrected Transverse Mass (GeV)	43.7 ± 1.5	81.5 ± 3.3	61.5 ± 3.2	68.2 ± 2.2
Matching Track p_T (GeV/c)	$22.3^{+6.8}_{-4.2}$	$44.1^{+33.0}_{-13.2}$	$42.9^{+17.8}_{-9.7}$	$35.9^{+13.8}_{-7.8}$
Track Charge	+1 ($4.3\,\sigma$)	+1 ($2.3\,\sigma$)	+1 ($3.4\,\sigma$)	+1 ($3.6\,\sigma$)

Table 10.2: *The properties of the 4 surviving events in the search for W production and decay $W \to e\nu$ from 1994-97. The numbers in brackets after the track charge indicate the significance of the track charge assignment. A global ±5% calorimeter scale uncertainty has not been included in the given errors.*

electron at the face of the calorimeter, and in addition correcting the measured energy for certain non-uniformities in the calorimeter energy response depending on the precise position of the electron within the given calorimeter tower or module [88]. Fig. 10.3(a) shows that on average the corrected electron energy is close to the true electron energy for $W \to e\nu$ Monte Carlo events. The difference between the true and uncorrected electron energy is given by the dotted histogram, showing a clear shift towards low measured electron energies. A Gaussian fit to the central part of the distribution gives a corrected electron energy resolution of $\sim 30\%/\sqrt{E}$, used here as an estimate of the error on the individual corrected electron energies. The hadronic system is corrected using an algorithm developed for DIS events that corrects each hadronic energy deposit [2] according to its measured energy and the amount of inactive material traversed between the interaction point and the face of the calorimeter [89]. The error on the corrected hadronic p_T is calculated by suitably combining the errors on each individual corrected island energy. Neither the electron or the hadron angles are corrected. Finally, the corrected electron and hadronic p_T's give rise to corrected values for and errors on the missing p_T, plotted in fig. 10.3(b) and transverse mass where, for the latter quantity, the resolution on the azimuthal separation between the electron and missing p_T vectors, plotted in fig. 10.3(c), is also taken into account. Note that a global ±5% calorimeter scale uncertainty has not been included in the given errors.

From table 10.2 it can be seen that for all 4 events the matching track p_T agrees closely with the calorimeter measured p_T and there is no evidence that any of the electromagnetic clusters are fake electrons. However, in candidate event number 3 there is evidence of significant energy leakage into the backing calorimeter that could account for the missing transverse momentum. Such events are observed in the neutral current background Monte Carlo and constitute a significant fraction of the remaining background to W production but, in order to avoid systematic uncertainties deriving from the Monte Carlo description of backing calorimeter energy deposits [3], a cut to remove such events is not made here.

The corrected transverse momenta and masses for the 4 data events are compared with W production Monte Carlo in fig. 10.4. It is noticeable that the 3 new candidate events have large hadronic p_T's compared to the W Monte Carlo. For example one of the clearest $W \to e\nu$ candidate events, shown in fig. 10.5, has a corrected hadronic p_T of around 19 GeV.

---

[2] Strictly, each *cone island* or cluster of energy in $\{\eta, \phi\}$ space.

[3] The description of backing calorimeter energy deposits relies critically on, for example, the correct description of hadronic shower development and composition. The calibration of the backing calorimeter itself poses considerable difficulties.

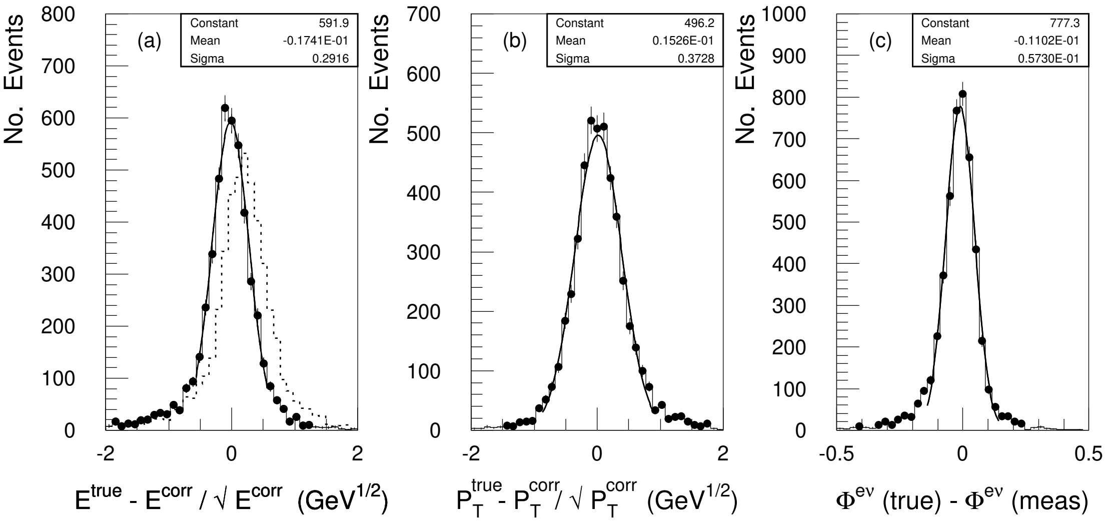

Figure 10.3: *(a) The mean difference between the true and corrected electron energy for $W \to e\nu$ Monte Carlo events. The dotted histogram shifted to the right is the comparison between the true and uncorrected electron energy. The difference between the true and corrected missing p_T, formed from the corrected electron energy and hadronic p_T, is plotted in (b) and the resolution on the measured azimuthal separation between the electron and missing p_T vectors is plotted in (c).*

10.2.2 Extracting a Cross Section

Since the expected number of events, listed in table 10.1, is in good agreement with the number observed and with a signal to background ratio close to 2 (although with a large error resulting from the uncertainty in the neutral current background), an attempt may be made to extract the W production cross section from the 1994-97 data. With small numbers of events a maximum likelihood method, with the likelihood function given simply by the Poisson probability for the combined background and signal to fluctuate to the observed number of events, is appropriate. This method, discussed in detail in appendix A, yields

$$\sigma(e^+p \to e^+W^\pm X) \;=\; 1.3\ {}^{+\,1.1}_{-\,0.8}\ \text{(stat)}\ \pm\ 0.2\ \text{(syst)}\ \ \text{pb}\ \ , \qquad (10.1)$$

where an average efficiency for $W \to e\nu$ and $W \to \tau\nu$ decays has been calculated in conjunction with a combined branching ratio of 22% to account for the contribution to the overall sensitivity from tau decays of the W. The systematic error takes into account the 40% uncertainty on the background estimate [4] and the errors on the selection efficiency and luminosity discussed in chapter 8. This cross section, although only a 1 σ measurement, is

---

[4] Slightly different from the value used in chapter 8 due to the revised neutral current background estimate.

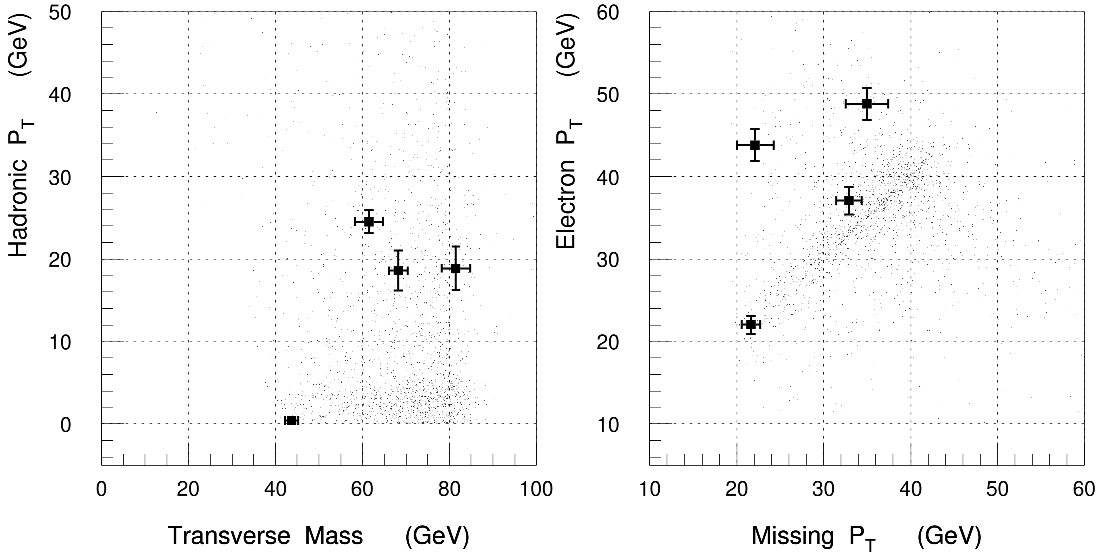

Figure 10.4: *The four surviving events in the missing p_T plus electron sample from 1994-97 (square points) and W production Monte Carlo corresponding to* 50 fb^{-1} *(dots) after all cuts. All quantities are corrected as described in the text and the approximate errors on these quantities are indicated by the error bars for the data points.*

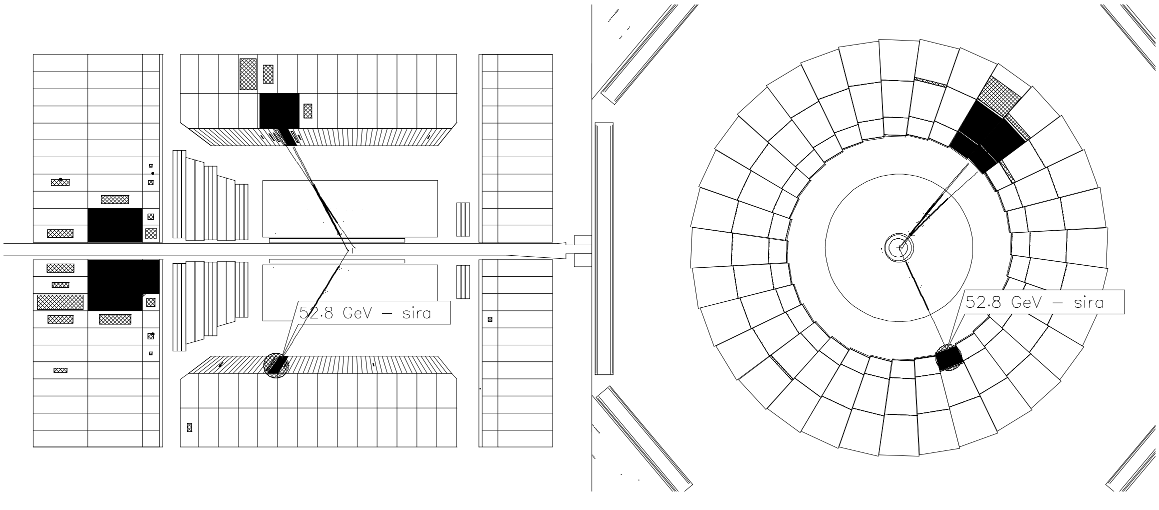

Figure 10.5: *A candidate $W \to e\nu$ event from 1997. A clear electron and hadron jet are visible in the barrel calorimeter with a large acoplanarity angle. See text for more details.*

in good agreement with the predicted Standard Model value of ~ 1 pb given in chapter 4.

An upper limit on anomalous W production can also be calculated for the combined 1994-97 sample using the same method applied in section 8.1.7 to give :

$$\sigma(e^+p \to e^+W^\pm X) \quad <_{95\%} \quad 3.7 \ \ \text{pb} \ , \tag{10.2}$$

from which stricter constraints on anomalous couplings $\Delta\kappa$ and λ can be derived. As a cross check, a very similar number is obtained by finding the 2σ upper bound on the cross section employing the log likelihood method used in the extraction of the cross section.

10.3 Radiative Charged Current Scattering

The charged current events from the combined 1994-97 sample in which a photon is identified are plotted in fig. 10.7. There is generally good agreement between the 44 data events and the ~ 41 expected from Monte Carlo. The cuts indicated in fig. 10.7(c)-(f) select the well isolated high p_T photons that are sensitive to couplings at the $WW\gamma$ vertex. The 6 data events selected by these WWGAMMA cuts are to be compared to an expected 6.8 (+ 0.1) charged current (+ background) events from Monte Carlo. One of the 5 such events from the 1997 data is shown in fig. 10.6, with a clear high energy photon well isolated from all hadronic activity in the event. Future high luminosity radiative charged current analyses will apply stricter cuts than those used here to select such clean radiative events with

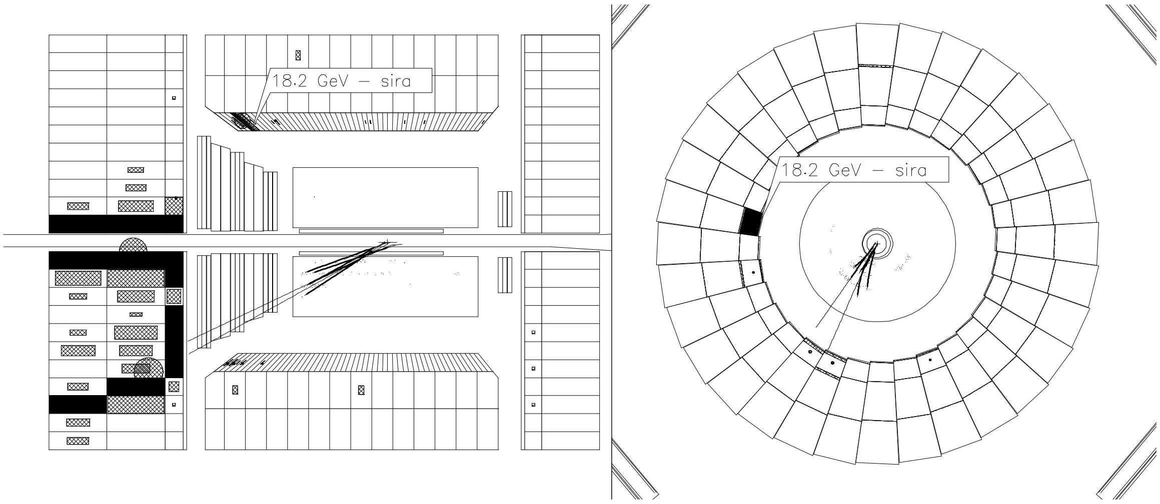

Figure 10.6: *A radiative charged current event from 1997. A well isolated* 19 GeV *photon is visible in the barrel calorimeter at a polar angle of* 41°. *The uncorrected total missing* p_T *for the event is around* 42 GeV.

correspondingly small photon misidentification backgrounds.

With the combined 1994-97 integrated luminosity an improved upper limit can be placed on the cross section for the anomalous production of isolated photons with $p_T > 10$ GeV in events with large missing p_T and other properties detailed in section 8.2 :

$$\sigma_{anom}(e^+p \to \bar{\nu}\gamma X) \quad <_{95\%} \quad 0.34 \quad \text{pb} \ , \tag{10.3}$$

which translates into an improved constraint on the total high p_T photon radiative charged current cross section :

$$\sigma(e^+p \to \bar{\nu}\gamma X) \ = \ \sigma_{anom}(e^+p \to \bar{\nu}\gamma X) \ + \ \sigma_{SM}(e^+p \to \bar{\nu}\gamma X) \ <_{95\%} \ 0.44 \ \text{pb} \ . \tag{10.4}$$

Relaxing certain topological cuts in the initial selection of charged current events as described in section 8.2.5 gives rise to an almost identical cross section upper limit of 0.42 pb for the full 1994-97 data, while making fewer assumptions about the distribution of high p_T photons in events with missing p_T. This upper limit is used in the extraction of anomalous coupling constraints in chapter 11.

10.4 $Z^0 \to e^+e^-$ Search

The search for high mass multi-electron events including the 1997 data yields no candidate events in the mass window for $Z^0 \to e^+e^-$ of $75 <$ IM < 100 GeV. Using the efficiency, background estimate and errors calculated in chapter 8 gives a revised upper limit of :

$$\sigma(e^+p \to e^+Z^0X) \ \times \ BR(Z^0 \to e^+e^-) \quad <_{95\%} \quad 0.18 \quad \text{pb} \ , \tag{10.5}$$

or a constraint on the total production cross section of 5.4 pb. While this represents more than a factor two improvement over the limit obtained from the 1994-96 data, it is still far from the Standard Model cross section of ~ 0.33 pb.

In addition, the inclusion of the 1997 data yields no multi-electron events with invariant masses greater than that of the highest mass event in the 1994-96 data. Taking the expected number of Bethe-Heitler and QED Compton events that pass all cuts and have an uncorrected invariant mass greater than 130 GeV results in a Poisson probability of 5% to observe one or more events [5]. There is therefore no evidence for an excess of multi-electron events at the highest invariant masses.

---

[5] Again, no attempt is made to calculate separately the expected number of elastic and inelastic events at the detector level.

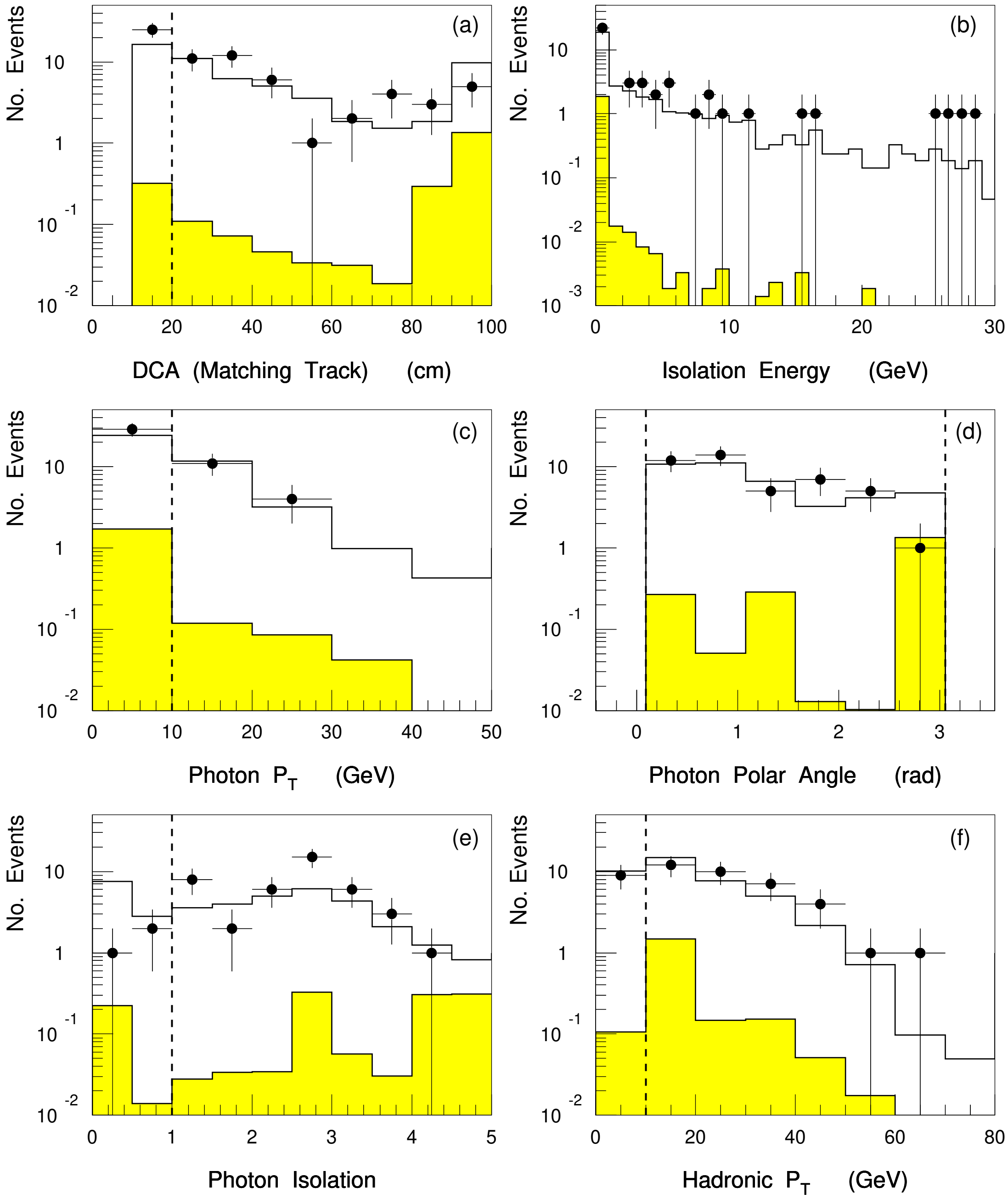

Figure 10.7: *Radiative charged current candidate events from the inclusive 1994-97 data sample (points) plotted against the Monte Carlo expectation (solid line). The non-charged current Monte Carlo contribution is given by the shaded histogram. The cuts to select isolated high p_T photons are given by the dashed lines in plots (c) to (f).*

10.5 $W \rightarrow \mu\nu$ Search

10.5.1 Events with Missing p_T

Fig. 10.9 shows a comparison of the full 1994-97 missing p_T plus muon data with Monte Carlo after cuts $\theta^{\mu} < 2.0$ rad and $p_T^{net} > 10$ GeV. There is good agreement both in terms of the overall normalisation of the data and the description of the different transverse momentum distributions. Applying the final cuts $p_T^{\mu} > 15$ GeV and $p_T^{net} > 15$ GeV leaves a single event surviving in the data, shown in fig. 10.8, against an expectation of around 0.65 (+0.6) W production (+ background) events. The error on the vertex fitted track p_T is significant and, in particular, the upper bound on the track momentum violates longitudinal momentum conservation :

$$(E - p_Z)_{cal} \; + \; (E - p_Z)_{\mu} \;\; \leq \;\; 55 \text{ GeV} \, ,$$

where the MIP contribution to the calorimeter $E - p_Z$ is subtracted in order to avoid double counting once the track is included in the sum. Note that by neglecting the contribution to the total $E - p_Z$ from any neutrino(s) in the event a conservative bound on the muon

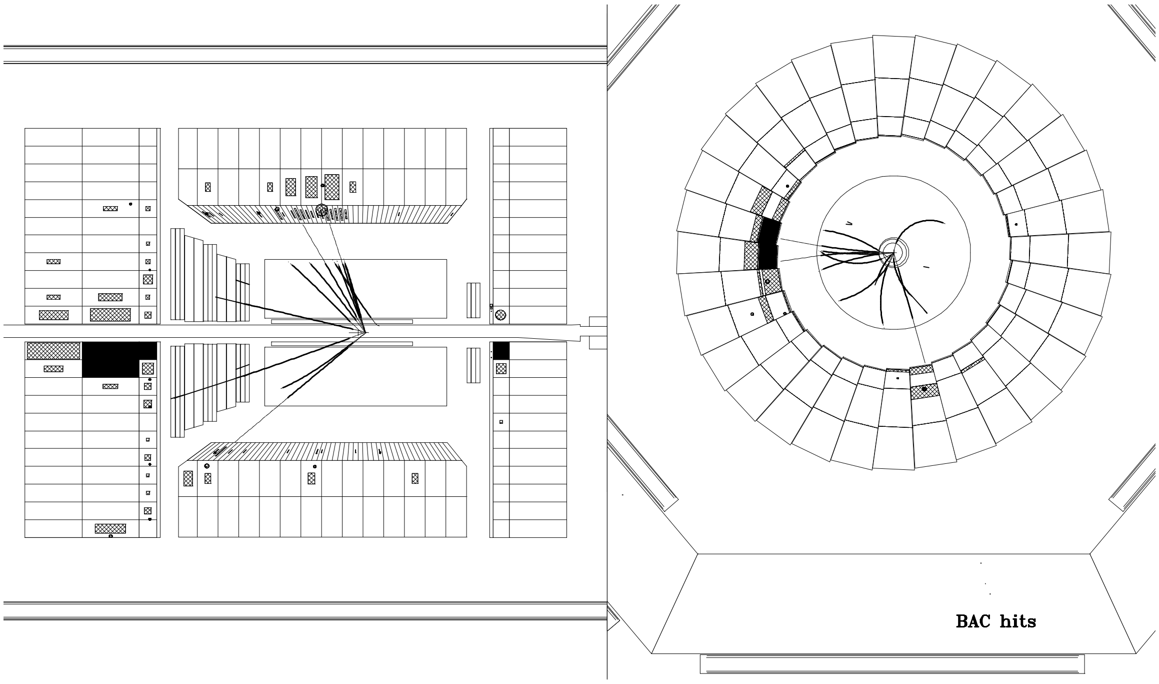

Figure 10.8: *The single surviving event in the 1994-97 missing p_T plus muon sample. The high p_T track making up the muon candidate is visible at $\theta \sim 40°$ and $\phi \sim 285°$. Hits in the backing calorimeter, indicated in the right hand view of the detector, confirm the presence of a high p_T muon in the event. More properties of the event are given in the text.*

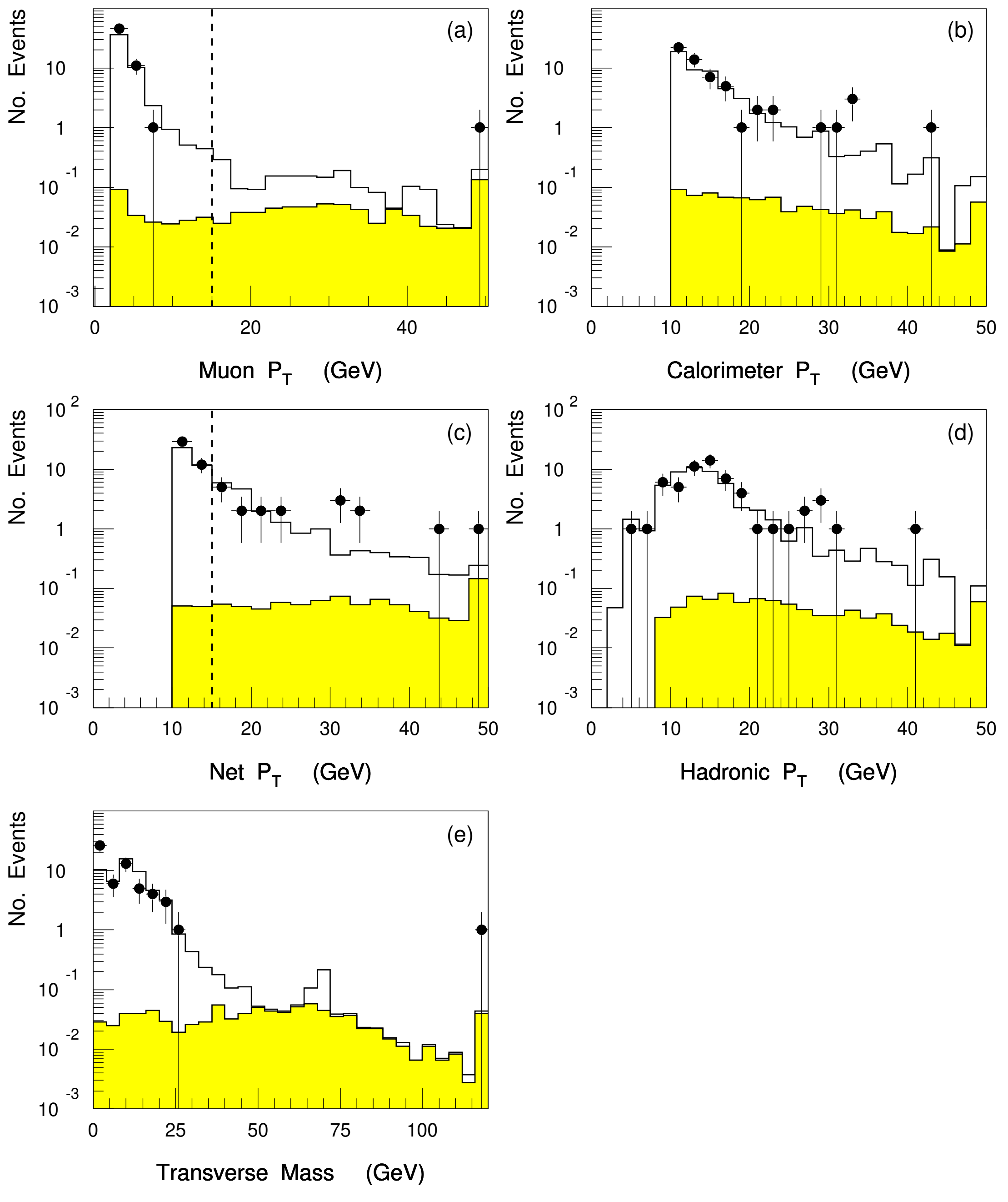

Figure 10.9: *Events with missing p_T and a muon from the 1994-97 data sample. The solid histogram is the combined luminosity weighted Monte Carlo expectation and the shaded part the contribution from W production. Cuts $\theta^{\mu} < 2.0$ rad and $p_T^{net} > 10$ GeV have already been applied. Final selection cuts are indicated by the dashed lines*

momentum is obtained. Imposing this constraint gives, in combination with the errors on the fitted track parameters, the following allowed ranges for the positively charged muon p_T and transverse mass for the event :

$$p_T^\mu = 76\,^{+5}_{-30}\ \text{GeV} \quad ; \quad M_T = 152\,^{+9}_{-60}\ \text{GeV}\ .$$

The corrected hadronic p_T for the event, calculated using the same routine described for $W \rightarrow e\nu$ events but excluding the calorimeter MIP rather than the electromagnetic cluster cells, is around 13 GeV. This enters into the calculation of upper limits for W production in the presence of large hadronic p_T's in the next chapter. The revised upper limit, calculated using the values for the selection efficiency, luminosity normalised background estimate and their respective uncertainties given in section 9.3, is :

$$\sigma(e^+p \rightarrow e^+W^\pm X) \quad <_{95\%} \quad 6.3\ \text{pb}\ . \tag{10.6}$$

10.5.2 Barrel and Rear Muon Events

All events from 1995-97 with a single barrel or rear muon candidate are compared to Monte Carlo in fig. 10.10. In general the agreement is good, although an excess of events is apparent at large muon and net transverse p_T, translating into large transverse masses. In fact, once the final cuts $p_T^\mu > 15$ GeV and $p_T^{net} > 15$ GeV have been applied there are 6 data events surviving against an expectation of only 1.6 from Monte Carlo, although with a significant error on this estimate (see section 9.4).

In order to examine whether this discrepancy is due to $W \rightarrow \mu\nu$ like events or not, tighter cuts are made to try to isolate a cleaner signal. It can be seen from fig. 10.10(h) that there is an excess of events at small acoplanarity angles. Demanding that $\Theta_{\text{ACOP}} > 0.2$ rad, with the usual requirement that the hadronic p_T be greater than 4 GeV for this quantity to be well defined, removes only a small fraction of the remaining W production signal. Finally, tightening the cut on the muon polar angle to 1.5 rad, the same requirement that is made in the analysis of $W \rightarrow e\nu$ events, reduces the overall signal efficiency to around 10%. Two data events remain, consistent with an expectation of 0.5 (+0.8) W production (+ background) events.

It is therefore most likely that the excess of events with looser cuts is due to an underestimate of the background at low acoplanarity angles and large polar angles rather than an excess of W production events. The muon chamber sample, unlike the missing p_T or high E_T samples, does not have a hard transverse momentum scale set by a calorimeter

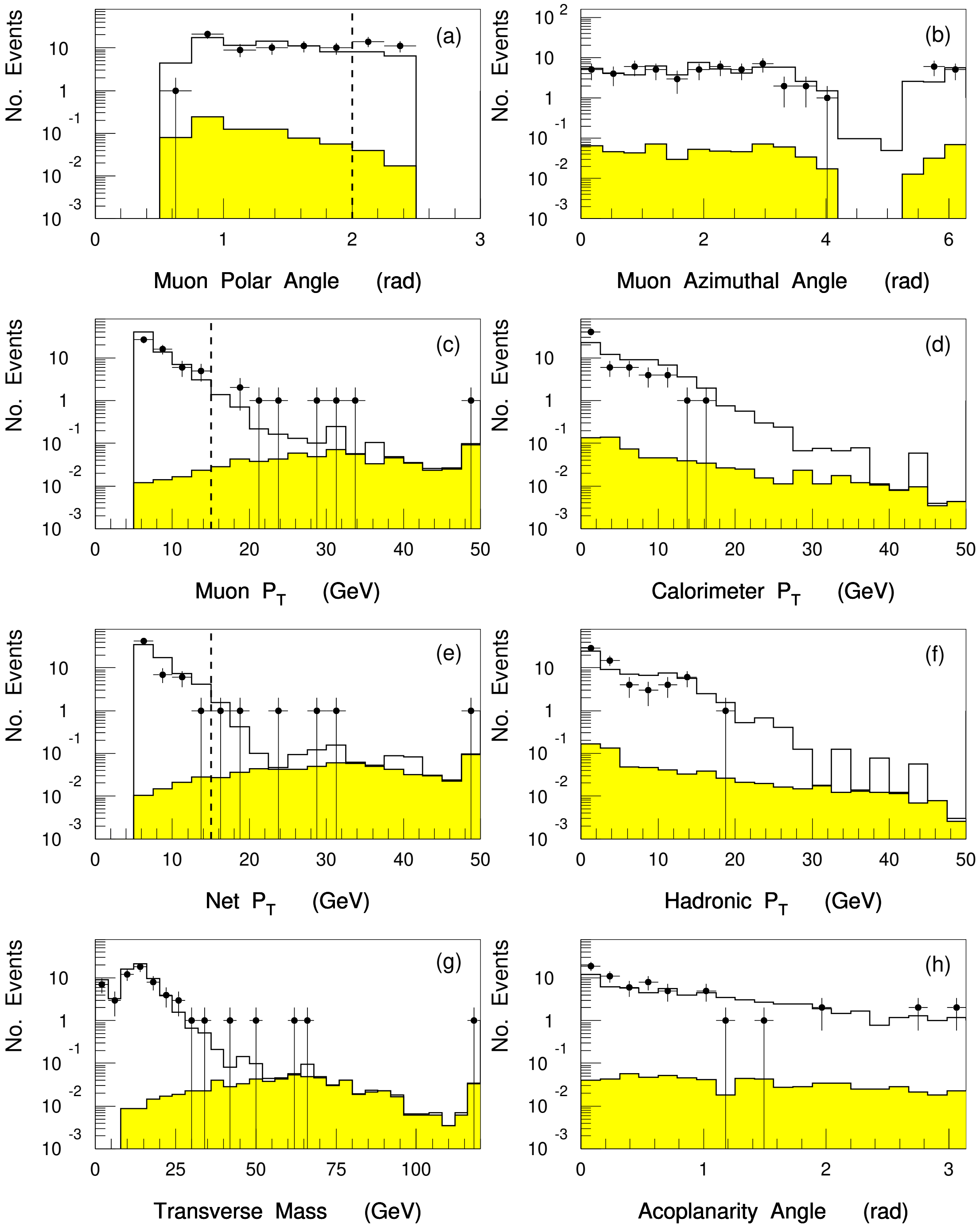

Figure 10.10: *Preselected single muon events from the 1995-97 barrel and rear muon sample. The solid histogram is the combined luminosity weighted Monte Carlo expectation and the shaded part the contribution from W production. The cut $\theta^{\mu} < 2.0$ rad has already been applied in (b) to (h) and further cuts in the selection of $W \to \mu\nu$ events are indicated by the dashed lines.*

energy measurement and is therefore more susceptible to poorly measured backgrounds at low p_T, such as low Q^2 neutral current scattering and photoproduction processes, that are not simulated here. Alternatively, discrepancies between the data and Monte Carlo rates for heavy quark production and decay might give rise to an excess of high p_T muon events in this sample [6]. These are all issues that need to be resolved with future measurements at HERA.

Using the revised background estimate [7] and selection efficiency in the upper limit calculation gives :

$$\sigma(e^+p \to e^+W^\pm X) \quad <_{95\%} \quad 11 \;\; \text{pb} \;, \tag{10.7}$$

which nevertheless represents a significant improvement over the limit derived from the 1995-96 data in section 9.5.4.

10.6 $Z^0 \to \mu^+\mu^-$ Search

The full 1995-97 multi-muon data is compared to Monte Carlo in fig. 10.11. In general there is very good agreement between the data and Monte both in terms of the overall normalisation and the description of the transverse momenta and invariant mass distributions. The highest mass event in the combined sample is shown in fig. 10.12. Both muons have transverse momenta in excess of 20 GeV and combine to give an invariant mass of 46^{+13}_{-9} GeV . This event, like the second highest mass event shown in section 9.5.1, has no proton remnant activity visible in the forward calorimeter. This is not unlikely since, from table 9.6, it can be seen that the ratio of true elastic to inelastic $\mu^+\mu^-$ production is greater than 1 even for Bethe-Heitler events with high p_T muons and at large invariant masses.

No events pass the final $Z^0 \to \mu^+\mu^-$ selection criteria, yielding an improved upper limit on the Z production cross section over than given in section 9.5.1 that simply reflects the ratio of luminosities for the two samples :

$$\sigma(e^+p \to e^+Z^0X) \;\times\; BR(Z^0 \to \mu^+\mu^-) \quad <_{95\%} \quad 0.34 \;\; \text{pb} \;. \tag{10.8}$$

This limit is still not of the same order as the central Standard Model value for the Z production cross section but is a useful constraint on anomalous sources of high mass $\mu^+\mu^-$ pairs. The electron and muon limits are combined and the prospect of observing real Z production at HERA is addressed briefly in the next chapter.

---

[6] Interestingly, the pattern of hits in the barrel muon system for the remaining candidate events indicates lower transverse momenta muons than given by the matching CTD track p_T's. This may also be due to meson decay inside the volume of the CTD or between the CTD and barrel muon system.

[7] Note that an underestimate of the background only leads to a more conservative upper limit (see fig. A.1).

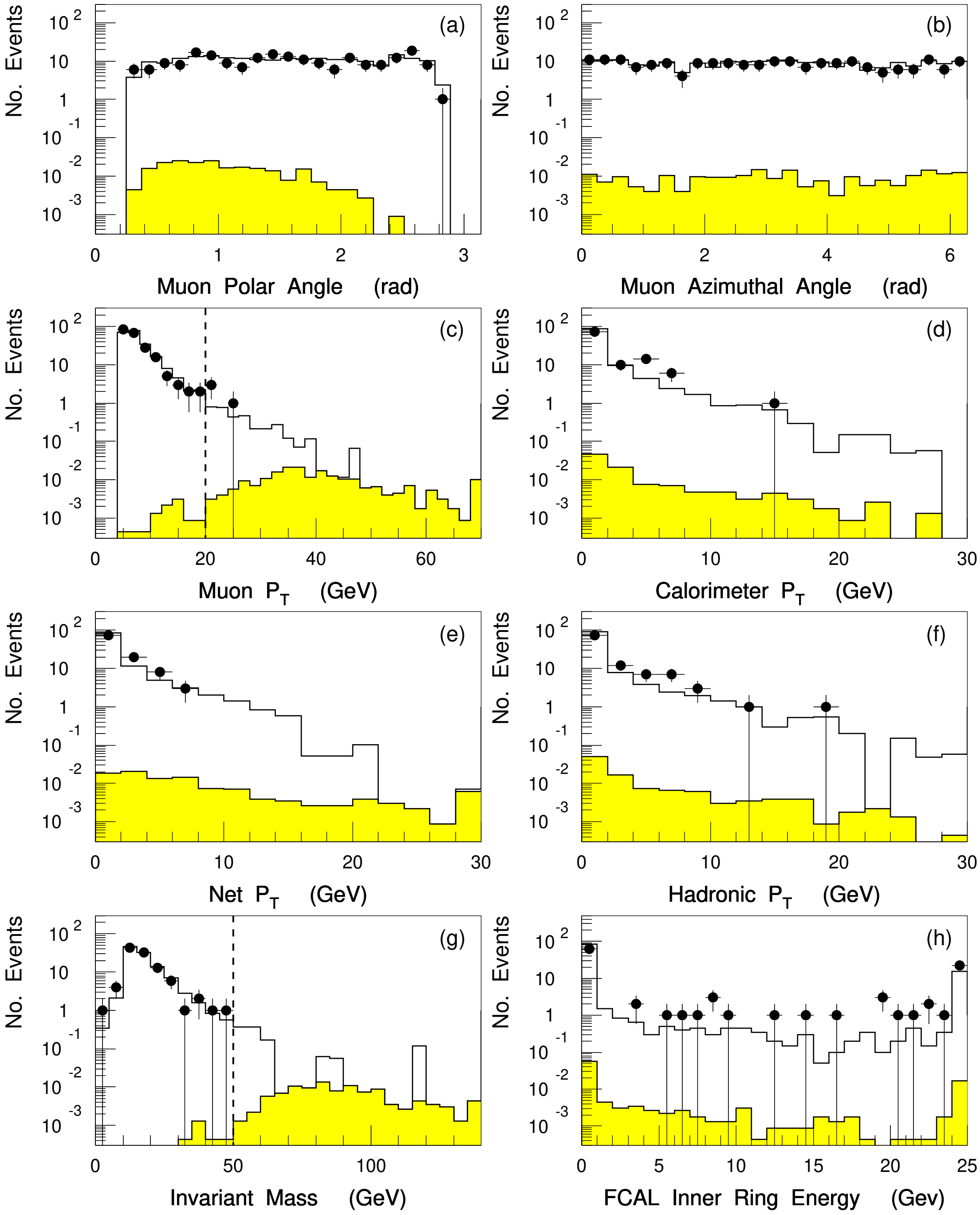

Figure 10.11: *Preselected di-muon events from the 1995-97 data sample. The solid histogram is the combined luminosity weighted Monte Carlo expectation and the shaded part the contribution from Z production. The final cuts to select* $Z^0 \to \mu^+\mu^-$ *events are indicated by the dashed lines.*

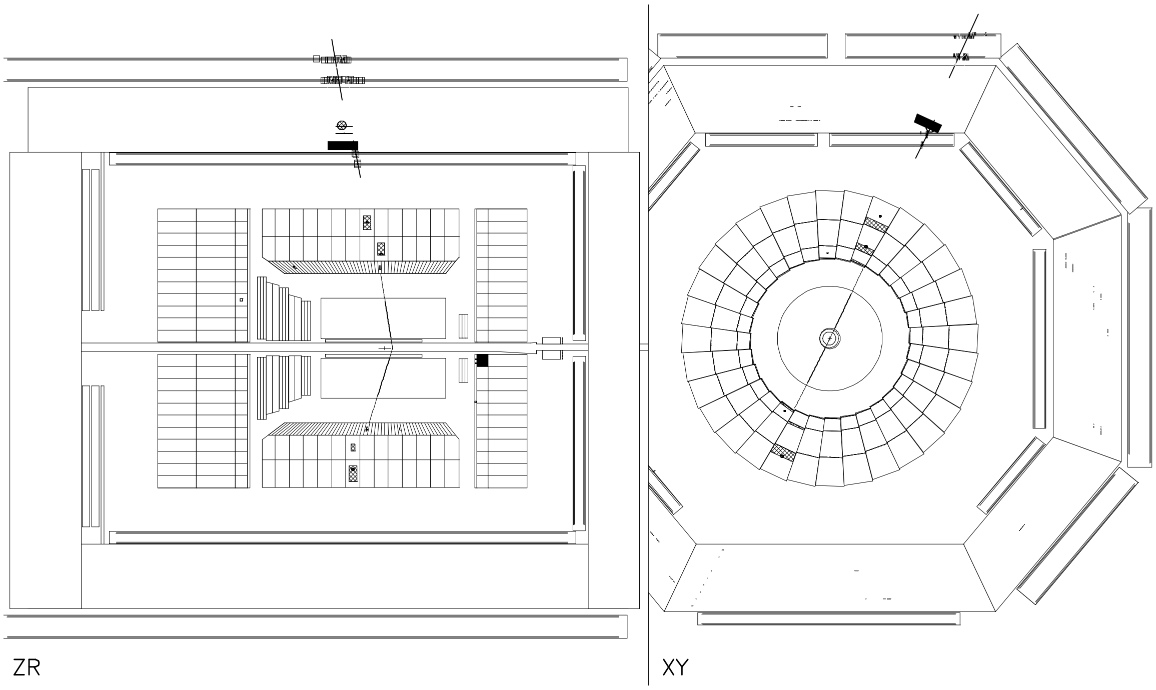

Figure 10.12: *The highest mass* $\mu^+\mu^-$ *event in the combined 1995-97 data. The two muons with transverse momenta of* 21 *and* 24 GeV *combine to give an invariant mass of* 46^{+13}_{-9} GeV

Chapter 11

Interpretations and Conclusions

Since the constraint on anomalous single W production is dominated by the results of the search for $W \to e\nu$ events and the selection efficiency is not a strong function of the values for the anomalous $WW\gamma$ couplings, only the results of this decay channel are considered in the extraction of constraints on $\Delta\kappa$ and λ in the next section. The results of the search for $W \to \mu\nu$ are used to place separate constraints on the cross section for W production in the presence of large hadronic transverse momenta in order to compare the ZEUS results with those presented in [2]. The results of the radiative charged current analysis and the search for $Z^0 \to l^+l^-$ are then briefly reviewed and, finally, some conclusions drawn about likely future measurements of triple gauge boson couplings at HERA.

11.1 W Production and Decay $W \to e\nu$

The 1994-97 missing p_T plus electron data allowed a 1σ measurement of the W production cross section in e^+p collisions that was in good agreement with the Standard Model prediction of ~ 1 pb. However, given the error on the measured cross section and the fact that the minimum cross section for any combination of anomalous couplings is around 0.7 pb (see section 4.1.4), only the upper limit quoted in equation 10.2 is useful here for the purposes of extracting constraints on anomalous $WW\gamma$ couplings. Note that in the presence of a precise cross section determination, the lower cross section limit can provide additional information about allowed couplings, giving rise to the more complicated constraints considered in section 11.6.1.

An upper limit on $\sigma(e^+p \to e^+W^\pm X)$ can be converted into corresponding limits on anomalous couplings $\Delta\kappa$ and λ by virtue of the parameterisations shown in fig. 4.5 of the anomalous W production cross section. Two complicating issues are, firstly, the possible dependence of the signal selection efficiency on the value for the anomalous coupling and,

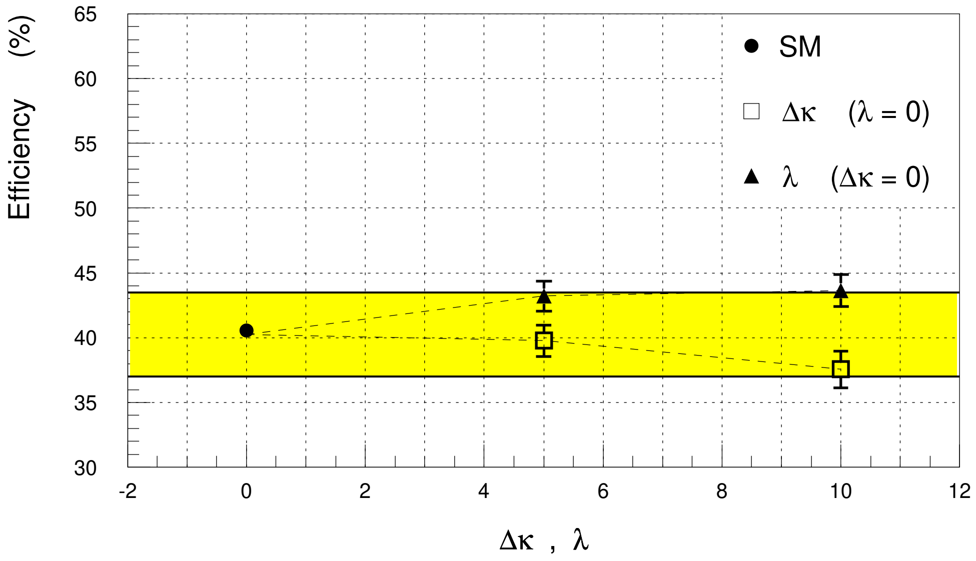

Figure 11.1: *The selection efficiency for $W \to e\nu$ events in the presence of anomalous $WW\gamma$ couplings $\Delta\kappa$ and λ for the 1996 detector configuration. The shaded band represents the* 8% *systematic uncertainty on the Standard Model selection efficiency. Statistical errors only are shown for each point.*

secondly, the 'theoretical' uncertainty on the given parameterisations.

Figure 11.1 shows the efficiency for selecting $W \to e\nu$ events for Standard Model W production as well as for $\Delta\kappa$ and λ equal to +5 and +10. The horizontal band represents the systematic uncertainty on the selection efficiency calculated in section 8.1.4 for Standard Model W production. There is some systematic variation of the efficiency with non-zero values for the anomalous couplings, due to changes in the lepton angular distributions for anomalous W production and an enhanced probability for the decay electron to be poorly isolated for W production in the presence of large hadronic p_T's. Given that the cross section limit is going to correspond to positive values for $\Delta\kappa$ of around 5, it is clear however that any such variation with anomalous couplings is within the systematic error already assigned to the selection efficiency. For simplicity therefore the efficiency is assumed to be constant at the Standard Model calculated value.

Note that the approximate independence of the selection efficiency from the values taken by the $WW\gamma$ couplings is expected in the case of $W \to e\nu$ decays, where the event selection is essentially on the basis of the W decay products and is therefore largely independent of other event properties such as the recoiling hadronic p_T. The dependence of the selection efficiency for $W \to \mu\nu$ events on the values for the anomalous couplings is much stronger, as discussed in the following section.

It has been noted at several points that the uncertainty on the Standard Model W production cross section deriving from a number of sources is considerable, and was estimated in section 4.1.2 to be around 35%. Assuming that the W production cross section in the presence of anomalous couplings suffers similar uncertainties [1], this ought to be reflected in the final upper limit. In order to estimate the effect of these theoretical uncertainties, the right hand side of the cross section upper limit formula A.8 is made an explicit function of the anomalous coupling in question. For instance, limits on $\Delta\kappa$ are found by making the substitution $\sigma_{UL} \to \sigma^0_{UL}(\Delta\kappa)$, where this function is just the parabola parameterised in section 4.1.4. Then, in the same spirit in which experimental uncertainties are incorporated into the upper limit, a further convolution is introduced into the integral in equation A.8. With σ_{UL} now representing a random variable, and writing the integral as a function $\mathcal{F}(\sigma_{UL})$, the explicit substitution is [2] :

$$\mathcal{F}(\sigma_{UL}) \quad \longrightarrow \quad \int_0^\infty G(\sigma_{UL}\,;\,\sigma^0_{UL}(\Delta\kappa), v_{\sigma_{UL}}) \;\times\; \mathcal{F}(\sigma_{UL}) \quad d\sigma_{UL}\ , \qquad (11.1)$$

where $v_{\sigma_{UL}} = 35\% \times \sigma_{UL}$. It must be stressed that this is a rather artificial treatment of a theoretical error that is difficult to incorporate naturally into a coupling constraint. The results thereby obtained should only be treated as a rough indication of the effect that such uncertainties can have on the final sensitivity to anomalous $WW\gamma$ couplings. In fact the results obtained with this prescription are similar to those that would be derived by converting the cross section upper limit directly into coupling constraints assuming a W production cross section that is 35% low throughout.

Figures 11.2 and 11.3 show how the cross section upper limit translates into limits on $\Delta\kappa$ and λ respectively using this procedure. The estimated theoretical error band is given by the dashed parabolae in each case. Incorporating the theory error results in roughly a 25-35% worse constraint on the anomalous couplings than would be obtained by using the central curve only. The final 95% confidence level constraints on $\Delta\kappa$ and λ are therefore :

$$\begin{aligned} -9.6 &< \Delta\kappa < 5.8\ , \\ -10.3 &< \lambda < 10.3\ . \end{aligned} \qquad (11.2)$$

These limits represent a significant improvement on the constraints resulting from an anal-

---

[1] This is probably too conservative, since W production for large anomalous couplings is dominated by DIS type production for which photon structure related uncertainties are relatively less important.

[2] Again, treating the theory error as Gaussian, the W production cross section thereby extending downwards to very small cross sections, is probably too conservative.

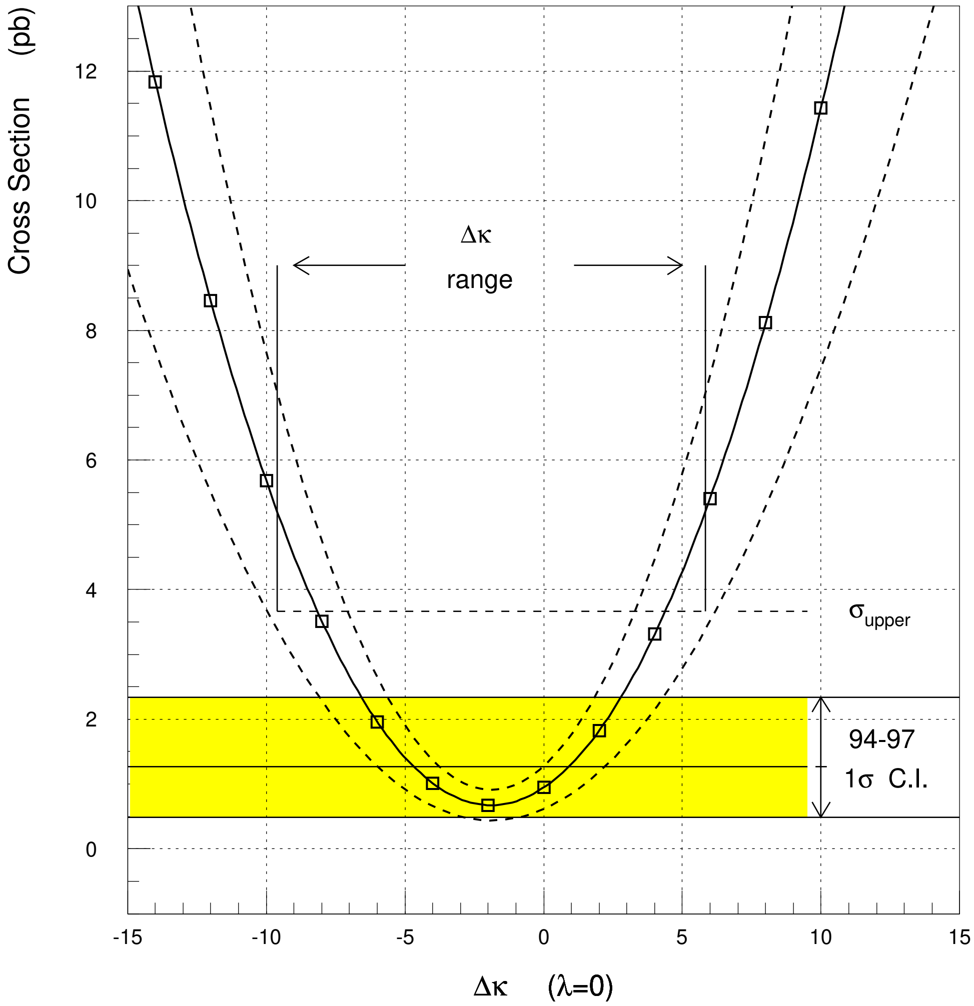

Figure 11.2: *The extraction of* 95% *confidence level constraints on the anomalous* $WW\gamma$ *coupling* $\Delta\kappa$ *for* $\lambda = 0$ *. The coupling limits in the absence of any theoretical uncertainties correspond to the intersection of the dashed horizontal line with the solid parabola. The dashed parabolae on either side of the solid curve represent the* 35% *theoretical error on the W production cross section. The range of allowed values for* $\Delta\kappa$ *corresponding to the indicated cross section upper limit is shown, where the theory error has been taken into account. The shaded band is the* 1σ *confidence interval corresponding to the measured cross section for* $e^+p \to e^+W^\pm X$ *.*

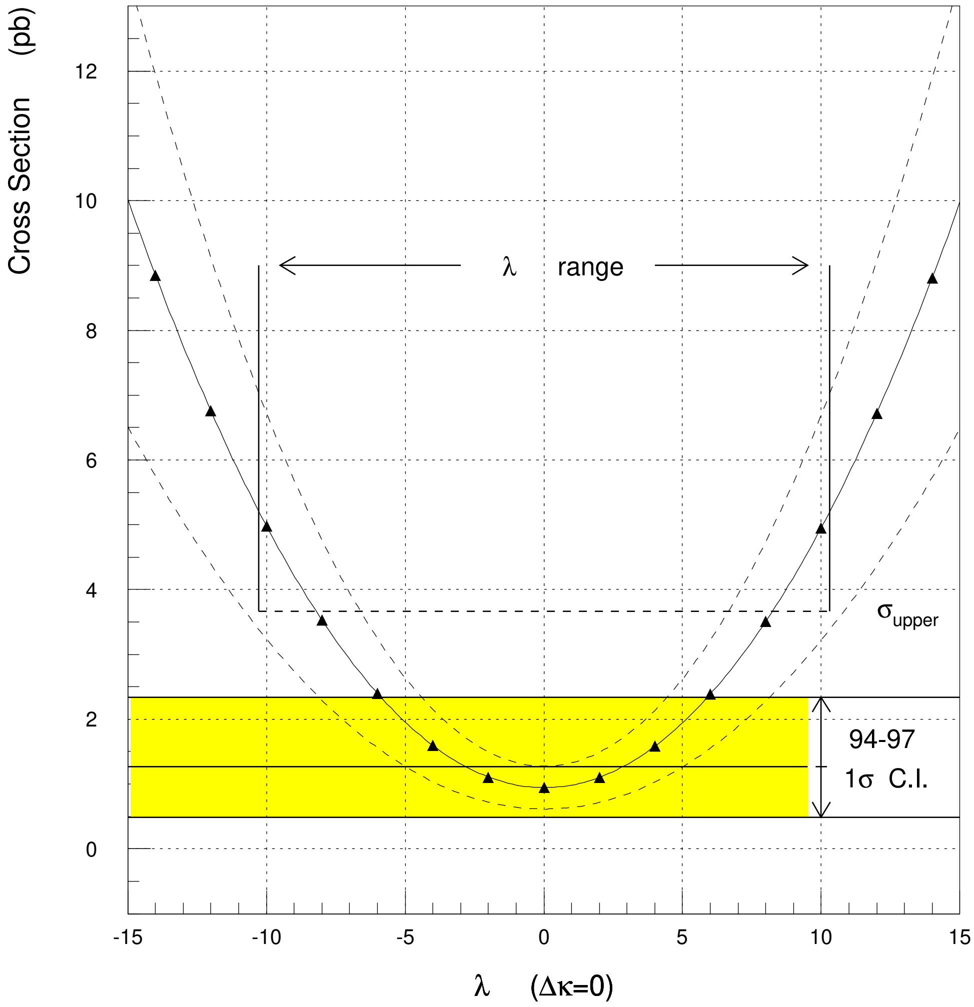

Figure 11.3: *The extraction of* 95% *confidence level constraints on the anomalous* $WW\gamma$ *coupling* λ *for* $\Delta\kappa = 0$ *. The coupling limits in the absence of any theoretical uncertainties correspond to the intersection of the dashed horizontal line with the solid parabola. The dashed parabolae on either side of the solid curve represent the* 35% *theoretical error on the* W *production cross section. The range of allowed values for* λ *corresponding to the indicated cross section upper limit is shown, where the theory error has been taken into account. The shaded band is the* 1σ *confidence interval corresponding to the measured cross section for* $e^+p \to e^+W^\pm X$ *.*

ysis of a smaller sample of ZEUS data published in [1] and are the best current constraints from e^+p collisions. They are, however, a weaker set of constraints on the couplings at the $WW\gamma$ vertex than is provided by recent measurements at the LEP II and Tevatron colliders and discussed in section 3.5.2. It is clear that single W production at HERA will always yield the tightest constraint for positive values of $\Delta\kappa$, in contrast to the case at the Tevatron where the analysis of radiative W production yields rather symmetric constraints on $\Delta\kappa$ significantly poorer than those on λ. For this reason the analysis of large luminosity data samples at HERA will provide information on $WW\gamma$ couplings complementary to that available from other colliders [37].

11.2 W Production and Decay $W \to \mu\nu$

Unlike the analysis of $W \to e\nu$ decays, the selection of $W \to \mu\nu$ events is not only on the basis of the W decay products but, in the case of events with missing p_T, relies on the recoiling hadrons to trigger the event. Since W production in the presence of anomalous couplings gives rise to events with large hadronic transverse momenta, this sample is particularly suited to searches for anomalous W production. Any measurement of the Standard Model W production cross section in the muon channel will, however, require a less biased selection such as that afforded by the barrel (and, in the future, forward) muon chambers. Combining the missing p_T and barrel muon chamber samples gives rise to the selection efficiencies in the various W production channels listed in table 11.1, where the extra cuts introduced in the analysis of the 1997 barrel muon data have been applied. The overall combined acceptance of $\sim 19\%$ is still less than half the acceptance in the electron channel, due mainly to the reliance on the CTD momentum measurement at small polar angles and the limited coverage of the barrel muon chambers in the polar angle region populated by W decay leptons.

11.2.1 Events with Large Hadronic Transverse Momenta

As mentioned in section 4.3, the predictions for the hadronic p_T spectrum at low transverse momenta are uncertain, due to approximations made in the calculation of the W photoproduction cross section. For large hadronic p_T's, the region most sensitive to non-Standard Model couplings, the spectrum should be well described by the Monte Carlo. In addition, a number of events with high p_T muons have been observed by the H1 experiment in a charged current sample containing events with calorimeter $p_T > 25$ GeV which also have

Method	Production Channel				Combined
	W^+ DIS	W^- DIS	W^+ PHP	W^- PHP	
Missing p_T	21.3 ±0.9 %	9.9 ±0.6 %	0 %	0 %	12.0 ±0.5 %
Barrel Muon	12.5 ±0.7 %	6.1 ±0.5 %	12.7 ±0.7 %	6.9 ±0.6 %	10.0 ±0.4 %
Combined	27.6 ±1.0 %	13.7 ±0.7 %	12.7 ±0.7 %	6.9 ±0.6 %	18.7 ±0.5 %

Table 11.1: *The efficiency for selecting $W \to \mu\nu$ events in the different W production channels for events with missing p_T and barrel muon triggered events, calculated using the 1995 Monte Carlo detector configuration. The combined values assume the mixture of deep inelastic and photoproduction type W production given in chapter 4. Statistical errors only are given.*

large hadronic transverse momenta [2]. It is therefore interesting to use the ZEUS data to place explicit constraints on the W production cross section at large hadronic transverse momenta. Fig. 11.4 shows the efficiency for selecting $W \to \mu\nu$ events in the missing p_T sample versus both the calorimeter p_T (required to be greater than 10 GeV in the analysis outlined in section 9.3) and the true struck quark p_T, all other cuts having been applied. The correlation between the two quantities is clear and for either transverse momentum above 20 GeV the selection efficiency is at least 30%, compared to a combined efficiency for selecting Standard Model $W \to \mu\nu$ events in this sample of only 12%.

The single surviving $W \to \mu\nu$ event in the 1994-97 missing p_T sample has a calorimeter p_T of only $\sim$ 12 GeV and a corrected hadronic p_T, an estimate of the struck quark p_T, of around 13 GeV. Therefore no data events survive a cut on either quantity of 20 GeV. Assuming the background to be negligible [3] and taking an efficiency of 30% (with the same systematic uncertainty calculated in section 9.3.1) gives rise to a 95% confidence level upper limit of 0.22 pb for high p_T W production and decay to muons. That is :

$$\sigma(e^+p \to e^+W^\pm X\ ;\ p_T > 20\ \text{GeV}) \quad <_{95\%} \quad 2.0\ \ \text{pb}\ , \tag{11.3}$$

where p_T denotes either the calorimeter or closely related hadronic transverse momentum. This excludes a high p_T W production cross section of sufficient magnitude to give rise to the four high p_T muon events observed by H1 in 24.7 pb^{-1} of data, assuming the given efficiency of 50-60% [4] for selecting events with hadronic $p_T > 30$ GeV [2]. It must be stressed, however, that the results of the two experiments are not directly comparable given, for example, the

---

[3] From fig. A.1 it can be seen that this only gives rise to a more conservative limit.

[4] A lower efficiency would only increase the calculated H1 cross section.

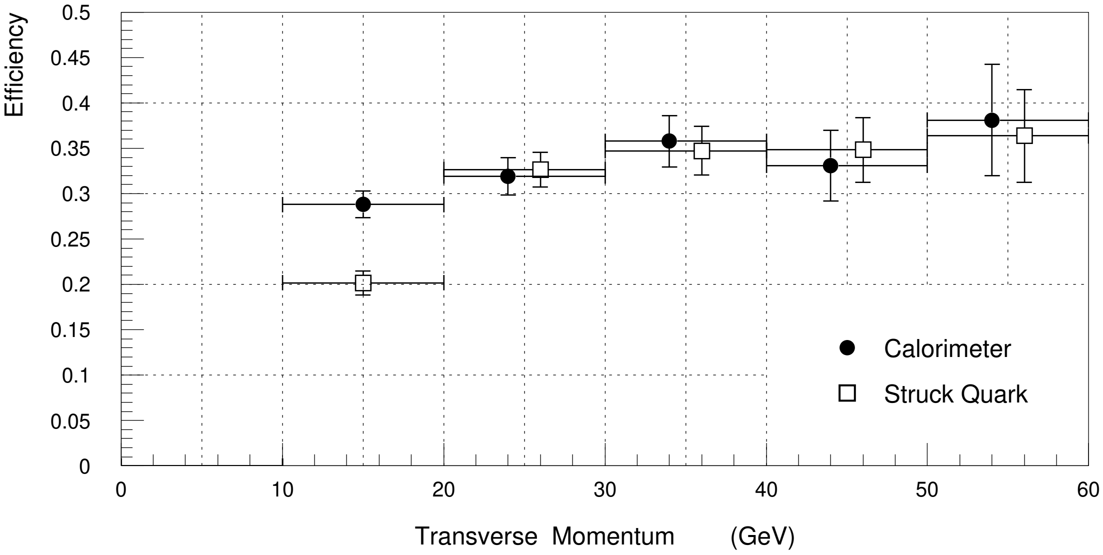

Figure 11.4: *The efficiency for selecting* $W \rightarrow \mu\nu$ *events in the missing* p_T *sample versus calorimeter* p_T *(points) and the true struck quark* p_T *(open squares) for Standard Model W production.*

different polar angle acceptances and detector resolutions. In particular, an enhanced rate of very forward going muon events might not be apparent in the sample selected here due to the implicit polar angle cut introduced by the requirement that the MIP matching track be well measured in the CTD.

11.3 Radiative Charged Current Scattering

It was shown in section 5.2 that the program WWGAMMA describing radiative charged current scattering including radiation from the W propagator agrees well with the event generator DJANGO for Standard Model $WW\gamma$ couplings, both in terms of the overall radiative cross section and the distributions of the final state particles. Moreover the data has been shown to be in good agreement with the DJANGO description of the process $e^+p \rightarrow \bar{\nu}\gamma X$. Therefore the upper limit on the anomalous production of isolated photons with $p_T > 10$ GeV, calculated in section 10.3 using the DJANGO calculated selection efficiency, can be interpreted as a constraint on the anomalous couplings $\Delta\kappa$ and λ using the WWGAMMA cross section parameterisations. Note that here, unlike the case of single W production, the theory error is assumed to be small. At most there is an uncertainty due to the choice of proton structure function and the current DIS data already constrains the total charged current cross section to much less than the 35% uncertainty on the W production cross section. In addition, the selection efficiency for radiative charged current scattering with relaxed topological cuts is assumed not to be a strong function of the anomalous $WW\gamma$ couplings themselves. Confirmation of this assumption requires, however, the inclusion of photon radiation from the W propagator into the full DJANGO event simulation.

The 95% confidence level upper cross section limit is shown in fig. 11.5 and the resulting anomalous coupling constraints are :

$$\begin{aligned} -18 &< \Delta\kappa < 27 \ , \\ -39 &< \lambda < 36 \ . \end{aligned} \tag{11.4}$$

The tightest constraint is on negative values for the coupling $\Delta\kappa$, in contrast to the case for single W production, but is nevertheless around a factor two worse than that given in 11.2 above. Such a factor in the relative sensitivity of the two measurements was anticipated in [63] for high luminosities. Although the agreement between the radiative charged current data and Monte Carlo confirms the current description of an interesting class of event, the information that can be extracted about couplings at the $WW\gamma$ vertex will probably only be important in the event that the measured rate of single W production is in conflict with Standard Model predictions. In addition a radiative charged current measurement may be useful in excluding certain combinations of anomalous couplings that give, in the case of single W production, cross sections close to the Standard Model value. This is discussed in section 11.6 below.

11.4 *Z* Production and Leptonic Decay

Combining the high mass e^+e^- and $\mu^+\mu^-$ search samples and the $Z^0 \rightarrow l^+l^-$ selection efficiencies results in an overall constraint on the Z production cross section :

$$\sigma(e^+p \rightarrow e^+Z^0X) \ \times \ BR(Z^0 \rightarrow l^+l^-) \ \ <_{95\%} \ \ 0.12 \ \ \text{pb} \ , \tag{11.5}$$

where $BR(Z^0 \rightarrow l^+l^-)$ is the branching ratio to a single charged lepton flavour. This combined limit is still roughly an order of magnitude larger than the Standard Model cross section. In general the prospect for isolating a clear signal for Z production in leptonic decay channels at HERA suffers from a combination of a small cross section and a smaller branching ratio to charged leptons than in the case of W production. Moreover, it may not be possible to separate any signal from the two photon background, as discussed in

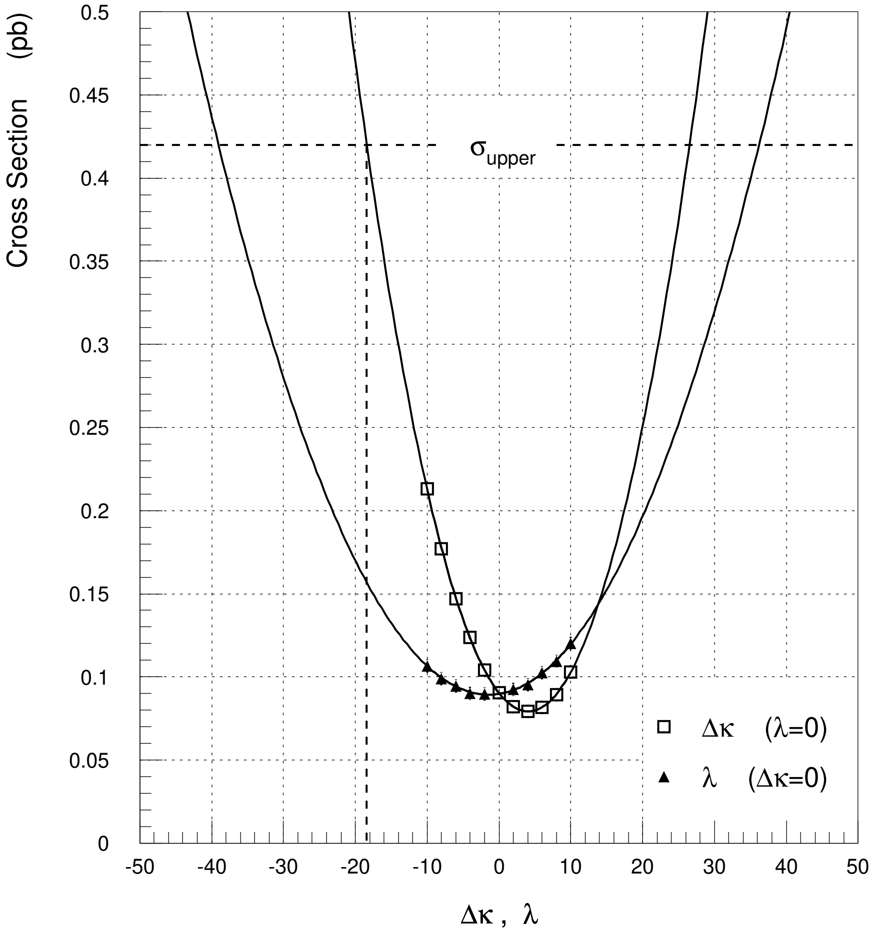

Figure 11.5: *The extraction of* 95% *confidence level constraints on the anomalous* $WW\gamma$ *couplings* $\Delta\kappa$ $(\lambda = 0)$ *and* λ $(\Delta\kappa = 0)$ *from the cross section upper limit for high* p_T *photon radiative charged current scattering. The best constraint, for negative values of the coupling* $\Delta\kappa$*, is explicitly indicated.*

sections 8.3.1 and 9.5.5. It is likely therefore that the main purpose of searches for high mass multi-lepton events at HERA will be to exclude certain exotic physics scenarios, some of which were outlined in chapter 3.

Interestingly, the $Z^0 \to \nu\bar{\nu}$ decay channel, of primary interest here as a background to the search for $W \to e\nu$ decays, may provide a means of measuring the Z production cross section at high luminosities. It remains to be seen, however, to what extent such a signal can be isolated from the W production and other backgrounds considered in section 8.1.1.

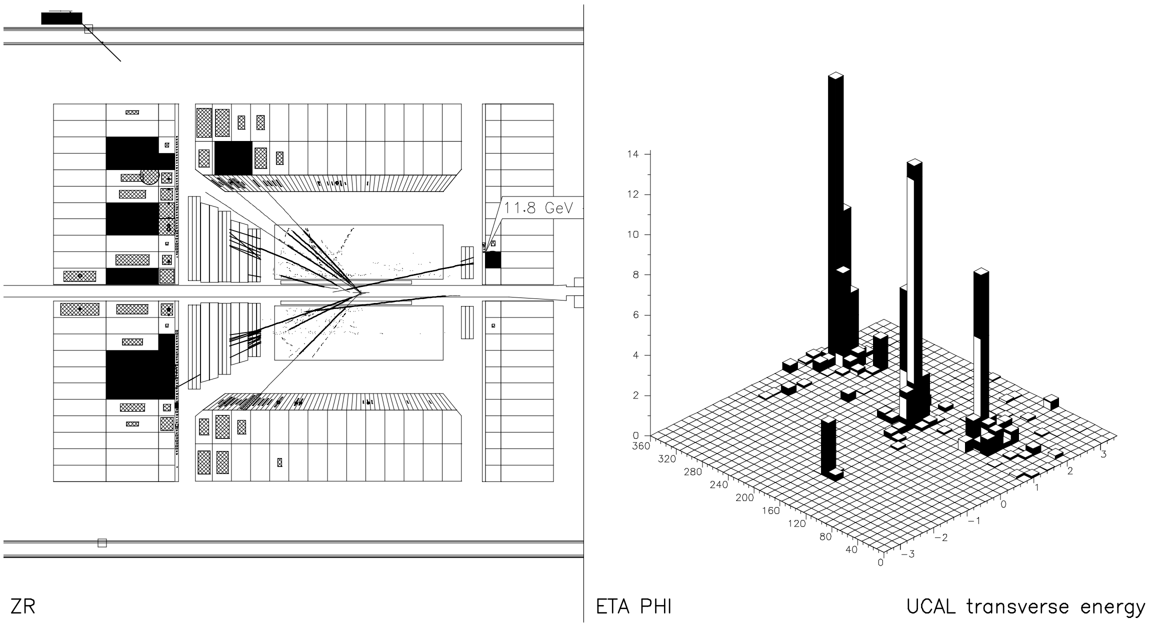

Figure 11.6: *A high invariant mass multi-jet event in the* $W/Z^0 \to jj$ *search sample. Three collimated jets are clearly visible in the* $\{\eta, \phi\}$ *view and a low energy electron in the RCAL. See text for more details.*

11.5 Hadronic Decay Channels

Although not considered here, the hadronic decay channels of the W and particularly the Z offer an increased event rate but suffer from difficult to evaluate QCD multi-jet backgrounds. Signal to background ratios can be increased, for example, by making use of the third jet from the struck quark in the case of DIS type W production and with higher luminosities a clear peak in the di-jet invariant mass spectrum should be visible [90], [91]. An example of a $W/Z^0 \to jj$ candidate event is shown in fig. 11.6, in which two jets combine to give an uncorrected [5] invariant mass of 72 GeV and a third jet, interpreted in the case of W or Z production as the current or struck quark jet, is also clearly visible in the $\{\eta, \phi\}$ view. In addition the low energy scattered positron is visible in the RCAL.

11.6 Discussion

As important as the first experimental estimate of the cross section for the process $e^+p \to e^+W^\pm X$ is the demonstration that it is possible to extract a clear signal for W production in both electron and muon decay channels at HERA. That is, signal to back-

---

[5] Jet energy corrections are significantly larger than those that have been applied here to measured lepton energies.

ground (S/B) ratios in excess of one are achievable with reasonable selection efficiencies. Given the limited size of the present data sample and hence the small numbers of events expected, the main objective here has been to maximise the efficiencies while paying less attention to the S/B ratio. It is correspondingly clear from many of the distributions comparing the signal to the combined background in chapters 8 and 9 that important selection cuts could be tightened in future to greatly increase the S/B ratio and isolate purer samples of leptonic W decay events. This statement relies on the generally good agreement between the data and the background Monte Carlo at all stages in the event selection, which is itself an important result given that neutral current events with missing energy or charged current events with fake electron signatures, for example, are atypical events that might not be well reproduced by current Monte Carlo's or the detector simulation.

11.6.1 Future Limits from Single W Production

The limits on anomalous $WW\gamma$ couplings derived here, although the first direct limits from e^+p collisions, are nevertheless not comparable to those currently being set by measurements at the LEP II and Tevatron colliders. It is worthwhile therefore to consider how anticipated future luminosities [6] might improve the sensitivity. A number of assumptions must be made in order to do this. Firstly, it is assumed that ZEUS will collect 1 fb^{-1} of data [7]. Then there will be around 100 events each from $W \to e\nu$ and $W \to \mu\nu$ decays. Secondly, an average selection efficiency in the two channels of 40% is assumed . This has already been exceeded in the search for $W \to e\nu$ events, but is a projection in the case of the $W \to \mu\nu$ analysis. Since in future the forward muon spectrometer will be included in the analysis and a micro-vertex detector and improved forward tracker should significantly improve the acceptance at small polar angles, a doubling of the current 20% combined muon acceptance is likely to be achieved. Therefore, a statistical error on the measured W production cross section in electron and muon channels of just over 10% is anticipated.

Much harder to estimate is the potential impact of remaining theory errors on a future measurement. Certainly with 1 fb^{-1} of data the parton densities in the proton will be known to far greater precision than they are now. A lot of data will also be available on the structure of the photon from HERA and elsewhere. Alternatively a cut may be made on the hadronic p_T, as considered in [50], to remove that part of the W production

---

[6] Discussed in section 2.1.3.

[7] Cross sections for e^+p collisions are used in this exercise. Sensitivities from both single W production and radiative charged current DIS will be further enhanced if, as seems likely, significant integrated luminosities are eventually accumulated in e^-p mode.

phase space most sensitive to the choice of photon structure function. Contributions to the theoretical uncertainty that are harder to estimate are those arising from the QCD scale and uncalculated QCD corrections. It has been suggested that observables such as the ratio of cross sections $\sigma(W)/\sigma(Z)$ are rather insensitive to QCD corrections [92] and may be used, although it is doubtful from the comments above relating to Z production that such quantities will ever be well measured at HERA. Nevertheless it is assumed here that the uncertainty on the Standard Model W production cross section can be significantly reduced in future and a figure of 10% is used, corresponding to the optimistic scenario considered in [50]. It should be mentioned here that future anomalous coupling constraints will almost certainly make use of the shape of the hadronic p_T distribution and not just the total cross section as considered here, allowing certain uncertainties arising from the overall normalisation to be further reduced [50]. Finally, it is assumed that systematic errors and errors arising from background subtraction can be made small compared to the statistical and theory uncertainties [8].

Assuming a measurement close to the Standard Model value and combining in quadrature the statistical and theory uncertainties, the parameterisations of section 4.1.4 can be used to estimate the constraints that will be placed on anomalous couplings $\Delta\kappa$ and λ with 1 fb^{-1} of data. The region of anomalous coupling parameter space that will be allowed at 1σ is indicated by the shaded region in fig. 11.7. The doughnut shape of this region is due to the W production cross section initially falling with negative values of $\Delta\kappa$ before rising as the anomalous contribution dominates the Standard Model and interference terms. The hole in the doughnut therefore corresponds to the 1σ lower bound on the measured cross section. At 2σ the lower bound is below the minima of fig. 4.5 and the allowed region is simply contained inside the dashed ellipse of fig. 11.7. In principle then, there will always be two preferred solutions for $\Delta\kappa$ (assuming $\lambda = 0$) given an accurate cross section measurement (again, other observables such as the hadronic p_T are not considered here). Measurements from other processes are needed to resolve the ambiguity. The possibility that one such process is radiative charged current scattering is discussed next.

11.6.2 Future Limits from Radiative Charged Current Scattering

The future sensitivity to anomalous couplings from the measurement of high p_T photon radiative charged current scattering is more speculative than for single W production. For

---

[8] Systematic uncertainties of $< 5\%$ are anticipated in future charged and neutral current cross section measurements.

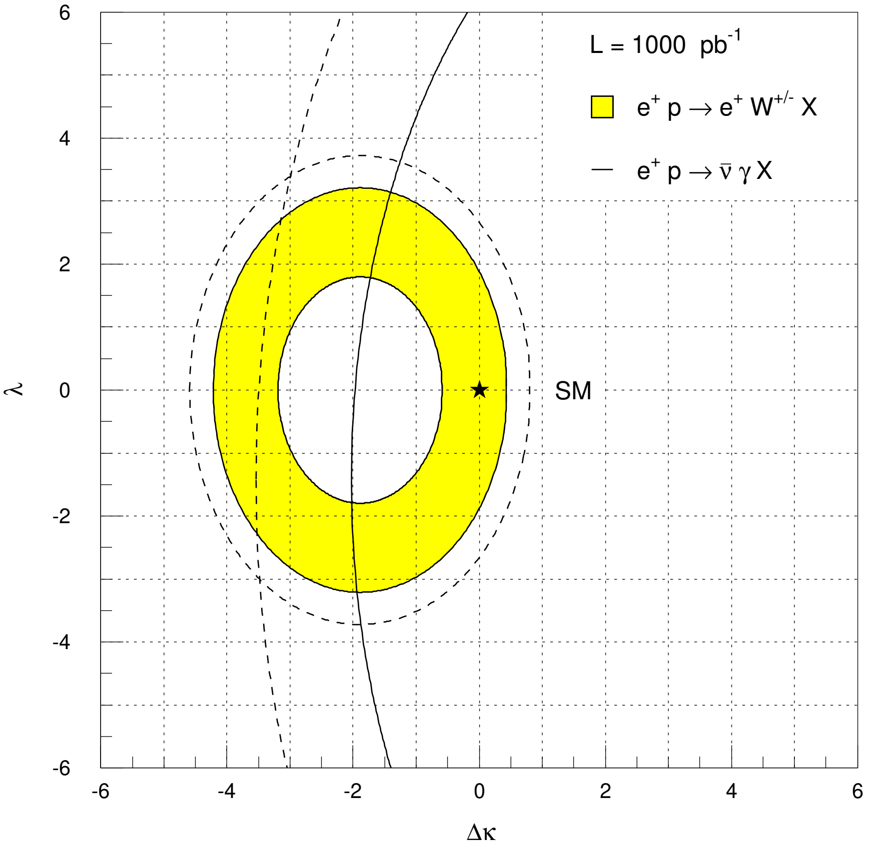

Figure 11.7: *The shaded region is an estimate of the* 1σ *constraint that will be placed on the anomalous coupling parameter space by a measurement of the single* W *production cross section in the combined channels* $W \to e\nu$ *and* $W \to \mu\nu$ *with a total integrated luminosity of* $1\ \mathrm{fb}^{-1}$. *Further assumptions are outlined in the text. The area to the left of the solid curve might be excluded by a measurement of the high* p_T *photon radiative charged current cross section with the same data set. The dashed curves give the corresponding* 2σ *exclusions.*

example the fraction of 'sensitive' events, or those containing high p_T radiated photons isolated from the direction of hadrons is, from table 8.4, only around 1/3. More detailed studies and, in particular, the optimisation of the sensitivity to anomalous couplings $\Delta\kappa$ and λ will require the inclusion of the full set of diagrams for radiative charged current scattering into DJANGO. It is therefore simply assumed here that high p_T radiated photons can be selected in 1 fb^{-1} of data with the same efficiency calculated in section 8.2.1 and effectively separated from poorly isolated photons and more importantly fake photon backgrounds. The resulting statistical precision with which the high p_T photon radiative charged current cross section might then be measured is around 16%. One attractive feature of radiative charged current scattering is that the theoretical uncertainties are comparatively small and remaining uncertainties, for example due to proton structure functions, will be greatly constrained by future precision cross section measurements.

Using the parameterisations of fig. 5.6, the anticipated cross section measurement can be converted into constraints on $\Delta\kappa$ and λ, shown in fig. 11.7. Since the tightest constraint is for negative values of $\Delta\kappa$, the possibility exists that a measurement of the radiative charged current cross section can exclude at 1σ the large negative values of $\Delta\kappa$ consistent with a Standard Model single W production cross section measurement.

It is clear from fig. 11.7 that the lower bound on $\Delta\kappa$ and to a lesser extent the constraints on λ will depend crucially on the final precision of both the single W production and radiative charged current cross section measurements and how they can be combined. Regardless of these issues, the best constraint at HERA will be for positive values of $\Delta\kappa$ which, given the assumptions outlined above, will be at the level of 0.5 (1.0) units at 1σ (2σ) confidence. Somewhat better constraints have been anticipated in [37], mainly due to more optimistic efficiency and theoretical error projections and the inclusion of hadronic W decay channels. The more modest projection outlined here nevertheless puts a measurement of the $WW\gamma$ couplings at HERA in an interesting region given some of the constraints shown in fig. 3.7, although future measurements from LEP II and an upgraded Tevatron collider will probably establish the best pre-LHC anomalous coupling constraints.

11.7 Conclusions

This thesis has dealt with the reconstruction and analysis of ZEUS events containing high p_T electrons and muons. In particular events that have missing momentum, high transverse energy, or final states containing more than one lepton have been considered. As well as being signatures for many exotic physics processes, such events are expected from the leptonic decays of W and Z bosons at HERA.

The production of real or on-shell W and Z bosons at HERA are rare processes with cross sections of $O(1)$ pb. Moreover, the Standard Model cross section values suffer from large uncertainties, estimated here to be as large as 30-40% in the case of the dominant W production channel $e^+p \rightarrow e^+W^\pm X$.

The analysis of events containing a high p_T electron and missing p_T, with the preliminary inclusion of the full 1997 ZEUS data to give a total integrated luminosity of almost 47 pb^{-1}, has enabled the first estimate of the cross section for single W production in e^+p collisions to be made :

$$\sigma(e^+p \rightarrow e^+W^\pm X) \;=\; 1.3 \;{}^{+\,1.1}_{-\,0.8}\;\; (\text{stat}) \;\pm\; 0.2 \;\; (\text{syst}) \;\; \text{pb} \;\; . \qquad (11.6)$$

The measured cross section is in good agreement with the Standard Model value of ~ 1 pb. A 95% confidence level upper limit on the W production cross section in the electron channel has been converted into constraints on the anomalous $WW\gamma$ couplings $\Delta\kappa$ and λ. The best constraint is for positive values of $\Delta\kappa$ which, at 5.8 , is not comparable with limits currently being set by data from LEP II and the Tevatron. The large theoretical uncertainties in the W production cross section have a significant impact on the final sensitivity to the anomalous $WW\gamma$ couplings.

The muon data is consistent with the results from the electron channel but, without the inclusion of the very forward direction, the sensitivity to W production is significantly reduced. However, the analysis of events with high calorimeter and muon p_T yields a constraint on the W production cross section in the presence of large hadronic transverse momenta that is significant in the interpretation of high p_T muon events observed by the H1 experiment.

The search for Z production and decay to leptons currently yields cross section limits much larger than the expected Standard Model cross sections, primarily due to the small cross sections and branching fractions involved. Moreover the background from high invariant mass Bethe-Heitler l^+l^- production is significant and extracting a clear signal will be difficult even in the future, probably requiring the inclusion of the hadronic decay channels of the Z which are themselves plagued by large QCD backgrounds. Importantly, the ZEUS data has been shown to be in good overall agreement with the Standard Model predictions for the rate of high mass e^+e^- and $\mu^+\mu^-$ production.

Radiative charged current scattering offers another probe of the $WW\gamma$ vertex in ep collisions. The 1997 data includes several charged current events with high p_T isolated photons, the rate of which is sensitive to anomalous couplings at this vertex. Although the current limit on the cross section for $e^+p \to \bar{\nu}\gamma X$ of 0.42 pb cannot currently exclude anomalous couplings not already ruled out by the single W production constraints, it has been shown that in future the analysis of radiative charged current events, due to the different dependence of the cross section on $\Delta\kappa$ and λ, might play an important role in excluding certain combinations of these couplings.

In general the high p_T lepton data considered here has been shown to be in good agreement with Standard Model expectations, while future integrated luminosities of $O(10^3)$ pb^{-1} will greatly increase the sensitivity to many interesting signals for new physics. No search for exotic high p_T lepton events, however, can be performed without an understanding of real W and Z production at HERA. In addition, future constraints on anomalous $WW\gamma$ couplings of $O(1)$ from the analysis of single W production will complement measurements made at other colliders.

Appendix A

Statistical Methods

The most important statistical method in the search for processes with small cross sections or new physics signals is the setting of upper limits at a certain confidence level. For the larger luminosity samples considered in chapter 10 a handful of events are selected in the presence of significant backgrounds, for which the methods described in section A.2 are appropriate for extracting information about a possible signal.

A.1 Upper Limits

A.1.1 Upper Limits in the Presence of a Known Background

The case is considered of a search for a signal with mean μ_s in the presence of a known background process with mean μ_b. The probability of observing n_0 events is given by the sum of the possible signal and background contributions to n_0

$$\begin{aligned} P(n_0) &= \sum_{n_b=0}^{n_0} P(n_b\,;\,\mu_b)\,P(n_s = n_0 - n_b\,;\,\mu_s) \\ &= \sum_{n_s=0}^{n_0} P(n_s\,;\,\mu_s)\,P(n_b = n_0 - n_s\,;\,\mu_b)\ , \end{aligned} \tag{A.1}$$

which itself is a Poisson distribution with mean $\mu_s + \mu_b$:

$$P(n_0\,;\,\mu_s+\mu_b) = \frac{e^{-(\mu_s+\mu_b)}(\mu_s+\mu_b)^{n_0}}{n_0!}\ . \tag{A.2}$$

An upper limit N on the contribution from the signal process corresponds to the value of μ_s such that a random repeat of the experiment would yield *more* than n_0 events with probability $(1-\alpha)$. For example $\alpha = 0.1$ yields a 90% confidence level limit, and N is defined by the equation

$$1-\alpha = \sum_{n=n_0+1}^{\infty} \frac{e^{-(N+\mu_b)}(N+\mu_b)^{n}}{n!}$$

$$= \ 1 - \sum_{n=0}^{n_0} \frac{e^{-(N+\mu_b)}(N+\mu_b)^n}{n!} \ . \tag{A.3}$$

However, for certain combinations of μ_b and n_0 equation A.3 yields a negative upper bound N. Furthermore we know that n_b, the number of background events, can at most equal n_0, the number of observed events. It has therefore been suggested that the probability distribution for n_b that enters A.1 should be restricted to the range $0 \leq n_b \leq n_0$ and appropriately renormalised [93] :

$$P'(n_b\,;\,\mu_b) \ = \ P(n_b\,;\,\mu_b) \ / \sum_{n_b=0}^{n_0} P(n_b\,;\,\mu_b) \ . \tag{A.4}$$

The upper limit N on the signal is then always positive definite and given by the modified formula

$$1-\alpha \ = \ 1 - \frac{e^{-(\mu_b+N)} \sum\limits_{n=0}^{n_0} (\mu_b+N)^n/n!}{e^{-\mu_b} \sum\limits_{n=0}^{n_0} \mu_b^n/n!} \ , \tag{A.5}$$

as quoted in the Particle Data Book [94]. Equation A.5 can alternatively be derived in the Bayesian approach by assuming a uniform *a priori* distribution for the signal μ_s [95].

A.1.2 Incorporating Experimental Uncertainties

In general the estimate of the background contribution μ_b can have a non-negligible error associated with it. This is particularly the case if, for example, Standard Model processes that are themselves rare provide a background to the search for a new signal. Further experimental uncertainties that must be incorporated in a consistent way are those associated with the estimate of the efficiency, ϵ, with which the new signal is selected and the data luminosity, $\mathcal{L}$. Methods have been proposed for modifying the limit setting procedure in the presence of an uncertainty in the experimental sensitivity $\epsilon \times \mathcal{L}$, but become prohibitively complex in the case of additional background uncertainties [96].

The method adopted here is a simple modification of equation A.5 to incorporate the above errors, which are assumed to be Gaussian [1]. Writing

$$\mu_b = \mathcal{L} \times \sigma_b \ , \tag{A.6}$$

---

[1] In addition the physical parameters μ_b,$\mathcal{L}$ and ϵ are constrained to be positive and $\epsilon \leq 1$ is imposed before appropriately re-weighting the truncated Gaussian distributions. This is only important if the error on μ_b, $\mathcal{L}$ or ϵ is comparable to the mean value or the efficiency is very close to 1, in which case the Gaussian approximation is anyway questionable. A further refinement of this method might employ positive definite probability distributions, for example the log-normal distribution.

where σ_b is an effective background cross section, and

$$N = \mathcal{L} \times \epsilon \times \sigma_{UL} \ , \tag{A.7}$$

then the cross section upper limit σ_{UL} is defined by :

$$\begin{aligned} 1 - \alpha \quad &= \quad 1 - \int_0^\infty \int_0^\infty \int_0^1 I(\mathcal{L}, \sigma_b, \epsilon, \sigma_{UL}) \quad \times \\ & G(\mathcal{L} \, ; \, \mathcal{L}^0, v_{\mathcal{L}}) \ G(\sigma_b \, ; \, \sigma_b^0, v_{\sigma_b}) \ G(\epsilon \, ; \, \epsilon^0, v_\epsilon) \quad d\mathcal{L} \, d\sigma_b \, d\epsilon \ , \end{aligned} \tag{A.8}$$

where

$$I(\mathcal{L}, \sigma_b, \epsilon, \sigma_{UL}) = \frac{e^{-\mathcal{L}\,(\sigma_b + \epsilon\,\sigma_{UL})} \sum_{n=0}^{n_0} \left[\mathcal{L}\,(\sigma_b \, + \, \epsilon\,\sigma_{UL})\right]^n / n!}{e^{-\mathcal{L}\sigma_b} \sum_{n=0}^{n_0} \left(\mathcal{L}\,\sigma_b\right)^n / n!} \ . \tag{A.9}$$

Here G represents the Gaussian distribution for random variables $\mathcal{L}$,σ_b and ϵ with indicated mean values and standard deviations. Equation A.8 can be solved numerically, for example by the Newton-Raphson method.

As an example, consider a search in a data sample corresponding to 1 pb^{-1}, with an estimated efficiency to select signal events of 50%. If four events are observed, the lower solid line in fig. A.1 shows the 90% confidence level upper limit on the signal cross section as a function of the estimated background cross section, assuming that $\mathcal{L}$, ϵ and σ_b are all known with negligible error. The various other curves show the calculated upper limits for fractional errors $v_{\sigma_b} = 50\%$, $v_\epsilon = 20\%$ and $v_{\mathcal{L}} = 10\%$. Finally, the upper limit calculated in the presence of all three experimental uncertainties combined is given by the upper solid line.

As expected, the upper limit deteriorates in the presence of any experimental uncertainty. However, the difference between the naïve limit and that calculated in the presence of such uncertainties is relatively small, as reported elsewhere [96]. For example, in the region for which the number of observed events is roughly in agreement with the background expectation the combined affect of the above error sources is to increase the limit by $\leq 20\%$.

A.2 Maximum Likelihood Cross Section Determination

In chapter 10 a small number of events are selected in the presence of a significant expected background. Clearly in this case straightforward background subtraction is not applicable,

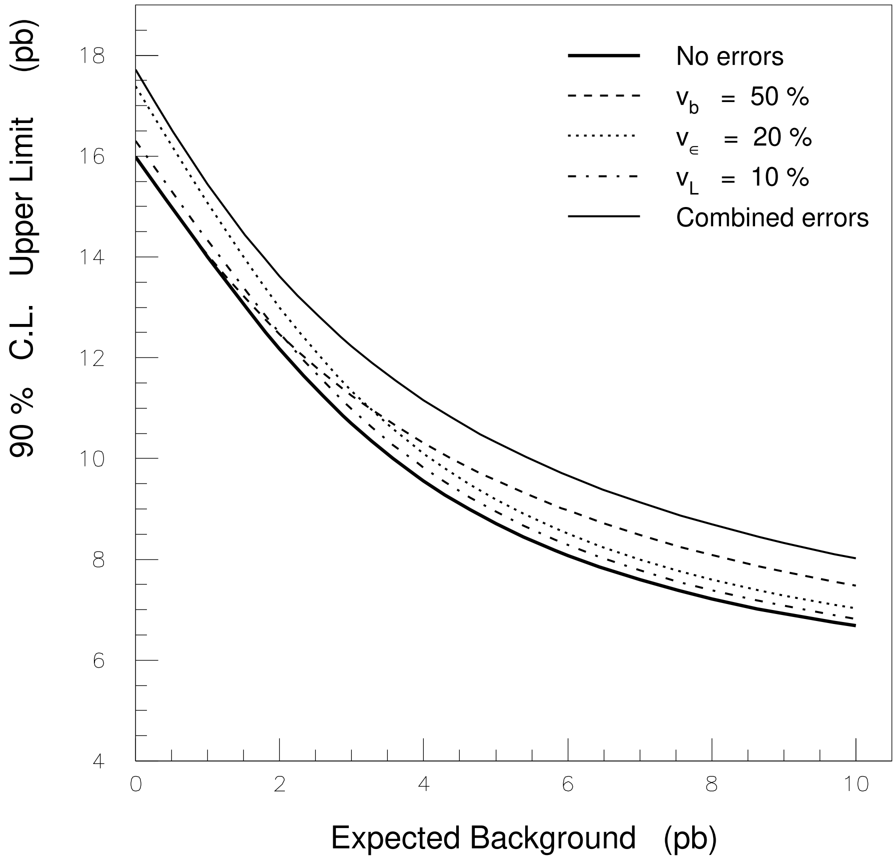

Figure A.1: 90% *confidence level upper limits for the experiment described in the text. The lower solid line is the upper limit calculated in the absence of experimental uncertainties and the upper solid line is the limit calculated with the combined errors indicated in the figure.*

since the background itself has a significant chance to fluctuate to the observed number of events. A suitable method for investigating the sensitivity to any signal in such a case, using the joint signal plus background probability distribution, is the method of maximum likelihood. The estimate of the mean number of signal events, S, in the presence of a mean expected background μ_b is given by the following equation :

$$\frac{d\ln\mathcal{L}(S)}{dS} = \frac{d}{dS}\ln\left(\frac{e^{-(S+\mu_b)}\,(S+\mu_b)^{n_0}}{n_0!}\right) = 0\ , \tag{A.10}$$

where n_0 once again represents the number of events observed and the argument of the logarithm on the right hand side is just given by equation A.2. Asymmetric 1σ confidence intervals are found in the conventional way by finding the higher and lower values of S for which $\ln\mathcal{L}$ falls by 0.5 from its peak. As an example, fig. A.2 shows the function $\ln\mathcal{L}(S)$ and the corresponding 1σ confidence interval for the case where the observed number of

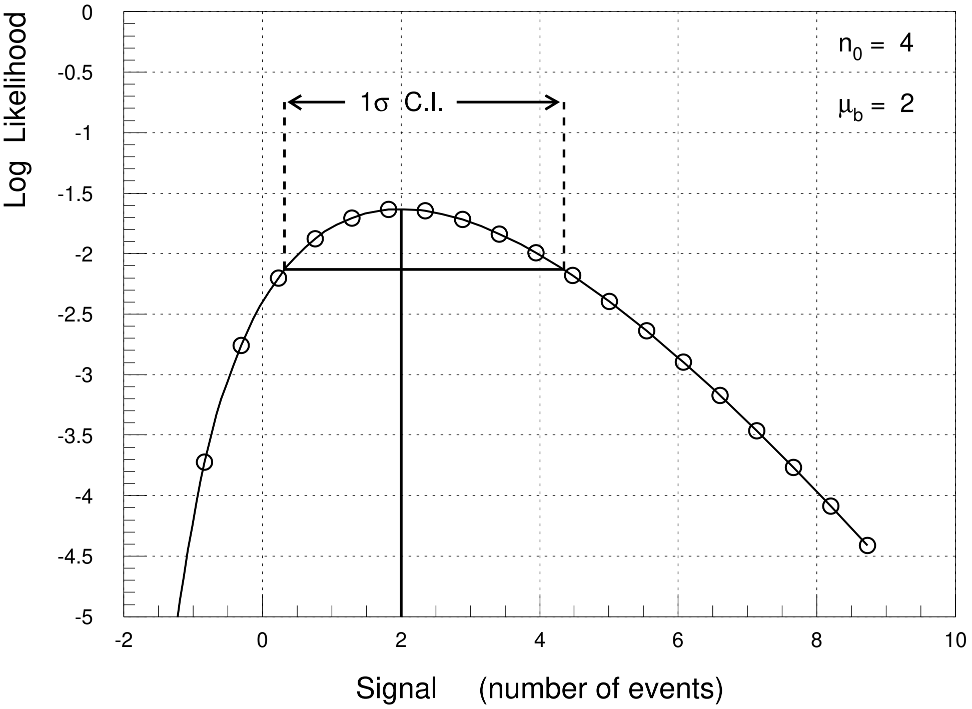

Figure A.2: *The log likelihood function for the case where 4 events are observed against an expected background of 2 events. The resulting* 1σ *confidence interval on the signal* S *is indicated.*

events is 4 against a mean background of 2 events.

Systematic uncertainties on the efficiency, luminosity and background estimate are taken into account by noting that the central value for the cross section estimate given by eq. A.10 is just :

$$\sigma_0 = \frac{n_0 - \mu_b}{\mathcal{L} \times \epsilon \times BR} \ , \tag{A.11}$$

where BR is the branching ratio for the decay in question. Errors on μ_b, $\mathcal{L}$ and ϵ are then propagated into errors on σ_0 which can be added in quadrature to give the total systematic uncertainty.

Bibliography

[1] D.S.Waters, 'Charged Current Deep Inelastic Scattering and W Production at HERA', in proc. of the 28th *International Conference on High Energy Physics*, ed. Z.Ajduk and A.K.Wroblewski, 1996.

[2] H1 Collaboration, 'Observation of Events with a High Energy Isolated Lepton and Missing Transverse Momentum at HERA', Abstract 708, submitted to *International Europhysics Conference on High Energy Physics, HEP97*, Jerusalem, Israel, August 1997.

[3] G.-A.Voss and B.H.Wiik,'The Electron Proton Collider HERA', *Ann. Rev. Nucl. Part. Sci.* **44**, 413 (1994).

[4] W.Bartel, E.Lohrmann and F.Willeke, 'HERA Upgrades and Impacts on Experiments', in proc. of the workshop on *Future Physics at HERA*, Vol. 2,p.1093, Eds. G.Ingelman, A.DeRoeck and R.Klanner, DESY (1996).

[5] R.Cashmore *et al.*, 'Electroweak Physics at HERA', in proc. of the workshop on *Future Physics at HERA*, Vol. 1,p.129, Eds. G.Ingelman, A.DeRoeck and R.Klanner, DESY (1996).

[6] F.Zetsche, 'Lepton Beam Polarisation at HERA', in proc. of the workshop on *Future Physics at HERA*, Vol. 1,p.222, Eds. G.Ingelman, A.DeRoeck and R.Klanner, DESY (1996).

[7] The ZEUS Collaboration, 'The ZEUS Detector', Status Report 1993, DESY(1993).

[8] The ZEUS Collaboration, 'The ZEUS Detector', Status Report 1989, or 'The Blue Book', DESY(1989).

[9] Jürgen Krüger, 'The Uranium Scintillator Calorimeter for the ZEUS Detector at the Electron-Proton Collider HERA', Internal Report, DESY F35-92-02 (1992).

[10] C.B.Brookes *et al.*, 'Development of the ZEUS central tracking detector', *Nucl. Instrum. Methods* A **283**, 477 (1989)

[11] B.Foster *et al.*, 'The design and construction of the ZEUS central tracking detector', *Nucl. Instrum. Methods* A **338**, 254 (1994).

[12] Krzysztof Piotrzkowski and Maciej Zachara, 'Determination of the ZEUS Luminosity in 1994',ZEUS Note 95-138.

[13] W.H.Smith *et al.*, 'The ZEUS Trigger System', ZEUS Note 89-084.

[14] F.Jacquet and A.Blondel, in proc. of the *Study for an ep Facility for Europe*, DESY 79-48, 391 (1979)

[15] S.Bentvelsen, J.Engelen and P.Kooijman, in proc. of the workshop on *Physics at HERA*, Vol. 1,p.23, Eds. W.Buchmüller and G.Ingelman, DESY (1992).

[16] ZEUS Collaboration, 'Observation of hard scattering in photoproduction at HERA', *Phys. Lett.* B **297**, 404 (1992)

[17] H1 Collaboration, 'Hard scattering in γp interactions', *Phys. Lett.* B **297**, 205 (1992)

[18] ZEUS Collaboration, 'Dijet Cross Sections in Photoproduction at HERA', *Phys. Lett.* B **348**, 665 (1995)

[19] ZEUS Collaboration, 'Measurement of the Proton Structure Function F_2 and $\sigma_{tot}^{\gamma^* p}$ at Low Q^2 and Very Low x at HERA', submitted to *Phys. Lett.* B.

[20] G.Ingelman and R.Rückl, 'Determination of Quark Distributions in ep Collisions', *Phys. Lett.* B **201**, 369 (1988).

[21] V.N.Gribov and L.N.Lipatov, *Sov. Journ. Nucl. Phys.* **15**, 438 (1972).

[22] G.Altarelli and G.Parisi, *Nucl. Phys.* B **126**, 297 (1977).

[23] Y.L.Dokshitser, *Sov. Phys. JETP* **46**, 641 (1977).

[24] D.C.Williams, 'The Neutral-Current Cross Section at High Q^2', ZEUS-Note 96-114. The latest NC results may be found in *Z. Phys.* C **74**, 207 (1997).

[25] ZEUS-Collaboration, 'Study of Charged-Current ep Interactions at $Q^2 > 200$ GeV^2 with the ZEUS Detector at HERA', *Z. Phys.* C **72**, 47 (1996).

[26] J.A.M. Vermaseren, 'Two-Photon Processes at Very High Energies', *Nucl. Phys.* B **229**, 347 (1983).

[27] H.Aihara *et al.*, 'Anomalous Gauge Boson Interactions',to be published in *Electroweak Symmetry Breaking and Beyond the Standard Model*, eds. T.Barklow, S.Dawson, H.Haber and J.Siegrist , FERMILAB-Pub-95/031 , hep-ph/9503425.

[28] K.Hagiwara, K.Hikasa, R.D.Peccei and D.Zeppenfeld, 'Probing the Weak Boson Sector in $e^+e^- \to W^+W^-$', *Nucl. Phys.* B **282**, 253 (1987).

[29] H.Aronson, 'Spin-1 Electrodynamics with an Electric Quadrupole Moment', PR **186**, 1434 (1969).

[30] K.J.Kim and Y.-S.Tsai, 'Magnetic Dipole and Electric Quadrupole Moments of the $W^\pm$ Meson', PRD **7**, 3710 (1973).

[31] H.Hagiwara, S.Ishihara, R.Szalapski and D.Zeppenfeld, 'Low-energy constraints on electroweak three gauge boson couplings', *Phys. Lett.* B **283**, 353 (1992).

[32] T.Barklow *et al.*, 'Anomalous Gauge Boson Couplings', to be published in proc. of the *1996 DPF/DPB Summer Study on New Directions in High-Energy Physics* ; hep - ph/9611454.

[33] M.S.Alam *et al.* (CLEO Collaboration), 'First Measurement of the Rate for the Inclusive Radiative Penguin Decay $b \to s\gamma$', *Phys. Rev. Lett.* **74**, 2885 (1995).

[34] S.Abachi *et al.* (DØ Collaboration), 'Limits on Anomalous $WW\gamma$ Couplings from $p\bar{p} \to W\gamma + X$ Events at $\sqrt{s} = 1.8$ TeV', *Phys. Rev. Lett.* **78**, 3634 (1997).

[35] B.Abbott *et al.* (DØ Collaboration), 'Limits on WWZ and $WW\gamma$ couplings from $p\bar{p} \to e\nu\ jjX$ events at $\sqrt{s} = 1.8$ TeV', *Phys. Rev. Lett.* **79**, 1441 (1997).

[36] F.Abe *et al.* (CDF Collaboration), 'Evidence for W^+W^- Production in $\bar{p}\,p$ Collisions at $\sqrt{s} = 1.8$ TeV', *Phys. Rev. Lett.* **78**, 4536 (1997).

[37] V.A.Noyes, 'Limits on $WW\gamma$ Couplings from Single W boson Production in ep Collisions', in proc. of the workshop on *Future Physics at HERA*, Vol. 1,p.190, Eds. G.Ingelman, A.DeRoeck and R.Klanner, DESY (1996).

[38] ZEUS Collaboration, 'Search for Leptoquarks with the ZEUS Detector', *Phys. Lett.* B **306**, 173 (1993).

[39] H1 Collaboration, ‘A search for Leptoquarks at HERA’, *Phys. Lett.* B **369**, 173 (1996).

[40] P.Haberl, H.-U.Martyn and F.Schrempp, ‘Contact Interactions and New Heavy Bosons at HERA’, in proc. of the workshop on *Physics at HERA*, Vol. 2,p.1133, Eds. W.Buchmüller and G.Ingelman, DESY (1992).

[41] J.Gilmore,‘Sensitivity of the ZEUS experiment to contact interactions at high integrated luminosities’, in proc. of the workshop on *Future Physics at HERA*, Vol. 1,p.256, Eds. G.Ingelman, A.DeRoeck and R.Klanner, DESY (1996).

[42] F.Boudjema *et al*, ‘New Leptons at HERA’, in proc. of the workshop on *Physics at HERA*, Vol. 2,p.1094, Eds. W.Buchmüller and G.Ingelman, DESY (1992).

[43] H1 Collaboration, ‘Search for Excited Fermions with the H1 Detector’, *Nucl. Phys.* B **483**, 44 (1997).

[44] ZEUS Collaboration, ‘A Search for Excited Fermions in e^+p Collisions at HERA’, DESY 97-112 (June 1997) , submitted to *Z. Phys.* C.

[45] R.Cashmore *et al.*, ‘Exotic Phenomena in High Energy ep Collisions’, *Phys. Rep.* **122**, 275 (1985).

[46] J.Butterworth and H.Dreiner, ‘R-parity violation at HERA’, *Nucl. Phys.* B **397**, 3 (1993).

[47] P.Schleper, ‘Searches for Minimal Supersymmetry at HERA’, in proc. of the workshop on *Future Physics at HERA*, Vol. 1,p.275, Eds. G.Ingelman, A.DeRoeck and R.Klanner, DESY (1996).

[48] H1 Collaboration, ‘A Search for Squarks of R_P - Violating SUSY at HERA’, *Z. Phys.* C **71**, 211 (1996).

[49] U.Baur,J.A.M.Vermaseren and D.Zeppenfeld, ‘Electroweak Vector Boson Production in High-Energy ep Collisions’, *Nucl. Phys.* B **375**, 3 (1992).

[50] U.Baur and D.Zeppenfeld, ‘Measuring the $WW\gamma$ Vertex in Single W Production at ep Colliders’, *Nucl. Phys.* B **325**, 253 (1989).

[51] C.F.Weizsäcker, *Z. Phys.* **88**, 612 (1934).

[52] E.J.Williams, *Phys. Rev.* **45**, 729 (1934).

[53] H.Plothow-Besch, 'PDFLIB : Nucleon, Pion and Photon Parton Density Functions and α_S Calculations', Users' Manual - Version 7.07, W5051 PDFLIB, 1996.12.09, CERN-PPE.

[54] A.D.Martin, W.J.Stirling and R.G.Roberts, 'Pinning down the glue in the proton', *Phys. Lett.* B **354**, 155 (1995) ; RAL Preprint, RAL/95-021 (1995).

[55] M.Glück, E.Reya and A.Vogt, *Phys. Rev.* D **45**, 3986 (1992).

[56] U.Baur (State University of New York at Buffalo, Buffalo, NY 14260), private communication.

[57] M.N.Dubinin and H.S.Song 'Anomalous W boson production at HERA', *Phys. Rev.* D **57**, 2927 (1998).

hep-ph/9708259, 1997.

[58] H.Spiesberger, DJANGO6 version 2.4, unpublished program manual (1996); version 1.0 described in G.A.Schuler and H.Spiesberger, in proc. of the workshop on *Physics at HERA*, Vol. 3,p.1419, Eds. W.Buchmüller and G.Ingelman, DESY (1992).

[59] H.Spiesberger, HERACLES version 4.5.2, unpublished program manual (1993); version 4.1 described in A.Kwiatkowski, H.-J.Möhring and H.Spiesberger, in proc. of the workshop on *Physics at HERA*, Vol. 3,p.1294, Eds. W.Buchmüller and G.Ingelman, DESY (1992).

[60] G.Ingelman, LEPTO 6.1, in proc. of the workshop on *Physics at HERA*, Vol. 3,p.1366, Eds. W.Buchmüller and G.Ingelman, DESY (1992); G.Ingelman, A.Edin, J.Rathsman, *LEPTO 6.5 - A Monte Carlo Generator for Deep Inelastic Lepton-Nucleon Scattering*, April 1996, DESY 96-057 (hep-ph/9605286).

[61] L.Lönnblad *Comp. Phys. Commun.* **71**, 15 (1992) ; L.Lönnblad, in proc. of the workshop on *Physics at HERA*, Vol. 3,p.1440, Eds. W.Buchmüller and G.Ingelman, DESY (1992).

[62] T.Sjöstrand *Comp. Phys. Commun.* **39**, 347 (1986) ; T.Sjöstrand and M.Bengtsson *Comp. Phys. Commun.* **43**, 367 (1987) ; T.Sjöstrand, CERN-TH.6488/92.

[63] T.Helbig and H.Spiesberger, 'Testing anomalous $WW\gamma$ couplings in radiative charged current ep scattering', *Nucl. Phys.* B **373**, 73 (1992).

[64] A.D.Martin, R.G.Roberts and W.J.Stirling, 'Precision analysis of $\Lambda_{\bar{M}S}$ and the gluon distribution and its implications for jet and top-quark cross sections', *Phys. Rev.* D **43**, 3648 (1991).

[65] A.D.Martin, R.G.Roberts and W.J.Stirling, 'Parton distributions for low Q^2', *Phys. Rev.* D **51**, 4756 (1995).

[66] G.Marchesini, B.R.Webber, G.Abbiendi, I.G.Knowles, M.H.Seymour and L.Stanco, *Comp. Phys. Commun.* **67**, 465 (1992).

[67] S.P.Baranov *et al.*, 'LPAIR - A Generator for Lepton Pair Production', in proc. of the workshop on *Physics at HERA*, Vol. 3,p.1478, Eds. W.Buchmüller and G.Ingelman, DESY (1992).

[68] Michele Arneodo and Luciano Lamberti, 'DIPSI Generator Update', ZEUS-Note 96-021.

[69] T.Carli *et al.*, 'Quasi-real QED Compton Monte-Carlo', in proc. of the workshop on *Physics at HERA*, Vol. 3,p.1468, Eds. W.Buchmüller and G.Ingelman, DESY (1992).

[70] GEANT 3.13: R.Brun, CERN DD/EE/84-1 (1987).

[71] ZGANA, ZEUS trigger simulation library, Els de Wolf (editor) *et al.*.

[72] Subroutine CALCORR, PHANTOM user library.

[73] R.Sinkus, H.Abramowicz and A.Caldwell, 'Neural Network based Electron Identification in the ZEUS Calorimeter', DESY 95-054 (1995).

[74] Subroutine ISLAND, PHANTOM user library. The island finding algorithm is explained in more detail in documentation to subroutine ISLANDS, PHANTOM user library; L.Wai, 'Search for Right-Handed Neutrinos at ZEUS', ZEUS-Note 94-126.

[75] Subroutine SirA95, PHANTOM user library.

[76] Subroutine elec5, PHANTOM user library.

[77] T.Doeker, A.Frey and M.Nakao, 'Electron Positron Reconstruction - Update of the ELECPO routines - (May 1994)', ZEUS-Note 94-23.

[78] Subroutine TRKCLU1, PHANTOM user library ; F.Wilson (CERN), private communication.

[79] Subroutine CALMIP, PHANTOM user library. Method of combining islands (condensates) described in L.Wai, ‘A Muon Separator’, ZEUS-Note 93-012.

[80] S.Limentani, M.Posocco and L.Stanco, ‘Muon Barrel Reconstruction’, ZEUS-Note 92-027.

[81] W.H.Smith *et al.*, ‘The ZEUS Calorimeter First Level Trigger’, *Nucl. Instrum. Methods* A **355**, 278 (1995).

[82] F.Chlebana, ‘Description of the ZEUS Global Second Level Trigger in 1994’, ZEUS-Note 94-102.

[83] Frédéric Bérnard *et al.*,‘The 1995 TLT Filter Software’, ZEUS-Note 95-164.

[84] CTEQ Collaboration, MSUHEP-60426, CTEQ-604.

[85] J.Alitti *et al.* (UA2 Collaboration), ‘An improved determination of the ratio of W and Z masses at the CERN $\bar{p}p$ collider’, *Phys. Lett.* B **276**, 354 (1992).

[86] Alessandro Bertolin (INFN Padua, Italy), private communication.

[87] Subroutine MBDEADLST, A.Bertolini (INFN Padua, Italy), private communication.

[88] Subroutine EMENERGYCORRECTION, B.Straub (Columbia University, New York), private communication.

[89] Subroutine CORANDCUT, J.Grosse-Knetter (Oxford, UK), private communication.

[90] H.Baer, J.Ohnemus and D.Zeppenfeld, ‘Hadronic W- decays at HERA’, *Z. Phys.* C **43**, 675 (1989).

[91] G.Grzelak (Institute of Experimental Physics, Warsaw University), ‘Production of Intermediate W and Z Bosons in ep Interactions at 300 GeV Center of Mass Energy’, Ph.D. Thesis.

[92] C.S.Kim, Jungil Lee and H.S.Song, ‘Anomalous gauge-boson couplings in high energy ep collisions’, *Z. Phys.* C **63**, 673 (1994).

[93] G.Zech, ‘Upper Limits in Experiments with Background or Measurement Errors’, *Nucl. Instrum. Methods* A **277**, 608 (1989).

[94] L.Montanet *et al.* (Particle Data Group), 'Review of Particle Properties', *Phys. Rev.* D **54**, 1 (1996).

[95] O.Helene, 'Upper Limit of Peak Area', NIM **212**, 319 (1983).

[96] R.D.Cousins and V.L.Highland, 'Incorporating Systematic Uncertainties into an Upper Limit', NIMA **320**, 331 (1992).